Fluid-structure interaction modelling of the left atrium and the mitral valve

A numerical and experimental study

Meskin, Masoud

Publication date:
2022

Document Version
Publisher's PDF, also known as Version of record

DTU Health Tech
Department of Health Technology

Ph.D. Thesis

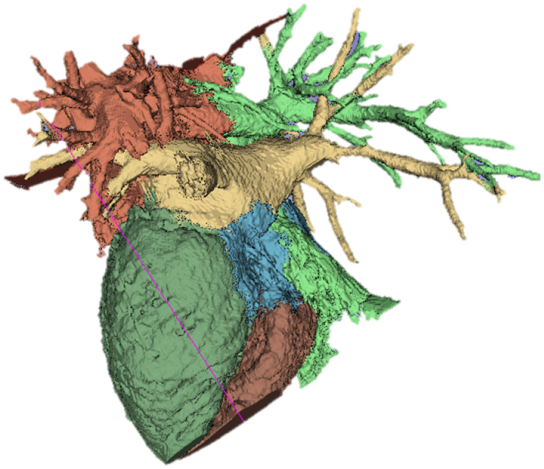

Fluid-structure interaction modelling of the left atrium and the mitral valve - A numerical and experimental study

Author: Masoud Meskin

Supervisor: Assoc. Prof. Marie Sand Traberg, Ph.D.
Co-supervisors: Prof. Jørgen Arendt Jensen, Ph.D., Dr. Techn., Assoc. Prof. Matthias Bo Stuart, Ph.D.

Technical University of Denmark, Kgs. Lyngby, Denmark, 2022

Cover image: A sagittal view of a segmented left heart structure from CT images, created by the author.

Cardiovascular biomechanics group
Department of Health Technology
Technical University of Denmark
Ørsteds Plads
Building 349
2800 Kgs. Lyngby, Denmark

Preface

This Ph.D. thesis has been submitted to the Department of Health Technology at Technical University of Denmark (DTU) in partial fulfillment of the requirements for acquiring the Ph.D. degree. The research providing the foundation for this thesis has been conducted for three years, from December 1st, 2018 to November 30th, 2021, in the cardiovascular bionechanics group, at the Department of Health Technology. The project has been supervised by Assoc. Prof. Marie Sand Traberg, and co-supervised by Prof. Jørgen Arendt Jensen and Assoc. Prof. Matthias Bo Stuart.

Masoud Meskin
Kgs. Lyngby, Denmark
November 2021

Contents

Summary

The left atrium and the mitral valve are the complex components of the human left heart which plays a crucial role in healthy cardiac function. Many cardiac diseases are attributed to the left atrium and the mitral valve, though the mechanics and hemodynamics of these components are not completely understood. In this numerical and experimental study, the mechanics and hemodynamics of the left atrium and the mitral valve was investigated. In the numerical study, using finite element analysis, a 2D and 3D simplified fluid-structure interaction model of coupled left atrium and mitral valve, and a realistic fluid-structure interaction model of the left atrium were designed and developed. The simplified and realistic models provided the opportunity to investigate the physiology and pathology of the left atrium and the mitral valve. In the experimental study, a novel left heart mock circulatory loop was designed and built and the hemodynamics of the left atrium and the mitral valve was investigated. To this aim, a left atrial chamber was molded, using invented in-house hyperelastic material, which can mimic the left atrium physiologic compliance. Having a hyperelastic left atrial chamber made it possible to design a mockloop which can mimic both the systolic and diastolic left heart phasic functions. Moreover, three more left atrial chambers with various compliance were molded and utilized in the mockloop, and then the impact of the left atrial compliance on the left heart hemodynamics was inspected. Both numerical and experimental studies opened new chapters in the perspective of studying left atrium and mitral valve, and can be developed further to be used in clinically oriented research. The numerical model of the realistic left atrium can be improved to couple with a realistic mitral valve geometry. Moreover, the mock circulatory loop can be developed to have a hyperelastic left ventricle instead of the rigid one, so it can replicate the physiologic function of the left heart.

Resumé

Det venstre forkammer og mitralklappen er komplekse komponenter i menneskets venstre hjertehalvdel, som spiller en afgørende rolle i hjertets mekaniske funktion. Mange hjertesygdomme tilskrives venstre forkammer og mitralklappen, selvom disse komponenters mekanik og hæmodynamikken omkring dem ikke er fuldstændigt forstået. I denne numeriske og eksperimentelle undersøgelse blev mekanikken og hæmodynamikken i venstre forkammer og omkring mitralklappen undersøgt. I den numeriske undersøgelse, ved hjælp af finite element-analyse, blev en simplificeret 2D og 3D fluid-struktur interaktionsmodel af venstre forkammer i sammenspil med mitralklappen, samt en realistisk fluid-struktur interaktionsmodel af venstre forkammer, designet og udviklet. De simplificerede og realistiske modeller gav mulighed for at undersøge fysiologien og patologien af venstre forkammer og mitralklappen. I den eksperimentelle undersøgelse blev en banebrydende strømningsmodel af venstre hjertehalvdel designet og konstrueret, og hæmodynamikken i venstre forkammer og gennem mitralklappen blev undersøgt. Til dette formål blev en model af venstre forkammer støbt i et innovativt in-house hyperelastisk materiale, som kan efterligne venstre forkammers fysiologiske eftergivelighed. Med en model af venstre forkammer med hyperelastiske vægge var det muligt at designe en eksperimentel opstilling af en strømningsmodel, som kan efterligne både den systoliske og diastoliske fase i hjertets pumpefunktion. Desuden blev der yderligere støbt tre forkamre med forskellig eftergivelighed, og disse blev anvendt i strømningsmodellen. Derefter blev effekten af væggens eftergivelighed i venstre forkammer undersøgt, og indflydelsen på hæmodynamikken i venstre hjertehalvdel inspiceret. Både de numeriske og eksperimentelle undersøgelser åbnede nye kapitler i perspektivet omkring at studere venstre forkammer og mitralklappen, og kan udvikles yderligere til brug i forskning med klinisk anvendelse som mål. Den numeriske model af det realistiske venstre forkammer kan udvikles til at kobles med en realistisk geometrisk repræsentation af mitralklappen. Desuden kan den eksperimentelle strømningsmodel udvikles til også at inkludere en eftergivelig hyperelastisk model af venstre hjertekammer i stedet for det stive materiale i den nuværende udgave, så den kan efterligne den fysiologiske funktion i venstre side af hjertet.

Acknowledgments

I would like to express my sincerest gratitude and appreciation to my main supervisor Marie Sand Traberg who helped me a lot to conduct this complex phd project. She always did her best, with good faith, to support and provide me with everything i needed to succeed in this project. My sincerest thanks to my co-supervisors Jørgen Arendt Jensen and Matthias Bo Stuart for their generous guidance. Jørgen is truly professional and experienced in behaving and dealing with students, especially in tough moments. Matthias and Jørgen always came up with brilliant ideas which helped my project a lot. My heartfelt thanks to Peter Johansen, the head of cardiovascular experimental laboratory at Aarhus University, for opening the door to success in my project. His great personality along with his extensive knowledge in the field of cardiovascular engineering was a great help to me. I should also thank Steffen Ringgaard, in the MR research center at Aarhus University Hospital, who helped me generously with patience and extensive knowledge to conduct MR scans. My warmest thanks to Alberto Redaelli, the head of biomechanics group at Polytechnic University of Milan, for his enlightening consultations. I should also thank my assistants, Alexander Emil Kaspersen from department of cardiothoracic and vascular surgery at Aarhus University Hospital, and Signe Gram Sand and Philip Starkey from Aarhus university, for their contribution in this project. Their presence was a great help and heartwarming. A special thank to my colleague, Rasmus Hvid for his generous and heartwarming help during my phd study. Rasmus is a knowledgeable guy whose presence helped me to stabilize at the beginning of my phd. I should also thank my colleague Iman Taghavi for his scientific helps. His presence made me not feel alone. I should also thank Mikkel Schou, a lovely guy who generously helped me when I had questions. Special thank to Dr. Hilde Larsson at COMSOL A/S, who helped me a lot with patience and kindness in the numerical studies. Many thanks to Kseniya Chetverikova and Borislav Tomov whose kindness and friendship always gave me energy. Finally, i thank all other colleagues and friends who helped me in this journey.

Dedicated to my beloved parents and siblings,

Ferdos Joharifard and Mostafa Meskin

Matin and Mahsa

List of Figures

List of Tables

Abbreviations

AV	Aortic valve
AVF	Aortic valve flowrate
BC	Boundary condition
CFD	Computational fluid dynamics
CT	Computed tomography
CVDs	Cardiovascular disease
DFF	Diastolic forward flow
DT	Deceleration time
ED	Early diastolic
EOA	effective orifice area
EOL	Effective orifice length
FEA	Finite element analysis
FSI	Fluid-structure interaction
LA	Left atrium
LAA	Left atrial appendage
LAP	Left atrial pressure
LAV	Left atrial volume
LD	Late diastole
LH	Left heart

LIPV	Left inferior pulmonary vein
LSPV	Left superior pulmonary vein
LV	Left ventricle
LVP	Left ventricular pressure
MCL	Mock circulatory loop
MV	Mitral valve
MVF	Mitral valve flowrate
MVS	Mitral valve stiffening
p-v	Pressure-volume
PC-MRI	Phase contrast magnetic resonance imaging
PDE	Partial differential equation
PVF	Pulmonary vein flowrate
PVs	Pulmonary veins
RA	Right atrium
RF	Retrograde flow
RIPV	Right inferior pulmonary vein
RSPV	Right superior pulmonary vein
RV	Right ventricle
SFF	Systolic forward flow
Sys	Systolic
TEF	Total emptying fraction
TV	Transmitral velocity
VTI	Velocity time integration
VTI-ED	Early diastolic velocity time integration
VTI-LD	Late diastolic velocity time integration

Symbols

a_1	Systolic amplitude of pulsatile piston head waveform
a_2	Early diastolic amplitude of pulsatile piston head waveform
a_3	Late diastolic amplitude of pulsatile piston head waveform
$A_{P_{mean}}$	Mean pulmonary vein cross sectional area
A	Left atrial wall area
W_{AS}	Left atrial active stroke work
$C.C.$	Correlation coefficient
c_{NH}	Stress-like material parameter
ΔV_{ave}	Average volume difference of molded left atrial chamber
J	Determinant of the deformation gradient tensor
δ	Elongation
A_{EOA}	Late diastolic peak of effective orifice area
E_{EOA}	Early diastolic peak of effective orifice area
A_{EOL}	Late diastolic peak of effective orifice length
E_{EOL}	Early diastolic peak of effective orifice length
E_p	Percentage of expansion
E_R	Error residual
η	Blood dynamic viscosity
F_A	Tension force per unit area

$\vec{F}^{act}$	Activation force
$\vec{F}_{ext}$	External or volume force vector
$\vec{F}_f$	Applied force from fluid to the solid
σ_1	Maximum first principal stress
I_{1c}	first invariant of the right Cauchy-Green strain tensor
I_{3c}	Third invariant of the right Cauchy-Green strain tensor
$\bar{\bar{I}}$	Identity tensor
k	Stiffness
K	Bulk modulus
K_e	Kinetic energy
K_{tot}	Total spring stiffness
A_{LD}	Left atrium area at the end of late diastolic phase
A_{Sys}	Left atrium area at the end of systolic phase
λ_1	First principal stretch
LAP_{mean}	Mean left atrial pressure
n	Length of cardiac cycle
L	Length
c_i	Material parameters
dv	Mesh scale factor in moving mesh frame
dV	Mesh scale factor in undeformed frame
μ	Lamé parameter
N	Number of cardiac cycle
n_d	Normalized difference
n_s	Number of samples
$\vec{n}$	Normal vector
p	Fluid pressure
W_{PS}	Left atrial passive stroke work
D	Pulmonary veins diameter

$\bar{\bar{C}}$	Right Cauchy-Green strain tensor
R_d	Relative difference
R	Radius of the mitral valve effective orifice area
$R(t)$	Resting length
R_e	Reynolds number
ρ	Blood density
r_{solid}	Displacement of the left atrial wall
r_0	Optional deformation offset
s_1	First systolic peak of pulmonary vein flowrate profile
s_2	Second systolic peak of pulmonary vein flowrate profile
S_d	Standard deviation
$S_{d_{mean}}$	Mean standard deviation
$\bar{\bar{\sigma}}$	Solid domain stress tensor
σ	Cauchy (True) stress
σ_e	Engineering stress
S_k	Skewness
λ	Stretch
t_1	Systolic time span of pulsatile piston head waveform
t_2	Early diastolic time span of pulsatile piston head waveform
t_3	Late diastolic time span of pulsatile piston head waveform
θ	Current angle of mesh elements
θ_e	Angle of vertices in an ideal element
$\vec{u}_f$	Flow field velocity vector
U	Average flow speed
$\vec{u}_M$	Moving mesh velocity vector
$\vec{u}_s$	Solid deformation velocity vector

V_0	Volume of molded left atrial chamber prior to pressurization
V	Left atrial volume
V_{max}	Maximal left atrial volume
V_{min}	Minimal left atrial volume
$\vec{\omega}$	Vorticity
V_{preA}	Left atrial volume prior to left atrial contraction
$\psi(\bar{\bar{C}})$	Strain energy density function
$\bar{y}_s$	Mean stress value
y_s	Stress value
E	Young's modulus

Part I

Introduction

CHAPTER 1

Introduction

1.1 Background and Motivation

The world health organization describes cardiovascular diseases (CVDs) as the leading cause of death globally. Based on its report, 17.9 million people died because of CVDs in 2016, which constitutes 31% of all global deaths (Finegold, Asaria, and Francis 2013). Moreover, over the past 25 years, the number of new cases of CVDs increased significantly (Wilkins et al. 2017). Amongst CVDs, disease in the left heart (LH) is the most prevalent, associated with high morbidity and mortality. For instance, the mitral valve (MV) in the LH is more related with valvular disease, which, in severe cases, lead to heart failure or death (Turi 2004). Any interruption in the functionality of the MV leads to left atrium (LA) and left ventricle (LV) malfunctions, which disables the LH and causes other problems throughout the circulatory system like pulmonary hypertension and aneurysms.

Along with the increasing rate of the CVDs, advanced diagnostic methods, like medical imaging, are in growth which allow clinicians to diagnose CVDs better. However, the complexity of the CVDs create the need of having more accurate and robust methods. For instance, medical imaging provides cardiovascular structural information, however, it does not provide clinicians with functional information of the cardiac flow which can support diagnosis of many CVDs (Wong et al. 2017). Advances in numerical methods, like computational fluid dynamics (CFD) (Morris et al. 2016), finite element analysis (FEA), and 3D medical imaging techniques have enabled the quantification of the cardiovascular mechanics to generate patient-specific models for more accurate diagnosis (Lantz et al. 2019; Mihalef et al. 2011). Combining CFD techniques and imaging modalities can be deployed in designing patient-specific modeling of the cardiovascular system for pre-operation preparations, medical intervention trials and finding out post-operation outcomes (Taylor and Figueroa 2009). Despite of having progressed significantly in utilizing numerical methods and imaging modalities, it is still a long way to reach the goal of generating a patient-specific holistic model of cardiovascular mechanics and fluid dynamics.

1.2 Hypothesis and Objectives

The LH is the birthplace of many cardiovascular dysfunctions and there is a vast amount of research about the LV. However, most of the research do not take into account the LA in the analysis or they substitute the MV structure with a set of boundary conditions due

to the lack of a holistic heart model (Domenichini and Pedrizzetti 2015; Peirlinck et al. 2019). Most other studies simply substitute the LA with a pipe or a simplified chamber (Doenst et al. 2009; Domenichini, Pedrizzetti, and Baccani 2005), or in more recent cases the LA geometry is constructed by computed tomography (CT) image acquisitions, which only gives instances of the cardiac cycle (Lantz et al. 2019; Mihalef et al. 2011). Furthermore, the LH mechanical and fluid dynamic motion are triggered from the LA, and any complexity in this part propagates through the entire LH. For instance, Mihalef et al. (Mihalef et al. 2011) shows that the vortices in the LV are generated mainly from the pulmonary veins (PVs) which enter into the LV. Moreover, studying the LH without considering the MV may have a huge impact on the simulation results (Long et al. 2003; Schenkel et al. 2009). Hence, based on the shortages indicated above, there is a need to build and develop a holistic accurate dynamic model of the LH, including dynamics of the LA and the MV, to gain new insights about the LA biomechanics. Thereby, the model can help clinicians having precise diagnosis of and predicting different cardiac disease scenarios.

In this project, the dynamics of the LA and the MV will be investigated by combining numerical and experimental methods with advanced medical imaging. To this aim, a fluid-structure interaction (FSI) method based on FEA is employed to build a numerical model, and a novel LH mock circulatory loop (MCL) is built to validate the numerical model, experimentally. The end goal of the study is to construct a holistic model of the LA, including the MV, based on healthy cases to calculate the LA and the MV mechanics and hemodynamics parameters.

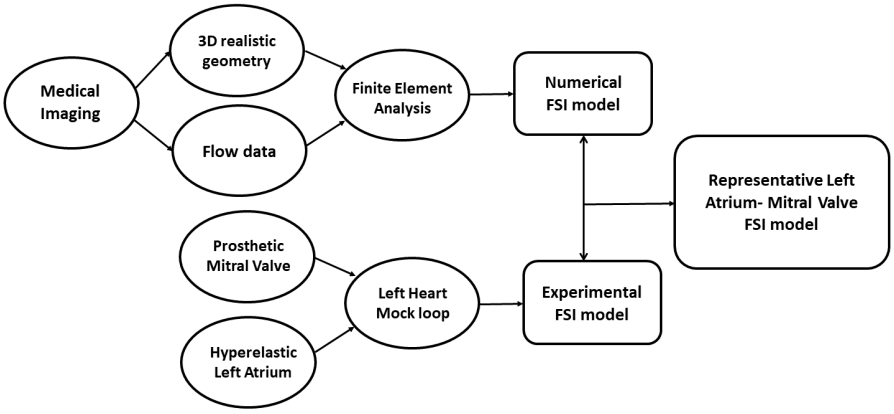

Figure 1.1: An overview of experimental and numerical 3D FSI modeling of the LA and the MV.

1.3 Intended outcomes

To accomplish the objectives, the modeling of the LA and the MV mechanics requires methods to: (a) Construct geometric models from CT, (b) Extract boundary conditions (BCs) from 4D phase contrast magnetic resonance imaging (PC-MRI) flow data, (c) Discretize the geometric model using automatic mesh generators and solving the equations governing blood flow, vessel wall dynamics and MV motion, (d) Visualize and quantify the mechanics and hemodynamics parameters, (e) Build a LH MCL with hyperelastic LA chamber to measure the mechanical and hemodynamic parameters (f) Validate the numerical model with the experimental set up. An overview of the above-mentioned steps is illustrated in Figure 1. The end goal of this project is to construct a representative LA-MV FSI model to gain better insight into the LA and the MV mechanics and hemodynamics.

1.4 Thesis structure

This study is divided into two main parts, 1) The numerical study and 2) The experimental study. In the numerical study, first the evolution of designing a 2D and 3D simplified LA and MV, and a realistic 3D LA is reported. Then, the results of the FSI simulations, using the simplified and realistic models, are presented and evaluated. At the end of the numerical part, the presented FSI simulation results are discussed. In the experimental study, the evolution of designing and developing the LH MCL is elaborated. In continue, the results of fluid dynamics measurements on the LH MCL are reported and analyzed. Then, the results of the measurements are discussed. Finally, the outcomes and limitations of the project are discussed and concluded, and suggested future works are presented.

Part II

Numerical study

CHAPTER 2

Background

The LA is one of the heart chambers which receives the oxygenated blood from lungs through the PVs and delivers it to the LV through the left atrio-ventricular valve, the MV. Then the LV pumps back the oxygenated blood to the body, through the aortic valve (AV).

The LA has three phasic functions in which it modulates filling of the LV and cardiovascular performance: 1) as a reservoir for the PVs return during LV systole, 2) as a conduit for passive blood flow from the PVs into the LV during early LV diastole, and 3) as a pump to actively empty into the LV during late diastole (LD) to boost the LV stroke volume. Any malfunctioning in one of the LA phasic functions generates and propagates complications to the LV chamber and disturbs the physiologic delivery of blood to the systemic circulation. Therefore, the mechanical function and hemodynamics indices of the LA are proven as strong markers of cardiovascular outcomes which augments the prognostics and predictability of many CVDs (Dodson et al. 2014; Gulati et al. 2013). However, examining the LA chamber functionality is a very challenging task, associated with several limitations and potential risks. For instance, measuring the left atrial pressure (LAP) in clinical examinations through measuring the pulmonary capillary wedge pressure is an invasive operation, imposing patients to cardiac damages.

Computational methods have become a fundamental tool in cardiac research which have enabled cardiologists to gain better insight into the cardiac biophysics without doing invasive measurements. Studying the cardiovascular system is a multiphysics enigma because it is driven by three physics, including electrophysiology, mechanics and fluid dynamics. Depending on the type of research, a computational model can be a combination of these physics (Lamata et al. 2014). One of the most common is the combination of solid and fluid mechanics which is used in FSI modelling (Mao et al. 2017; Vellguth et al. 2018; Wong et al. 2017).

FSI models give a comprehensive understanding of the cardiac mechanics and hemodynamics because they can demonstrate the counter effects of blood and cardiac chambers walls. Considering the LA as an example, during the reservoir phase the left atrial volume (LAV) increases as the blood flows into the LA chamber and in the last phase, during LA active pump function, the LA wall contracts as the result of depolarization, pushing the blood into the LV chamber. As it can be inferred, the fluid, means blood, and the solid, means the LA wall, affect each other simultaneously. Therefore, any cardiac model without considering this counter effect does not represent the cardiac function, correctly.

A few FSI studies have been done on the LA chamber. Lemmon and Yoganathan

(Lemmon and Yoganathan 2000a,b) employed the immersed boundary condition method to develop a 3D FSI thin-wall LH model including the LA and the LV tissue fibers, to investigate the LH hemodynamics during normal diastolic function and LV dysfunction. The model demonstrated in details the fluid flow development in the LH during diastolic function. It shows how flow develops in the LV while passing through the MV. Moreover, it presents a uniform transmitral velocity (TV) during the early diastolic (ED) phase and skewed TV during the LA contraction in the LD phase. Furthermore, the evolution and transmission of diastolic LAP and left ventricular pressure (LVP) is demonstrated. Despite of outstanding results, their model have some limitations such as 1) it does not represent the systolic (Sys) portion of the LH function, 2) the LA and the LV geometries are not realistic, 3) the model does not include the MV geometry, and 4) it is a thin-wall model.

In another study, Zhang and Gay (2008) investigated the effect of the left atrial appendage (LAA) on the LA hemodynamics by building a simplified LA and LAA CAD model including the LA tissue fibers. Like the Lemmon and Yoganathan's model, they used the immersed boundary condition method to develop the model. The findings of Zhang and Gay show that the ejection fraction of the LA reduces in atrial fibrillation which is an important biomarker of the thrombose formation. Furthermore, the magnitude of the peak of the ED portion of transmitral flowrate profile is greater in atrial fibrillation than sinus rhythm. Moreover, it is shown that the LAA is not functional in sinus rhythm, however, it increases the vortex formation in the LA. Therefore, in the atrial fibrillation condition, these high number of vortices are not washed out completely due to the absence of the LA contraction and they increase the risk of thrombose formation. This model mimicked the LA three phasic functions and showed in details the impact of the LAA on the LA hemodynamics in the LA fibrillation pathology, however, the geometry is not realistic and that may affect the final results.

In a recent study, a fully coupled LA and MV FSI model was developed by Feng et al. (2019) through the immersed boundary method, investigating the LA and the MV mechanics and hemodynamics in physiological and different pathological conditions, such as MV regurgitation and LA fibrillation and also with uniform and non-uniform LA wall thickness. This comprehensive study includes a realistic LA and MV geometry, reconstructed from CT images, consisting of tissue fiber architectures. The results of this comprehensive study elaborated the LA and MV functions and shed light on unknown LA and MV hemodynamics phenomena. For instance, considering the vortex formation in the LA chamber during the LA reservoir function in the Sys phase, the results show that the MV regurgitation destroys the vortex rings. Moreover, the MV regurgitation causes LA enlargement due to the elevated LAP. Interestingly, the findings of this study show that the MV regurgitation reduces the risk of embolism in patients with MV regurgitation or LA fibrillation. In this study, however, the inlet pressure boundary conditions generated hemodynamics results which do not resemble the physiologic ones. For instance, the calculated pulmonary vein flowrate (PVF) profile does not include a physiologic PVF profile characteristics (Keren et al. 1985).

In the present study, using FEA, first a simplified FSI model of the LA and the MV

was built. The goal of making the simplified FSI model is to investigate if the applied FEA method on the simplified FSI model is able to reproduce the LA and MV mechanics and hemodynamics. Secondly the same method was applied on a realistic LA geometry, reconstructed from CT images, to build a holistic model of the LA to mimic the LA phasic functions. In this work, realistic inlet and outlet BCs were applied on the FSI model. To this aim, 4D PC-MRI was employed to obtain the PVs flow data as the inlet BC, and the outlet BC, which is the LVP, is a realistic baseline pressure measured on a porcine heart.

CHAPTER 3

Materials and methods

The FSI model of the LA and the MV is a coupling model between the blood fluid dynamics and the tissue structural mechanics. The fluid flow pressure and velocity exert forces on the tissue structure and generates stress and strain, which results in the deformation or displacement of the solid structure, which is quite large (Basnight et al. 1991; Blume et al. 2011; Kuecherer et al. 1990). Mutually, solid structure deformation alters the flow velocity and pressure. The resultant stress-strain in the solid structure and velocity-pressure variations in the fluid flow are highly related to the geometry (shape) of the solid structure, the boundary conditions of the solid and the fluid domain, the movement of the solid structure, and, most importantly, the solid and fluid domain material properties. To have a precise FSI model, all the mentioned parts should be chosen and set up so that it replicates the physiological conditions of the human heart. The following sections explain in details how a representative FSI model of the LA and the MV with all the required components is generated.

3.1 Left atrial and mitral valve anatomy

The LA structure is located posteriorly, close to the T5, T6 and T7 vertebra, above the LV and below the arch of the aorta and the pulmonary artery. The LA chamber has a complex heterogeneous structure with an elliptical cross section which begins posteriorly from the distal part of the PVs at the veno-atrial junction, and ends anteriorly at the MV ostium on the MV plane (Barbero and Ho 2017). Fig. 3.1 illustrates the position of the LA structure with respect to the other cardiac structures.

Anatomically, the LA chamber includes four parts, the venous part, the vestibule, the septum, and the appendage (Barbero and Ho 2017). The large part of the LA is formed by the venous part. Normally, the LA is connected to four PVs; the right superior pulmonary vein (RSPV), the left superior pulmonary vein (LSPV), the right inferior pulmonary vein (RIPV) and the left inferior pulmonary vein (LIPV). However, in some cases there may be fewer or supernumerary PVs (Schwartzman, Lacomis, and Wigginton 2003). The LAA, which is positioned antero-superiorly on the right side of the LA, below the left pulmonary artery, helps to reduce the LAP.

The MV, connecting the LA to the LV, guarantee a unidirectional flow from the LA to the LV during the diastolic phase of the cardiac cycle. The intricate structure of the MV consists of four parts, the annulus, the anterior and posterior leaflets, the chordae tendineae, and the papillary muscles (DalBianco and Levine 2013).

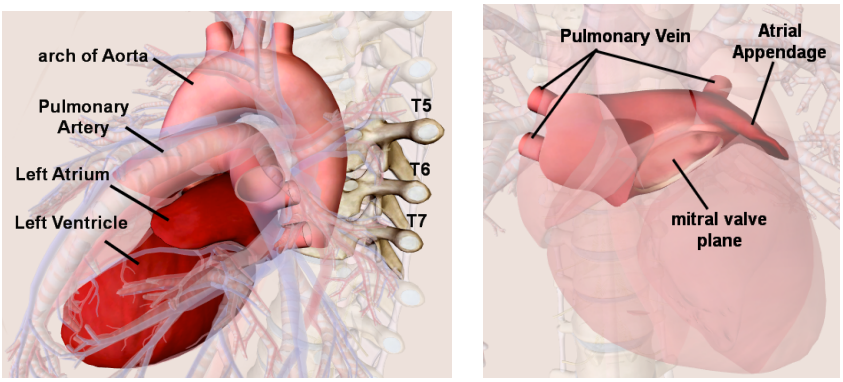

Figure 3.1: On the left, the anatomical position of the LA, which is surrounded by the aorta, the Pulmonary Artery, the LV and the vertebra, is shown. On the right, the LA structure including the PVs, the LAA and the MV plane, is pictured. The raw images are taken from www.healthline.com but they are processed and land-marked by the author.

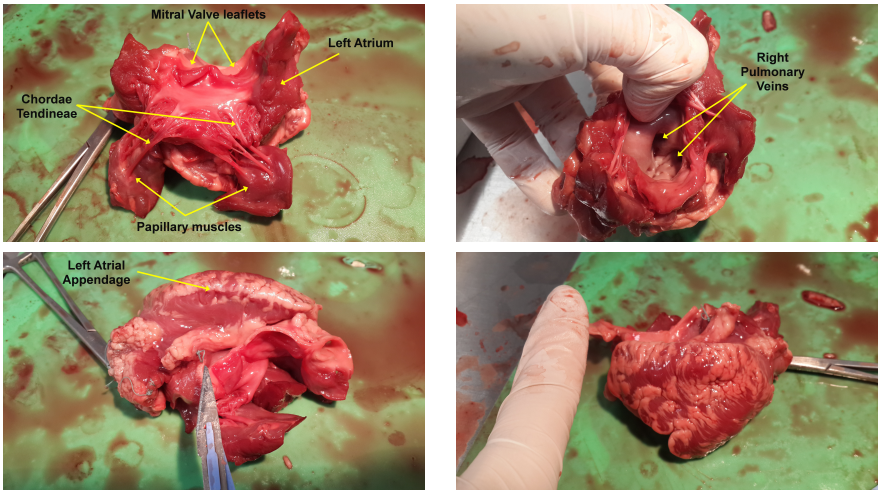

Figure 3.2: The MV and the LA structures are shown on a dissected porcine heart. In the upper left panel, the MV components including leaflets, chordae tendineae, and papillary muscles are marked. In the upper right panel, the RIPV and RSPV ostium are visible. In the lower left panel, the broccoli shaped LAA is shown. In the lower right panel, the size of the LA is compared to a finger. The porcine heart is dissected in CAVE lab at Aarhus University, and the pictures are taken by the author.

The annulus has an oval saddle shape area and its size is used as marker of some cardiac disease like LA enlargement (DalBianco and Levine 2013). The anterior leaflet is connected to the aortic root and the AV and the posterior leaflet is attached to the posterior wall of the LA (DalBianco and Levine 2013; Henein 2012). The chordae tendineae and papillary muscles act passively in early diastole, and function actively in late diastole to keep the leaflets closed and avoid them to bulge toward the LA, causing MV regurgitation. The LA and the MV structures are shown in Fig. 3.2.

3.1.1 Realistic 3D left atrial geometry

To reconstruct a realistic geometry of the LA, a voxel-based segmentation technique with an "intensity range masking" method was employed in the free open source software "3DSlicer" (www.slicer.org). The LA geometry was segmented from 4D CT images acquired through retrospective image acquisition with ECG-triggered dose modulation. One of the challenges in reconstructing the LA geometry from the CT scans was to read and landmark the cardiac structures on the images. Fig. 3.3 shows two slices of the cardiac structure at the beginning of the systole (R-peak). A full guide towards landmarking and segmenting the LA geometry from the CT images is provided in Appendix A. The segmented LA structure with the four PVs is displayed in Fig. 3.3.

3.1.2 Simplified 2D and 3D left atrium - CAD model

As it is described in the previous section, and displayed in Fig. 3.3, the realistic LA has a complex asymmetric geometry. Starting a numerical study with the realistic LA geometry is a cumbersome task because it needs a very fine mesh which makes it numerically expensive, and applying boundary conditions on the complicated LA geometry may generate numerical errors which overshadows the progress of the whole numerical study. Therefore, to avoid the distracting intricacies, it was decided to generate and employ a simplified LA geometry. To this aim, it was assumed that the LA has a spherical symmetric structure with four PVs positioned symmetrically around the sphere as shown in Fig. 3.4. The minimal volume information of the LA chamber at the end of the diastole was taken from the volume-time curve determined with cine magnetic resonance imaging reported in (Jarvinen et al. 1994), and used to calculate the dimension of the spherical LA.

The LA wall thickness is heterogeneous, with an average value between 1-4 mm (Whitaker et al. 2016). However, in the simplified model, a homogeneous wall thickness of 2 mm was considered for the LA wall. The PVs were assumed to have circular rather than oval cross sectional area. To calculate the PVs diameter, the PVs area values reported in (Chnafa, Mendez, and Nicoud 2014), were averaged over four PVs, and the diameter of the PVs was calculated from the averaged area. The CAD model was designed in COMSOL Multiphysics® v.5.4. (COMSOL AB, Stockholm, Sweden). The 2D and 3D simplified geometries are displayed in Fig. 3.4.

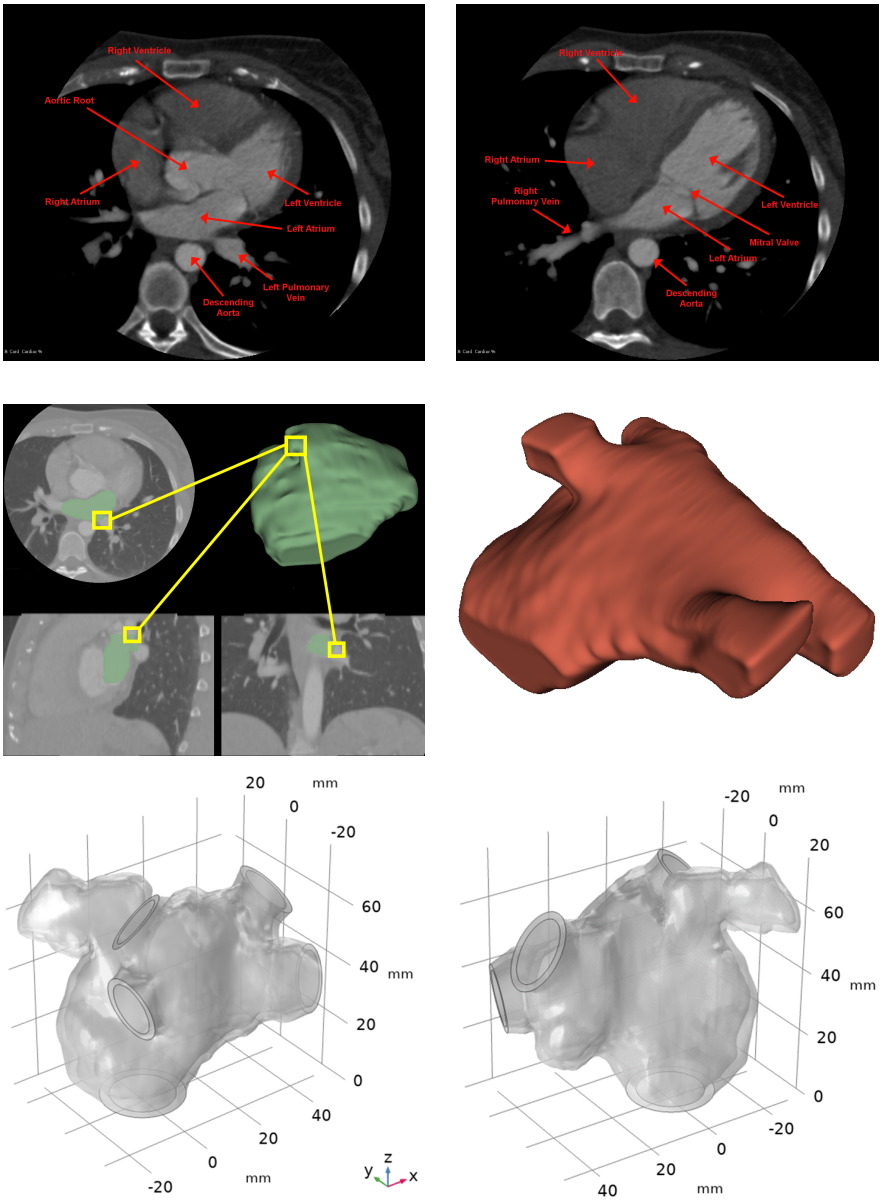

Figure 3.3: The landmarked CT images and the final 3D realistic LA geometry are shown in the figure. In the upper panel, two axial 4 chamber views of heart are landmarked. In the middle panel, the voxel-based segmentation technique, and the final result of the segmented 3D LA geometry with the "intensity range masking" method are illustrated. The lower panel shows the anterior and posterior views of the LA FSI model geometry.

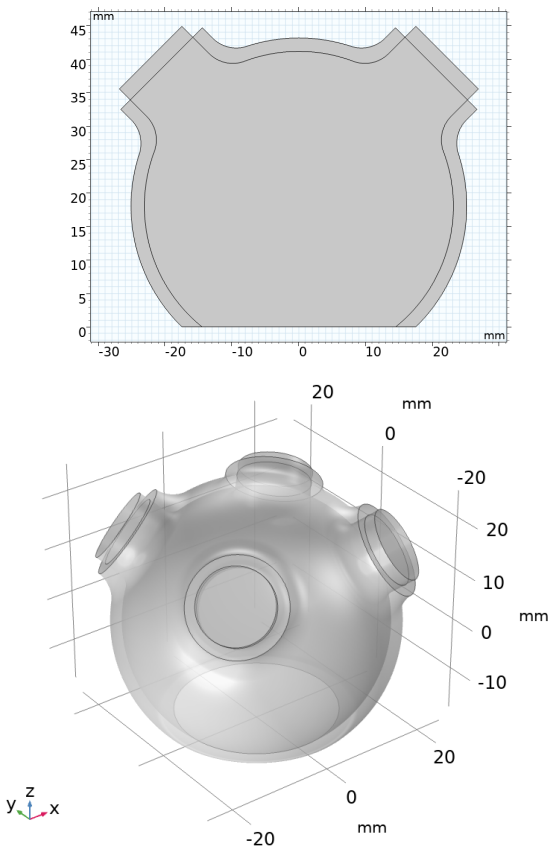

Figure 3.4: The simplified 2D and 3D CAD geometries of the LA are shown in the figure. The top panel displays the 2D geometry and the bottom panel shows the 3D geometry. The MV plane and the four PVs are visible in the image. The diameter of the MV plane is 29 mm.

3.1.3 Simplified 2D and 3D mitral valve - CAD model

The MV structure has a complex saddle shaped asymmetric heterogeneous geometry. Therefore, to design a simplified model of the MV, the characteristic features of the MV annulus and leaflets should be known. To make the model simpler, the chordae tendineae and papillary muscles were excluded from the MV model.

The posterior leaflet is made up of three scallops accounting for 2/3 of the MV annulus circumference and the anterior leaflet has only one continuous cusp which occupies 1/3 of the MV annulus (Kheradvar and Pedrizzetti 2012). The four main dimensions used

in designing the leaflets of the MV are coaptation distance, coaptation depth, coaptation length, and the thickness of the leaflets. To make the MV model even simpler, the coaptation length was excluded from the geometry. The coaptation distance of the anterior leaflet is longer than the posterior leaflet. However, an equal averaged value was considered for both leaflets to make a symmetric MV model. The coaptation depth is almost the same for the anterior and posterior leaflets, thus the same averaged value was used for both leaflets. The values of the coaptation distance and coaptation depth are taken from Gogoladze et al. (2010).

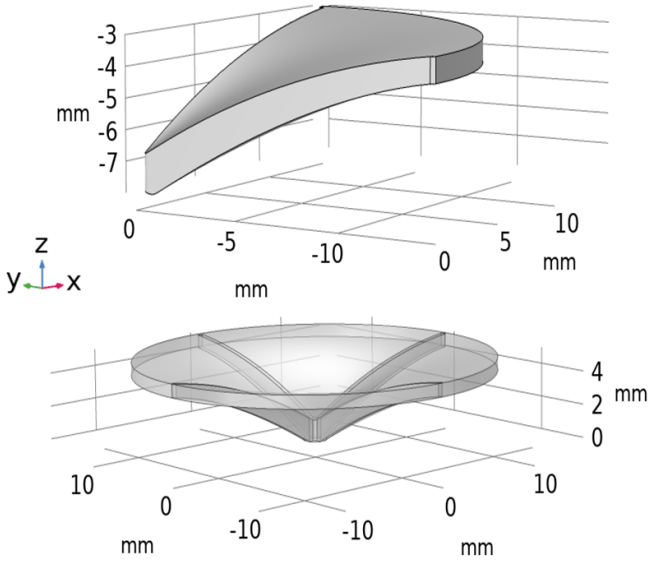

Figure 3.5: The top panel shows one of the leaflets of the MV. It is visible in the image that the thickness of the leaflet is different from side to tip. The bottom panel illustrate the 3D simplified CAD model of the MV with the four leaflets. The geometry is symmetric, but the thickness is not uniform. The diameter of the annulus is 29 mm.

The MV thickness is heterogeneous, and it is not only different between the leaflets, but also through various segments of the leaflets. For instance, the thickness is higher in the coaptation zone compared to the regions close to the annulus. To respect the thickness difference, a b-spline curve with a vertex and two tangents was utilized to design the cross section of the leaflets to vary the thickness gradually from $0.8 - 1.3\ mm$. The thickness data were taken from Sahasakul et al. (1988). In order to preserve the topology of the MV leaflets in the numerical simulation, a gap of 400 µm was generated between the leaflets. The diameter of the annulus is $29\ mm$, which is close to the value reported by Pan et al.

(2005). The simplified MV is shown in Fig. 3.5. The model is designed in Autodesk® Inventor LT™ (Autodesk, San Rafael, CA, US).

The result of the simplified 2D and 3D coupled LA and MV models are presented in Fig. 3.6. Intrinsically, FSI simulation of the LA and the MV is a multivariate problem, and many parameters, like boundary conditions, material properties, boundary movements etc. should be considered. Therefore, working on a simplified geometry would lessen the model complexity, and helps to have control over the model, to speed up the trial and error procedure regarding implementation of different BCs and material models, and makes the simulations computationally less expensive. It is noteworthy that, working on simplified models is not trivial and in many studies, simplified models were utilized to investigate cardiac chambers mechanics and hemodynamics (Hassaballah et al. 2013; Hazan et al. 2018; Lemmon and Yoganathan 2000b; Zhang and Gay 2008).

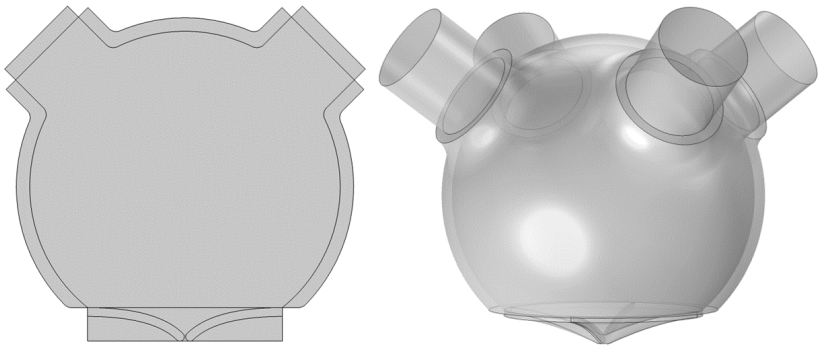

Figure 3.6: Left panel shows the coupled 2D LA and MV model, and right panel displays the coupled 3D LA and MV model. The simplified models reduce the unnecessary complexities of the numerical study.

3.2 Boundary conditions

3.2.1 Inlet

The flow in the PVs is pulsatile (Rajagopalan et al. 1979) and at the entrance of the LA is not fully developed because the length of the PVs are not long enough for the flow to develop through the PVs. This could also be clearly observed in the 4D PC-MRI images acquired from five volunteers (Sec. 8.3.1). The flow, however, is not blunt and the velocity is different on each point at the inlet. A typical flow profile at the veno-atrial junction is displayed in Fig. 3.7.

In this study, to replicate the pulsatility of blood flow in the PVs, first the averaged velocity profile is calculated from the measured flowrate profile (Fig. 3.8), having the area

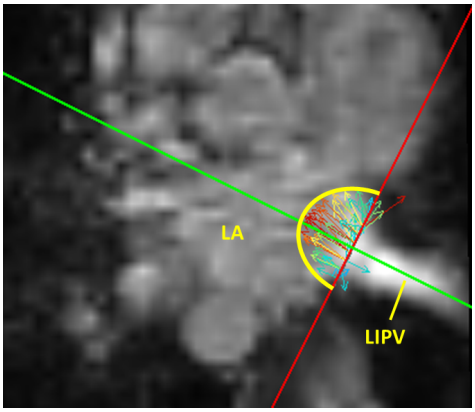

Figure 3.7: The flowrate profile at the LIPV ostium in mid systole is shown. The flow profile is neither blunt nor fully developed. The LIPV and LA are shown on the image. The image is original and obtained at Aarhus University Hospital in the MR research center.

of the inlets. Then, by utilizing the Womersely equations, the averaged velocity profile is converted into a pulsatile velocity profile, which is also a function of the spatial position (Jensen 2013). All the calculations are done in MATLAB® (The MathWorks Inc., MA, US) and the implemented code is presented in Appendix B. The measured flowrate profile and the pulsatile velocity profile are shown in Fig. 3.8.

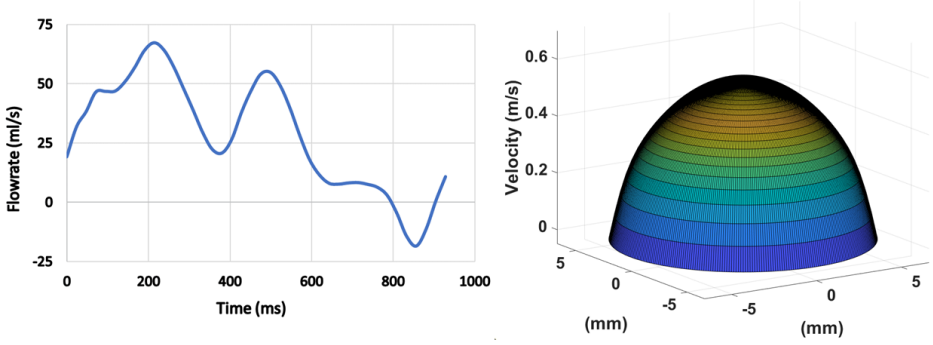

Figure 3.8: The right panel displays the measured LIPV flowrate through 4D PC-MRI. The flowrate profile is a 1D time dependent function. The left panel shows the pulsatile velocity profile in mid-diastole generated from the averaged velocity profile calculated from flowrate profile. The pulsatile velocity profile is a time-space dependent function.

3.2.2 Outlet

In some CFD and FSI studies of the LA, zero pressure or free flow was considered for the outlet BC (Dahl et al. 2012; Hazan et al. 2018; Zhang and Gay 2008). This approach toward determining the outlet BC is not correct in analysing the hemodynamics of the LA because it is highly correlated with the pressure gradient of the LH. For instance, the transmitral **E** and **A** peaks are greatly affected by the LVP and LV preload. Also, one of the determinants of the PVF during diastole is the LVP (Barbier et al. 2000, 1999; Hellevik et al. 1999; Nishimura and Tajik 1997). This pressure interdependence is discussed in details in Sec. 9.2. Therefore, imposing zero pressure at the LA outlet may result in overestimating or underestimating the hemodynamic characteristics which generates false interpretations.

Hence, in this work a realistic LVP at the outlet was applied. A baseline (before intervention) LVP was measured in-vivo in a native porcine heart in an open-heart surgery (Fig. 3.9). However, only the diastolic portion of the LVP profile was used because the LV geometry is not included in the model, and therefore the LVP Sys portion does not affect the LA hemodynamics during systole.

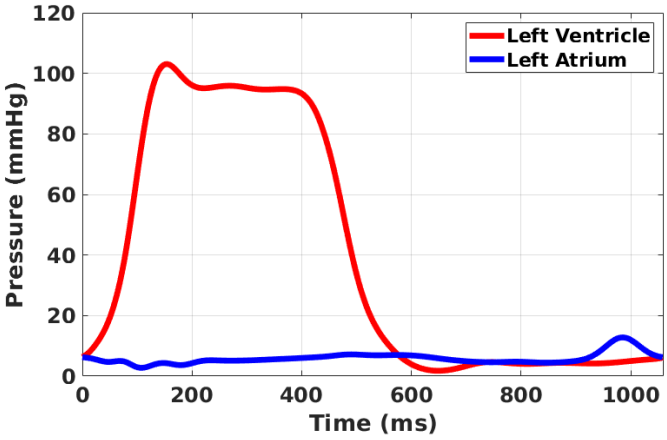

Figure 3.9: In-vivo measured porcine baseline LVP and LAP profiles for one cardiac cycle. The red curve is the LVP and the blue curve is the LAP.

3.2.3 Left atrium-mitral valve structure movement

During the three LA phasic functions, the LA wall, the MV annulus, and the PVs move. The PVs cross sectional area increases and decreases during the cardiac cycles because they have a large compliance (Rajagopalan et al. 1979). It is also shown in Sec. 8.3.2 that

the PVs cross sectional area change, though the variation is negligible (Tab. 8.4). In this work, it is assumed that the PVs cross sectional area does not change.

The MV annulus moves downward during Sys phase due to the longitudinal shortening of the LV fibers because of the LV contraction. The descending MV annulus movement impacts the LAP and the LAV in the Sys phase, resulting in a reduction of the LAP and an increase in the LAV. This movement is reflected on the s_2 peak of the PVF profile, shown in Sec. 8.3.1. However in this work, the MV annulus was assumed as a fixed BC to simplify the FSI simulations. To mimic the effects of the MV descending movement on the LAV and LAP, the PVs BC were left unconstrained and consequently they could move freely normal to the PVs cross sectional plane. The PVs normal movement generates the same effect of the LAP reduction and the LAV increase.

The LA wall expands (distension+stretching), recoils, and contracts during the reservoir, conduit and active pump phasic functions, respectively. During the reservoir phase in the Sys phase, when the MV is closed, the LA wall distends due to the change in blood pressure caused by the PVs inflow, and stretches because of the descending movement of the cardiac base (Barbier et al. 2000, 1999; Hellevik et al. 1999). The LA in this phase acts as a hyperelastic balloon which stores elastic energy while it expands. It is worth mentioning that the amount of LA expansion is very much related to the LA chamber compliance which is one of the main determinants of the LA reservoir phase (Barbier et al. 2000, 1999). When the MV opens, the blood passes through the MV and the LAP drops. As a result, the LA wall releases the elastic energy and recoils. In the last phasic function, the LA contracts due to the LA depolarization. In this study, the LA wall movement in the Sys and ED phases is generated by the interaction between the solid and the fluid domain in the FSI model. To mimic the LA contraction at the end of the diastole, a tension force per unit area F_A was applied to the LA wall area A:

$$F_A = -\frac{K_{tot}}{A}(r_{solid} - r_0) - d_A \frac{\partial (r_{solid} - r_0)}{\partial t}. \tag{3.1}$$

In Eq. 3.1, the K_{tot} (N/m) is total spring stiffness, A (m^2) is the area on which the tension force is applied, r_{solid} (m) is the displacement of the LA wall, r_0 (m) is an optional deformation offset, describing the stress-free state of the LA wall, which is not valid in this case. The K_{tot} is a triangle function which activates during the third phase of the LA function. The function includes two parts, a linear rise and a linear decline, with a maximum value in the middle of the LD phase. The tension force equation and the triangle function are explained in the reference manual and structural mechanics module of COMSOL Multiphysics® v.5.6. documentation (COMSOL AB, Stockholm, Sweden. 2020).

This method of mimicking the LA contraction using a tension force is used in several works, though with some differences. In the LA FSI model generated by (Zhang and Gay 2008), they considered an activation force $\vec{F}^{act}$ which depends on the stiffness k and resting length $R(t)$ of the LA muscle fibers:

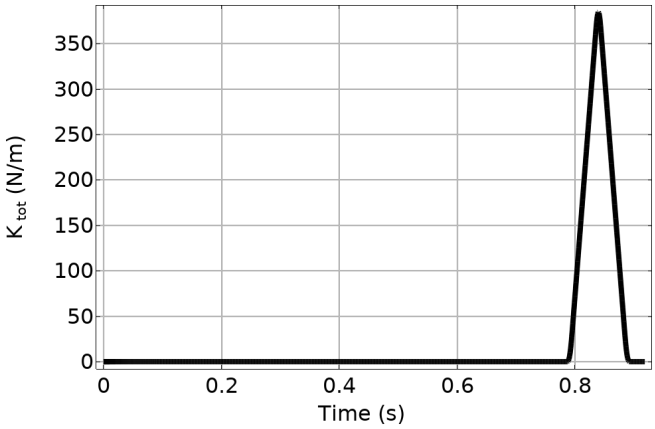

Figure 3.10: The total spring stiffness versus time in the form of a triangle function is displayed. It is constituted with two linear parts with the maximum value in the middle of late diastolic time span. It causes the tension force to activate only in the LD phase.

$$\vec{F}^{act} = kR(t). \tag{3.2}$$

This activation force model is developed for the first time with Lemmon and Yoganathan (2000a,b). In another FSI study on the LA done by Feng et al. (2019), a time-varying isometric tension in the form of a triangle function was accounted for the LA contraction.

3.3 Material properties

The geometry of the LH includes two solid domains, which are the MV leaflets and the LA wall, and one fluid domain, which is the inner part of the LA chamber.

3.3.1 Solid hyperelastic model

Different hyperelastic constitutive models were adapted to the solid domains. Because of the large deformation of the cardiac chambers and the valves, hyperelastic models best describe their mechanical properties. For the LA chamber, two different hyperelastic models were considered to compare the effect of the LA material model on the LA hemodynamics. The first hyperelastic constitutive model (Eq. 3.3) is formulated by (DiMartino, Bellini, and Schwartzma 2011), through fitting a nearly incompressible hyperelastic model on biaxial tensile tests conducted on porcine hearts. The resulting strain energy density function $\psi(\bar{\bar{C}})$ is:

$$\psi(\bar{\bar{C}}) = c_{NH} I_{1c} (I_{3c})^{-1/3} - 3 + \frac{1}{2} K (J-1)^2, \tag{3.3}$$

where c_{NH} is the stress like material parameter equal to $8.38\ kPa$, I_{1c} and I_{3c} are the first and third invariants of the right Cauchy-Green strain tensor $\bar{\bar{C}}$, respectively, K is the bulk modulus equal to $10^6\ kPa$, and J is the determinant of the deformation gradient tensor. In (DiMartino, Bellini, and Schwartzma 2011), different values for the c_{NH} for different regions on the LA pericardium are presented. However, because in this study the LA wall was considered as a homogeneous isotropic structure, an average was made over the c_{NH} values and the mean value was assigned to the LA wall of the FSI model.

Regarding the MV material, there are plenty of linear and non-linear material models proposed in the literature, like linear isotropic elastic models (Lau et al. 2010), linear orthotropic elastic models (Votta et al. 2007), isotropic hyperelastic models (May-Newman and Yin 1998) and transverse isotropic hyperelastic models (May-Newman and Yin 1995). It is true that the MV is constituted with a fibrous tissue network, but in this study the MV leaflets were considered as a structure without fiber networks and therefore, an isotropic nearly incompressible neo-Hookean hyperelastic constitutive model was allocated to the MV leaflets:

$$\psi(\bar{\bar{C}}) = \frac{1}{2} \mu (I_{1c} - 3) + \frac{1}{2} K (J-1)^2, \tag{3.4}$$

where μ is the Lamé parameter equal to $150\ kPa$ and K is equal to $2^6\ kPa$. For both the LA chamber and the MV leaflets, the same value of density of $1120\ kg/m^3$ (DiMartino, Bellini, and Schwartzma 2011) was considered.

A sub-study was conducted on the 2D model to investigate the impact of mitral valve stiffening (MVS) on the LA and the MV hemodynamics. To this purpose, four different Lamé parameters, $\mu_1 = 150\ kPa$, $\mu_2 = 450\ kPa$, $\mu_3 = 850\ kPa$ and $\mu_4 = 1100\ kPa$, were assigned to the MV and the hemodynamics indices of the LA and the MV were calculated.

3.3.2 Fluid domain

Blood was set as the material of the fluid domain, and it was considered as a Newtonian, incompressible fluid which is a fair approximation for the blood behavior in cardiac chambers (Jensen 2013). The material properties of blood (Tab.3.1) were considered according to the physiological condition of human body.

The fluid flow regime was also assumed as a laminar regime. In general, the flow in human cardiovascular system is in the laminar domain (Truskey, Yuan, and Katz 2004). However, in some locations like the ascending aorta, the flow prone to have a turbulent regime because of a very high velocity. A turbulent regime is usually a sign of pathology. For instance the blood flow in patients with MV or AV thrombosis is turbulent (Pibarot and Dumesnil 2000; Roudaut, Serri, and Lafitte 2007). To confirm if the blood flow in

Parameter	Description	Value	Unit
ρ	density	1060	kg/m^3
η	dynamic viscosity	0.004	$Pa \cdot s$

Table 3.1: Blood material properties are presented in the table. The properties are allocated according to the physiological condition of human body.

the LA chamber is laminar, Reynolds number R_e at the inlets of the LA chamber was calculated:

$$R_e = \frac{\rho U D}{\eta} \approx \frac{inertial force}{viscous force}, \tag{3.5}$$

where ρ is the blood density, η is the dynamic viscosity, D is the PVs hydraulic diameter, which is simply the PVs diameter in case of circular cross sectional area, and U is the average flow speed. Usually, flow with R_e<2000 is considered as laminar and R_e>2500 indicates a turbulent flow (Truskey, Yuan, and Katz 2004). The R_e calculates the ratio between inertial forces and viscous forces. Low R_e, means the inertial forces are lower than viscous forces, indicating the flow has a laminar regime, while high R_e shows that the inertial forces are greater than viscous forces, which results in a turbulent flow regime.

3.4 Finite element mesh

As it is explained in Sec. 3.5, the solver algorithm solves partial differential equations (PDEs) to calculate the structural mechanics or fluid dynamics parameters, like stress, pressure, velocity, etc. To solve the discrete differential equations, the geometry must be discretized or "meshed" into smaller finite elements called grid cells. Then the solver calculates discrete values on each cell, which results in resolving the whole meshed structure and control volume.

To generate the mesh, triangular and quadrilateral mesh elements for the 2D geometry, and tetrahedral, quadrilateral (brick), and prism elements for the 3D geometry were utilized. The mesh elements are displayed in Fig. 3.11.

Between triangle/tetrahedron and quadrilateral/hexahedron, the later is preferred because; 1) they provide solution with higher quality with significantly fewer elements, 2) they offer higher aspect ratio (ratio between longest and shortest edge), and 3) they reduce the numerical diffusion in the case of mesh and flow alignment (Lintermann 2021; Tu, Inthavong, and Wong 2015). However, for complex geometries, it would be impractical to generate quadrilateral/hexahedron mesh elements. Therefore, triangle/tetrahedron mesh elements are better choices to discritize complex geometries. In this FSI study, the first choice amongst different types of mesh elements were triangle/tetrahedron.

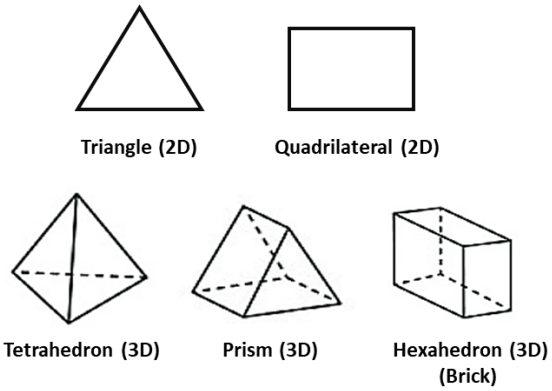

Figure 3.11: Different mesh elements employed for generating the meshed geometry. Triangular and quadrilateral elements for the 2D geometry, and tetrahedral, prism and hexahedral elements for the 3D geometry. The image was made by the author, however, it was inspired by (Lintermann 2021; Tu, Inthavong, and Wong 2015).

Nonetheless, to have more accurate solution of the boundary layer generated on the walls, quadrilateral/hexahedron, and prism elements were used here.

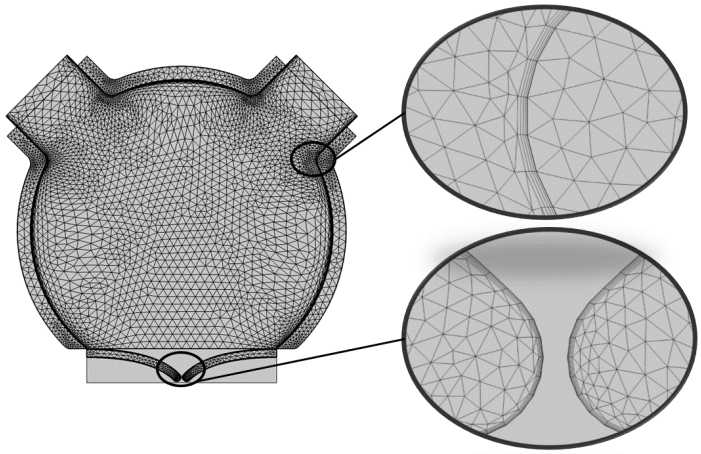

Figure 3.12: The Generated mesh on the 2D geometry with 2D mesh elements. Triangular and quadrilateral (brick) elements are shown in the figure. The bricks were used for generating boundary layer mesh adjacent to the wall of the solid domains, i.e. on the inner surface of the LA chamber and on the MV surface.

The generated mesh on the 2D FSI model, using triangular and quadrilateral elements, is displayed in Fig. 3.12. Moreover, the complete and section views of discretized 3D simplified MV, 3D simplified LA, and 3D realistic LA are shown in Fig. 3.13, Fig. 3.14 and Fig. 3.15, respectively. In these figures, the mesh elements look discontinuous because they were shrunk by the factor of 0.7 of the original dimension only for the matter of illustration. Otherwise the mesh is continuous and elements are connected together at the elements vertices.

The boundary layer is a layer of fluid adjacent to the solid wall whose motion is affected by the adherence of the fluid to the wall due to the viscous effect. Therefore, the velocity of the fluid attached to the wall is zero, and as the fluid moves away from the wall, the velocity goes up. The boundary layer plays a crucial role in a fluid field because 1) it affects the wall shear stress, and 2) boundary layer separation is the main mechanism of the vortex generation in incompressible fluids (Kheradvar and Pedrizzetti 2012). Both wall shear stress and vortices are amongst fundamental phenomena reported in cardiovascular studies.

The symmetric feature of the 3D simplified LA geometry provided the possibility to run the simulations on only a quarter of the geometry to lessen the computation time. As it is shown in Fig. 3.16, symmetry boundary conditions were defined on the symmetric surfaces. To discretize the symmetric surfaces, 2D triangular and quad elements were employed. Moreover, the outlet of the model was considered at the end of a long tube, which is accounted as the LV, shown in Fig. 3.16 and Fig. 3.17.

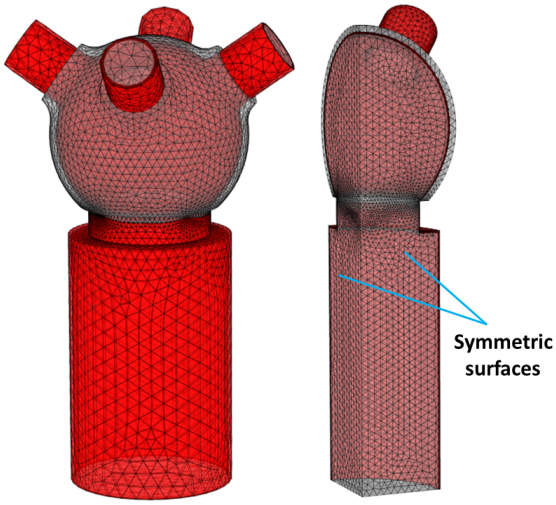

Figure 3.16: Complete and cut geometries are shown in the figure. On the cut surfaces, a symmetry boundary condition was defined, and discretized with 2D triangular and quad elements.

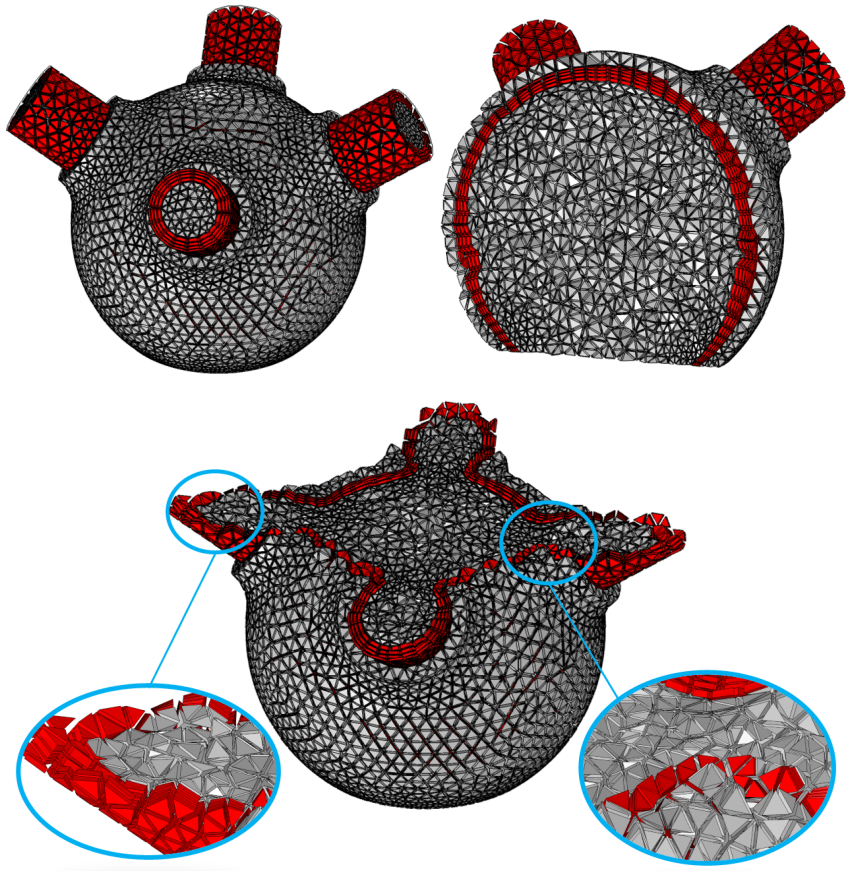

Figure 3.13: The complete and section views of discretized 3D LA geometry are shown. The geometry is meshed with tetrahedral elements, displayed in gray color and prism elements illustrated with red color. Prism elements are utilized for generating boundary layer elements on the inner surface adjacent to the LA wall.

There are many criteria for inspecting the mesh quality in COMSOL like skewness, growth rate, maximum angle, condition number, etc. None of the criteria alone is sufficient for determining the quality of the mesh. In this study, the skewness and the maximum angle were used to inspect the mesh quality. An ideal mesh element is an equilateral element in which the ratio of the larger angle to the smaller angle is one or close to one, see Fig. 3.18.

The skewness S_k is a measure of equiangular skews which penalizes the elements

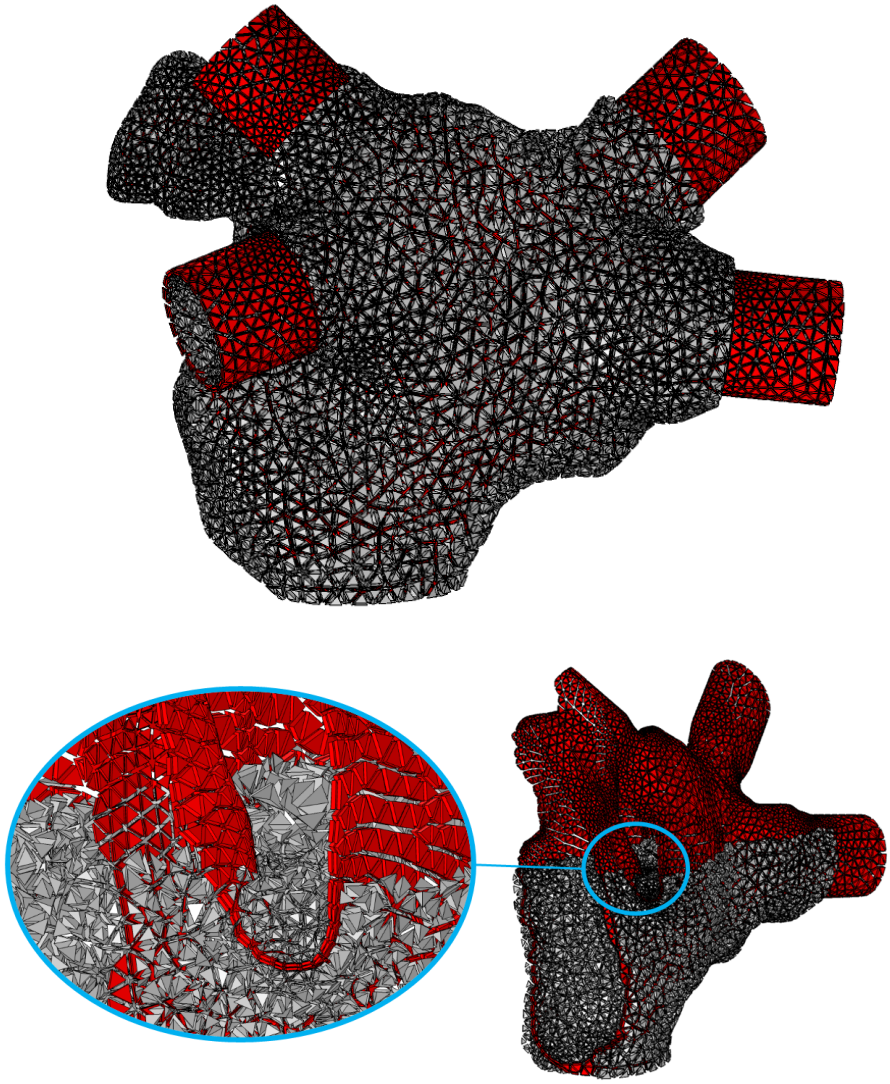

Figure 3.14: The complete and section views of discretized realistic 3D LA geometry are shown. The mesh structure is the same as 3D simplified LA displayed in Fig. 3.13.

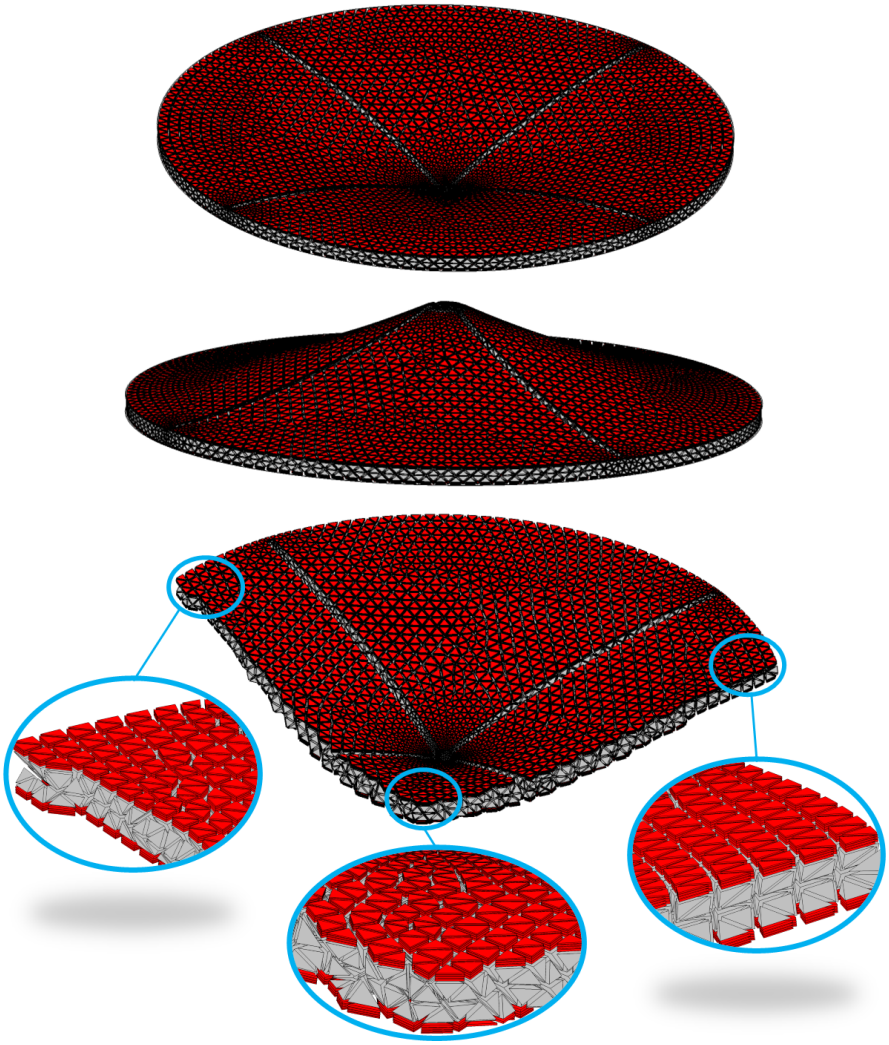

Figure 3.15: The complete top, bottom, and section views of the the generated mesh on the 3D MV geometry are shown. Tetrahedral (gray color) and prism (red) elements are used to discretize the geometry. Prism elements cover the surface of the MV leaflets, which is in touch with the fluid, to create the boundary layer mesh. The MV volume is meshed with tetrahedral elements.

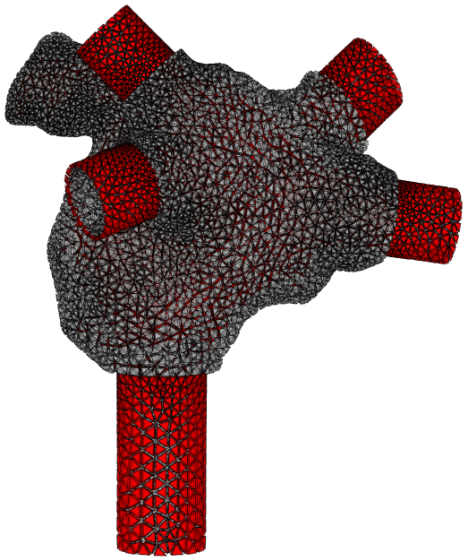

Figure 3.17: Complete geometry of the 3D realistic LA is shown in the figure. Tetrahedral (gray color) and prism (red) elements are used to discretize the geometry.

with a very large or a very small angle based on:

$$S_k = min\left\{1 - max\left(\frac{\theta - \theta_e}{180 - \theta_e}, \frac{\theta_e - \theta}{\theta_e}\right)\right\} \tag{3.6}$$

in which the θ_e is the angle of vertices in an ideal element, and θ is the current angle of the element. For example, considering the element **d** in Fig. 3.18, it is assumed that the $\theta_e = 60°$, $\theta_1 = \theta_3 = 0.5°$, and $\theta_2 = 179°$. Therefore, the S_k for element **d** would be the $min\,\{0.0083, 0.0083, 0.9917\}$ which is 0.0083.

Another criteria for evaluating the mesh quality is "maximum angle" which only penalizes the elements with large angles. If there is not any angle larger than the largest angle in the corresponding ideal element, the maximum angle is 1. As the angle of the vertex with the largest angle in the element increases, the maximum angle criteria approaches zero. This criteria is mainly used for evaluating the boundary layer elements. Further explanation about mesh quality measures can be found in the reference manual of COMSOL Multiphysics® v.5.6. (COMSOL AB, Stockholm, Sweden. 2020).

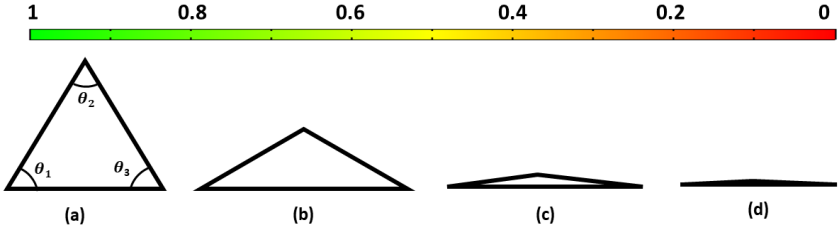

Figure 3.18: The value of the mesh quality measures used in Comsol is between 0 and 1, which indicates the elements with poorest and optimal quality, respectively. For instance, the skewness of the element **a** is 1 while it is close to 0 for element **d**, which is highly skewed. The figure is made by the author but it was inspired by COMSOL mesh quality inspection workshop.

3.5 Fluid-structure interaction multiphysics interface

The model includes two physics, a solid structure which is the LA wall and the MV leaflets, and a fluid flow physics, which is the blood flow through the LA chamber and across the MV. A set of PDEs are defined for each physics. The FSI multiphysics interface then couples and solves the PDEs numerically to calculate "approximate" values of the required parameters of the two physics. It is said approximation because the exact solutions of PDEs can only be obtained through analytical methods. However, PDEs are mostly very complex or even impossible to be solved analytically due to geometry and BCs. Therefore, the PDEs are approximated with different discretization methods like finite volume, finite difference or FEA.

In this study, the FEA was employed to solve the FSI PDEs. In FEA analysis, the geometry is discretized into small finite cells, and each dependent variable in the PDEs are approximated on each cell with sets of first order or second order basis functions. In FSI, a moving mesh is defined for the fluid domain, and the velocity of the moving mesh is one of the coupling equations in solving the PDEs. Moreover, the FSI uses the arbitrary Lagrangian-Eulerian method to solve the fluid flow domain with an Eulerian description in the spatial frame, and the solid structure with a Lagrangian description in the material frame.

The motion of the fluid flow in the fluid domain is described by the Navier-Stokes PDEs. The Navier-Stokes PDEs are similar to Newton's second law of motion, and it relates the velocity and the pressure in the fluid domain:

$$\rho\frac{\partial\vec{u}_f}{\partial t} - \nabla[-p\bar{\bar{I}} + (\eta(\nabla\vec{u}_f + (\nabla\vec{u}_f)^T)] + \rho((\vec{u}_f - \vec{u}_M)\cdot\nabla)\vec{u}_f = \vec{F}_{ext}. \tag{3.7}$$

where p (Pa) is the fluid pressure, $\bar{\bar{I}}$ is the identity tensor, $\vec{u}_f = (u, v, w)$ is the fluid

velocity field vector, $\vec{u}_M = (u_m, v_m, w_m)$ is the moving mesh velocity vector and $\vec{F}_{ext}$ is the vector of external or volume forces applied on the fluid. This equation is always solved with the continuity equation (Eq. 3.8). The continuity equation describes the mass conservation as,

$$\nabla \cdot \vec{u}_f = 0. \tag{3.8}$$

When the blood flow enters into the LA chamber, the pressure and the velocity of the fluid exert force on the LA wall, resulting in chamber expansion, and stresses arise due to the chamber deformation. The applied force from the fluid flow to the LA wall $\vec{F}_f$ is calculated by:

$$\vec{F}_f = \vec{n} \cdot (-p\bar{\bar{I}} + \eta(\nabla \vec{u}_f + (\nabla \vec{u}_f)^T)), \tag{3.9}$$

where $\vec{n}$ is the normal vector to the fluid-solid interface boundary. Because the force $\vec{F}_f$ is calculated with the Eulerian description in the spatial frame, it should be transformed into the material frame. This transformation is done through Eq. 3.10 which couples the fluid and the solid domain,

$$\vec{F} = \vec{F}_f \frac{dv}{dV}, \tag{3.10}$$

where dv is the mesh scale factor in the moving mesh frame, and dV is the mesh scale factor in the undeformed frame. Then, the stress can be calculated as:

$$\bar{\bar{\sigma}} \cdot \vec{n} = \vec{F} \cdot \vec{n}, \tag{3.11}$$

where $\bar{\bar{\sigma}}$ is the solid domain stress tensor.

Another coupling PDE, which couples the rate of solid domain deformation to the rate of the fluid domain moving mesh displacement, is described as:

$$\frac{\partial \vec{u}_s}{\partial t} = \frac{\partial \vec{u}_M}{\partial t}, \tag{3.12}$$

where $\vec{u}_s$ is the velocity of the solid deformation, and $\vec{u}_M$ is the moving mesh velocity vector explained above. In fact, Eq. 3.12 adjust the moving mesh velocity with the solid domain wall velocity. Using all the described equations, the FSI algorithm calculates the velocity and pressure in the fluid domain, and the resulting stress and strain in the solid domain. The complete and comprehensive explanation of the arbitrary Lagrangian-Eulerian finite element method, and the FEA and the FSI theories can be found in the structural mechanics documentation and cyclopedia of COMSOL Multiphysics® (COMSOL AB, Stockholm, Sweden. 2020).

3.6 Mechanics and Hemodynamics analysis

As it was mentioned in the introduction, the main goal of the numerical study was to make a FSI model of the LA and the MV, which can replicate the physiological conditions. To investigate if the FSI model has achieved the defined goal, the mechanics and hemodynamics of the LA and the MV were inspected and compared with physiological mechanics and hemodynamics of the LA and the MV. To probe the hemodynamics, the average absolute LAP, the LAV, the LA pressure-volume (p-v) loop, the average vorticity magnitude, the maximum TV profile, the MV Effective orifice area (EOA), and the LA kinetic energy were calculated and plotted.

In analyzing the incompressible fluids, vorticity $\vec{\omega}\ (1/s)$ is one of the fundamental quantities which provides the information on the flow structure. It is a psudovector describing the local spinning of the flow field. Mathematically, $\vec{\omega}$ is the gradient of the flow velocity $\vec{u}_f$, which is calculated as the curl of the flow field velocity (Kheradvar and Pedrizzetti 2012):

$$\vec{\omega}(t,\vec{\chi}) = \nabla \times \vec{u}_f(t,\vec{\chi}) = \begin{bmatrix} \frac{\partial w}{\partial y} - \frac{\partial v}{\partial z} \\ \frac{\partial u}{\partial z} - \frac{\partial w}{\partial x} \\ \frac{\partial v}{\partial x} - \frac{\partial u}{\partial y} \end{bmatrix}. \tag{3.13}$$

where $\vec{\chi}$ is the position vector.

The kinetic energy $K_e\ (J)$ is one of the important quantities in analyzing the dynamics of the flow field, representing the state of energy of the flow, and serves also as a diagnostic tool in cardiovascular examinations (Arvidsson et al. 2016; Fyrenius et al. 2001; Gaeta et al. 2018). K_e is calculated as:

$$K_e = \frac{1}{2}\rho V {U_{LA}}^2, \tag{3.14}$$

in which $V\ (m^3)$ is the left atrial volume and $U_{LA}\ (m/s)$ is the maximum flow velocity magnitude inside the LA fluid domain. To obtain the U_{LA}, the solver first calculates the velocity magnitude inside each mesh element in the LA fluid domain, and then, it peaks up the maximum value as the U_{LA}. To obtain the TV profile, the velocity component normal to the center point of the MV plane was calculated. To plot the p-v loop, the average LAP was calculated and plotted against the LAV. The p-v loop is another index used in investigating the function of mechanics-fluid dynamics function of the cardiac chambers (Hoit 2017). To analyze the mechanics of the LA and the MV, the maximum first principal stress and stretch values were plotted for both the LA wall and the MV leaflets.

CHAPTER 4

Results

In this chapter, at the beginning the quality of the mesh is inspected through mesh quality indices. Investigating about the quality of the discretization is very important since it has a high impact on the numerical results. In continue, the mechanics and hemodynamics of the 2D, 3D simplified and 3D realistic FSI models will be analysed under physiological conditions. To do so, the mechanics and hemodynamics indices are compared with the literature.

4.1 Mesh quality inspection

Two different meshes with the same structure, but with different element numbers were generated on the 3D simplified FSI model. The first set is called "normal" mesh and the second one, with higher number of elements, is called "fine" mesh. The overall information about the mesh size and quality, and the type of mesh elements used for discretization is reported in Tab. 4.1 and Tab. 4.2.

Index	Normal	Fine
Total number of elements	163866	425437
Minimum element quality	0.027	0.047
Average element quality	0.683	0.675

Table 4.1: Overall information about normal and fine mesh structures are presented in the table. The average element quality is high for both meshes, however, the minimum element quality is very low in both discretizations.

The total number of mesh elements in the fine mesh is 2.6 times larger than the total number of elements in the normal mesh, however, the mesh structure and the types of elements used for discretization are the same. There is not an absolute value serving as an index for evaluating the mesh quality because it is very much related to the type of numerical study. In general, elements with a quality below 0.1 is considered as poor quality elements (reference manual of COMSOL Multiphysics®).

Considering the elements quality reported in Tab. 4.1, the average element quality is high and it is quite the same for both the normal and the fine meshes. The minimum element quality is improved in the fine mesh compared to the normal mesh, yet it is below

0.1 for both discretizations. Having elements with quality lower than 0.1 is not always problematic, on the condition that they are located in places with less importance in the geometry. Therefore, to check for the numbers and the locations of the mesh elements with quality lower than 0.1, they are plotted and displayed in Fig. 4.1. As it is shown, the number of low quality elements are too few and they are located in the junction of the LA chamber and MV annulus which does not affect the results of the FSI simulations.

	Number of elements	
Element type	Normal	Fine
Tetrahedrals	144409	392115
Prisms	18955	32491
Pyramids	438	755
Triangles	15122	31028
Quads	1307	1592

Table 4.2: The types of elements and their numbers are reported for both meshes in the table. The tetrahedral element is the dominant one amongst other mesh elements.

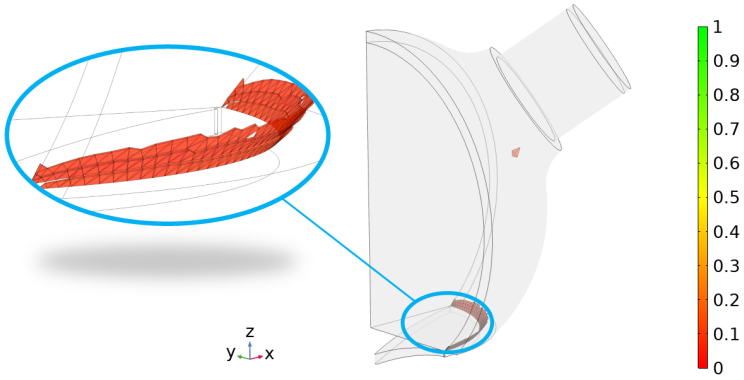

Figure 4.1: The mesh elements with quality less than 0.1 is shown in the geometry for the normal mesh structure. The color bar quantify the element quality.

To further inspect the mesh quality, skewness and maximum angle of the mesh structure were analyzed in the normal mesh. Fig. 4.2 illustrates the histogram of the skewness and the maximum angle. For both criteria, the tail of the histogram is very short and thin, and the histograms are skewed to the right closer to 1, which shows that the quality of the mesh is good.

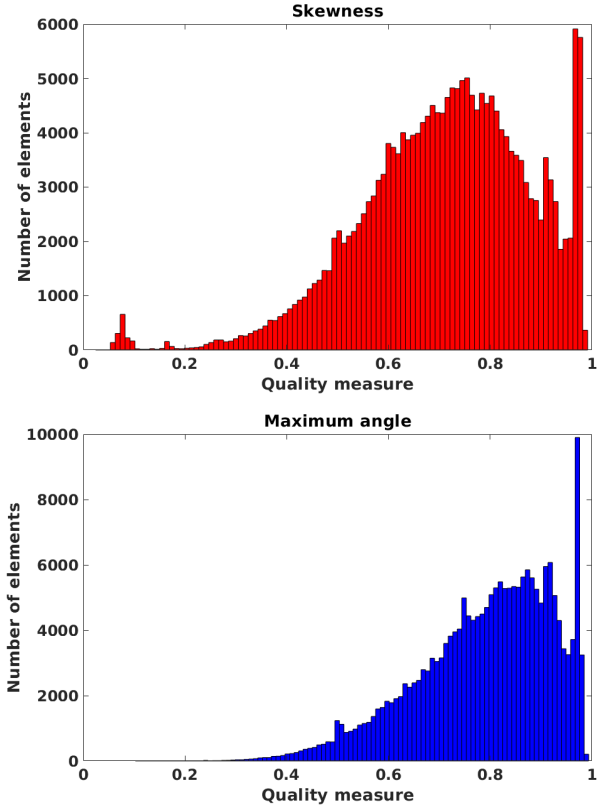

Figure 4.2: The skewness and maxmimum angle histograms are displayed in the figure. For both criteria, the tail of the histograms are very short and thin, and the histograms are skewed to the right closer to 1, which shows that the mesh quality is good.

In this work, the numerical studies were conducted with a normal mesh. However, for the purpose of mesh convergence analysis, explained in Sec. 4.1.1, the simulations were also run with a fine mesh, and the results were compared with the outcomes of the simulations with normal mesh.

4.1.1 Mesh convergence analysis

The results of the FSI simulations with two different total mesh element numbers, normal and fine mesh, were compared. Please note that the mesh structure is the same, and only the number of mesh elements is different between the normal and the fine discretization. The comparison between the hemodynamics results is displayed in Fig. 4.3.

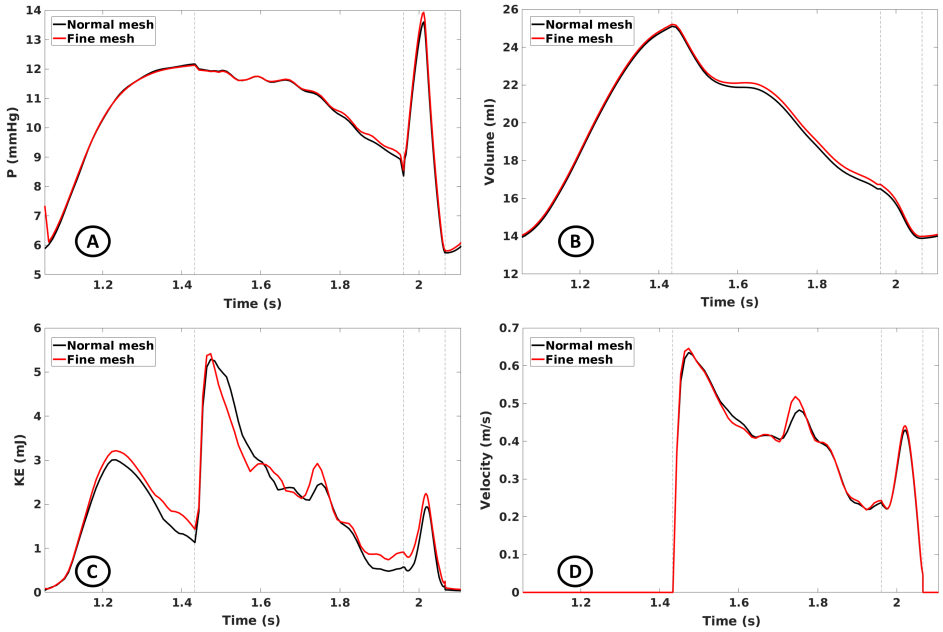

Figure 4.3: The hemodynamic results were compared between two different discretizations. The red curves belong to the fine mesh, and the black curves are obtained from the normal mesh. A) LAP, B) LAV, C) Kinetic energy, and D) TV.

To quantify the variation between the results of two discretizations, the percentage of relative difference, R_d, was calculated and reported in Tab. 4.3. The difference between the normal mesh and the fine mesh for the LAP is 1.4%, for the LAV is 0.7% and for the TV is 1.9%, which are negligible. In the case of K_e (Fig. 4.3C), however, the difference is 36.0% which is high compared to the other measures. It should be considered that the magnitude of the K_e is very low, and therefore, the high difference does not mean that the results vary too much between the two discretizations. The very low R_d confirms that the results are mesh independent, and therefore there is no big difference between using the normal mesh and the fine mesh. The mesh convergence analysis was conducted only on the 3D simplified model, however, it is presumed that the same result would be obtained for the 2D simplified, and 3D realistic models. Hence, to reduce the computational time, the FSI simulations were run with normal mesh on all the FSI models.

4.2 2D simplified left atrium-mitral valve model

In this section, the calculated hemodynamic indices of the 2D model are presented and the impact of MVS on the LA hemodynamics is investigated.

Index	LAP	LAV	KE	TV
R_d %	1.4	0.7	36.0	1.9

Table 4.3: The R_d between the FSI results with normal mesh and fine mesh are reported in the table.

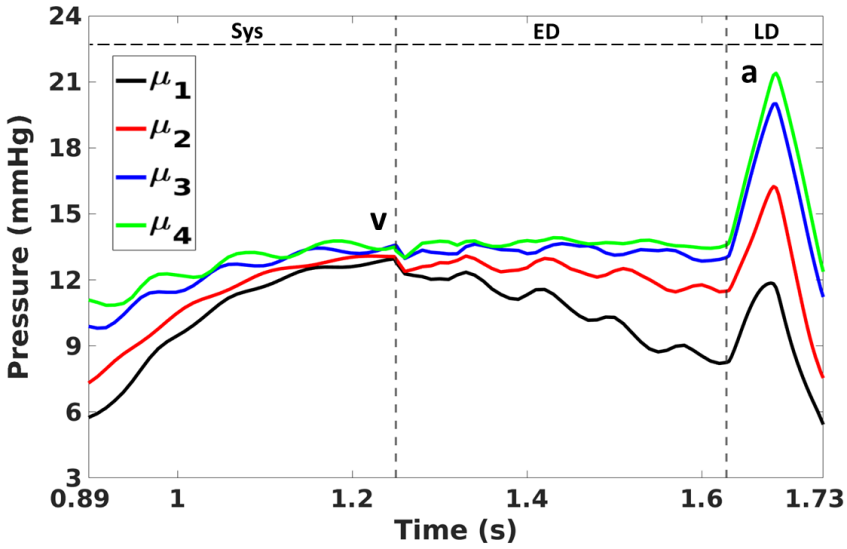

Figure 4.4: The LAP profiles for different MV lame parameters are displayed in the figure. As the MV stiffness increases, the LAP_{mean} increases, and the a-peak is amplified. The LAP indices are reported in Tab.4.4.

4.2.1 Hemodynamics analysis

As it was explained in Sec. 3.3.1, four different Lamé parameters (μ_i) were considered for the 2D MV leaflets, to investigate the impact of MVS on the LA hemodynamics. The LAP, the LA area, the TV and the the MV effective orifice length (EOL) are calculated and displayed in Figs. 4.4-4.7. Moreover, the hemodynamic indices, such as the v-peak and the a-peak of the LAP profile, the E-peak, the A-peak and the E/A ratio of the TV profile, the early diastolic peak of effective orifice length, E_{EOL}, and late diastolic peak of effective orifice length, A_{EOL}, the early diastolic velocity time integration (VTI-ED) and the late diastolic velocity time integration (VTI-LD) of the TV profile, left atrium area at the end of systolic phase A_{Sys}, the LA area at the end of systolic phase, A_{LD}, and the total emptying fraction (TEF) are reported in Tab. 4.4.

The results, presented in Tab. 4.4, show that the MVS hinders the MV leaflets opening, which drastically reduces the E_{EOL} from 16.1 mm to 6.4 mm, and A_{EOL} from 9.6

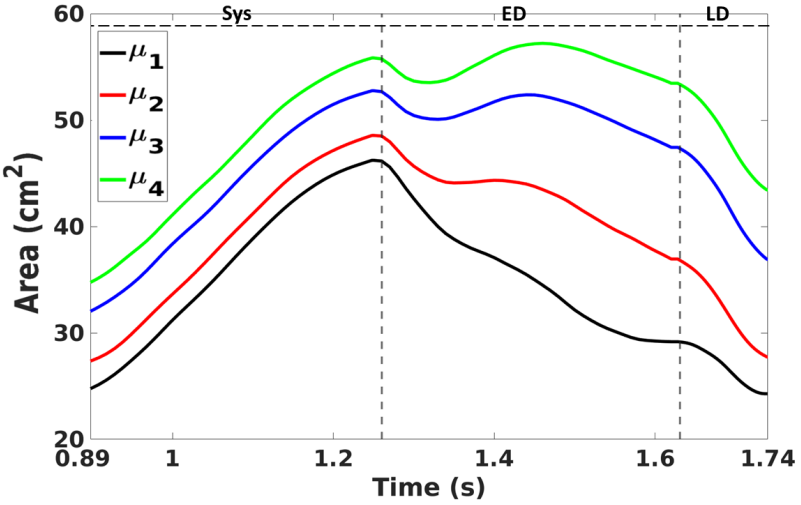

Figure 4.5: The LA area profiles for different MV stiffness are shown in the figure. The MV stiffening disrupts the LA emptying, which is reflected in the reduction in the TEF. The LAV indices are reported Tab.4.4.

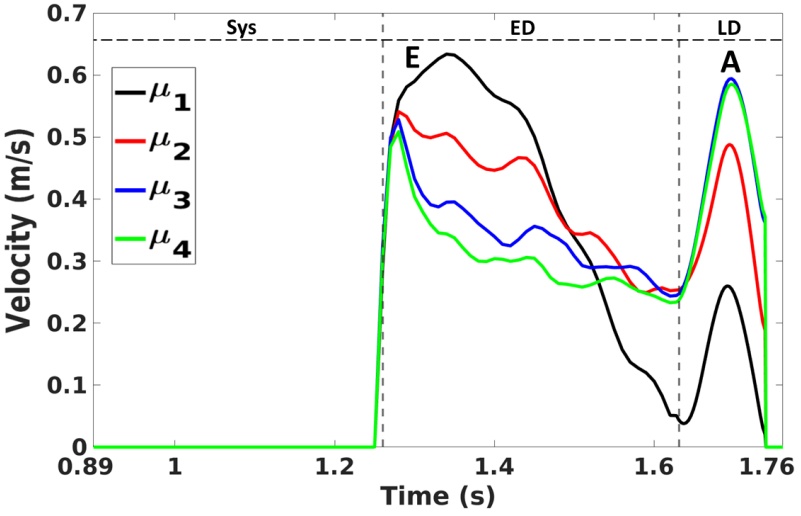

Figure 4.6: The TV profiles for different MV Lamé parameters are displayed in the figure. As the MV stiffens, the E-peak declines, the A-peak amplifies, the VTI-ED decreases, and the VTI-LD increases. The TV indices are reported in Tab.4.4.

Parameter	v-peak (mmHg)	a-peak (mmHg)	LAP_{mean} (mmHg)	E_{EOL} (mm)	A_{EOL} (mm)	E-peak (m/s)	A-peak (m/s)	E/A	VTI-ED (cm)	VTI-LD (cm)	A_{Sys} (cm^2)	A_{LD} (cm^2)	TEF
μ_1	13.0	11.9	10.2	16.1	9.6	0.63	0.26	2.42	15.4	1.6	46.2	24.3	0.47
μ_2	13.1	16.2	12.1	10.6	8.3	0.54	0.49	1.10	15.0	3.9	48.5	27.7	0.43
μ_3	13.5	20.0	13.9	7.9	7.4	0.53	0.59	0.9	12.9	4.9	52.7	36.9	0.3
μ_4	13.6	21.4	14.5	6.4	6.5	0.51	0.59	0.86	11.5	4.8	55.7	43.4	0.22

Table 4.4: The FSI-calculated hemodynamic indices for the different MV Lamé parameters are presented in the table. v-peak = end systolic LAP peak, a-peak = late diastolic LAP peak, LAP_{mean} = mean left atrial pressure, E_{EOL} = early diastolic peak of effective orifice length, A_{EOL} = late diastolic peak of the effective orifice length, E-peak = End systolic peak of the TV profile, A-peak = Late diastolic peak of the TV profile, VTI-ED = early diastolic velocity time integration of the TV profile, VTI-LD = late diastolic velocity time integration of the TV profile, A_{Sys} = Left atrium area at the end of the systolic phase, A_{LD} = Left atrium area at the end of the late diastolic phase, and TEF = total emptying fraction. The TEF is explained in Tab. 4.6.

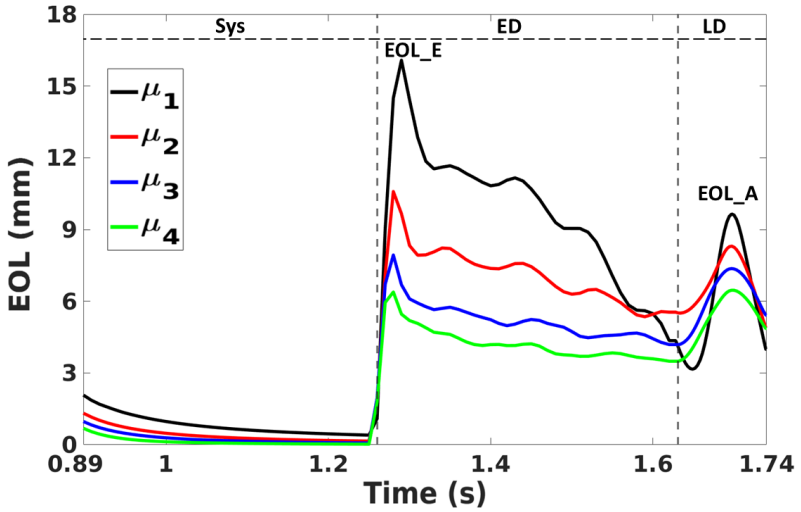

Figure 4.7: The EOL profiles for different MV stiffness are shown in the figure. The MVS hinders the opening of the leaflets, reducing the E_{EOL} and increasing the A_{EOL}. The EOL indices are reported in Tab.4.4.

mm to 6.5 mm (see Fig. 4.7). The reduction of EOL decreases the TEF from 0.47 to 0.22 (see Fig. 4.5), resulting in enhancement of mean left atrial pressure LAP_{mean} from 10.2 $mmHg$ to 14.5 $mmHg$. The increase in LAP_{mean} keeps the LAP elevated and amplifying the a-peak from 11.9 $mmHg$ to 21.4 $mmHg$ (Fig. 4.4). Considering the TV profile, shown in Fig. 4.6, the E-peak is suppressed from 0.63 m/s to 0.51 m/s, and the A-peak is amplified from 0.26 m/s to 0.59 m/s. The alterations of the E-peak and the A-peak reduce dramatically the E/A ratio from 2.42 to 0.86, decrease the VTI-ED from 15.4 cm to 11.5 cm, and increase the VTI-LD from 1.6 cm to 4.8 cm.

4.3 3D simplified left atrium-mitral valve model

In this section, the results of FSI simulation of the 3D simplified model are shown and FSI-calculated mechanics and hemodynamic indices were compared with the literature to investigate if the 3D simplified FSI model replicate the LA and the MV physiological conditions.

4.3.1 Hemodynamics analysis

The calculated R_e profile at the LA inlets for three cycles is shown in Fig. 4.8. The R_e is less than 2000, which confirms that the flow regime in the LA chamber is laminar.

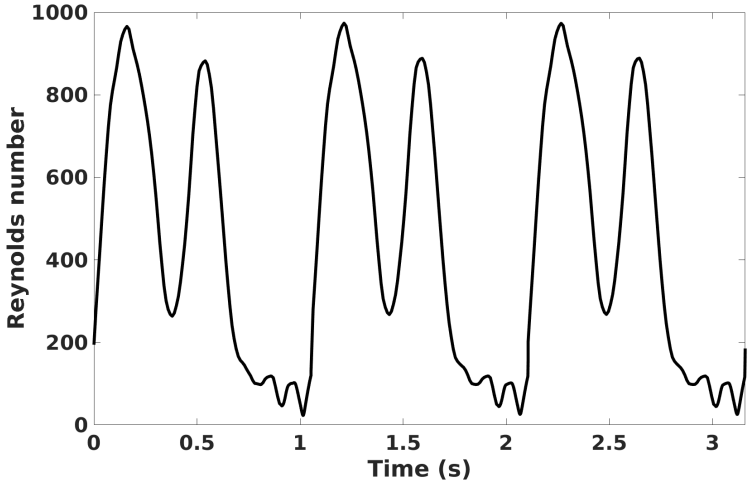

Figure 4.8: The calculated R_e at the LA inlets is displayed for three cycles. The value of the R_e shows that the flow in the LA chamber is laminar.

One of the important indices by which the phasic functions of the LA can be evaluated is the LAP. The calculated LAP waveform of the FSI model and the physiological LAP waveform are displayed in Fig 4.9. The LAP waveform consists of three positive waves, **v**, **a** and **c**, and two negative descents, **x** and **y**. The v-wave represents the LA reservoir phase in which the MV is closed and there is inflow from PVs into the LA chamber. Therefore the pressure in the LA chamber increases, forming the first positive deflection. The peak value in this phase, v-peak, is $12.2\ mmHg$. The subsequent MV opening and LA emptying into the LV, which results in the LAP decrease, is reflected in the negative **y** descent. The LAP descent continues to the onset of the LA contraction. In the LA active pump phasic function, the LA chamber contracts as the result of LA depolarization, results in the LAP second positive wave, marked as the a-wave. The maximum value of the LAP in this phase, a-peak, is $13.6\ mmHg$. After sudden LAP increase, it drops and forms the negative deflection, the **x** descent. The LAP decline continues due to the LA chamber relaxation subsequent to the LAP drop (Zipes et al. 2019). The calculated LAP_{mean} is equal to $6.9\ mmHg$. The calculated values of the LAP components together with the physiological values reported in the literature are presented in Tab. 4.5. All the calculated indices are within the reported range and very close to the reported mean values.

Another index which helps clinicians to diagnose the LH disease is the LAV. Large LAV is a prognostic biomarker of many complications like LA fibrillation, pulmonary hypertension or LA diastolic dysfunction (Blume et al. 2011; McGann et al. 2014; D. A. Patel et al. 2009). The physiological (Jarvinen et al. 1994) and FSI-calculated LAV

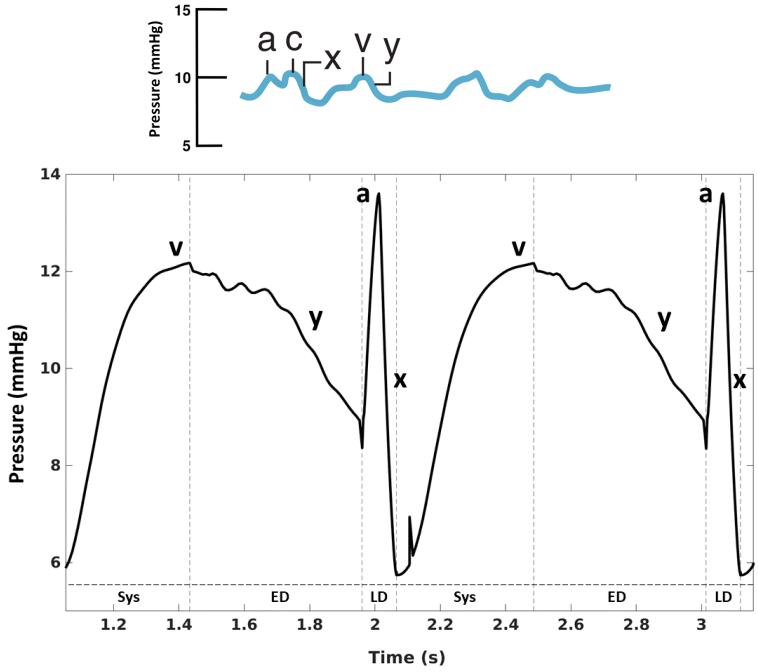

Figure 4.9: The top panel displays the physiological LAP waveform of one cardiac cycle, including three positive waveforms, the **v**, the **a** and the **c** waves, and two negative deflections, **x** and **y**. The image is taken from (Zipes et al. 2019). The bottom panel shows two cardiac cycles of the FSI-calculated LAP waveform of the 3D simplified model. The waveform includes two positive waveforms, **v** and **a** waves, and two negative descents, **x** and **y**. The c-wave is absent in the calculated LAP waveform.

LAP $(mmHg)$	FSI-calculated	Mean*	Range*
a-peak	13.6	10	4-16
v-peak	12.2	12	6-21
Mean	6.9	8	2-12

Table 4.5: The FSI-calculated and physiological LAP indices are presented in the table. The (*) are physiological values reported in Braunwald's Heart Disease medical text book (Zipes et al. 2019).

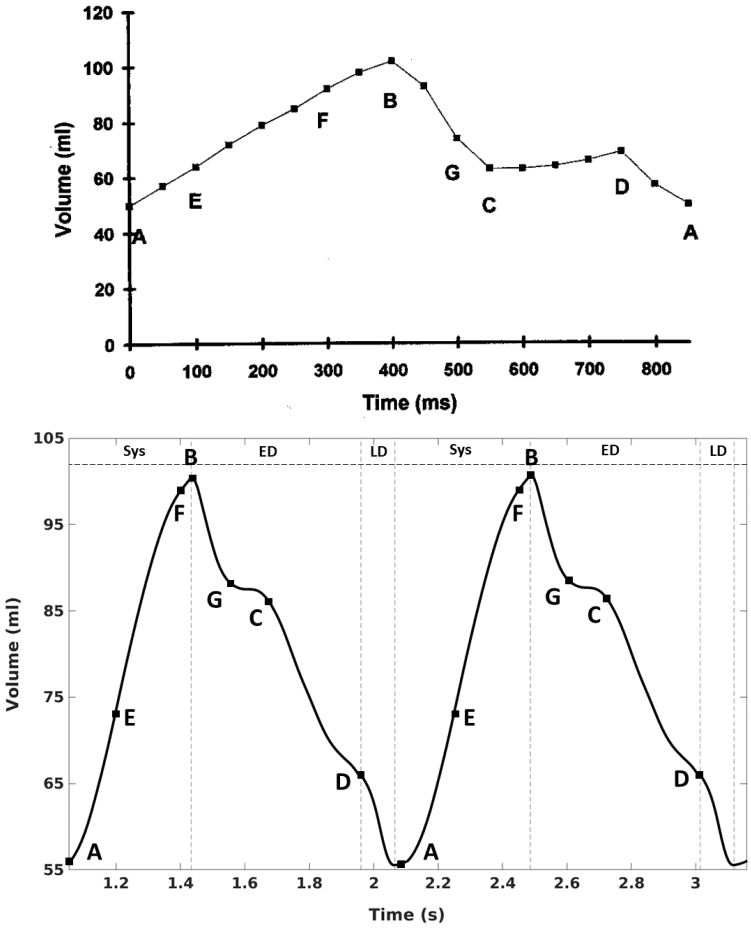

Figure 4.10: The FSI-calculated and physiological LAV waveforms are displayed in the figure. The top panel shows a physiological LAV waveform of one cardiac cycle assessed by cine-MRI examination, presented by Jarvinen et al. (1994). The bottom panel shows the FSI-calculated LAV waveform of the 3D simplified model. The waveform shows two cardiac cycles.

profiles are displayed in Fig. 4.10.

The A-B segment of the profile represents the LA reservoir function in which the MV is closed and the LAV increases as the result of the inflow from PVs into the LA chamber. The maximal LAV V_{max} occurs in this phase at point **B**, which is equal to 100 ml (see Tab. 4.6). The B-D segment reflects the LA conduit function in ED phase, with the point

Index	unit	Description	Value	Reported value
V_{max}	ml	maximal LAV	100	65-139 [§]
V_{min}	ml	minimal LAV	56	32-74 [§]
V_{preA}	ml	LAV prior LA contraction	66	–
$\frac{(V_{max}-V_{min})}{V_{max}}$	–	TEF*	0.44	–
$\frac{(V_{max}-V_{preA})}{V_{max}}$	–	passive emptying fraction*	0.34	0.4 ± 0.1 [†]
$\frac{(V_{preA}-V_{min})}{V_{preA}}$	–	active emptying fraction*	0.15	0.3 ± 0.2 [†]
W_{AS}	$mmHg.ml$	active stroke work**	43.5	44.8 ± 5.5 [‡]
W_{PS}	$mmHg.ml$	passive stroke work**	4.2	–

Table 4.6: The FSI-calculated and physiological LAV indices of the 3D simplified model are reported. (*) reported by (Blume et al. 2011; Kebed, Addetia, and Lang 2019), (**) reported by (Barbier et al. 1999; Dernellis et al. 1998; Grant, Bunnell, and Greene 1964; Hoit 2017; Matsuda et al. 1983), ([§]) reported by (Jarvinen et al. 1994), ([†]) reported by (Reda et al. 2015), ([‡]) reported by (Stefanadis et al. 1998)

C marking the mid diastolic time. In this LA phasic function, the MV opens passively as the LAP exceeds the LVP and LA empties passively into the LV chamber. Hence, the LA chamber releases the elastic energy stored during reservoir phase and contracts which results in a LA volume decline. The volume at point **D** reflects the LAV prior to the LA contraction V_{preA} which is equal to 66 ml (see Tab. 4.6). The D-A segment reflects the LA active pump phasic function in which the LA contracts actively as the result of depolarization and empties the residual blood into the LV chamber. The LAV at point **A** represents the minimal LAV V_{min} equal to 55 ml (see Tab. 4.6). The **E** and **F** points marked the LAV in $0.2s$ interval during LA filling and **G** points is the LAV $0.1s$ after the end of systole (Jarvinen et al. 1994). Similar points are marked on the LAV of the FSI model. As it is shown in Fig. 4.10, regardless of the C-D segment, the FSI LAV waveform is very much similar to the physiological one.

The LA p-v loop is another useful index employed in evaluating the LA mechanical and hemodynamic function. For instance, by measuring the slope of the V-loop, the LA chamber compliance can be evaluated, or by assessing the A-loop characteristics the LA contractility can be analysed. The physiological and FSI-calculated p-v loops are shown in Fig. 4.11. Considering the FSI p-v loop in the bottom panel of Fig. 4.11, on the lower left side, the LA reservoir phase starts which results in the LAP and the LAV increase.

The reservoir phase closes the A-loop and continues to the **v** point, forming the upper limb of the V-loop. At point **v**, the LA reaches to its maximum pressure and volume, and causes the MV opening. The reservoir phase is displayed with red color on the p-v loop. The LA conduit phase, shown in blue color, starts from the **v** point, and results in the LAP and the LAV decrease. This phase continues to the onset of the third phase, the LA active

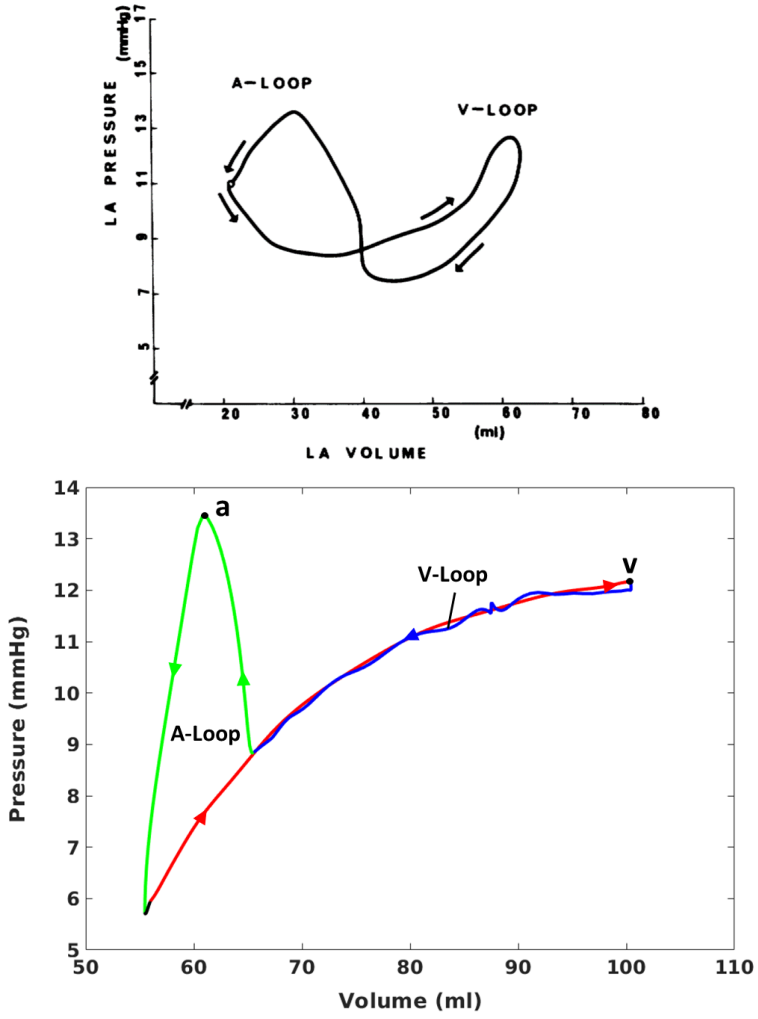

Figure 4.11: The FSI-calculated and physiological LA p-v loop is displayed in the figure. The top panel shows a typical p-v loop, reported by Stefanadis et al. (1998). The lower panel displays the FSI-calculated p-v loop. It contains two loops, A-Loop corresponds to the LA active pump function, and V-Loop reflects the LA conduit phase. The **a** and the **v** points on the graph are the a-peak and v-peak of the LAP reported in Tab. 4.5. The area under the A-Loop is W_{AS}, and the area enclosed by V-Loop is W_{PS}, reported in Tab. 4.6.

pump phase function, marked with green color. In the third phase, the LAP increases and the LAV declines due to the LA contraction, closing the V-loop and forming the A-loop on the p-v loop diagram. The loop is completed with the black line segment, showing the isovolumic relaxation phase. The FSI calculated p-v loop has some differences compared to the physiological one, shown in the upper panel of Fig. 4.11. First of all, the beginning of the reservoir phase, which is the lower limb of the A-loop, is convex while it is concave on the FSI p-v loop. On the physiological p-v loop, when the LA reaches its maximum pressure and volume at the end of reservoir phase, the MV opens, and results in a parallel fall in the LAP and the LAV. After, there is a short instance in which the LAP increases while the LAV remains constant, called LA diastasis. This constant line crosses the V-loop and starts the A-loop. The LA diastasis is absent on the FSI p-v loop. The shape of the A-loop is almost the same on both curves.

The LA function indices are reported in Tab. 4.6. The TEF is equal to 0.44, the passive emptying fraction is 0.34, and the active emptying fraction is 0.15. The left atrial active stroke work W_{AS}, equal to $43.5\ mmHg \cdot ml$, is defined as the enclosed area by the A-loop on the p-v loop diagram, corresponding to the LA work during the LA contraction in the LD phase contributing $15 - 30\ \%$ of the LV stroke volume (Blume et al. 2011). The area under V-Loop reflects the left atrial passive stroke work W_{PS}, equal to 4.2 $mmHg \cdot ml$, results in a passive emptying of blood from the LA to the LV during the ED phase. The calculated indices are all within the reported range in the literature which demonstrates that the FSI model replicated the LAV successfully. For some of the indices, however, a specific reported value was not found. The prognostic importance of these LA function indices in evaluating the LA function is discussed in the literature (Barbier et al. 1999; Blume et al. 2011; Dernellis et al. 1998; Grant, Bunnell, and Greene 1964; Hoit 2017; Kebed, Addetia, and Lang 2019; Matsuda et al. 1983).

Acquisition of the TV profile is one of the routine non-invasive quick clinical examinations used to evaluate the mechanics and hemodynamics of the LA, and in general the LH. A typical TV profile is shown in the upper panel of Fig. 4.12. It consists of three time peaks, the **E**, the **L** and the **A** peaks. The TV profile is zero during the LA reservoir function in Sys phase when the MV is closed. At the end of the Sys phase, the LA conduit phase begins in which the MV opens and the blood is passively emptied to the LV, and forms the E-peak on the TV profile. This phase is also called LV rapid filling phase. The second peak on the TV profile is the L-peak which is attributed to the PVs diastolic forward flow (DFF). After the E-peak, the velocity declines and then surges again due to the third peak of the PVF profile (see Fig. 8.7). The L-peak is introduced for the first time with (Keren et al. 1986), and it is called **L** to be named right after the **J** and the **K** peaks on the PVs velocity profile (Keren et al. 1986). After the L-peak, the velocity continues dropping to the onset of the LA active pump function in the LD phase. Due to the LA contraction, the LAP exceeds the LVP abruptly, which results in the pumping of the residual blood from the LA to the LV, and creates the A-peak on the TV profile. Right after the A-peak, the velocity declines and goes to zero due to the closure of the MV as the result of the reversing pressure gradients between the LA and the LV. The FSI-calculated

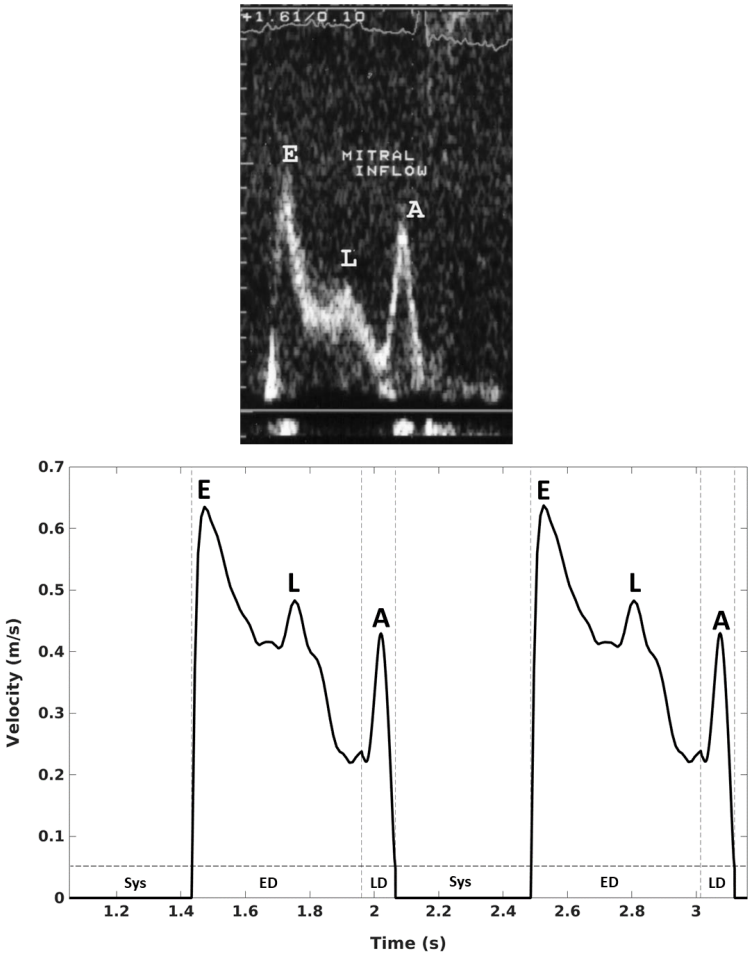

Figure 4.12: The FSI-calculated and physiological TV profiles are displayed in the figure. The upper panel shows one cardiac cycle of the TV profile pattern of a patient measured with Echo-Doppler (Kerut 2008). The lower panel displays two cardiac cycles of the calculated TV profile of the 3D simplified model. The **E**, **L** and **A** waves are marked on the profiles corresponding the velocity in ED, mid-Diastole, and LD phases, respectively.

TV profile, shown in the lower panel of Fig. 4.12, matches with the velocity profiles reported in the literature (Keren et al. 1986; Kerut 2008; Nagueh 2018; Nishimura et al. 1990; Zipes et al. 2019).

All the three phases of the LA function is reflected very well on the FSI-calculated TV profile. The important indices of the TV profile are reported in Tab. 4.7. The E-peak is equal to $0.63\ m/s$, the L-peak is $0.48\ m/s$, and the A-peak is $0.43\ m/s$. The velocity time integration (VTI) is calculated as the area under the TV profile. The VTI-ED, equal to $22.0\ cm$, is the area under the ED and VTI-LD, equal to $3.0\ cm$, is the area under the LD portion of the TV profile. deceleration time (DT), equal to $500\ ms$, is calculated as the time the TV takes to decline from the E-peak to the onset of the LD phase. The FSI-calculated E-peak, A-peak, E/A ratio and DT are within the reported range in the literature which shows the model replicated the physiological TV profile.

Index	unit	FSI simulation	Reported values
E-peak	m/s	0.63	$0.54 \pm 0.13^{*}$
L-peak	m/s	0.48	-
A-peak	m/s	0.43	$0.44 \pm 0.21^{*}$
E/A	–	1.47	0.8-1.7**
VTI-ED	cm	22.0	-
VTI-LD	cm	3.0	-
DT	ms	500	$225 \pm 39^{*}$

Table 4.7: The FSI-calculated and physiological TV profile indices of the 3D simplified model are reported. VTI-ED = Early diastolic velocity time integration. VTI-LD = Late diastolic velocity time integration. DT = Deceleration time. (*) and (**) are reported in (Nishimura et al. 1990) and (Zipes et al. 2019), respectively.

The MV is an important atrioventricular valve which transmits the blood flow energy from the LA into the LV. MV dysfunction generates complications in the cardiac mechanics and disturbs, specifically, the mechanical function of the LA and the LV. One method to evaluate the mechanical function of the MV is to measure the EOA of the MV during the valve opening in the diastolic phase. The EOA was assumed to be a circular plane and therefore, it is simply calculated with πR^2. To calculate the radius of the circular EOA, $R\ (mm)$, the displacement magnitude of the tip of the MV leaflets in XY plane was measured. The calculated EOA and R are shown in Fig. 4.13. There are two main peaks on the EOA profile, the E_{EOA} and the A_{EOA}, which shows the maximum MV opening in the ED and the LD phases, respectively. The E_{EOA} is equal to $100\ mm^2$, and A_{EOA} is equal to $69\ mm^2$.

Another index which can be used to analyse the cardiac function is the kinetic energy K_e of the blood pool. The K_e is assumed to be an important measure of the cardiac

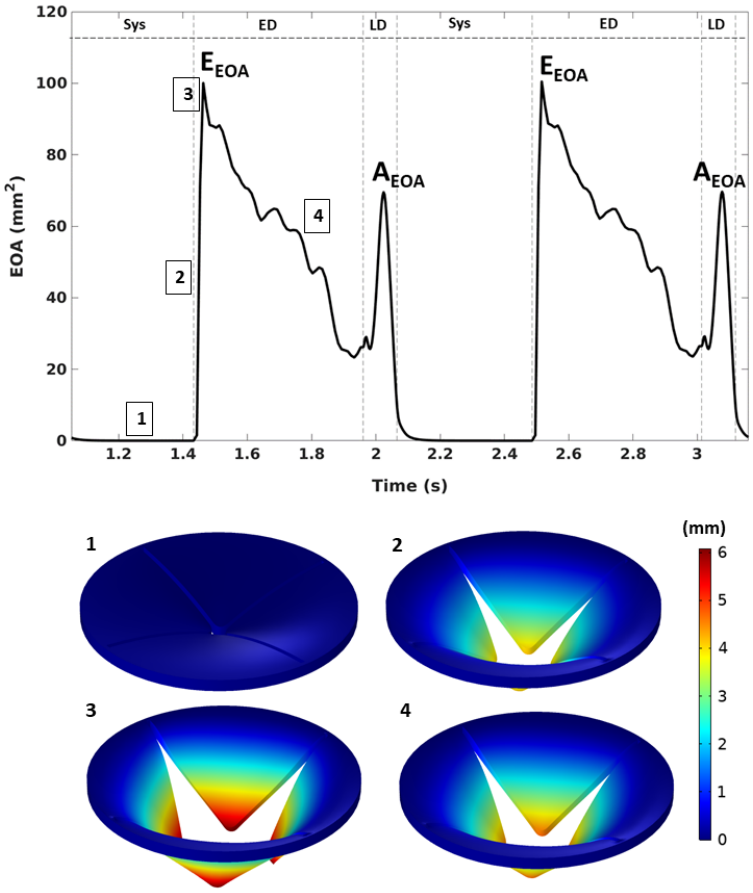

Figure 4.13: The FSI-calculated EOA profile of the 3D simplified model. The upper panel displays the EOA of the MV opening during ED and LD phases. The EOA is calculated as a circular plane. The diameter of this plane is the displacement of the tip of the leaflets in XY plane. The upper panel shows the displacement magnitude of the tip of the leaflets in the XY plane in 4 time instants, marked on the EOA diagram.

pumping efficiency (Arvidsson et al. 2013). It constitutes a part of the heart external work, which is applied to pump the blood out of the heart. In fact, it is a measure of how much potential energy is needed to accelerate a volume of blood pool in and out of the cardiac chambers (Arvidsson et al. 2013). In some cardiac diseases the K_e may be influenced, while the pressure is normal, and therefore, it can be served as a diagnostic index (Arvidsson et al. 2013). A typical physiological K_e and the FSI-calculated K_e profile are presented in Fig. 4.14.

The physiological K_e profile (Arvidsson et al. 2013) has three peaks related to the three cardiac phasic function. The first peak occurs in ventricular systole during the LA reservoir function in which the MV is closed. The K_e increase during the systolic phase is attributed to three mechanisms, 1) the MV annulus movement, 2) LAV increase and 3) the extracardiac blood accelerating into the LA. During systole, the LV contracts longitudinally to pump the oxygenated blood to the body. This longitudinal movement causes the MV annulus downward movement. This is the main cause of the s_2 peak of the PVF profiles, explained in Sec. 8.3.1, resulting in LA filling. The LAV increases due to the LA relaxation right after the LA contraction, the downward movement of the MV annulus, and the continuous inflow from the PVs into the LA. The downward MV movement and the LA relaxation have a counter effect on the PVF, resulting in accelerating the PVs inflow into the LA chamber. Here, it can be postulated that the anatomical structure and the size of PVs affect the K_e. The two diastolic K_e peaks, demonstrating that the K_e increase during the ED and the LD phases are generated due to the acceleration of blood flowing from the LA into the LV. This acceleration is attributed to the pressure gradient between the LA and the LV. This pressure gradient is generated due to the LAP increase during the LA reservoir phase, the LAP drops at the end of Sys phase, generating LV diastolic suction, the LA passive pumping action during the LA conduit phase due to the LA elastic energy release, and the LA active pumping function due to the LA depolarization (Arvidsson et al. 2013). The FSI-calculated K_e indices are presented in Tab. 4.8. The first peak which is the Sys-peak is equal to $3\ mJ$, the second peak, ED-peak is equal to $5.3\ mJ$ and the third peak, LD-peak is $1.9\ mJ$. The FSI-calculated indices are not far from the reported values in the literature, and the FSI-calculated K_e profile, shown in Fig. 4.14 displays the same pattern as the physiological K_e profile. Therefore, the FSI model can replicate the K_e of the LA.

The evolution of the K_e along with the vortex rings in the flow field during the three LA phasic functions are presented in Figs. 4.15-4.17. During the LA reservoir function in the systolic phase (see Fig. 4.15), the maximum K_e is located in the PVs at the beginning, and then it is translated into the LA above the MV plane at the end of the reservoir phase. Taking into account the streamlines in the LA, the flow at the beginning is straight (non-rotational). As the flow moves into the chamber, the rotational flow starts forming and generating the vortex rings. The maximum K_e at the end of Sys phase is translated into the chamber and concentrated in the vortex rings. At the beginning of the LA conduit function in ED phase, the K_e sharply increases as shown in Fig. 4.14. During this phase, as displayed in Fig. 4.16, the flow is mainly straight in the LA chamber and located across

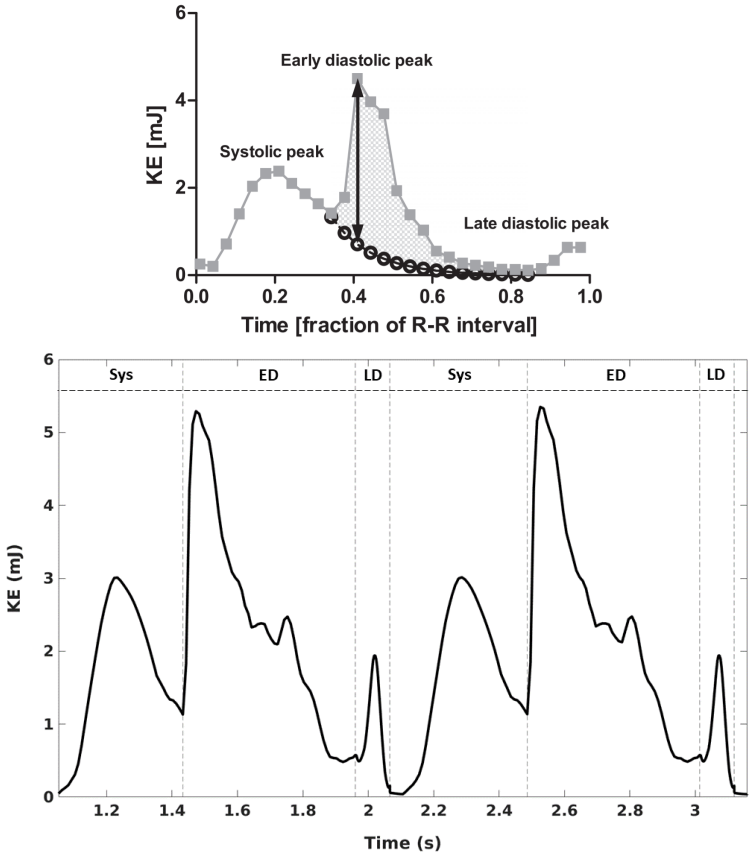

Figure 4.14: The physiological and FSI-calculated K_e profiles of the 3D simplified model are displayed. The upper panel shows one cardiac cycle of the physiological K_e profile, reported by Arvidsson et al. (2013). The gray boxes show the physiological K_e and the black cicrles indicate hypotheticalK_e. The lower panel presents two cardiac cycles of the FSI-calculated K_e profile of the 3D simplified model. The FSI-calculated must be compared with the gray boxes in the upper panel.

$K_e\ (mJ)$	FSI-calculated	Reported values*
Sys-peak	3	1.5 ± 0.1
ED-peak	5.3	3.5 ± 0.25
LD-peak	1.9	0.8 ± 0.1

Table 4.8: The FSI calculated K_e indices of the 3D simplified model. The (*) are physiological values reported by Arvidsson et al. (2013).

the MV, which can be seen as a streak from the middle of the LA chamber to the MV outlet. Again, the K_e conservation in the vortex rings, generated behind the MV leaflets, is clearly displayed. In the last LA phasic function (Fig. 4.17), like the conduit phase, the flow is mainly straight with vortex formation behind the MV leaflets and the maximum K_e is seen across the MV. The difference with the previous phase is, the backward flow in the PVs act as an outlet. Hence, the LA is not only pumping the flow out to the LV through the MV, but also pushing the blood out through the extraparenchymal PVs.

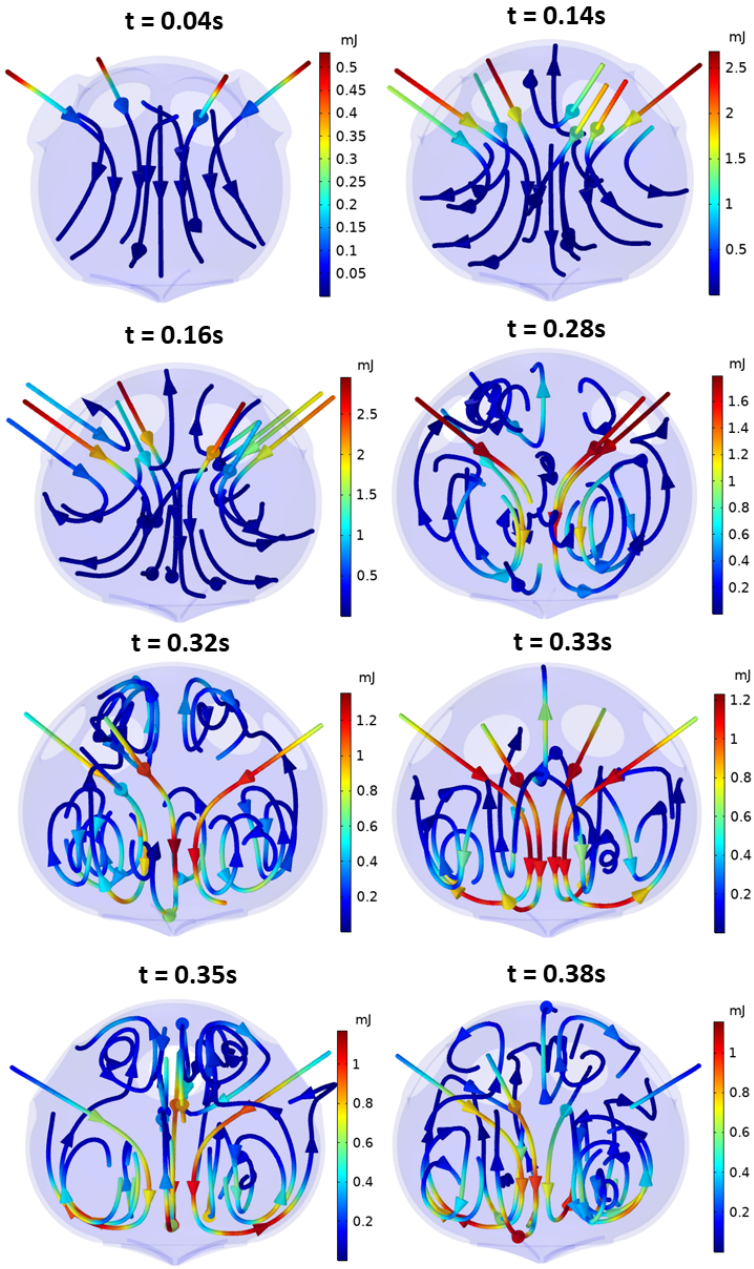

Figure 4.15: The evolution of the K_e in the flow field streamlines is displayed for eight time instants during the LA reservoir function in the Sys phase. At the beginning, the flow is mainly straight and the maximum K_e is located at the PVs. As it approaches to the end of the reservoir phase, the rotational flow is dominant and the maximum K_e is located and conserved in the vortex rings in the LA chamber above the MV plane.

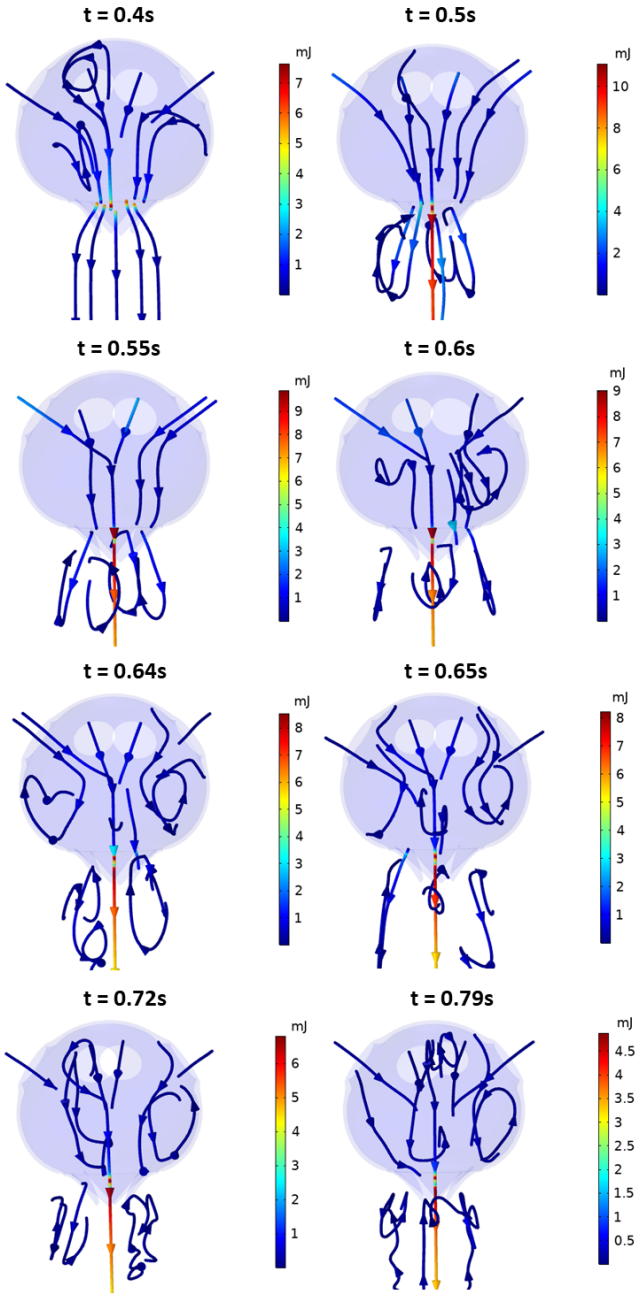

Figure 4.16: The flow field streamlines for eight time instants during LA conduit function in the ED phase is displayed in the figure. It is clearly shown that the LA chamber acts like a conduit which delivers the blood flow from PVs to the LA through the MV. The maximum K_e is located across the MV. The flow in the LA chamber is mainly straight, and vortex rings are formed behind the MV leaflets.

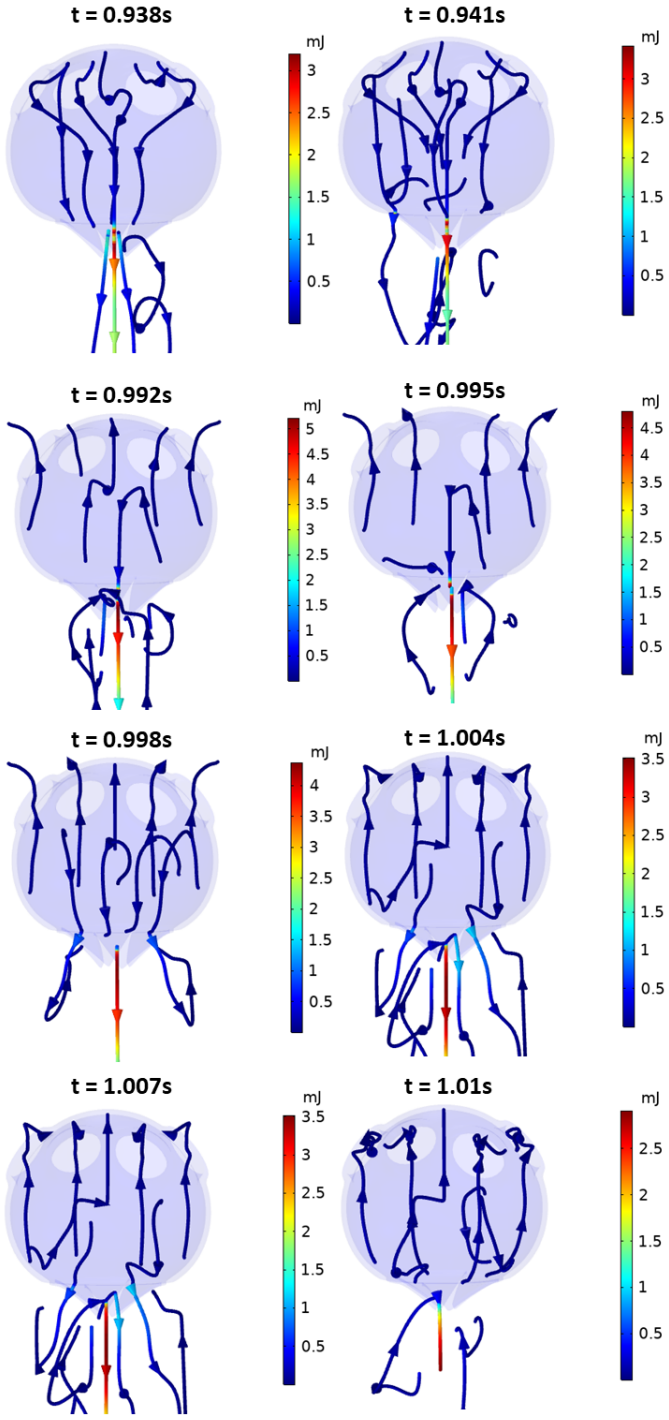

Figure 4.17: The blood flow direction in eight time instants during LA active pump function in the LD phase is displayed in the figure. The backward flow through the PVs is clearly shown, which confirms that in this phase, the PVs act as outlets for the LA chamber. The maximum K_e is still seen as a streak from the middle of LA chamber to the MV outlet.

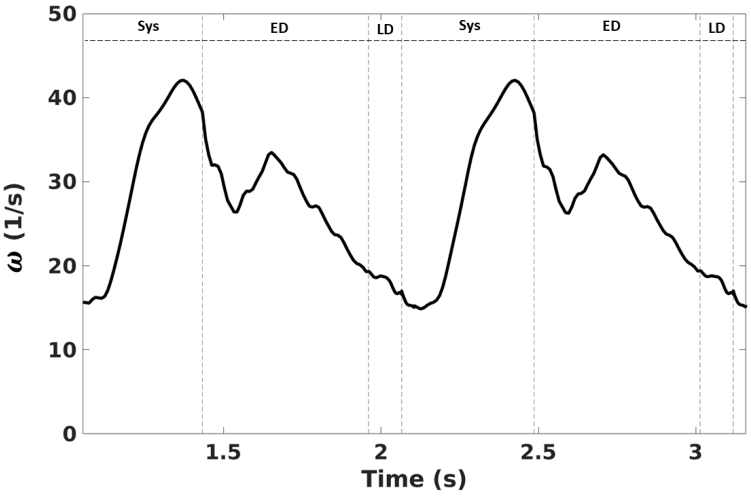

Figure 4.18: The FSI-calculated average vorticity magnitude of the 3D simplified model for two cardiac cycles is displayed. The vorticity is higher in the Sys phase compare to the ED and the LD phases. It confirms the results shown in Fig. 4.15.

The FSI-calculated average vorticity magnitude is shown in Fig. 4.18. The vorticity describes the evolution of the local rotation of the fluid. Considering the vorticity magnitude, it is higher in the Sys phase compare to the ED and LD phases. Taking into account the evolution of the rotational flow in Fig. 4.15 and compare it with the flow field evolution in Figs. 4.16-4.17, it can be observed that the rotational flow is more dominant than straight flow in the reservoir phase. The rotational flow still exist in the ED phase, however, in the LD phase the straight flow is more dominant than rotational flow. Therefore, the vorticity magnitude during the LA active pump function is lower compared to the other phases.

4.3.2 Mechanical analysis

The maximum principal stress profile for the LA chamber and the MV are displayed in Fig. 4.19. The maximum principal stress of the LA chamber is similar to the LAP profile shown in Fig. 4.9. It confirms the findings of Feng et al. (2019) that the maximum principal stress follows the pressure evolution in the LA chamber. The maximum value of the LA maximum principal stress, equal to 143 kPa, is at the end of the reservoir phase, corresponding to the V_{max}. The LA maximum principal stress reaches to its minimum value, equal to 24 kPa, at the end of the LD phase. Interestingly, the maximum principal stress of the MV leaflets resembles the TV and the EOA profiles displayed in Fig. 4.12 and 4.13. It contains two peaks, one in the ED phase equal to 400 kPa, and one in the

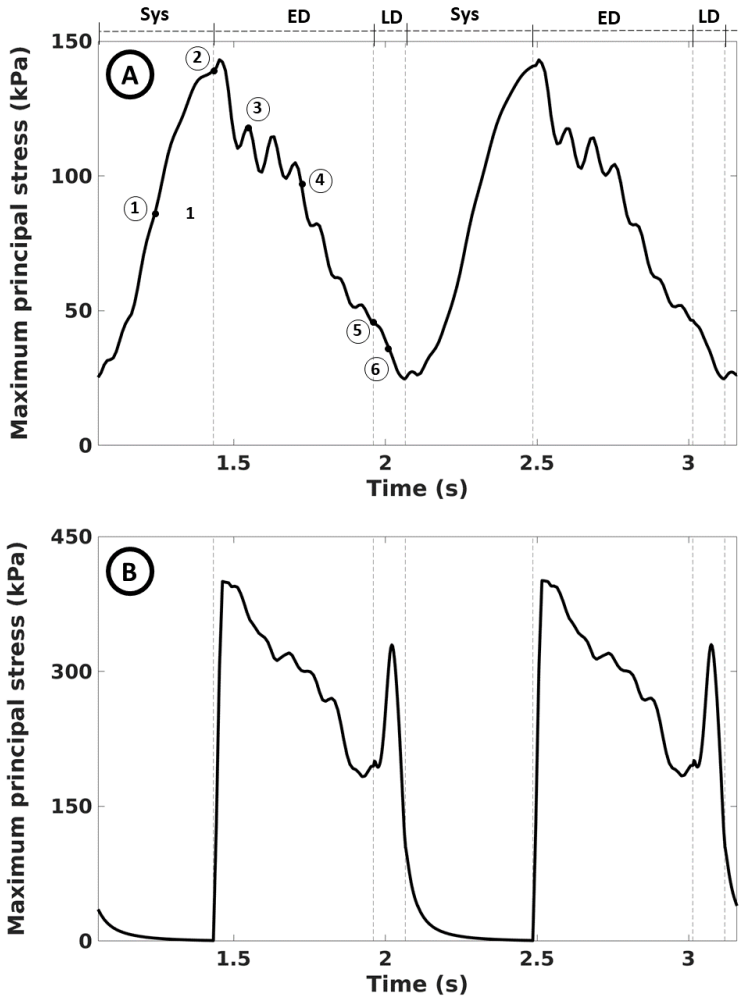

Figure 4.19: Two cardiac cycles of the maximum principal stress profile of the 3D simplified model for A) the LA chamber and B) the MV are displayed in the figure. The numbers 1-6 on the plot **A** corresponds to the numbers in Fig. 4.20.

LD phase, equal to 329 kPa. These two peaks are attributed to the E_{EOA} and A_{EOA}, where the maximum displacement of the leaflets happens.

The evolution of the maximum principal stress in six time instants during one cardiac cycle is illustrated in Fig. 4.20. The first two images (1-2) show the maximum principal

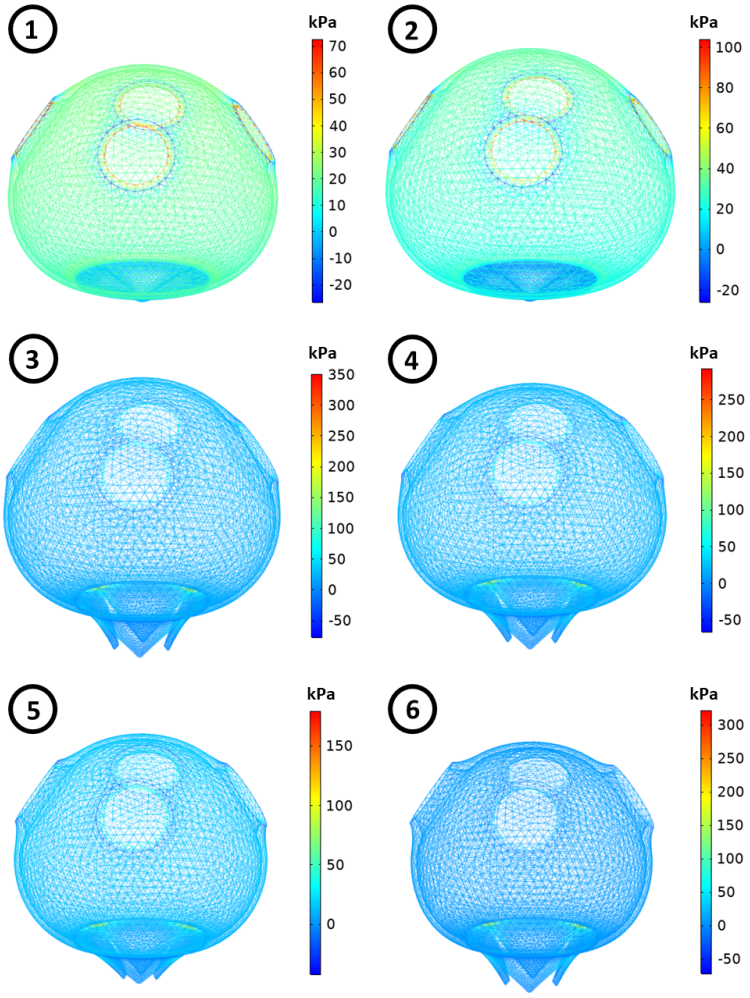

Figure 4.20: The evolution of the maximum principal stress in the LA chamber and MV leaflets are illustrated in the figure. 1-2, 3-4 and 5-6 corresponds to the maximum principal stress of the Sys, the ED and the LD phases, respectively. The points 1-6 are also marked on the Fig. 4.19. In the Sys phase (1-2), the maximum principal stress is high in the LA wall. In the diastolic phase (3-6) the maximum principal stress is high around the MV annulus.

stress during mid and late LA reservoir phasic function. Regardless of the maximum stress concentration around the PVs ostium, which may be caused by the LA design features, the stress is uniformly distributed all around the LA chamber. The next two images (3-4) displays the maximum principal stress distribution during the LA conduit function in the ED phase. Here, the maximum stress is concentrated around the MV annulus. The last two images (5-6) illustrate the maximum principal stress in LA active pump function in LD phase. Like the the ED phase, the maximum stress is concentrated around the MV annulus.

To further analyze the LA and the MV mechanical structure, the maximum principal stretch in both the LA and the MV was calculated and presented in Fig. 4.21. Very similar to the maximum principal stress profiles, the maximum principal stretch profiles of the LA and the MV resembles the LAP and the TV profiles, respectively. The evolution of the maximum principal stretch in six time instants in one cardiac cycle is displayed in Fig. 4.22. During the LA reservoir phase (1-2), the LA reaches to its maximum stretch, equal to 2.4, due to the PVs inflow and the increase in the LAV. In the ED phase, as the MV opens and the LA empties into the LV, the LA maximum stretch drops. However, it does not decline instantly since the PVs inflow continues flowing into the chamber. In the LD phase (5-6), the LA maximum stretch reaches to its minimum value, equal to 1.3, due to the LA contraction, to actively pump the blood out of the LA chamber.

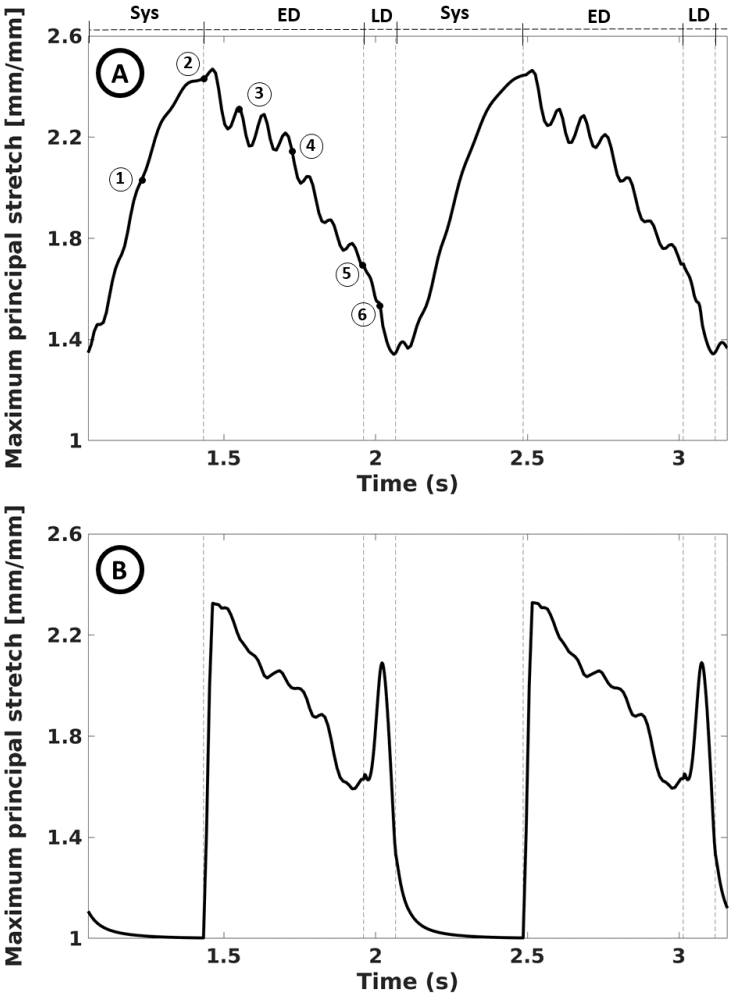

Figure 4.21: Two cardiac cycles of the maximum principal stretch of the 3D simplified model for A) the LA chamber and B) the MV leaflets are shown in the figure. The numbers 1-6 on plot **A** corresponds to the numbers in Fig. 4.22.

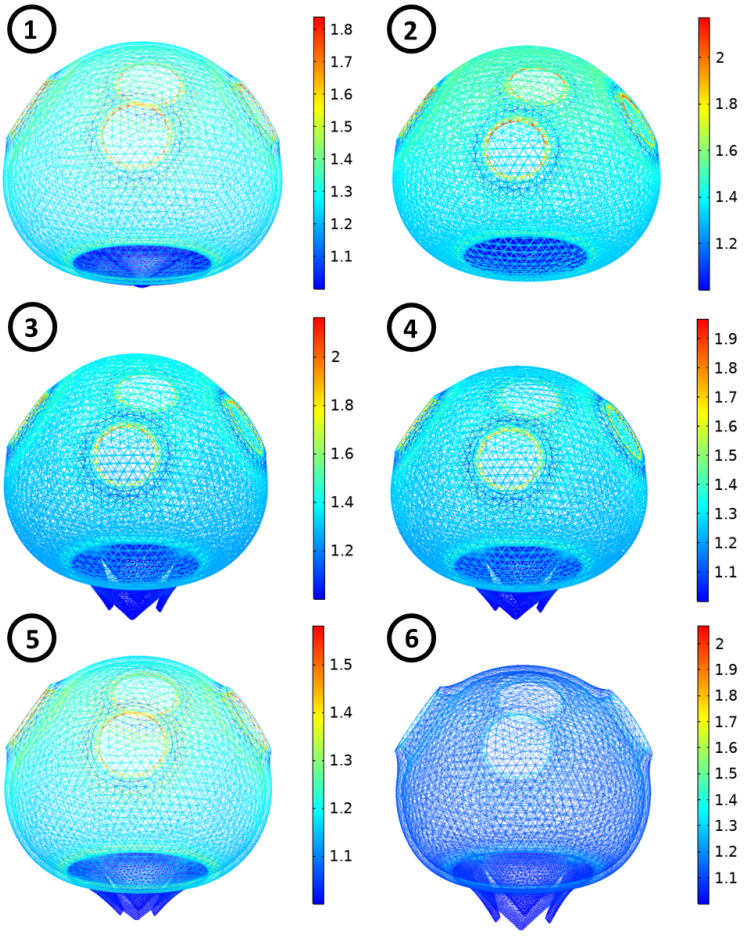

Figure 4.22: The evolution of the maximum principal stretch in the 3D simplified model for six time instants in one cardiac cycle is displayed in the figure. 1-2, 3-4 and 5-6 corresponds to the maximum principal stretch of the Sys, ED and LD phases, respectively. The points 1-6 are also marked on Fig. 4.21.

4.4 3D realistic left atrium model

In this section, the FSI-calculated mechanics and hemodynamics of the 3D realistic LA model was analyzed to inspect if the adapted FSI method from 3D simplified model works well for the 3D realistic model.

4.4.1 Hemodynamic analysis

The LAP is the first index to be calculated as it plays a crucial rule in clinical examinations. The FSI-calculated LAP profile is shown in Fig. 4.23. The LAP profile contains the main elements of a physiological LAP waveform, **v** and **a** peaks, and **x** and **y** descents. The calculated indices are reported in Tab. 4.9. The v-peak, corresponding the LAP peak in the Sys phase, is equal to 7.7 $mmHg$, the a-peak which shows the maximum LAP in the LD phase is 9.3 $mmHg$, and the LAP_{mean} is equal to 4.5 $mmHg$. All the FSI-calculated indices are within the physiological ranges reported in the literature (Zipes et al. 2019). Moreover, the LAP waveform resembles the physiological one displayed in Fig. 4.9. It shows that the 3D realistic LA model can replicate the physiological LAP.

The next calculated hemodynamics parameter is the LAV. The calculated LAV profile is displayed in Fig. 4.24.

The LAV waveform is similar to the physiological LAV profile displayed in Fig. 4.10. The key FSI calculated LAV indices are presented in Tab. 4.10. The LA TEF is equal

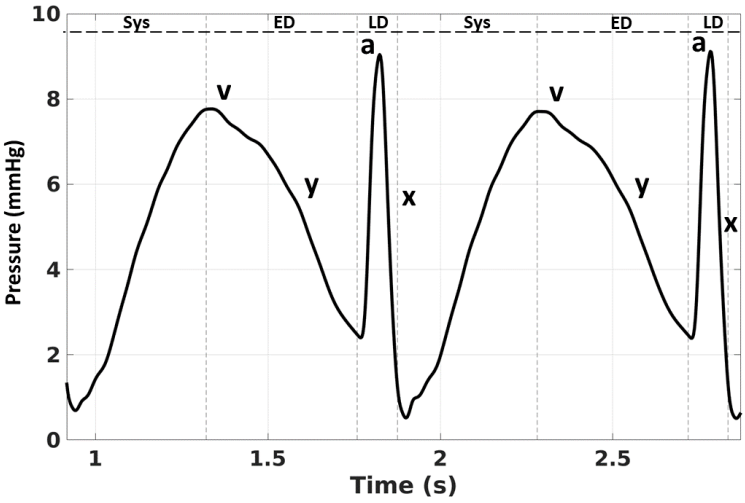

Figure 4.23: The FSI-calculated LAP waveform of the 3D LA realistic model for two cardiac cycles is shown in the figure. The waveform includes two positive waveforms, **v** and **a** waves, and two negative descents, **x** and **y**.

LAP $(mmHg)$	FSI-calculated	Mean*	Range*
a-peak	9.3	10	4-16
v-peak	7.7	12	6-21
Mean	4.5	8	2-12

Table 4.9: The FSI-calculated and physiological LAP indices are presented. The (*) are physiological values reported in Braunwald's Heart Disease medical text book (Zipes et al. 2019).

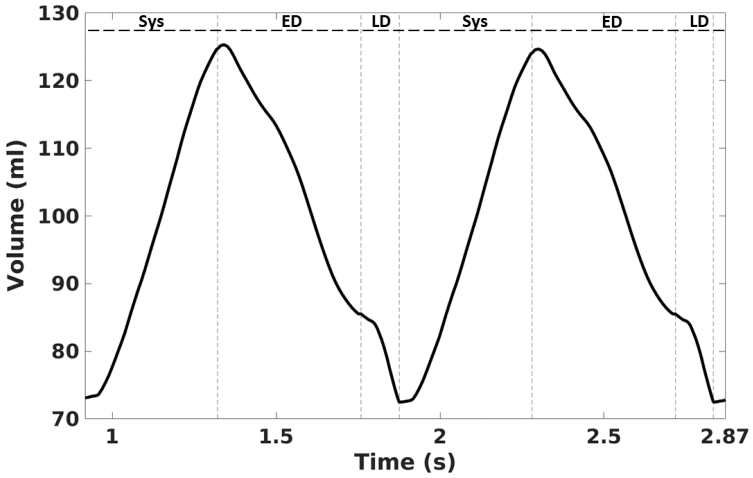

Figure 4.24: The FSI-calculated LAV waveform of 3D realistic model for two cardiac cycles is displayed in the figure. The calculated LAV profile resembles the physiological waveform displayed in Fig. 4.10.

to 0.42, the LA passive emptying fraction is 0.32, and the LA active emptying fraction is equal to 0.14. The calculated passive and active emptying fractions are within the reported physiological values in the literature.

The The FSI-calculated p-v loop of the 3D realistic model is displayed in Fig. 4.25. The W_{AS} is $50.9\ mmHg \cdot ml$ and the W_{PS} is $4.4\ mmHg \cdot ml$. The FSI-calculated W_{AS} is in the physiological range reported in the literature (Tab. 4.10).

The FSI-calculated TV profile of the 3D realistic model is displayed in Fig. 4.26. The TV profile pattern includes the E-peak, equal to $0.75\ m/s$, reflecting the maximum TV during the ED phase, and the A-peak, equal to $0.48\ m/s$, representing the maximum TV in the LD phase. Excluding the L-wave (Fig. 4.12), the FSI-calculated TV profile captured the main TV events, and is identical to the TV profiles reported in the literature

Index	Unit	Description	Value	Reported value
V_{max}	ml	maximal LAV	125	65-139 [§]
V_{min}	ml	minimal LAV	73	32-74 [§]
V_{preA}	ml	LAV prior LA contraction	84	–
$\frac{(V_{max}-V_{min})}{V_{max}}$	–	TEF*	0.42	–
$\frac{(V_{max}-V_{preA})}{V_{max}}$	–	passive emptying fraction*	0.32	0.4 ± 0.1 [†]
$\frac{(V_{preA}-V_{min})}{V_{preA}}$	–	active emptying fraction*	0.14	0.3 ± 0.2 [†]
W_{AS}	$mmHg.ml$	active stroke work**	50.9	44.8 ± 5.5 [‡]
W_{PS}	$mmHg.ml$	passive stroke work**	4.4	–

Table 4.10: The FSI-calculated and physiological LAV indices of the 3D realistic model are reported. (*) reported by (Blume et al. 2011; Kebed, Addetia, and Lang 2019), (**) reported by (Barbier et al. 1999; Dernellis et al. 1998; Grant, Bunnell, and Greene 1964; Hoit 2017; Matsuda et al. 1983), ([§]) reported by (Jarvinen et al. 1994), ([†]) reported by (Reda et al. 2015), ([‡]) reported by (Stefanadis et al. 1998)

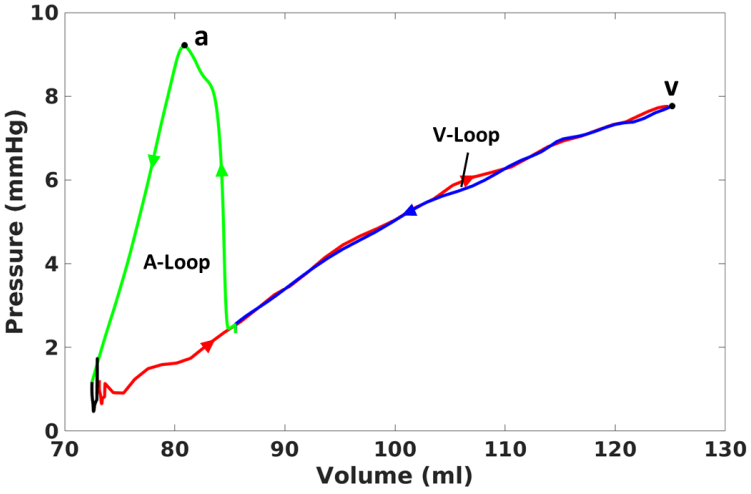

Figure 4.25: The FSI-calculated p-v loop of the 3D realistic model is displayed in the figure. The **a** and **v** points on the graph are the a-peak and the v-peak of the LAP reported in Tab. 4.9.

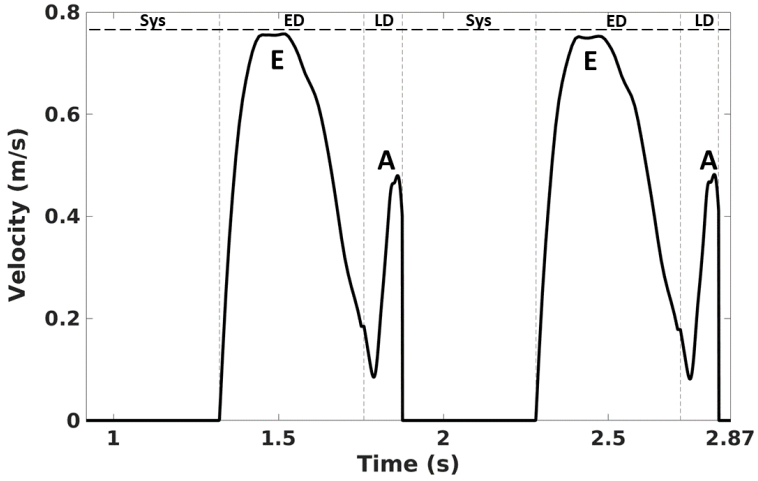

Figure 4.26: The FSI-calculated TV profile of the 3D realistic model for two cardiac cycles is displayed in the figure. The E-peak and the A-peak correspond to the peak velocities in the ED and the LD phases, respectively.

Index	unit	FSI simulation	Reported values
E-peak	m/s	0.75	$0.54 \pm 0.13^{*}$
A-peak	m/s	0.48	$0.44 \pm 0.21^{*}$
E/A	–	1.56	0.8-1.7**
VTI-ED	cm	24.1	-
VTI-LD	cm	3.3	-
DT	ms	338	$225 \pm 39^{*}$

Table 4.11: FSI calculated TV profile indices of the 3D realistic model are reported. VTI-ED = Early diastolic velocity time integration. VTI-LD = Late diastolic velocity time integration. DT = Deceleration time. (*) and (**) are reported by Nishimura et al. (1990) and Zipes et al. (2019), respectively.

(Nishimura et al. 1990; Zipes et al. 2019). Moreover, the FSI-calculated TV indices, A-peak, E-peak, E/A ratio and DT, reported in Tab. 4.11, are within the reported values in the literature.

The FSI-calculated K_e profile of the 3D realistic LA model is displayed in Fig. 4.27. The FSI-calculated K_e profile has three peaks, which resembles the physiological K_e profile displayed in Fig. 4.14. The K_e in the LA reservoir function in the Sys phase is attributed to 1) the MV annulus movement, 2) LAV increase and 3) the PVs inflow into

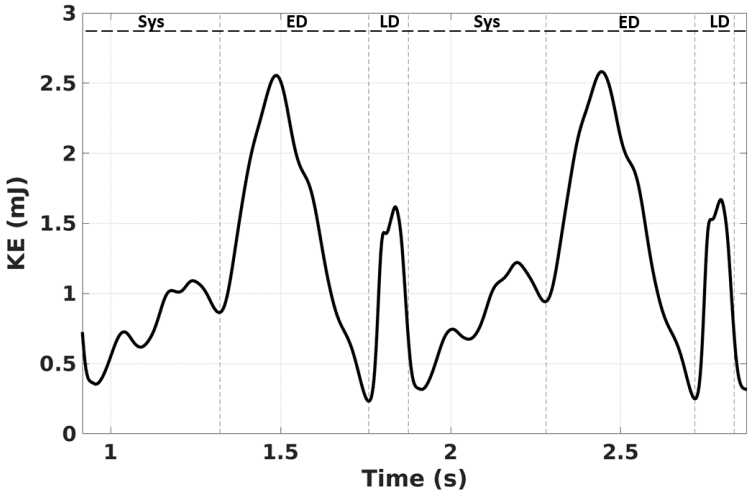

Figure 4.27: The FSI-calculated K_e profile of the 3D realistic model for two cardiac cycles is displayed in the figure. The K_e profile has three peaks corresponding to the three LA phasic functions, the reservoir, the conduit and the booster pump functions.

$K_e\ (mJ)$	FSI simulation	Reported values*
Sys-peak	1.3	1.5 ± 0.1
ED-peak	2.7	3.5 ± 0.25
LD-peak	2.2	0.8 ± 0.1

Table 4.12: The FSI-calculated K_e indices of the 3D realistic LA model. The (*) are physiological values reported by Arvidsson et al. (2013).

the LA. The K_e in the LA conduit and active pump phases, however, is attributed to the pressure gradient between the LA and the LV. The FSI calculated K_e peaks are reported in Tab. 4.12. The Sys peak of the K_e is equal to $1.3\ mJ$, the ED peak is $2.7\ mJ$, and the LD peak is equal to $2.2\ mJ$. All the FSI-calculated K_e peaks are in the physiological range reported by Arvidsson et al. (2013).

The evolution of the K_e in the LA chamber is displayed by flow streamlines in Figs. 4.28 - 4.30. At the beginning of the Sys phase, the flow is mainly straight and the maximum K_e is located at the LA inlets. As it goes to the end of the Sys phase, the flow in the LA chamber becomes rotational and the maximum K_e is transmitted to the LA chamber above the MV plane. During the ED (see Fig. 4.29) and the LD (see Fig. 4.30) phases, the flow in the LA is mainly straight and the maximum K_e is seen as a streak from the middle of the LA chamber to the MV outlet. The backward flow in the LD phase

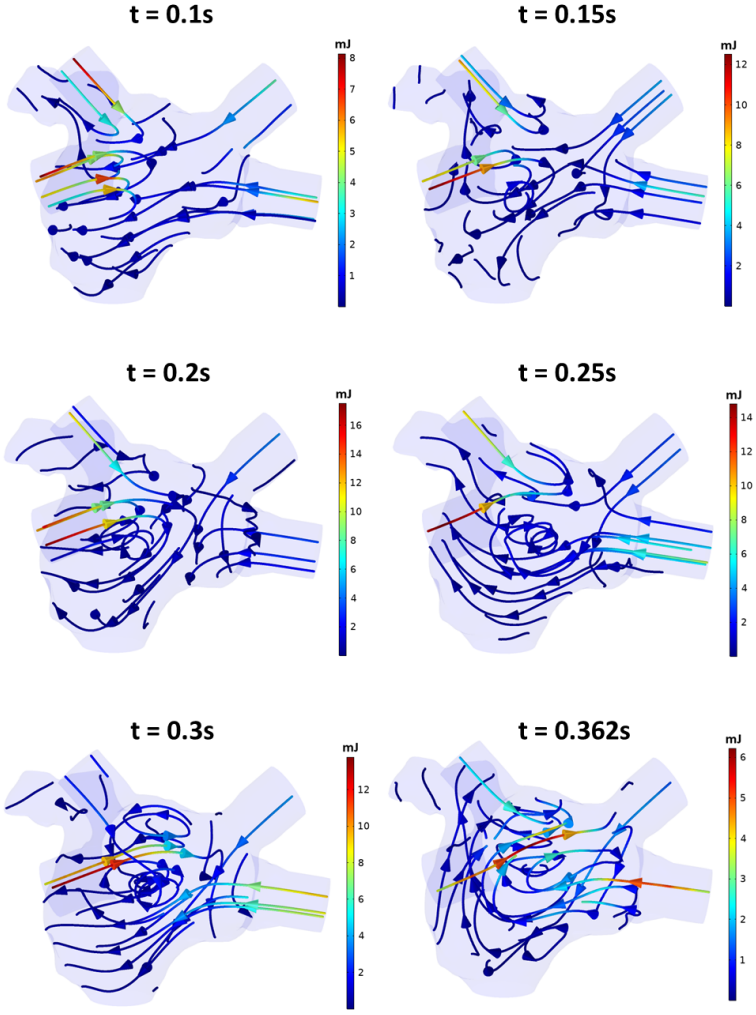

Figure 4.28: The evolution of the K_e in the flow field streamlines of the 3D realistic model is displayed for six time instants during LA reservoir function in the Sys phase.

is visible in Fig. 4.30.

Looking at the average vorticity magnitude displayed in Fig. 4.31, it contains three peaks in the Sys, ED and LD phases, like the K_e diagram in Fig. 4.27. The vorticity magnitude in the Sys phase surges at the end of the phase, confirming the generation of the rotational flow at the end of the reservoir phase, displayed in Fig. 4.28. The next two

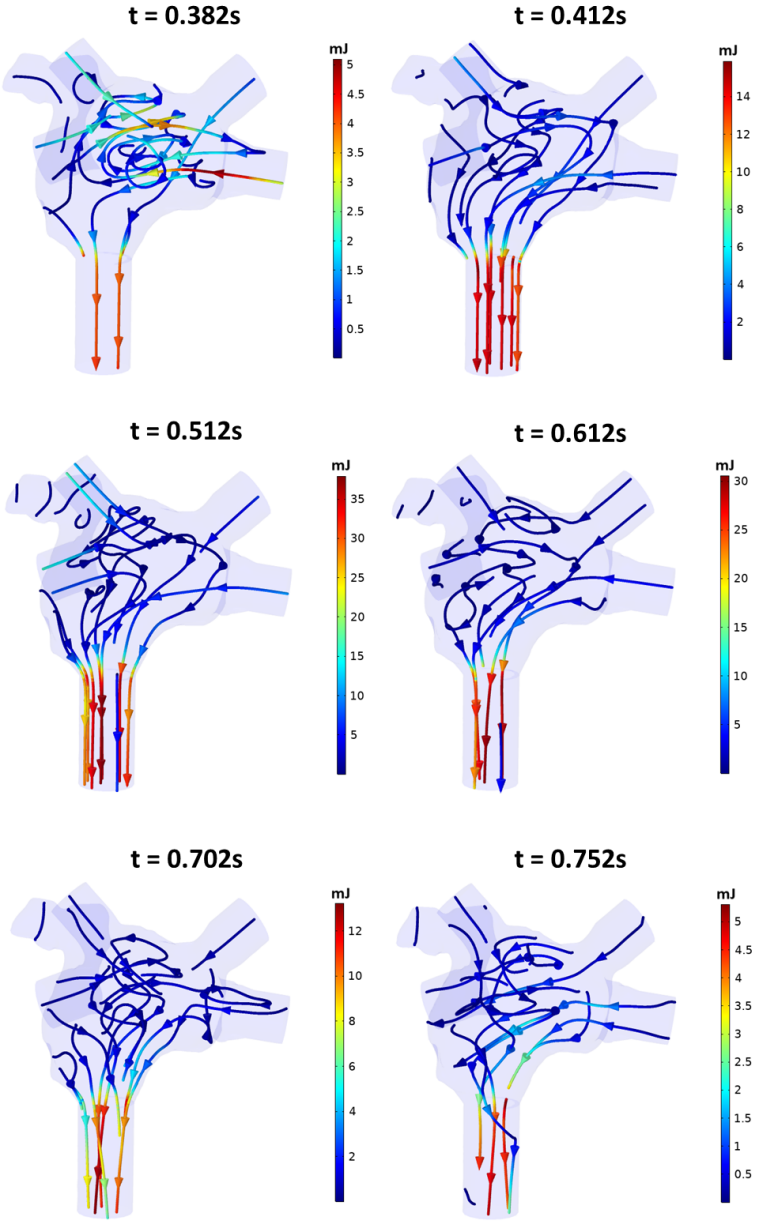

Figure 4.29: The evolution of the K_e in the flow field streamlines of the 3D realistic model is displayed for six time instants during the ED phase.

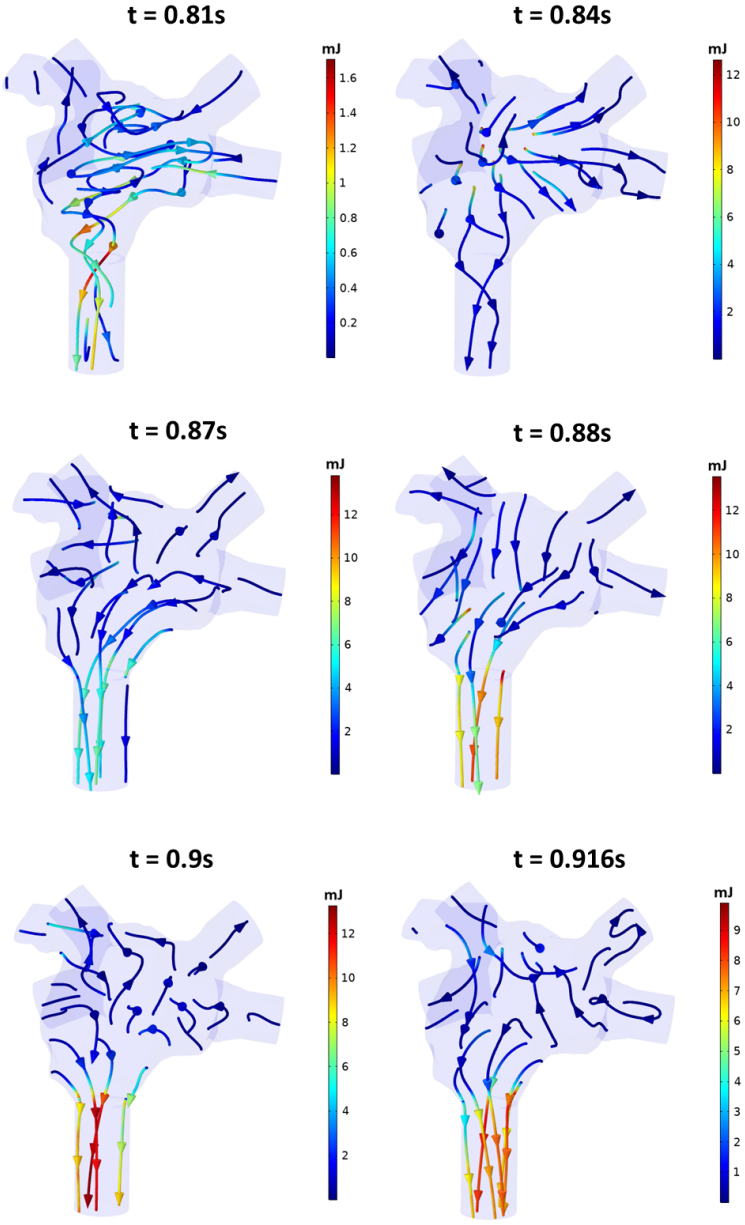

Figure 4.30: The evolution of the K_e in the flow field streamlines of the 3D realistic model is displayed for six time instants during the LD phase.

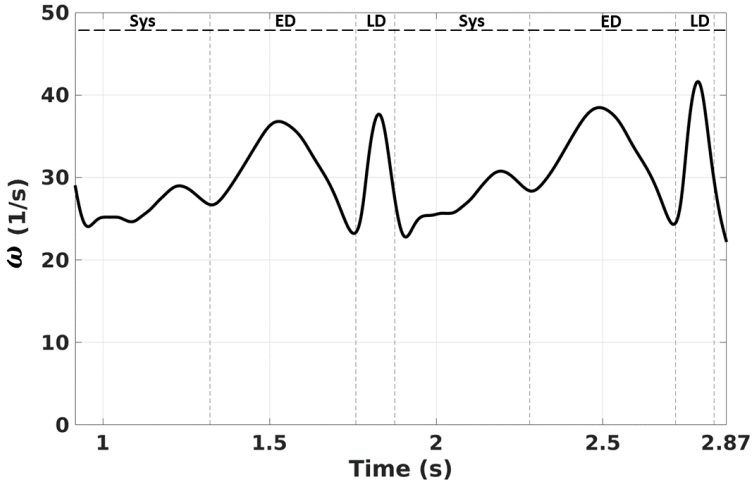

Figure 4.31: The FSI-calculated average vorticity magnitude of the 3D realistic model for two cardiac cycles is displayed in the figure.

peaks of the vorticity magnitude in the ED and the LD phases synchronize with the peaks of the K_e profile.

4.4.2 Mechanical analysis

The FSI-calculated maximum first principal stress and the maximum first principal stretch of 3D realistic LA model were calculated and displayed in Fig. 4.32 and Fig. 4.34. Both diagrams resemble the LAP profile, with the peak value at the end of the reservoir phase, when the LAP is maximum due to the PVs inflow and the closed MV. The maximum value of the maximum principal stress is equal to $87\ kPa$, and the peak of the maximum principal stretch is 2.6. However, unlike the LAP profile, they have only one peak at the end of the Sys phase without the second peak in the LD phase. The reason is, when the LAP increases in the LD phase, it is transmitted to the LV and PVs, and not to the LA wall. The maximum principal stress and stretch drop to their minimum values, i.e. $15\ kPa$ and 1.3, at the end of the LD phase and beginning of the Sys phase due to the LAP drop and LA chamber relaxation.

The anterior and posterior views of the 3D plots of the stress and stretch distribution on the 3D realistic LA model, at the instant of the maximum stress and stretch corresponding to the end of the Sys phase, are shown in Fig. 4.33 and Fig. 4.35. The maximum stress is concentrated on the anterior part on the vestibule, and on the superior part on the pulmonary part of the LA structure. As expected, the maximum principal stretch location is the same as the maximum principal stress regions on the LA chamber.

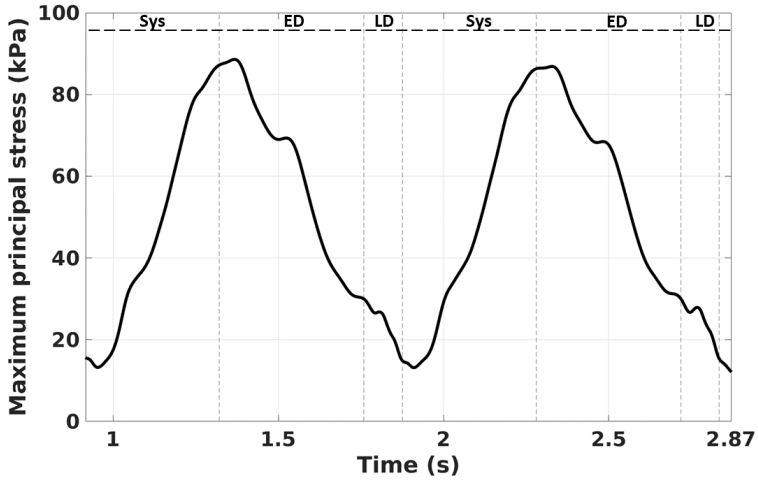

Figure 4.32: The FSI-calculated maximum principal stress profile of the 3D realistic model for two cardiac cycles is displayed in the figure. The LA maximum principal stress profile is similar to the LAP profile.

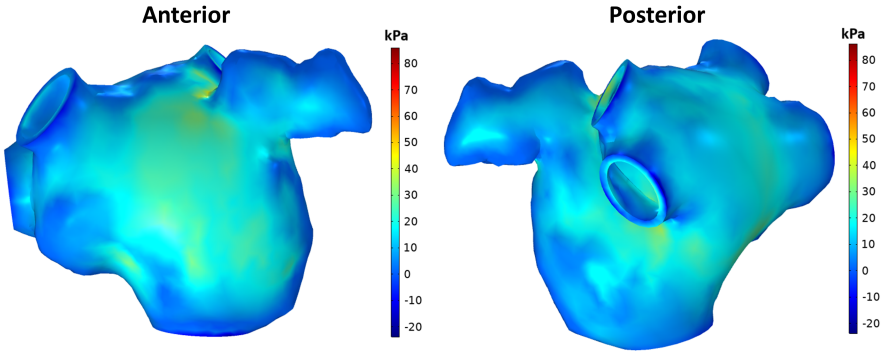

Figure 4.33: The anterior and posterior views of the 3D plot of first principal stress distribution on the 3D realistic model at the peak of the maximum stress profile (Fig. 4.32) is displayed in the figure. The maximum stress is located on the LA anterior wall on the vestibule, and on the superior part on the pulmonary part of the LA.

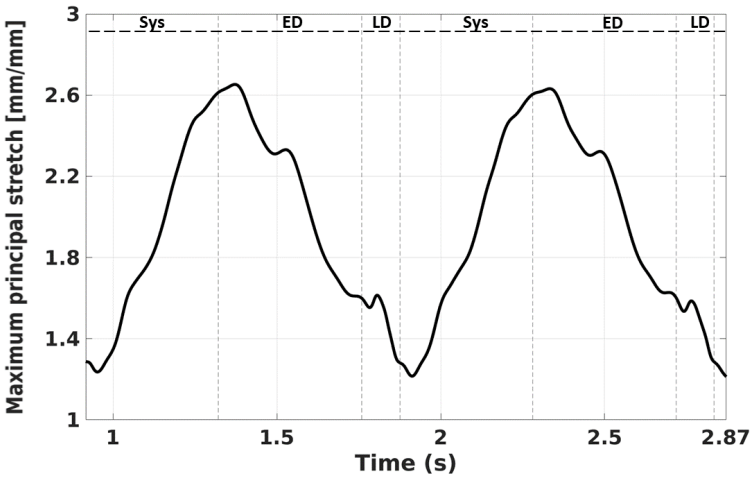

Figure 4.34: The FSI-calculated maximum principal stretch profile of the 3D realistic model for two cardiac cycles is shown in the figure. Like the maximum principal stress profiles in Fig. 4.32, the maximum principal stretch profiles are similar to the LAP.

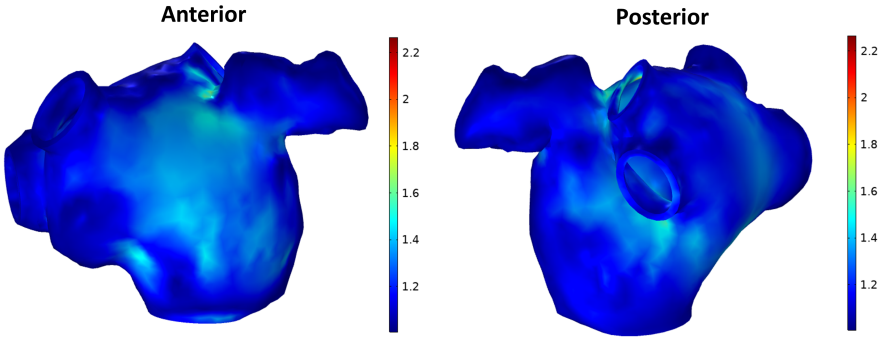

Figure 4.35: The anterior and posterior views of the 3D plot of first principal stress distribution on the 3D realistic model, at the peak of the maximum stretch profile (Fig. 4.34) is displayed in the figure.

CHAPTER 5

Discussion

5.1 2D left atrium-mitral valve model

In this study, the 2D simplified model was made to help in setting up the 3D simulations and conduct a sub-study on the impact of the MVS on the LA and the MV hemodynamics.

One of the main issues in FSI simulations using FEA is the expensive computational time. To build a realistic FSI model, different material models and different inlet and outlet BCs should have been tested. However, conducting this kind investigation on 3D models is a tedious, computationally expensive task. Therefore, the 2D model played a key role in setting up the 3D FSI simplified and realistic models because it reduced the complexity of the models from 3D to 2D and the computational time to a fraction of an hour.

Moreover, a novel sub-study with the 2D FSI model was carried out to investigate the impact of MVS on the LA hemodynamics. It is well known that the MV plays a crucial role in a healthy cardiac function and is more prone to heart valve diseases among the four heart valves (Li et al. 2019). Some MV diseases like valve stenosis or valve calcification cause MVS and result in a malfunctioning MV and disruption of the physiological performance of the LH. Though, the impacts of the MVS on the LA hemodynamics are not completely known. Therefore, this novel FSI study, which has not been done before, has a clinical usage. As the MV stiffness increases, the biomarkers of the LA hemodynamics drastically change (Tab. 4.4). Considering the LA area, the MVS severely impact the TEF as the MVS hinders the opening of the MV and lowers the EOL. The EOL reduction and the subsequent TEF decline, results in increasing the LAP_{mean} and amplifying the a-peak of the LAP profile. The MVS also affect the hemodynamics of the MV, which is reflected in the E/A ratio of the TV profile. As the EOL decreases, the E-peak of the TV profile declines and the A-peak amplifies, resulting in increasing the E/A ratio.

5.2 3D simplified left atrium-mitral valve model

To investigate if the 3D simplified model can replicate the physiological function of the LA and the MV, the FSI-calculated results were compared to the literature. Considering the FSI-calculated LAP profile, it captured the LAP events very well when compared to the physiological LAP profile (Fig. 4.9). Moreover, all the FSI-calculated LAP indices are within the reported physiological values (Tab. 4.5). However, there are two main

differences between the FSI-calculated and the physiological LAP profiles. First, the c-wave is absent in the FSI-calculated profile. In the physiological LAP profile, c-wave represents a sudden increase in the LAP right after the MV closure. While the LAP drops below the LVP after the LA contraction, the MV leaflets closes. Due to the LV contraction, the MV leaflets bulges into the LA chamber, resulting in the LAP increase, which is seen as the c-wave (Zipes et al. 2019). But in this study, the LV chamber and bulging of the MV leaflets were not simulated. Therefore, the c-wave is not captured on the FSI-calculated profile. The second difference is, the v-peak is lower than a-peak on the FSI-calculated profile. Physiologically, unlike the right atrium (RA), the v-peak is greater than the a-peak for the LA because the PVs do not move while the superior and inferior vena cava move in the RA, causing lower v-peak compared to the a-peak in the RA (Zipes et al. 2019).

Looking at the FSI-calculated LAV, all the elements of a physiological LAV profile is captured (Fig. 4.10). Furthermore, all the FSI-calculated LAV indices are in the physiological ranges presented in literature (Tab. 4.6). However, amongst the FSI-calculated indices, it seems that the W_{PS} has no clinical usage, and to the best of knowledge of the author, it is not mentioned in previous works (Dernellis et al. 1998; Grant, Bunnell, and Greene 1964; Hoit 2017; Papaioannou and Stefanadis 2005). Moreover, the C-D segment on the FSI-calculated profile (Fig. 4.10) is descending, while the C-D segment levels off in the physiological LAV profile. The C-D segment is attributed to the LA diastasis in the mid-diastolic phase, during which the pressure gradient in the LH is being balanced between the LA and the LV chambers. In this phase, the inflow from PVs is controlled by the LVP. Therefore, because the LVP goes up to the LAP level and even exceeds the LAP, it slows down the inflow from PVs and therefore the LAV levels off during diastasis. Since, the FSI model does not include the LV chamber, and the applied LVP at the outlet boundary condition (Fig. 3.9) is not synchronized with the PVs flowrate profile, the C-D segment of the FSI-calculated is descending.

Considering the p-v loop (Fig. 4.11), the W_{AS} reported in Tab. 4.6 is in the physiological range. However, there are two major differences between the FSI-calculated and the physiological p-v loops. First, as it is visible in the upper panel of Fig. 4.11, the beginning of the A-loop is concave, reflecting the pressure drop and volume increase at the beginning of systole during LA reservoir phase, which happens due to the LA fibers relaxation and the MV downward movement. Because the FSI model does not contain the LA fiber and the MV plane is fixed, the LAV and the LAP increase simultaneously. The second difference is, in the FSI p-v loop profile the V-loop is very narrow compared to the typical physiological one. This happens because of two main reasons, 1) the FSI model does not simulate the muscle fibers, and therefore the stored elastic energy would be lower, and 2) the considered MV diameter is not accurate, resulting in a narrow EOA. Both reasons affect the LA passive emptying, and as the result, the V-loop becomes narrow.

Inspecting the FSI-calculated TV profile displayed in Fig. 4.12, it shows all the elements of the physiological one reported in the literature. Moreover, the FSI-calculated TV indices (excluding the VTI-ED, VTI-LD, and L-peak) are within the reported physiological values (Keren, Meisner, et al. 1986; Keren, Sherez, et al. 1985; Nagueh 2018;

Zipes et al. 2019). The reason for the high VTI-ED is the small EOA which affects the LA passive emptying, and therefore, prolongs the VTI-ED. An interesting observation is, that the EOA profile resembles the TV profile, and it is constituted with E_{EOA} and A_{EOA} peaks, which are related to the E-peak and A-peak of the TV profile. Hence, it can be speculated that the mechanics and hemodynamics of the MV are interrelated, and any alteration in one is an indication of change in the other.

Looking at the FSI-calculated K_e profile in Fig. 4.14, it contains three peaks in the Sys, the ED and the LD phases which is identical to the physiological profiles presented in the literature (Arvidsson et al. 2016; Feng et al. 2019; Fyrenius et al. 2001). Apart from the K_e in the LD phase, which is generated by the LA contraction, the K_e in the Sys and the ED phases is the result of the LV longitudinal contraction and the LV suction, respectively (Arvidsson et al. 2016). An important observation can be made here on the resemblance of the K_e profile with the PVF waveform shown in Fig. 8.6. Like the PVF profile, the K_e has three main peaks. Moreover, the mechanism of generating K_e in the LA is very similar to the mechanism of the flow generation in the PVs (Sec. 8.3.1). Regardless of the s_1 peak in the early Sys phase, the s_2 peak is the consequence of the LV longitudinal contraction which increases the LAV, decreases the LAP, and therefore, drives the atrial filling. In the ED phase, the LVP is lower than the LAP and therefore, the LV sucks the flow from the LA into the LV which generates the D-peak of the PVF profile. This LV action in driving the PVs flow in the Sys and the ED phases is exactly the mechanism of the K_e generation in the LA. Moreover, the LA contraction is the mechanism of generating the A-peak of the PVs retrograde flow and the third peak of the K_e in the LD phase.

Considering the LA and the MV maximum principal stress and stretch profiles in Fig. 4.19 and Fig. 4.21, they are identical to the hemodynamics of the LA and the MV. The LA maximum principal stress resembles the LAP profile, and the MV maximum principal stress is identical to the TV profile. This similarity implies that the stress and strain state, and the hemodynamics of the LA and the MV are interrelated and have mutual impacts on each other. This effect can be seen in many LA diseases like LA fibrillation or hypertension, in which the LA remodeling occurs in the form of LA enlargement (Eshoo, Ross, and Thomas 2009; Feng et al. 2019; Vaziri et al. 1995). The value of the maximum principal stress and the profile of the LA maximum principal stretch is quite similar to Feng et al. (2019). However, in this study the profile of the maximum principal stretch has no peak in the LD phase, unlike the one showed in Feng et al. (2019). The reason can be explained by the lack of muscle fibers in modeling of the LA and the MV, and the application of a non-physiological tension force (Eq. 3.1).

5.3 3D realistic left atrium model

The results of the 3D realistic model are similar to the outcomes of the 3D simplified model. However, due to the variation of the LA geometry between two models and the

absence of the MV in the 3D realistic model, there are some differences between the results.

Considering the hemodynamics results, the LAP, the LAV, the p-v loop, the K_e, and the average vorticity magnitude profiles are identical to the ones obtained for the 3D simplified model. Moreover, their FSI-calculated hemodynamic indices presented in Tabs. 4.9-4.11 are within the reported values in the literature. Amongst the calculated hemodynamic results, nevertheless, there is a difference between the TV profiles of the two models. Comparing the TV profile of the 3D realistic model (Fig. 4.26) with the 3D simplified model (Fig. 4.12), it can be noticed that the L-wave is not captured on the 3D realistic model. As it is explained in Sec. 4.3, the L-wave is generated due to the mid-diastolic PVs flow (Fig. 8.6) and the undulation of the MV leaflets. After the rapid filling of the LV, which is reflected as the E-wave on the TV profile, the TV drops and the MV leaflets closes gradually. However, due to the increase in the PVF, reflected as the D-peak (Sec. 8.3.1), the MV opens and the TV increases again. This mid-diastolic TV enhancement is recorded as the L-wave. Since the same PVF profile is applied to both simplified and realistic models, it is therefore postulated that the L-wave is missed on the TV profile of the 3D realistic model (Fig. 4.26) because of the MV absence.

Inspecting the maximum principal stress and strain distribution on the 3D realistic model (Fig. 4.33 and Fig. 4.35), there is a considerable difference between the 3D realistic and the 3D simplified models. Because of the symmetric geometry of the 3D simplified model, the maximum principal stress is distributed homogeneously, while the maximum principal stress distribution on the 3D realistic geometry is located on the anterior and posterior part.

The stress distribution on the 3D realistic model is identical to the results presented by Feng et al. (2019), in which the maximum principal stress is located on the anterior part around vestibule, and on the posterior part around the pulmonary section of the LA. However, the magnitude of the maximum principal stress is not comparable with the value reported by Feng et al. (2019). The maximum value of the maximum principal stress in the 3D realistic model is $\approx 90\ kPa$, while it is $\approx 200\ kPa$ in Feng et al. (2019). Three reasons can be considered for this difference. First, the topology of the LA used in this work is different than the one used in Feng et al. (2019). Second, in this research, a physiological glspvf profile was applied at the LA, while a pressure profile was applied at the inlet BC in Feng et al. (2019). As the result, different inlet BC generated different LAP profile. The LAP reported by Feng et al. (2019) is higher than the calculated LAP in this work. Hence, the higher LAP can explain the higher maximum principal stress in Feng et al. (2019). Third, the application of the LA fibers is another reason for this difference, because different fibers orientation and dispersion results in various state of the maximum principal stress.

Part III

Experimental study

CHAPTER 6

Background

The LA has three phasic functions, 1) the reservoir, 2) the conduit (passive emptying), and 3) the booster pump (active emptying) (Blume et al. 2011; Kuhl et al. 2012; Rosca et al. 2011). All these three phases are in close interplay with the LV and the PVs. In the reservoir phase, the LAV and LAP are affected by the PVs systolic forward flow (SFF) and the MV annulus downward displacement due to the systolic contraction of the LV. The PVs SFF and the LV Sys function, on the other hand, are influenced by the LA relaxation and compliance (Barbier et al. 2000, 1999; Chao et al. 2000; Hollander et al. 2004; Keren, Sherez, et al. 1985; Kuecherer et al. 1990; Nishimura et al. 1990; Smiseth et al. 1999). During the conduit phase, with the contribution of the PVs DFF, the LA passively empties the accumulated blood to the LV, and increases its pressure and volume. Mutually, the LV preload and filling pressure during early diastole, has high impact on the LA emptying and the PVs DFF (Hellevik et al. 1999; Keren, Meisner, et al. 1986; Kuecherer et al. 1990; Nishimura et al. 1990). In the active emptying phase, the LA contracts to kick the rest of accumulated blood to the LV chamber. The LA contraction augments the LV end diastolic volume which in turn increases the stroke volume by 15-30% (Blume et al. 2011; Rosca et al. 2011) and strengthens the PVs SFF by reducing the LAP (Chao et al. 2000; Kuecherer et al. 1990; Nishimura et al. 1990). Again, the LV filling pressure and the PVs pressure have reciprocal influence on the LA afterload in this phase (Barbier et al. 1999; Basnight et al. 1991; Nagueh 2018, 2020; Rosca et al. 2011; Smiseth et al. 1999). Therefore, the interdependence of the LA with the LV and the PVs is crucial for a healthy functioning LA, and for a normal cardiac function.

As the LA plays a pivotal role in the LV and the PVs function, evaluating the LA size, shape, function, and hemodynamic indices has prognostic implications. For instance, LA enlargement is related to several CVDs, like MV dysfunction, LV hypertrophy, systemic and pulmonary hypertension, or LA fibrillation (Blume et al. 2011; Dodson et al. 2014; Gulati et al. 2013; Kuecherer et al. 1990; Maron et al. 2014; Matsuda et al. 1983; McGann et al. 2014; Rosca et al. 2011; Thomsen et al. 2017). However, assessing the LA physiology is very complicated because of its complex shape and function. Moreover, in clinical examinations, assessing the LA hemodynamics, like LAP, is often invasive and many uncontrolled phenomena affect the outcome of the measurements. These complexities make it difficult for clinicians to have accurate and thorough investigations of the LA hemodynamics.

The potential of in-vitro MCLs in studying physiology and pathology of the cardio-

vascular system is well recognized (Gulan et al. 2017) and plays an important role in reducing the amount of animal experiments or invasive operations on patients (Rasmussen et al. 2019; Sharghbin et al. 2018). Moreover, MCLs are widely employed in testing and validating cardiovascular devices like ventricular assist devices, heart valves, balloon catheters, and vascular stents (Leopaldi, Vismara, Tuijl, et al. 2015; Vismara, Fiore, et al. 2010; Vismara, Pavesi, et al. 2011). They also enable the researchers and clinicians to mimic various pathological scenarios which are impossible to carry out in-vivo (Dimasi et al. 2019; Meskin et al. 2019).

The cardiac chambers have an intricate fluido-electro-mechanical function, which in addition to its complex geometry, makes the cardiac in-vitro studies cumbersome for researchers. Therefore, in many in-vitro studies with MCLs, simplifications are applied, either in geometry or in function of the LA chamber. For instance, in some works, a porous media (Balducci et al. 2004; Dimasi et al. 2019; Meskin et al. 2019; Vismara, Fiore, et al. 2010; Vismara, Pavesi, et al. 2011), a rigid reservoir (Akutsu and Masuda 2003; Cenedese et al. 2005; Kini et al. 2001; Marassi et al. 2004; Morsi and Sakhaeimanesh 2000; Pierrakos, Vlachos, and Telionis 2004; Rasmussen et al. 2019; Sharghbin et al. 2018; T. Steen and S. Steen 1994) or an elastic spherical-like shape with a voluminous inlet as PVs (Kadem et al. 2005; Reul, Talukder, Mu, et al. 1981) were embedded as the LA chamber. In (Leopaldi, Vismara, Lemma, et al. 2012) and (Leopaldi, Vismara, Tuijl, et al. 2015), however, they integrated a biological native LA chamber into an in-vitro MCL to preserve the geometry, but it only mimics the LA passive phase functions. There are only two works (Mouret et al. 2004; Tanne et al. 2009) with holistic MCLs with anatomically-shaped LA chambers, and proper active-passive phasic functions. Nevertheless, it seems the LA chamber compliance and thickness are not physiologically correct. The reported chamber thickness is 0.1 mm, while the mean LA chamber wall thickness is 1-4 mm (Ho, Cabrera, and S. 2012; Whitaker et al. 2016). Moreover, (Mouret et al. 2004) and (Tanne et al. 2009) had challenges regarding the LA compliance as the replicated PVF and LAP profiles are not comparable to the physiological ones. The impact of the LA compliance on the PVF and the LAP are well defined (Barbier et al. 1999; Hellevik et al. 1999; Kuecherer et al. 1990). Therefore, utilizing a material with proper compliance to cast the LA chamber is of high importance in recreating the physiological conditions.

The main objective of this study was to develop a versatile holistic in-vitro MCL of the LH with a hyperelastic LA chamber to replicate the physiological function of the LA chamber. The MCL will be a valuable asset in studying LH disease given that it can meet the following criteria:

1) Include an LA geometry with four PVs and a MV outflow to establish a realistic reservoir and conduit phasic function.

2) An LA chamber that mimics a physiological compliance to provide a physiological passive and active LA function.

3) A contraction phase mimicking the LA active pumping phase.

4) Interplay and coordination between the LA and the LV events.

5) Ability to adjust with the LV volumetric profile to replicate various clinical scenarios.

6) A static PVs preload.

To validate the functionality of the MCL, hemodynamic indices such as LAP, LVP, mitral valve flowrate (MVF), aortic valve flowrate (AVF) and PVF were measured, and the results were compared to the physiological indices reported in literature. Furthermore, to investigate the effect of the LA compliance on the LH hemodynamics, the same measurements were carried out with different LA chambers having various compliance.

CHAPTER 7

Materials and methods

To achieve the aims of this study, several sub-studies were performed. First, the compliance of the LA should be physiologically matched to achieve the passive function of the LA (reservoir and conduit phase). Therefore, the choice of the LA material with proper mechanical properties is imperative. Then, the inlet flow to the LA from the PVs must be understood to enable replicating the correct LA preload, specifically during the LA reservoir phase. Moreover, the LA must have a physiological pressure signature and range during the reservoir phase. Furthermore, to be synchronous with the LA and the PVs functions, the action of the LV must carefully be controlled to provide proper adjustment of the LV systolic and diastolic function. Finally, the peripheral unit must assure proper mimicking of the systemic vascular resistance and compliance.

In this chapter, first the method of dissecting a porcine heart to isolate LA chamber is explained. The porcine LA was used to measure the physiological compliance of the LA chamber. Then, the designing and casting procedure of a hyperelastic LA chamber is elaborated. Casting the hyperelastic LA chamber includes casting a soluble core and 3D-printing an elastic mold. Following this, expansion tests were conducted to measure and compare the compliance of the porcine and the molded LA chambers, is described. Thereafter, the procedure of calculating mechanical properties of the molded hyperelstic LA chamber through uniaxial tensile test is described. Afterwards, building of the LH MCL and the software for data acquisition is illustrated. At the end, the in-vivo measurement of the PVF profiles through PC-MRI is explained.

7.1 Left Atrial Compliance

To establish a reference on the LA compliance, a sub-study was carried out on nine fresh porcine hearts to measure the LA compliance through pressure-volume measurements. Therefore, the LA needed to be isolated and mounted in an experiment set up, see Fig. 7.1. To isolate the LA, first the left side of the heart was separated from the right side. To identify the attachment of the right ventricle (RV) wall on the interventricular septum, the apex was removed by a cross-sectional slice through both ventricles approximately 1 cm from the apex. The RV was opened by an incision in the anterior wall from the cross-sectional opening along the anterior interventricular sulcus to the coronary sulcus. The aortic arch was removed from the ascending aorta by a cross-sectional cut approximately 3 cm from the aortic annulus.

The LA was separated from the RA with two incisions, one in the anterior wall of the RA from the coronary sulcus through the pulmonary trunk close to the left leaflet, and another in the posterior wall from the transverse pericardial sinus to the coronary sinus. Finally, the RA and the RV was completely separated from the left side by an incision from the coronary sinus, following the posterior interventricular sulcus.

An incision in the interventricular septum was made from the cross-sectional opening in the LV to approximately 1.5 cm above the aortic ostium to get access to the MV. Both papillary muscles were isolated from the myocardium to fixate the anterior leaflet of the MV above the aortic ostium to prevent leakage, while the posterior leaflet was sutured to the wall to keep the MV open. The PVs were sutured to completely seal the LA inlets. Then, a transparent tube was installed in the LV, ensuring the tip of the tube to be lined up with the edges of the MV annulus, and it was fixated with zip ties. The final result of the LA isolation is displayed in Fig. 7.1. When no leakage was detected from the LA, the LA and the tube was placed in the experiment setup. Hereafter, the actual expansion test for measuring the compliance was conducted. All the steps of porcine heart dissection and LA isolation are recorded and more than 5 hours of instruction videos are available. The author was playing the role of an assistant in dissecting the hearts.

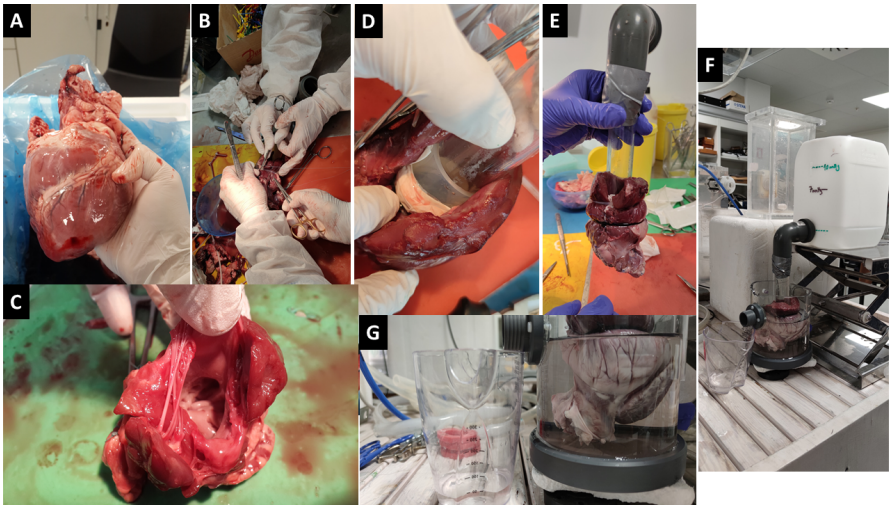

Figure 7.1: The LA isolation and installation on the experiment setup is shown in the figure. A) One of the 9 fresh porcine hearts received from Danish Crown. B) LA isolation and sealing procedure. C) Isolated LA chamber. D) Transparent tube mounted in the LA chamber in the way that the tip of the tube is placed right on the MV annulus. E) Mounted LA chamber on the transparent tube. F) Experiment setup. G) Expanded LA chamber at the end of the expansion measurement. The porcine heart is dissected in the CAVE lab at Aarhus University, and the pictures are taken by the author.

7.2 3D CAD modeling of the simplified left atrium

The geometry of the LA was simplified to reduce the complexity and facilitate the casting of the LA chamber. The LA chamber was considered as a smooth symmetrical spherical chamber with four cylindrical inlets as PVs, a circular outlet as the MV ostium, and without the LAA and the LA trabeculae. It is shown by Zhang and Gay (2008) that the LAA is not functional in sinus rythm and therefore it is expected that excluding the LAA from the model will have negligible impact on the results. To design the spherical LA chamber, the LAV at the end of the LA systole (Jarvinen et al. 1994) was used to calculate the radius of the sphere. The PVs radius is $6.6\ mm$, which was calculated from the averaged PVs ostia area reported in (Chnafa, Mendez, and Nicoud 2014), and the MV radius is $25\ mm$, equal to the radius of the mechanical heart valve used in the MCL. The LA chamber wall thickness is $2\ mm$ (Whitaker et al. 2016). The model was designed in Autodesk® Inventor LT™ (Autodesk, San Rafael, CA, US) and is shown in Fig. 7.2.

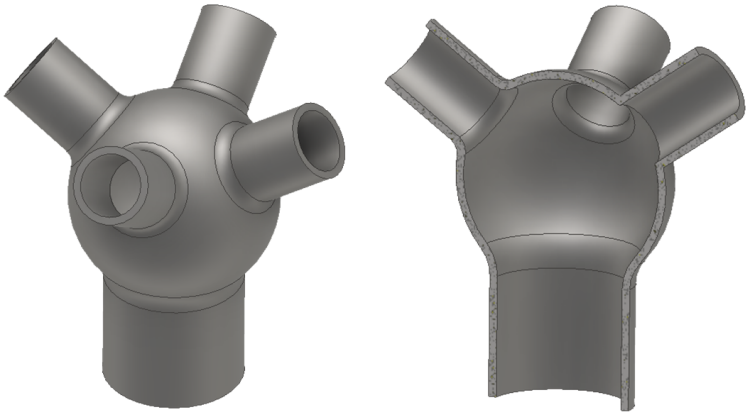

Figure 7.2: The CAD geometry of the simplified LA chamber is displayed in the figure. A) Shows the complete view. B) Displays the section view of the chamber.

7.3 Casting silicone mold

Before starting the silicone-rubber mold casting, the master (male) part was designed and 3D-printed in rigid clear resin. The master part will then be encapsulated with the molding material to form the negative (female) part. To start the casting process, a frame made from a cardboard box, with dimensions 3 to $5\ cm$ bigger than the master part in all directions to avoid any contact between the frame and the master, was prepared. The

frame is made from cardboard, because it is cheaper, the dimensions can be modified conveniently, and the frame can be separated or be destroyed easily to extract the mold.

Half of the box was filled with play dough and the master part was positioned in the box in such a way that half of the master was in the play dough and the other half was out of the play dough (Fig. 7.3B). To prevent the integration of play dough with the cardboard, the inside of the box was covered with transparent tape before placing the play dough (Fig. 7.3A). To create a sprue for the mold, more play dough was added to the top of the core to keep this place free from silicone material. To prevent the two halves of the mold from sticking together, conic indentations were created on the surface of the play dough with a conic-tip object. For the same purpose, the surface of the play dough was coated with a thin layer of Vaseline. The mixing ratio for making the silicone material is $1\ kg$ of silicone with $0.8\ dl$ of hardener. To have an idea of how much the mixture should be stirred, food coloring was added to the mixture. The stirring continued until the mixture was colored homogenously (Fig. 7.3C). Then the silicone mixture was poured into the box to $3\ cm$ above the level of the master part. The mold was shaken slightly to remove the air bubbles, and then it was left for 7 hours to cure. To make the other half, the top of the box was closed off and it was turned upside down. The bottom was opened, the play dough was removed, and again the silicone mixture was poured into the other half of the box (Fig. 7.3D). When the silicone mold was completely cured, it was removed from the box, and the two halves were separated with a scalpel. The master part and the rest of the play dough was removed, and the mold was ready to use. To fasten the two halves of the mold, elastic bands were used (Fig. 7.3E).

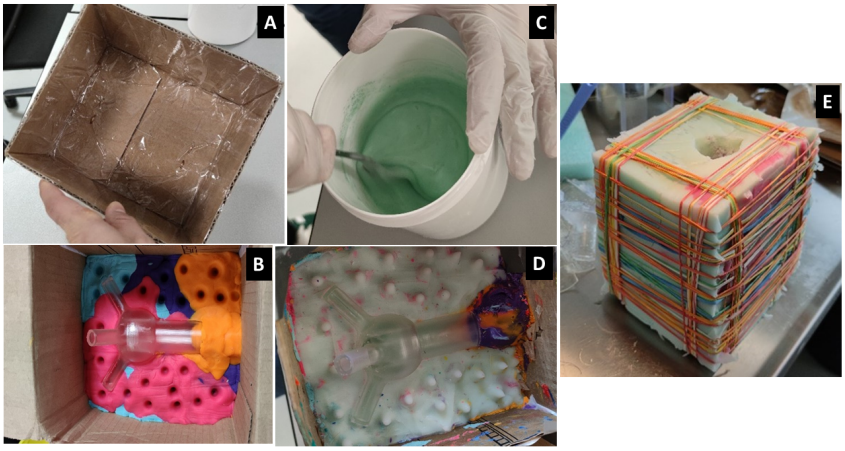

Figure 7.3: The process of casting the silicone mold is displayed in the figure. A) The frame made from cardboard, B) The master part placed in the play dough to cast half of the silicone mold, C) The silicone material mixed with food color, D) Half of the silicone mold and E) The completed silicone mold.

7.4 Casting water-soluble wax

The Ferris 2283-A Green soluble wax was chosen for casting the core of the LA chamber. This kind of wax is suitable for melt and pour, and it can pick up all the details of the object (Freeman Manufacturing & Supply Company - OH/US). After melting the solid wax, it was stirred to obtain a homogenized temperature all over the liquid wax. The melting temperature was kept bellow 90°C during the procedure. The liquefied wax was then poured into the mold and left for three hours in the fridge to solidify. After three hours, the core was extracted out of the mold and put in the fridge again for two hours to completely solidify. The process of casting the soluble wax is shown in the Fig. 7.4.

Figure 7.4: The procedure of casting the soluble core is displayed in the figure. A) Melting the solid wax in the melting pot, 2) Monitoring the temperature of the liquefied wax, 3) Pouring liquid wax into the silicone mold, and D) The final solidified water-soluble core.

7.5 Casting hyperelastic left atrium chamber

Gravity casting using an elastic mold was employed to cast the LA chamber. Because the LA chamber is a hollow object, casting was done in two steps. In the first step, a water-soluble core was cast as described in Sec. 7.4. In the second step, the LA chamber was cast using an elastic mold. The elastic mold was designed in Autodesk inventor

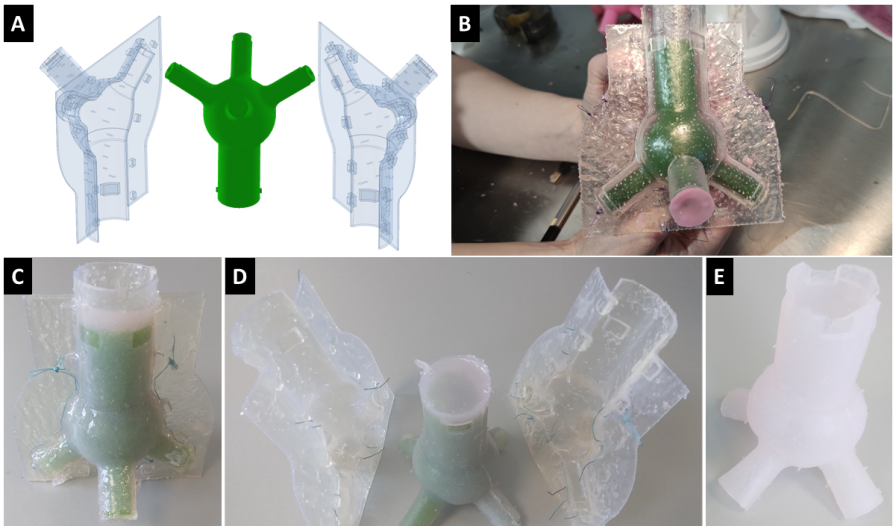

Figure 7.5: A) CAD model of the simplified LA chamber. The LA was assumed as a symmetrical spherical chamber with four cylindrical inlets and a circular outlet as MV ostium. B) The elastic mold containing the soluble core, before filling it with the Silicone-Elite mixture. C,D) The elastic mold and molded LA chamber. The elastic mold was sutured to be completely sealed. E) The molded hyperelastic LA chamber after dissolving the core in water.

(Autodesk® Inventor LT™) and 3D printed with Formlabs elastic 50A transparent resin (Formlabs Inc. - MA,USA). To attain a sufficient chamber compliance, two materials, "Elite Double 8" and "Silicon Rubber ZA-SFX-0020 with platinum catalyst" (Zhermack SpA – RO, Italy) were mixed together in different proportions. The portion of the mixture was changed in the range of 50% to 5% for the Elite Double 8 and 50% to 95% for the Silicone-Rubber. 11 chambers were cast in total. The elastic mold and a molded LA chamber are shown in Fig. 7.5.

7.6 Expansion test on porcine and molded left atrium chambers

After securing the sealing of the porcine and molded LA chambers, their volume prior to pressurization, V_0, was measured. To measure V_0, water was poured with a syringe into the chambers up to the MV plane, and the volume of the water was recorded as V_0. Then they were installed in the experiment setup shown in Fig 7.6. The experiment setup consists of a bucket, a Polica 90 degree elbow joint tube, a transparent straight polycarbonate plastic tube, a transparent container, and a measuring cup. The molded and

porcine LA chambers were mounted on the transparent straight tube such that the tip of the tube was placed at the MV plane.

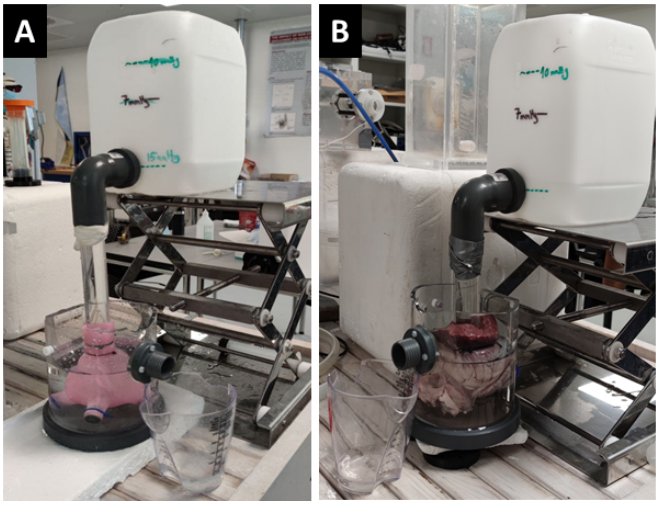

Figure 7.6: The expansion experiment setup. The experiment setup consists of a bucket, a Polica 90 degree elbow joint tube, a transparent straight polycarbonate plastic tube, a transparent container and a measuring cup. The left panel shows testing the porcine heart and the right panel displays the test on molded LA chambers.

Then the chambers were pressurized with water at 2000 Pa ($\approx$15 $mmHg$) and the volume of the accumulated water in the measuring cup was recorded as the volume difference. The measurements were repeated three times for each chamber, and the averaged volume difference ΔV_{ave} was calculated. The experiment set up mimic the LA reservoir phase function. The reason of choosing 2000 Pa to pressurize the chambers was because it is close to the porcine LAP during the reservoir phase (Barbier et al. 1999), and also it facilitates having more tangible expansion. Then the percentage expansion E_p was simply calculated as:

$$E_p = \frac{\Delta V_{ave}}{V_0} \times 100 \tag{7.1}$$

The expansion tests on the porcine LA chambers were done in several days and the hearts were kept in the freezer to preserve the freshness. It was also assumed that the aging has minor impact on the expansion result, as the mechanical properties do not degrade too much (Jernigan et al. 2007).

7.7 Tensile test

To obtain the mechanical properties of the Silicone-Elite mixture, destructive uniaxial tensile tests were carried out on 13 samples according to the ASTM D412 tensile test standard. The Instron low force electromechanical universal testing machine (Instron® - MA, US) was employed for conducting the tests. To cast the dumbbell shaped specimens, a mold was designed based on the ASTM D412 Die C, in Autodesk inventor, and 3D printed with Formlabs clear V4 resin. The specimens dimensions, the mold for casting the specimens and the specimen installed on the tensile test machine are shown in Fig. 7.7. The rate of the testing machine was set to $500\ mm/min$. The thickness of the specimens was measured on three spots based on the ASTM D412 protocols, before installing them on the machine. Their thicknesses vary from $2.2 - 3\ mm$ with the mean value of $2.6\ mm$. The force-displacement data were recorded with a sampling frequency of $10\ Hz$.

7.8 Numerical Simulation

To analyze the data acquired in the tensile test, the data sets were undergone 1) a curve fitting procedure, and 2) the FEA using the FSI method. For all the numerical simulations, the Silicone-Elite mixture was assumed to be an incompressible isotropic material, which is a general assumption for rubber like materials (Erman and Mark 1997; Martins, Jorge, and Ferreira 2006).

First, because the Silicone-Elite mixture exhibited large elastic stretch and nonlinear behavior (Fig. 8.1), hyperelastic material models are ideally suited for characterising its mechanical properties. Therefore, five parametric analytical functions representing five different hyperelastic material models, neo-Hookean, Yeoh, Ogden, Humphrey and Martins, were chosen to fit to the experimental data. The strain energy density function, $\psi(\bar{\bar{C}})$, and the stretch-dependent Cauchy (true) stress expression, σ, of the five material models are reported in Tab. 7.1. Because the material was considered as an incompressible isotropic hyperelastic material, the analytical expressions of the material models are simplified. Therefore, the analytical models depend only on the first principal stretch λ_1, and there is no dependency on the second and third principal stretches, and on the third invariants of the right Cauchy-Green strain tensor. The Cauchy stress expression of the material models was used in the curve fitting procedure to calculate the material parameters c_i. The curve fitting was done by implementing the Levenberg-Marquardt algorithm (Levenberg 1944; Marquardt 1963) in MATLAB (The MathWorks Inc., MA, US), using the global optimization toolbox with the Multistart option. The calculated material parameters are reported in Tab. 8.3.

Second, five FSI simulations with the 3D simplified LA model (Fig. 3.4), using the five fitted hyperelastic models, were carried out. The model simulates the LA reservoir phase function in which the MV is closed. Therefore, the systolic portion of the PVF profile of case 1 (Fig. 8.6) was considered as the inlet BC. The material of the fluid

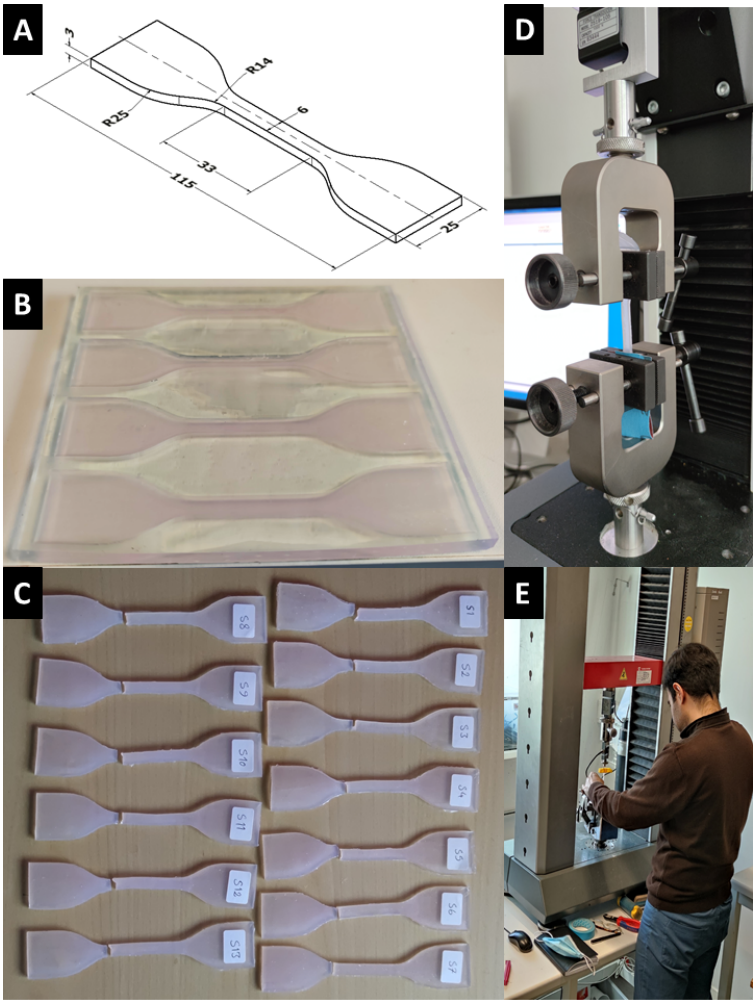

Figure 7.7: A) The specimen dimensions based on the ASTM D412 protocols "Die C", B) The mold and the molded specimens with the Silicone-Elite mixture material, C) 13 destructed specimens, D) A specimen installed on the Instron low force electromechanical universal testing machine, and E) Installation of the specimen on the tensile test machine by the author.

Material model	Analytical expression
neo-Hookean	$\psi(\bar{\bar{C}})_{NH} = c_1\,(I_{1c} - 3)$ $\sigma_{NH} = 2c_1({\lambda_1}^2 - \frac{1}{\lambda_1})$
Yeoh	$\psi(\bar{\bar{C}})_{Ye} = \sum_{i=1}^{3} c_i(I_{1c} - 3)^i$ $\sigma_{Ye} = 2({\lambda_1}^2 - \frac{1}{\lambda_1})(c_1 + 2c_2({\lambda_1}^2 + \frac{2}{\lambda_1} - 3) + 3c_3({\lambda_1}^2 + \frac{2}{\lambda_1} - 3)^2)$
Mooney-Rivlin	$\psi(\bar{\bar{C}})_{MR} = \sum_{i=1}^{2} c_i(I_i - 3)$ $\sigma_{MR} = 2({\lambda_1}^2 - \frac{1}{\lambda_1})(c_1 + c_2\frac{1}{\lambda_1})$
Ogden (N=3)	$\psi(\bar{\bar{C}})_{Og} = \sum_{i=1}^{N} \frac{c_{(2i-1)}}{c_{2i}} \left({\lambda_1}^{c_{2i}} + 2(\frac{1}{\sqrt{\lambda_1}})^{c_{2i}} - 3\right)$ $\sigma_{Og} = \sum_{i=1}^{N} c_{2i-1}({\lambda_1}^{c_{2i}} - {\lambda_1}^{-c_{2i}/2})$
Humphrey	$\psi(\bar{\bar{C}})_{Hu} = c_1(e^{c_2(I_{1c}-3)} - 1)$ $\sigma_{Hu} = 2({\lambda_1}^2 - \frac{1}{\lambda_1})c_1c_2e^{c_2({\lambda_1}^2 + \frac{2}{\lambda_1} - 3)}$
Martins	$\psi(\bar{\bar{C}})_{Ma} = c_1(e^{c_2(I_{1c}-3)} - 1) + c_3(e^{c_4(\lambda_1-3)^2} - 1)$ $\sigma_{Ma} = 2({\lambda_1}^2 - \frac{1}{\lambda_1})c_1c_2e^{c_2({\lambda_1}^2 + \frac{2}{\lambda_1} - 3)} + 2\lambda_1(\lambda_1 - 1)c_3c_4e^{c_4(\lambda_1-1)^2}$

Table 7.1: The energy density functions and Cauchy stress expressions of the five material models are presented. c_i is the material parameters, calculated through the curve fitting procedure, λ_1 is the first principal stretch, and I_{1c} is the first invariant of Cauchy–Green strain tensor. For more details about the model equations, readers are referred to (Martins, Jorge, and Ferreira 2006).

domain is blood which was assumed as a Newtonian incompressible fluid. The blood material properties are reported in Tab. 3.1. The FSI simulations were performed in COMSOL Multiphysics® v.5.6. (COMSOL AB, Stockholm, Sweden).

7.9 Left heart mock circulatory loop set-up

The mock loop structure, which aims to mimic the LA phasic function, is an upgraded version of the pulsatile left heart in-vitro model used in Rasmussen et al. (2019) and Sharghbin et al. (2018). For pump control and data acquisition, a software was designed in LabVIEW (National Instruments, Austin, TX) which enables the MCL operator to generate a desirable pulsatile pump piston waveform, and collect the measured data, simultaneously.

7.9.1 Flow loop

The flow loop (Figs. 7.8 and 7.9) consists of a pulsatile electromechanical pump (Super-Pump AR Series, ViVitro Labs, Victoria, Canada) replicating the LV volumetric change in systole and diastole. The pump is connected to a rigid LV chamber with an outflow to an AV housing. The valve housing connects the LV chamber through a medical silicone tubing to a rigid compliance chamber, simulating the arterial compliance. The AV is a mechanical bi-leaflet valve. The outflow from the compliance chamber, which empties into a rigid venous reservoir, was also clamped to control the systemic resistance. The rigid venous reservoir was connected to the molded LA chamber through four medical silicone tubing. A big rigid reservoir was chosen because the pulmonary capillaries can be considered as a structure with large reservoir capacity which is isolated from the pressure variation in the LA chamber (Keren et al. 1985). The molded LA chamber is embedded into a container (LA container), which can be pressurized to replicate the LA pulsatility. An MV housing connects the LA container to the LV chamber, and it holds a mechanical heart valve (St. Jude Medical bileaflet 25mm, St. Paul, USA). The PVF and the MVF are measured using tubing flow sensors connected to a Dual-Channel tubing module (PXL11,PXL25, TS410, Transonic Systems Inc., Ithaca, NY, USA). LAP and LVP are recorded using fluid-filled pressure probes connected to a patient monitoring screen, and Micro-tip pressure catheters (SPC-350MR; Millar Inc., Houston, TX, USA) connected to a two-channel amplifier pressure control unit (PCU-2000, Millar Instruments). The LA contraction phase is replicated by pressurizing and venting the LA container using normally-closed and normally-open solenoid valves type EV210A (Danfoss A/S, Denmark), respectively. Therefore, the normally-closed valve is connected to a compressor, and the normally-open valve opens to the atmospheric pressure. Compressors are utilized for pressurizing the LA container and compliance chamber. The working fluid is distilled water.

7.9.2 Software for data generation and acquisition

A harmonious interplay between all the cardiac events is crucial for a well-functioning cardiac system because the cardiac components are all interconnected and have mutual impacts on each other. Hence, the hemodynamic and mechanical function of the PVs, the LA, the MV and the LV should be synchronous for maintaining the normal LH operating condition.

To control and synchronize the LV and the LA pulsatile behaviour of the MCL, a dedicated custom made software was designed. The software specifically generates a LV volumetric waveform to control the pulsatile pump piston position, and triggering signal to control the LA pulsatility through controlling the normally-closed and normally-open valves. Moreover, while controlling the pump and the valves, the software is also able to calibrate, display and record the flowrate and pressure data through a NI USB-6259 module (National Instruments, Austin,TX).

To generate the LV volumetric waveform, the displacement course of the pulsatile

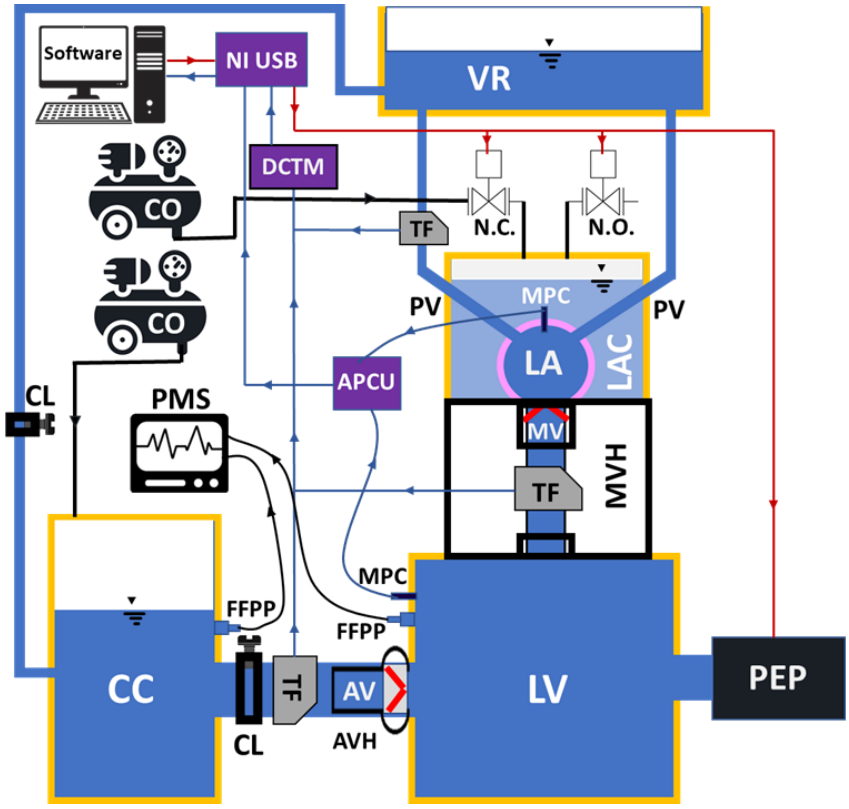

Figure 7.8: The schematic representation of the MCL. VR = Venous reservoir, N.C. = Normally closed valve, N.O. = Normally open valve, TF = Tubing flowsensor, PV = Pulmonary vein, MPC = Micro-tip pressure catheter, LA = Left atrial chamber, LAC = Left atrial container, MV = Mitral valve, MVH = Mitral valve house, LV = Left ventricular chamber, PEP = Pulsatile electromechanical pump, FFPP = Fluid filled pressure probes, AV = Aortic valve, AVH = Aortic valve house, CL = Clamp, CC = Compliance chamber, PMS = Patient monitoring screen, CO = Compressor, APCU = Amplifier pressure control unit, DCTM = Dual channel tubing module, NI USB = NI USB-6259 module. The red arrow lines indicate the generated triggering signal from the software, controlling the PEP piston head, the N.C. and the N.O. valves. The blue arrow lines are the measured pressure and flowrate data, which are sent to the designed software. The pressure measured by the FFPP was only visualized on the PMS to watch the mock loop condition. The working fluid inside the LAC is static, and only used to pressurize the LA. The clamps are utilized to adjust the systemic and pulmonary vascular resistance.

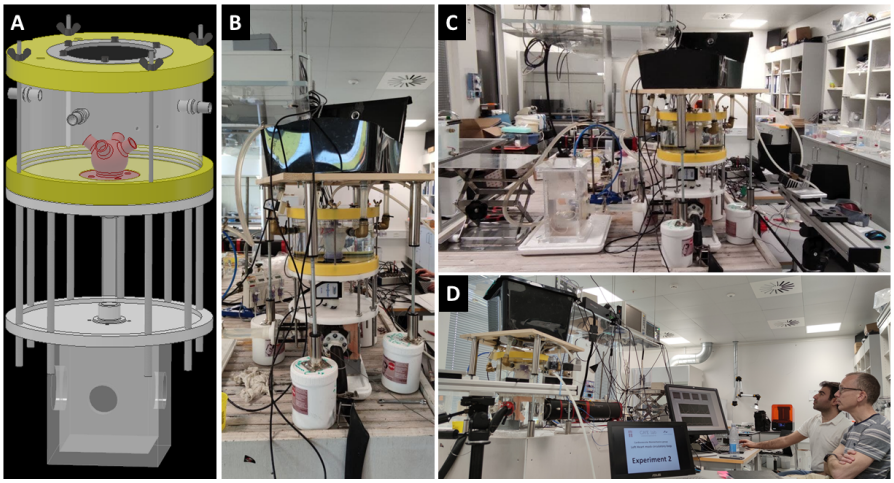

Figure 7.9: A) The CAD assembly model of the LA chamber, the left atrial container, the MV house, and the LV chamber. B,C,D) The LH MCL set up during the experiment in the CAVE lab.

pump piston head must be controlled during the three cardiac phases; Sys, ED and LD. Therefore, a waveform, made up of three separated cosine waveforms related to the three cardiac phases, were generated,

$$n : [0 \rightarrow t_1] : f(t) = -a_1 \cdot cos\left(n \cdot \frac{\pi}{t_1}\right) + 0.5, \tag{7.2}$$

$$n : [t_1 \rightarrow t_1 + t_2] : f(t) = -a_2 \cdot cos\left((n - t_1) \cdot \frac{\pi}{t_2}\right) + 0.6, \tag{7.3}$$

$$n : [t_1 + t_2 \rightarrow t_1 + t_2 + t_3] : f(t) = -a_3 \cdot cos\left((n - (t_1 + t_2)) \cdot \frac{\pi}{t_3}\right) + 0.1, \tag{7.4}$$

$$-a_1 + a_2 + a_3 = 0, \tag{7.5}$$

where n (ms) is the length of the cardiac cycle, and t_1, t_2, t_3 and a_1, a_2, a_3 are the Sys, ED and LD time spans and amplitudes, respectively. Eq. 7.5 ensures that the waveform starts and stops at the same voltage. The piston waveform and the triggering signal are shown in Fig. 7.10.

This custom waveform enhanced the versatility of the MCL because the time span and the amplitude of each cosine waveform can be adjusted for replicating different clinical

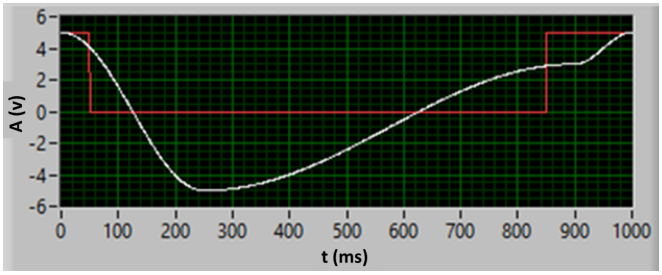

Figure 7.10: The white curve shows the pulsatile piston head waveform which is constituted with three cosine waveforms (Eqs. 7.2-7.5). The red curve displays the valves triggering signal, which opens the normally-closed valve when it is high, and opens the normally-open valve when it is low. The vertical axis is the amplitude in voltage and the horizontal axis is time in millisecond.

scenarios. The output rate was set to 1000 Hz, and changing the length of the waveform would alternate the heart rate. The triggering signal for the valves was constructed as a TTL signal. Since the normally-open and normally-closed valves are operating in asynchrony, the same control signal was used. To replicate the LA contraction phase, the triggering signal is high, causing opening of the normally-closed valve to pressurize the LA container. The low triggering signal, however, causes the normally-open valve to open to the atmospheric pressure to replicate LA relaxation phase.

7.9.3 Mock circulatory loop hemodynamics measurements

Four molded LA chambers, CH1,CH5, CH10 and CH11, with different compliance (Tab. 8.2) were selected for the measurements. The selected chambers are the representatives of the compliance range of the 11 molded chambers. The flow sensors, micro-tip pressure catheters, and fluid-filled pressure probes were calibrated and connected to the measurement sites. The duration of the cardiac phases and the cardiac output was adjusted by regulating the time and amplitude of the three cosine waveforms (Eqs. 7.2-7.5). The Sys time span was set to 350 ms, ED to 500 ms and LD to 150 ms. The amplitudes were set to obtain a cardiac output of 4.5 L/min. The MCL was run for some time to make sure that there is no air bubbles in the system, and that the cardiac output reaches to 4.5 L/min. The pressure and flowrate data were recorded for 60 cycles. To check the stability and reproducibility of the measurements, the mean standard deviation, $S_{d_{mean}}$, was calculated over 20 randomly selected cycles:

$$S_{dj} = \sqrt{\frac{1}{N-1}\sum_{i=1}^{N}(x_{ij} - \bar{x})^2} \quad , \quad j = 1, 2, 3, ..., n_s, \tag{7.6}$$

$$S_{d_{mean}} = \sqrt{\frac{\sum_{j=1}^{N} S_{d_j}^2}{N}}, \tag{7.7}$$

where N is the number of cycles, n_s is the number of samples in each cycle, x_{ij} is the measured data components, and $\bar{x}$ is the mean value of a component of a cycle over N cycles. In the conducted measurements n_s= 1000 as the sampling rate was set to 1000 Hz and the cardiac cycle duration was set to 1 s.

7.10 Magnetic resonance phase contrast flow imaging

In-vivo 2D PC-MRI was conducted on five healthy young volunteers (four males and one female, ages 23-33) to measure the PVF and MVF profiles, see Fig. 7.11. The imaging was done with a Philips MR scanner (Achieva dStream 1.5T, Philips Healthcare, The Netherlands). Initially, a multi-slice, multi-phase Balanced-Steady-State-Free-Precession sequence was applied over the whole heart for localizing the position and orientation of the vessels. The flow in each of the four PVs was measured with a 2D phase contrast sequence. The slice thickness was 8 mm, and the pixel size was 1.2 mm. Forty cardiac phases were acquired, and the velocity encoding parameter was 60 cm/s. The flowrate of each PVs was measured in a slice orthogonal to, and 3 mm proximal to the PVs ostium. The images where analyzed with an in-house written software (Siswin). The software environment is displayed in lower panel of Fig.7.11.

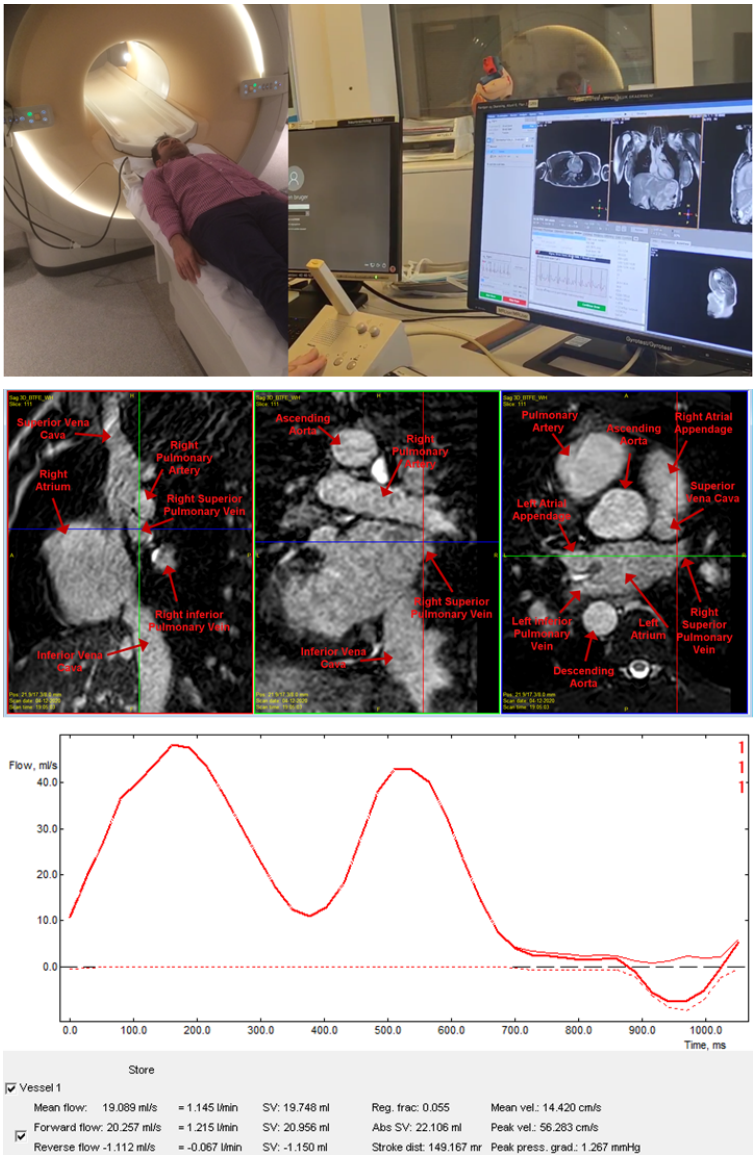

Figure 7.11: The in-vivo PC-MRI procedure is shown in the figure. The upper panel displays the author as one of the volunteers in the magnetic resonance scanner, and the control room. The middle panel shows an example of post-processing of the sagittal, axial, and coronal views of the images in the Siswin software. All the cardiac structures are landmarked on the image. The lower panel displays a measured LSPV flowrate profile.

CHAPTER 8

Results

In this chapter, first the results of the expansion tests on the porcine and molded chambers are compared, and four representative molded chambers are chosen for the LA hemodynamics measurements. Then the outcome of the curve fitting on the uniaxial tensile test data are presented, and the material model with better performance in describing the mechanical behavior of the Silicone-Elite mixture is chosen. In continue, the results of the in-vivo PC-MRI measurements are displayed, and the characteristics of the measured flowrate profiles are illustrated. At the end, the outcomes of the conducted measurements on the LH MCL with four representative molded LA chambers are elaborated.

8.1 Expansion test on porcine and molded left atrium chambers

The results of the expansion tests on the porcine hearts are reported in Tab. 8.1. The E_P of porcine LA chambers are between 107% and 263%, with the mean value of 165%. The lowest expansion belongs to heart $\#1$, and the largest compliance is for heart $\#3$. The results of the expansion tests on the molded LA chambers are presented in Tab. 8.2. The difference in V_0 amongst the molded chambers is due to the molding tolerances and shrinkage of the material after casting. The molded chambers are divided into three groups, 1) The ones with expansion in the range of porcine LA chambers are considered as normal-compliance chambers, 2) The chambers below the porcine expansion range are tagged as low-compliance chambers, and 3) The chambers above the porcine expansion range are categorized as high-compliance chambers. Therefore, CH1 to CH9 are categorized in the low-compliant group, CH10 is a normal-compliant chamber, and CH11 is a high-compliant chamber. Amongst the 11 chambers, CH1, CH5, CH10 and CH11 were chosen. Two chambers were chosen from low-compliance group because most of the chambers (9 out of 11) are in the low-compliance range.

8.2 Hyperelastic curve fitting on the tensile test data

The tensile test was done on the specimens which were cast with the same Silicone-Elite mixture ratio as the normal-compliance chamber CH10. Having the specimen dimensions, the engineering stress was calculated, and multiplied by the stretch values to obtain the true stress components. Then the true stress was plotted vs. stretch for all 13 specimens, displayed in Fig. 8.1. Afterwards, the true stress values were averaged over all the

Heart #	$V_0\ (ml)$	$\Delta V_{ave}\ (ml)$	$E_p\ \%$
1	27	29	107
2	32	50	156
3	38	100	263
4	30	40	133
5	45	70	156
6	14	30	214
7	34	48	141
8	37	46	124
9	38	74	195
mean	33	54	165

Table 8.1: Porcine LA chamber expansion test results. V_0 is the primary volume, ΔV_{ave} is the volume difference after pressurization and the E_p is the percentage of expansion.

Chamber	$V_0\ (ml)$	$\Delta V_{ave}\ (ml)$	$E_p\ \%$
CH1	67	19	28.4
CH2	65	22	33.8
CH3	66	21	31.8
CH4	66	24.3	36.9
CH5	70	30	42.9
CH6	65	29	44.6
CH7	68	32.3	47.5
CH8	68	34.7	51
CH9	70	64.7	92.4
CH10	69	76.3	110.6
CH11	69	>500	>300

Table 8.2: Molded LA chamber expansion test results. V_0 is the primary volume, ΔV_{ave} is the volume difference after pressurization and the E_p is the percentage of expansion.

specimens to plot mean stress vs. stretch. Moreover, the minimum and maximum stress values were selected amongst all the stress components and plotted vs. stretch. The mean, maximum and minimum stress-stretch curves are displayed in Fig. 8.1. It can be seen that the specimens exhibits large deformation (λ>5) and nonlinear behavior under a uniaxial tensile test, which clearly indicates the hyperelasticity of the Silicone-Elite mixture.

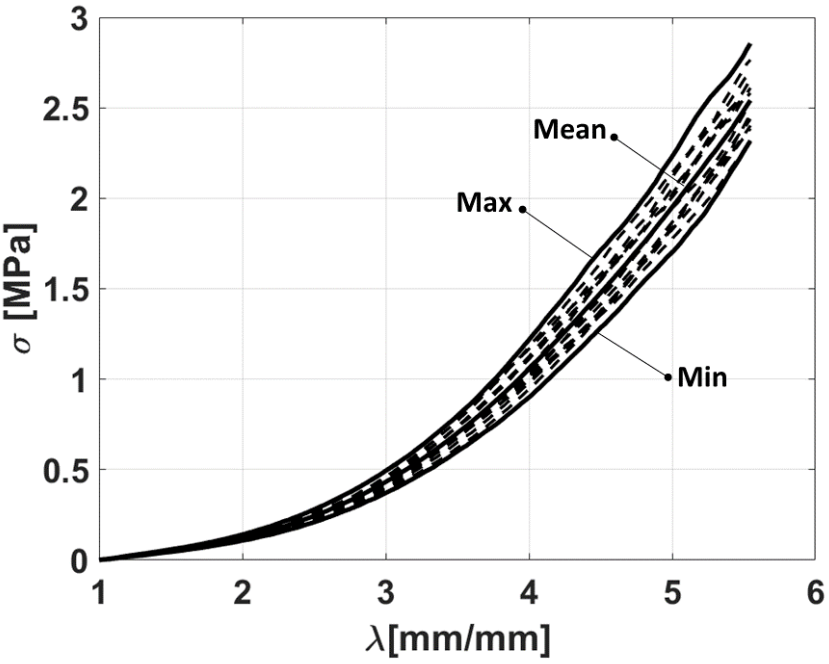

Figure 8.1: True stress (σ) vs. stretch (λ) curve of the 13 specimens which underwent uniaxial tensile test. The dashed lines (−−) represent the stress-stretch curves of the 13 specimens. The solid lines (—) display the minimum, mean and maximum stress values plotted vs. stretch.

The outcome of the fitted six hyperelastic models on the mean stress-stretch (σ-λ) curve is displayed in Fig. 8.2, and the obtained material parameters are presented in Tab. 8.3. In the small stretch zone (λ<2), all the material models have high accuracy and predict the behavior of the material well, as the material has a linear behavior. However, in the large stretch zone (λ>2), where the material nonlinearity increases, the neo-Hookean has the lowest and Yeoh has the highest accuracy in capturing the nonlinearity of the material. Moreover, amongst the six models, the Mooney-Rivlin model exhibits a negative slope in the small stretch zone, shown with purple arrow on Fig. 8.2.

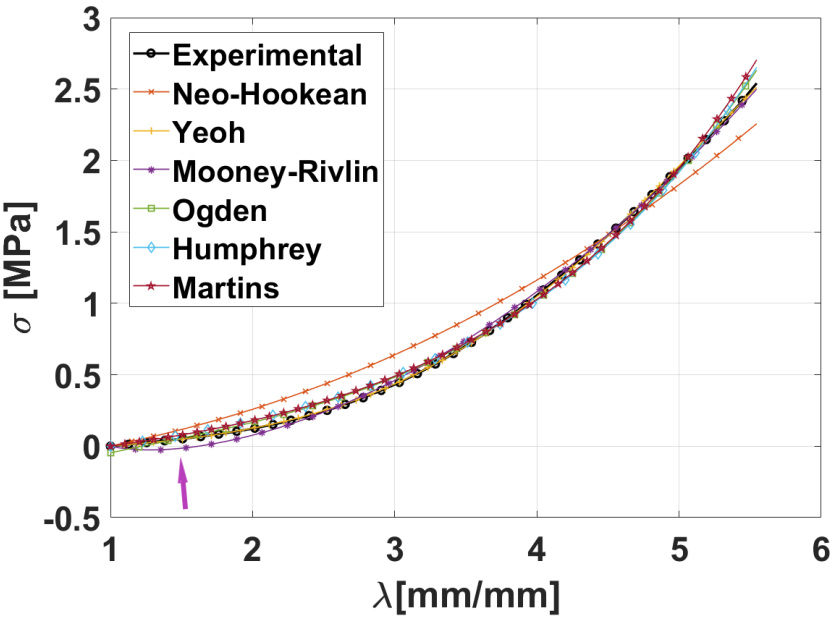

Figure 8.2: Six fitted hyperelastic models on the mean stress-stretch values of experimental data. The negative slope of the Mooney-Rivlin curve is pointed to by the purple arrow on the figure.

This negative slope generates material instability. What does "material instability" mean? Based on the Hooke's law, elongation δ of a bar is calculated as,

$$\delta = \frac{\sigma_e L}{E}, \tag{8.1}$$

where σ_e is engineering stress, L is length of the bar, and E is Young's modulus. For positive E (positive slope of the σ_e-λ curve), the loading and the elongation are in the same direction, and the conducted work is stored as strain energy in the deformed body, which is restored after unloading. However, negative E (negative slope of the σ_e-λ curve) means that the elongation is in the opposite direction of the load application, generating a strain energy which is physically impossible.

To evaluate the goodness of the fit, the correlation coefficient $C.C.$ between the experimental data and the theoretical predictions was calculated for each material model (Humphrey 2013),

$$C.C. = \frac{\sum_{i=1}^{m}(y_{si} - \bar{y}_s)_t (y_{si} - \bar{y}_s)_e}{\sqrt{\sum_{i=1}^{m}(y_{si} - \bar{y}_s)_t^2} \quad \sqrt{\sum_{i=1}^{m}(y_{si} - \bar{y}_s)_e^2}}, \tag{8.2}$$

Material model	Material Parameters	$C.C.$
neo-Hookean	$c_1 = 3.692 \times 10^4\,[Pa]$	0.99267
Yeoh	$c_1 = 1.450 \times 10^4\,[Pa]$ $c_2 = 898.5\,[Pa]$ $c_3 = -10.1\,[Pa]$	0.99997
Mooney-Rivlin	$c_1 = 5.772 \times 10^4\,[Pa]$ $c_2 = -9.345 \times 10^4\,[Pa]$	0.99907
Ogden (N=3)	$c_1 = -5.334 \times 10^4\,[Pa]$ $c_2 = 1.578$ $c_3 = 2.021 \times 10^4\,[Pa]$ $c_4 = 3.913$ $c_5 = 1.182 \times 10^4\,[Pa]$ $c_6 = 1.591$	0.99858
Humphrey	$c_1 = 1.239 \times 10^6\,[Pa]$ $c_2 = 0.02$	0.99836
Martins	$c_1 = 1.168 \times 10^6\,[Pa]$ $c_2 = 0.021$ $c_3 = 3.202 \times 10^4\,[Pa]$ $c_4 = 0.015$	0.99820

Table 8.3: The calculated material parameters and correlation coefficients are presented. Yeoh model has the highest $C.C.$ amongst the models.

where y_{si} is the stress components, $\bar{y}_s$ is the mean stress value, and m is the number of components of each data set. The subscript t stands for theoretical, and the subscript e stands for experimental. The $C.C.$ index evaluates the overall quality of the fit. The calculated $C.C.$ for each material model is presented in Tab. 8.3. Evidently, the Yeoh has the highest $C.C.$ and the neo-Hookean has the lowest one. The $C.C.$ of the Mooney-Rivlin model is also higher compared to the neo-Hookean, Ogden, Martins and Humphrey models. However, because it causes material instability, it was excluded from further investigations.

Another index for evaluating the goodness of the fit is the error residual E_R, which calculates the relative difference between theoretical and experimental data at each stretch level (Martins, Jorge, and Ferreira 2006; Meaney 2003),

$$E_R(\lambda) = \frac{|y_e(\lambda) - y_t(\lambda)|}{y_e(\lambda)} \times 100\,, \tag{8.3}$$

where y_t is the theoretical stress components, and y_e is the experimental stress values. The calculated E_R for each fitted hyperelastic model is displayed in Fig. 8.3. The E_R

is lower in Yeoh compared to the other models. It is observed by (Martins, Jorge, and Ferreira 2006) that the lobes of the E_R graph of the neo-Hookean, Ogden and Humphrey models represent the number of model parameters, but it is inconclusive for the Yeoh and Martins models. A similar observation was made in this work, which confirms their findings.

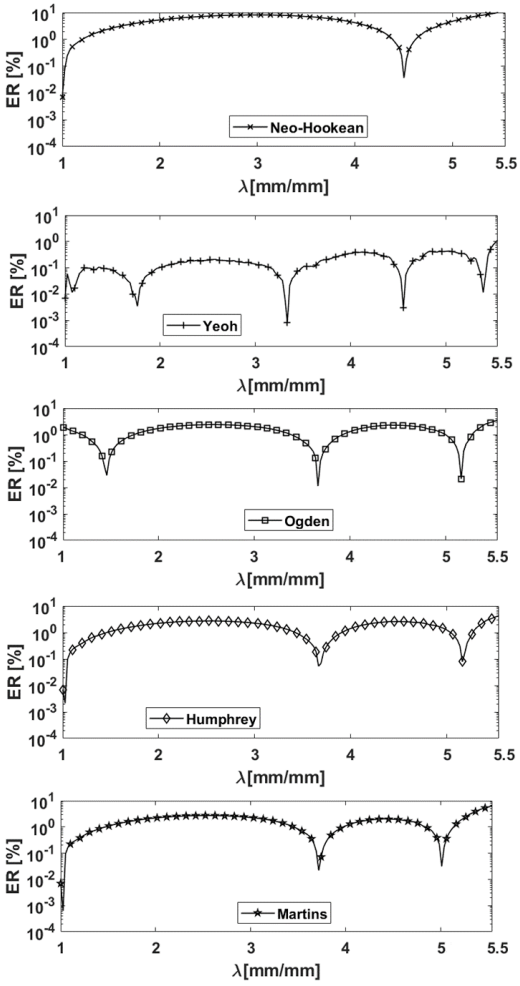

Figure 8.3: The calculated E_R for fitted hyperelastic models. The Yeoh model has the lowest and the neo-Hookean model has the highest E_R amongst the fitted models.

Furthermore, to investigate which model represents better the mechanical behavior

of the material, FEA with the different material models was implemented on the LA simplified geometry. To this aim, the five material models were fitted on the maximum and minimum curves, shown in Fig. 8.1, and the optimal model parameters were calculated. For each set of the material model parameters, the maximum first principal stress σ_1 was obtained through the FSI simulation. Then, the normalized difference n_d was calculated at each stretch level between the σ_1, obtained by c_i of the curve fitting on the minimum curve (σ_{1min}), and the σ_1 of the c_i of the curve fitting on the maximum curve (σ_{1max}),

$$n_d(\lambda) = \frac{|\sigma_{1max}(\lambda) - \sigma_{1min}(\lambda)|}{\sigma_{1max}(\lambda)}. \tag{8.4}$$

Fig. 8.4 shows the maximum principal stress and stretch distribution at the end of the reservoir phase, resulted from the FSI simulation with the Yeoh material model. The maximum principal stress is about $0.12\ MPa$, which is located around the pulmonary vein ostium. Interestingly, the maximum principal stretch is less than 2, showing that the material behavior is in the low stretch zone (Fig. 8.2).

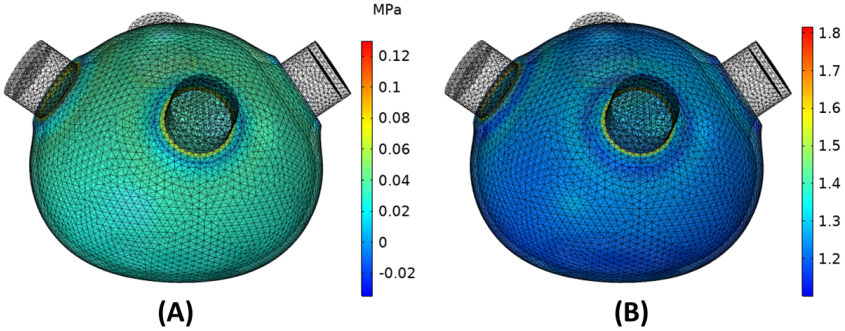

Figure 8.4: The FEA analysis of LA simplified model. The figure displays the A) Maximum principal stress and B) Maximum principal stretch distribution on the LA model at the end of reservoir phase using the Yeoh material model.

The results of the n_d are shown in Fig. 8.5. Amongst the five material models, Yeoh has the lowest n_d, which means that the discrepancy between stress-strain state presented by the minimum and maximum sets of Yeoh material parameters is very low. This further implies that the Yeoh model represents better the mechanical characteristics of the Silicone-Elite material. To best of the authors knowledge, this is the first time such an index is employed for evaluating analytical models in curve fitting exercises.

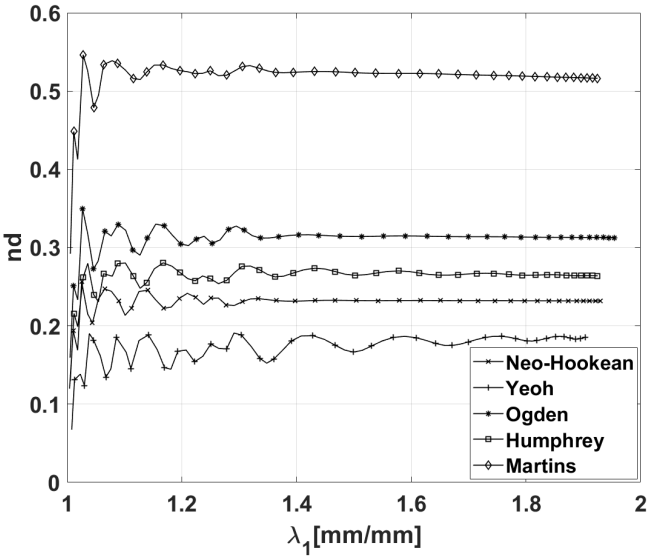

Figure 8.5: The normalised first principal stress difference vs first principal stretch is shown. The n_d was calculated based on the difference of the σ_1 between model parameters of the curve fitting on the maximum and minimum curve (Fig. 8.1).

8.3 Magnetic resonance phase contrast flow imaging

8.3.1 In-vivo pulmonary veins flowrate measurement

All volunteers who underwent PC-MRI had four PVs, i.e. LIPV, LSPV, RIPV and RSPV. For each PVs, the flowrate profile was measured proximal to the PVs ostium. The measured data points were interpolated with a quadratic polynomial function. The results are shown in Fig. 8.6.

To elaborate the measured PVF profiles, the constituents of the flowrate profiles of case 1 are marked on Fig. 8.7. The in-vivo 4D PC-MRI measurements of the PVs flowrate show a four-wave pattern, including three antegrade flow waves and a retrograde flow wave, as reported in the literature (Barbier et al. 2000; Bukachi et al. 2005; Chao et al. 2000; Hellevik et al. 1999; Keren, Meisner, et al. 1986; Keren, Sherez, et al. 1985; Kuecherer et al. 1990; Nishimura et al. 1990; Smiseth et al. 1999). The two peaks, s_1 and s_2, which builds the SFF wave in the Sys phase, and the DFF wave in the ED phase, are antegrade waves. At the ED phase, a retrograde flow (RF) wave occurs due to the LA contraction. However, there is a new observation that the RF at the end of the Sys phase is not a pure backward flow rather a combination of backward and forward flow. It is speculated that, this short instant of forward flow is generated due to the swift LAP

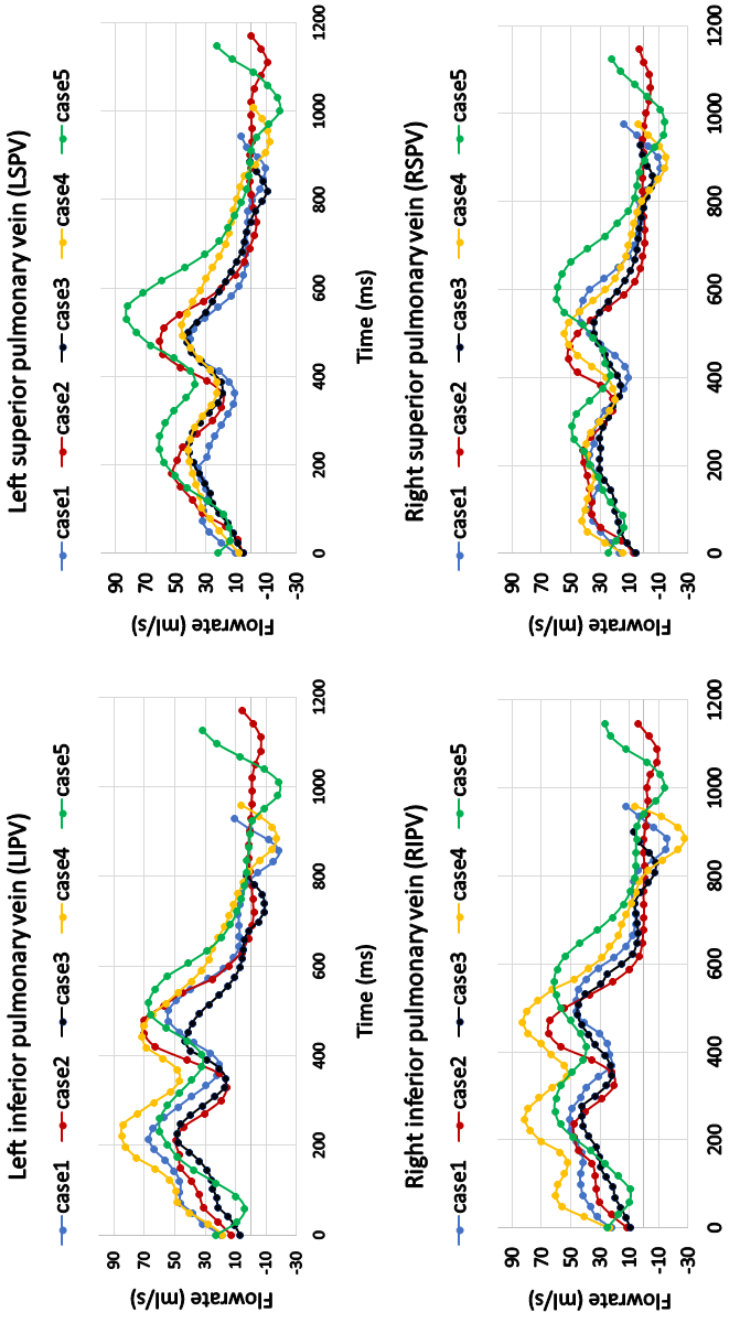

Figure 8.6: The PVF profiles of five healthy young volunteers. The PVF profiles were measured 3 mm proximal to the PVs ostium.

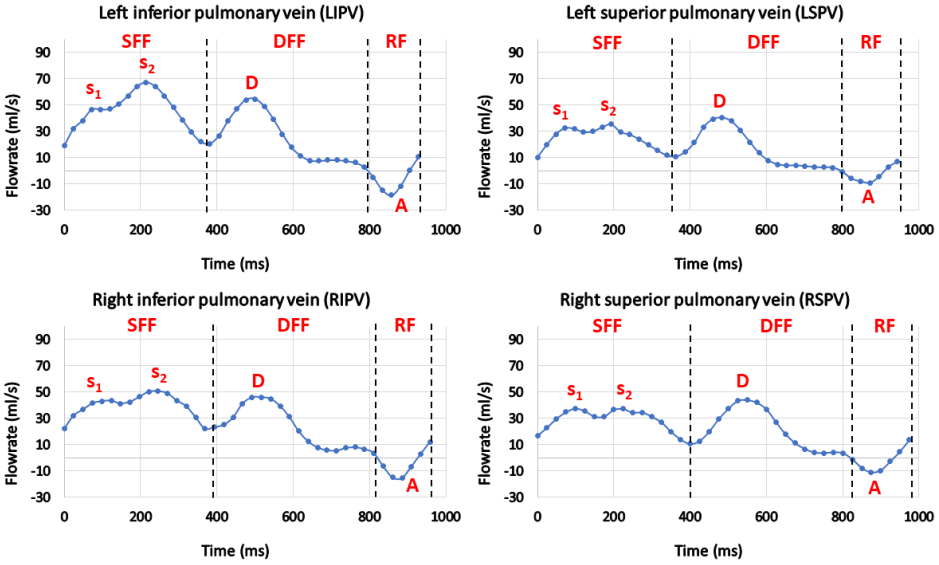

Figure 8.7: PVF profiles of the case1 is displayed. The PVF profiles include three forward flow waves, s_1, s_2 and **D**, and one backward flow wave, **A**, in the LD phase. SFF = systolic forward flow, DFF = diastolic forward flow, RF = retrograde flow.

drop at the end of the LA contraction, which reverses the backward flow to a forward flow. This event occurs during the LV isovolumetric contraction phase.

Another observation is, the duration of the Sys phase in all the cases is almost the same, between $350\ ms$ to $400\ ms$. However, the diastolic time span differs a lot among the cases. It is inferred that the difference in heart rate among the cases is reflected in the duration of the diastolic phase. Interestingly, in case 2 and case 5, in which the duration of the diastolic phase is longer, zero or negative flow can be seen before RF wave.

8.3.2 Pulmonary veins cross sectional area

To investigate the variation of the PVs dimension during cardiac cycles, the four PVs cross sectional area of the case 1 was measured. Fig. 8.8 displays the variation of the PVs cross sectional area in one cardiac cycle. To quantify the variation of the area during the cardiac cycles, the mean PVs cross sectional area, $A_{P_{mean}}$, and the S_d were calculated and reported in Tab. 8.4. As it can be seen in Fig. 8.8, and based on the reported $A_{P_{mean}}$ $(\pm S_d)$, the variation of the PVs cross sectional area is less than 15%, which is not considerable. This finding is close to the value reported by Rajagopalan et al. (1979), which showed the PVs cross sectional area decreases by approximately 20%.

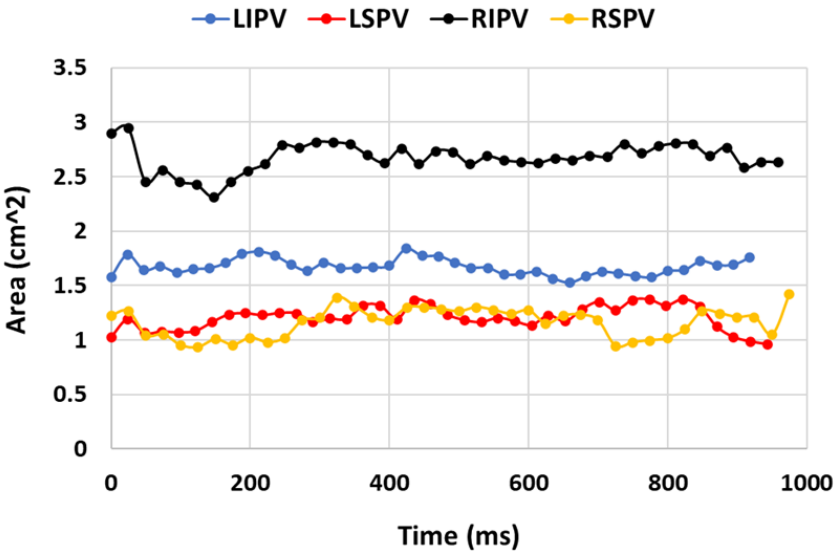

Figure 8.8: The measured PVs cross sectional area of case 1 in one cardiac cycle (Fig. 8.6) is displayed in the figure. The area was measured 3 mm proximal to the PVs ostium.

PVs	$A_{P_{mean}}$ ($\pm S_d\%$) [cm^2]
LIPV	1.67 ($\pm$7)
LSPV	1.20 ($\pm$11)
RIPV	1.16 ($\pm$14)
RSPV	2.67 ($\pm$13)

Table 8.4: The $A_{P_{mean}}$ and S_d of the PVs cross sectional area of case 1 are reported in the table. The variation of the area is less than 15%.

8.3.3 Mitral valve flowrate profiles

The measured MVF profile is displayed in Fig. 8.9. The MVF was measured on a plane, 3 mm in LV chamber, normal to the flow axis. The MV leaflets have unequal dimensions and the anterior leaflet is larger than the posterior leaflet. The anterior one is positioned between the LV outflow track and the MV orifice area, and the posterior leaflet is located behind the MV orifice next to the LV wall (Kheradvar and Pedrizzetti 2012). Because the anterior leaflet is larger than the posterior one, the flow jet axis is inclined towards the LA wall, rather than the heart apex. That is the reason why the MVF was measured on a plane normal to the flow jet axis, and not normal to the MV annulus. The MVF profile

characteristics, E-peak and A-peak, are captured clearly and shown on Fig. 8.9. The measured MVF profile is in well agreement with the reported TV profiles in the literature (Keren, Meisner, et al. 1986; Keren, Sherez, et al. 1985; Nagueh 2018; Nishimura et al. 1990; Zipes et al. 2019). The MVF profile consists of two peaks, the E-peak and the A-peak. The E-peak, equal to 430 ml/s, is the maximum flowrate in the LV rapid filling phase. After the E-peak, the MVF diminishes to zero, as the LA empties rapidly into the LV. But again the flowrate surges in the LD phase due to the LA contraction, and forms the A-peak, equal to 250 ml/s. The MVF during the Sys phase is around 50 ml/s, while it should be zero as the MV is closed. The reason is, that the MV annulus moves up and down due to the LV function in the Sys phase. Therefore, the velocity of the MV annulus movement is captured by the PC-MRI and reflected on the diagram as if there is flowrate during the Sys phase. In fact, the velocity component of this portion of the MVF profile comes from the MV annulus movement, and not from the blood flow.

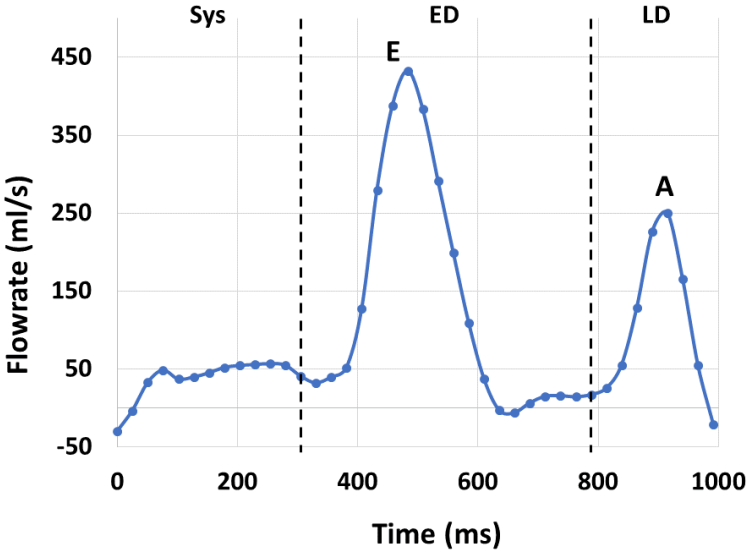

Figure 8.9: The measured in-vivo MVF profile is displayed. It includes two forward flow waves, the E-wave and the A-wave. The measured MVF belongs to the case 1.

8.4 Fluid dynamics measurements with normal-compliance left atrium chamber

The results of the in-vitro LH fluid dynamics measurements with the normal-compliance chamber, CH10, are displayed in Fig. 8.10 and Fig. 8.11.

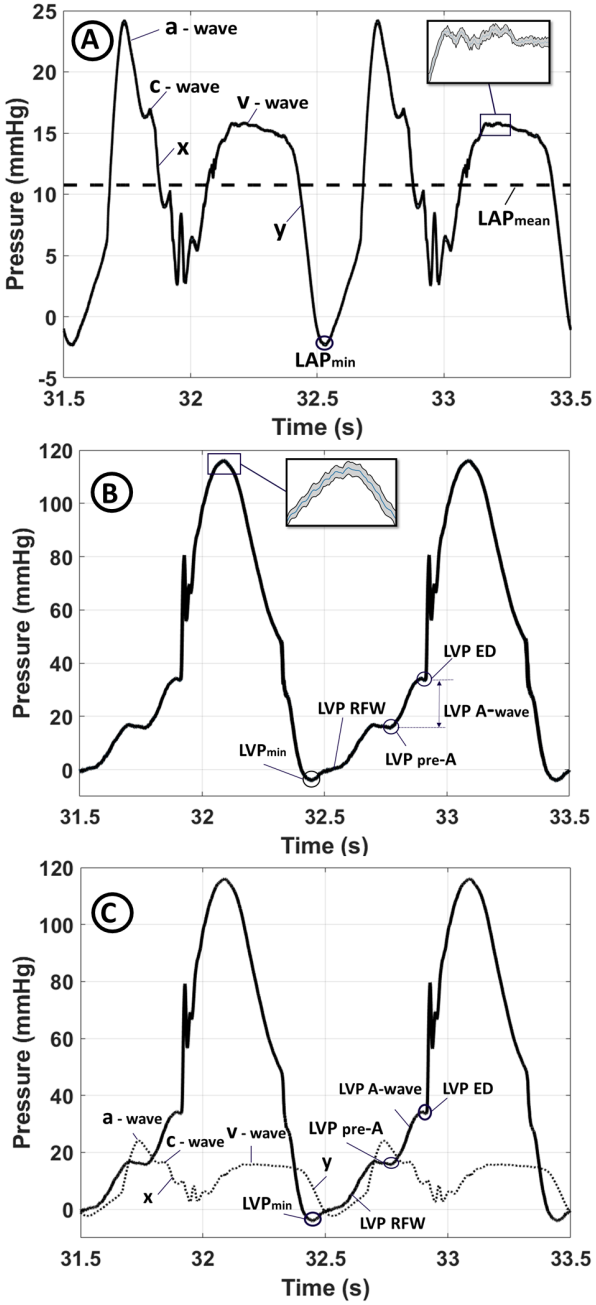

Figure 8.10: The MCL pressure measurements with the normal-compliance chamber CH10. A) The measured LAP in two cycles. The a-wave, v-wave, c-wave and x and y troughs are marked on the graph. The mean LAP is shown with dashed line. B) The measured LVP in two cycles. LVP_{min} = minimum LVP, LVP RFW = LVP rapid filling wave, LVP pre-A = LVP prior to the LA contraction, LVP EDP = end diastolic LVP. C) The LAP (dotted line) is displayed over LVP (solid line) to compare the pressure components of the two chambers. In all the graphs, the zoomed area shows the mean and the S_d.

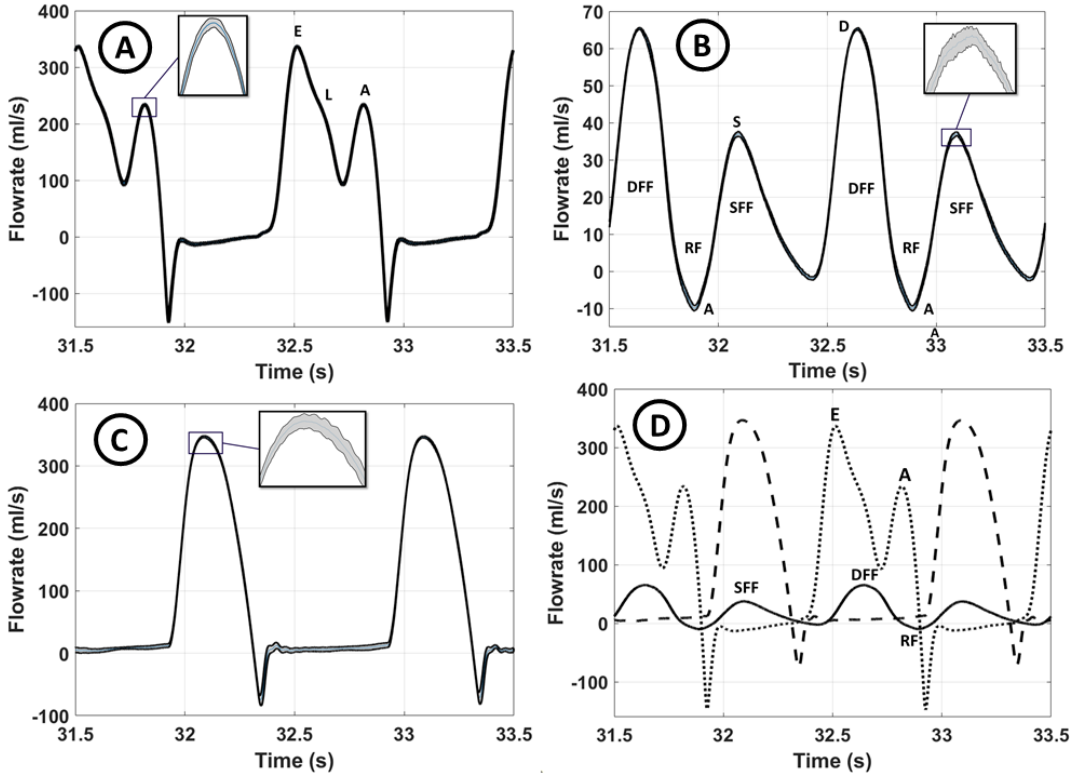

Figure 8.11: The MCL fluid dynamics measurements with the normal-compliance chamber CH10. A) The MVF profile. E = early diastolic peak, and A = atrial kick. B) The PVF profile. DFF = diastolic forward flow, SFF = systolic forward flow, RF = retrograde flow, D = diastolic peak, and S = systolic peak. C) The AVF. D) The MVF, PVF and AVF profiles are displayed together for comparison. In all the graphs, the zoomed area shows the mean and the S_d.

The zoomed regions show the mean and the S_d of the measured values. The calculated $S_{d_{mean}}$ of the pressure and the flowrate measurements over 20 randomly selected cycles (Eq. 7.7) are reported in Tab. 8.5. The highest $S_{d_{mean}}$ value belongs to the AVF, equal to $4.13\ ml/s$, which is very small compare to the maximum AVF amplitude $330\ ml/s$. The same argument is valid for the LAP, the LVP, the PVF and the MVF profiles as the $S_{d_{mean}}$ values are very small compare to the magnitude of the measured profiles. Therefore, the small $S_{d_{mean}}$ values show that the measurements are very stable and reproducible.

Measurement	LAP (mmHg)	LVP (mmHg)	PVF (ml/s)	MVF (ml/s)	AVF (ml/s)
$S_{d_{mean}}$	0.14	0.61	0.72	2.32	4.13

Table 8.5: Calculated $S_{d_{mean}}$ of the MCL measurements with the normal-compliance chamber CH10.

8.4.1 Left atrial and left ventricular pressure profiles

Considering the LAP waveform, shown in Fig. 8.10(A), the three positive deflections, **a**, **c**, **v**, and the two negative deflections, **x** and **y** troughs, are visible (Barbier et al. 1999; Bonow et al. 2011; Kuecherer et al. 1990). A typical physiological LAP waveform is also shown in Fig. 4.9. The v-wave reflects the LAP increase during the reservoir phase function due to the PVF SFF while the MV is closed. The value of the v-peak is $15.8\ mmHg$, which is in the normal range $6 - 21\ mmHg$ reported in Zipes et al. (2019). The **y** trough shows the abrupt LAP drop due to the LA passive emptying into the LV following the MV opening when the LVP drops below the LAP. The a-wave reflects the 3rd phase of the LA phasic function in which the LA contracts, and as the result, the LAP increases instantly. the a-peak is $24.1\ mmHg$, which is higher than the range $4 - 16$ $mmHg$ reported in Zipes et al. (2019). The **x** trough shows the LAP decline caused by the LA relaxation following the LA contraction. The **c** deflection reflects the sudden rise in the LAP due to the closure of the MV. The oscillations at the downhill of the a-wave before the beginning of the v-wave is generated due to the MV closure, recorded by the Micro-tip catheter.

Looking at the LVP waveform in Fig. 8.10(B), the LVP drops to its minimum value, the LVP_{min}, right after the MV opening. Then the LVP increases during the LVP rapid filling wave to the inflection point, the LVP pre-A, before the LA contraction. Due to the LA contraction, the LVP surges upward and generates the LVP A-wave. The LVP ED trough reflects the LVP decline before the LVP systolic rise. The peak systolic value of the LVP is $115\ mmHg$, which is in the range $90 - 140\ mmHg$, reported in Zipes et al. (2019). The sharp peak and oscillations after LVP ED and before the systolic peak of the LVP reflects the AV opening recorded by the Micro-tip catheter.

To evaluate the synchrony between the LVP and the LAP events, the LAP and the LVP waveforms are displayed together in Fig. 8.10(D). The simultaneity of the LAP events

with the LVP components are visible. Considering the v-wave on the LAP waveform, when the LVP drops below the LAP, the MV opens. As the result, the LAP drops and generate the **y** trough. Then, as the result of the LA contraction, the LAP surges again, forming the a-wave. Moreover, the LVP increases due to the LA contraction and generates the LVP A-wave. In continue, the LAP diminishes and the LVP surges to the systolic peak. Afterwards, the LAP increases again due to the inflow from the PVs while the MV is closed, forming the v-wave on the LAP waveform.

8.4.2 Pulmonary vein, mitral valve and aortic valve flowrate profiles

Fig. 8.11 displays the measured MVF, PVF and AVF profiles. The measured MVF, shown in Fig. 8.11(A) captured all the characteristics of a typical MVF profile reported in the literature (Keren, Meisner, et al. 1986; Keren, Sherez, et al. 1985; Nagueh 2018; Nishimura et al. 1990; Zipes et al. 2019). The profile contains the E-peak and the A-peak, reflecting the ED and the LD filling phases of the LV chamber. The measured MVF indices for the CH10, the E-peak, the A-peak, the E/A ratio and the DT are reported in Tab. 8.8. The E/A ratio is 1.44, and the DT is 206 ms which both are within the reported physiological ranges presented in Tab 4.7.

Fig. 8.11(B) shows the measured PVF with all the components of the PVF structure. The PVF profile includes two antegrade waves, the SFF and the DFF waves, and one retrograde wave, which is the RF wave. The S-peak is 37.1 ml/s, the D-peak is 65.3 ml/s, and the S/D ratio is 0.57. The S/D ratio is in the range reported for normal patients by Kuecherer et al. (1990). The AVF profile is displayed in Fig. 8.11(C). The PVF is zero in the ED and LD phases, and surges during the Sys phase when the AV opens.

In Fig. 8.11(D), the MVF, the PVF and the AVF are displayed together to evaluate the synchrony between the measured flowrate profiles. Because the MVF has a very high correlation with the LH pressure gradient, it contains vital prognostic information. When the LVP drops below the LAP, the AV closes and the MV opens. The E-peak represents the passive early diastolic LV filling, corresponding to the beginning of the DFF wave of the PVF profile, and to the zero AVF. This phase of the MVF has been ascribed to many factors, including the LV relaxation, the LV compliance and the LAP (Bonow et al. 2011; Nishimura et al. 1990). The A-wave represents the LA contraction, and corresponds to the beginning of the RF wave of the PVF, and zero AVF in the LD phase. This part is attributed to the LA contractility and the LA afterload (Kuecherer et al. 1990). In the Sys phase the LVP exceeds the LAP, and therefore, the AV opens and the AVF increases, corresponding to the SFF wave of the PVF. In this phase, the MVF is zero due to the closure of the MV. Hence, the sequence of the flowrate events proves the synchronized interplay between the PVF, the MVF and the AVF.

8.4.3 Interplay between flowrate and pressure

Fig. 8.12 shows the reverse relation between the PVF, the LAP and the LVP, reported in the literature (Barbier et al. 2000; Smallhorn, Freedom, and Olley 1987; Smiseth et al.

1999). While the LAP increases, the PVF SFF declines until the MV opens. The DFF starts to rise as the LAP drops because of the LA passive emptying into the LV. As the LV filling pressure increases, the DFF diminishes to zero and in continue, due to the LA contraction, the LAP propagates through the extra parenchymal PVs and generates the RF.

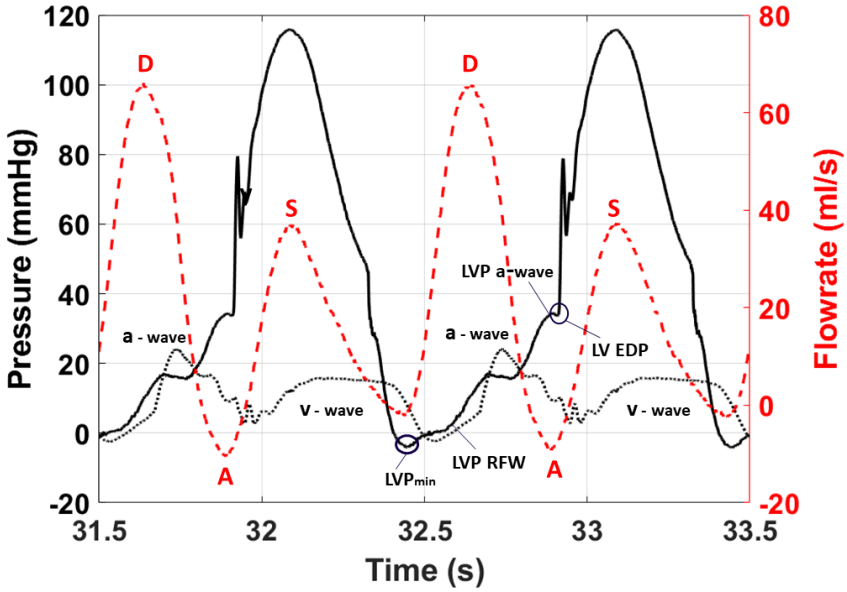

Figure 8.12: The measured in-vitro LAP (black dotted line), LVP (black solid line) and PVF (red dashed line) plotted together to show their reverse relations.

8.5 Fluid dynamics measurements with different left atrium chamber compliance

The results of the LH in-vitro fluid dynamics measurements with different LA chambers with various compliance are displayed in Fig. 8.13 and Fig. 8.14. Considering the measured LAP in Fig. 8.13(A) and Tab. 8.6, the reduction of the LA compliance impacts the LAP dramatically. As the LA compliance declines, the maximum systolic pressure, v-peak, increases from 12 $mmHg$ to 18.7 $mmHg$, and the maximum LA diastolic pressure, a-peak, increases from 21.7 $mmHg$ to 26.4 $mmHg$. The change in LAP_{mean} is not considerable, however, the difference between the LAP_{min} and the a-peak increased from 21.3 $mmHg$ to 31.9 $mmHg$. Fig. 8.13(B) shows that the change in LA compliance has no impact on the maximum systolic LVP. The measured PVF indices are reported in Tab. 8.6.

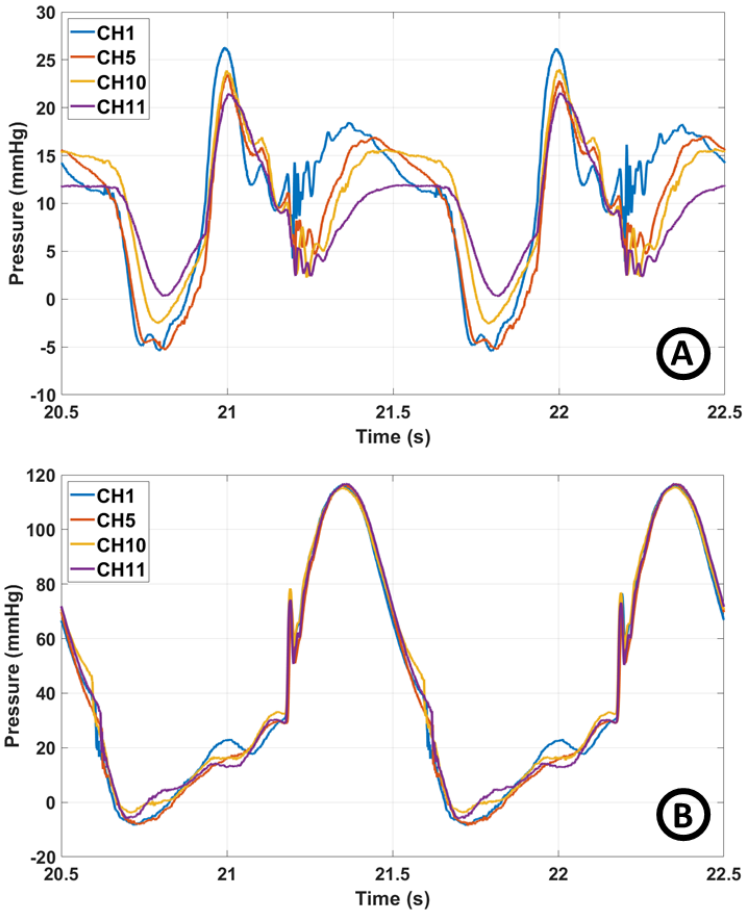

Figure 8.13: The measured LAP and LVP in the CH1, CH5, CH10 and CH11 chambers to investigate the impact of the LA compliance on the pressure. A) The LAP profile. B) The LVP profile.

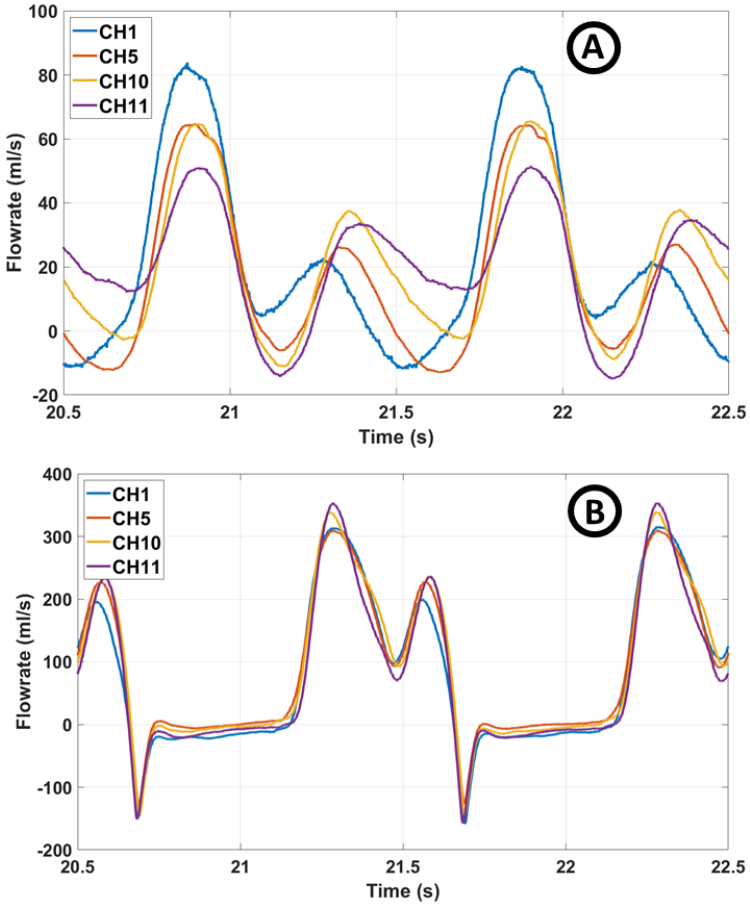

Figure 8.14: The measured in-vitro flowrate for the CH1, CH5, CH10 and CH11 chambers to evaluate the impact of the LA compliance on the flowrate. A) The PVF profile. B) The MVF profile.

Moreover, it is visible in Fig. 8.14(A) that the PVF profile is drastically changed due to the decline in the LA compliance. The VTI SFF declines from 10.4 ml to 4.4 ml, and the S-peak reduced from 34.9 ml/s to 23.9 ml/s. Similarly, the VTI RF decreased from 1.7 ml to 0 ml and the A-peak diminished severely from -14.9 ml/s to 0 ml. On the contrary, the VTI DFF increased from 11.7 ml to 19.8 ml, and the D-peak is raised from 51.5 ml/s to 82.6 ml/s. This implies that the reduction of the LA compliance diminishes the SFF and the RF waves, but amplifies the DFF wave. This change in the SFF and DFF is also reflected in the S/D ratio. The measured PVF indices are reported in Tab. 8.7.

The effect of the LA compliance on the MVF is displayed in Fig. 8.14(B). As the LA compliance declines, the E-peak reduces from 353.1 ml/s to 312.8 ml/s, and the A-peak declines from 234.4 ml/s to 195.5 ml/s. Moreover, the DT reduces from 198 ms to 186 ms. The measured MVF indices are reported in Tab. 8.8.

LAP (mmHg)	v-peak	a-peak	LAP_{mean}	LAP_{min}
CH11	12	21.7	9.5	0.4
CH10	15.8	24.1	10.8	-2.3
CH5	17.2	23.4	9.5	-5.4
CH1	18.7	26.4	10.6	-5.5

Table 8.6: The measured LAP indices for the different LA chambers with various compliance are reported in the table. All the reported values are marked in Fig. 8.10(A).

PVF	VTI SFF (ml)	VTI DFF (ml)	VTI RF (ml)	A (ml/s)	S (ml/s)	D (ml/s)	S/D
CH11	10.4	11.7	1.7	-14.9	34.9	51.5	1.48
CH10	8.1	13.5	0.81	-10.1	37.1	65.3	0.57
CH5	4.9	14.5	0.54	-6.9	29.2	64.8	0.45
CH1	4.4	19.8	0	0	23.9	82.6	0.29

Table 8.7: The measured PVF indices for the different LA chambers with various compliance are reported in the table. VTI SFF = velocity time integral of systolic forward flow. VTI DFF = velocity time integral of diastolic forward flow. VTI RF = velocity time integral of retrograde flow. A-wave, S-wave, and D-wave are all marked in Fig.8.11(A).

MVF	E (ml/s)	A (ml/s)	E/A	DT (ms)
CH11	353.1	234.4	1.51	198
CH10	336.8	233.6	1.44	209
CH5	308.4	227.1	1.36	192
CH1	312.8	195.5	1.6	186

Table 8.8: The measured MVF indices for the different LA chambers with various compliance are presented in the table. The E-peak and the A-peak are displayed in Fig. 8.11(B).

CHAPTER 9

Discussion

9.1 Hyperelastic curve fitting on the tensile test data

Elite Double 8 is used in dentistry for dental impressions, offering a very high elastic recovery (99.99%), high tear strength and laceration resistance, and provides high detail reproduction (courtesy of Zhermack SpA). However, it was unable to provide the expected compliance because of low elasticity (380%). Then, Silicon Rubber ZA-SFX-0020 was added as it offers a very high elasticity (770%). Therefore, the Silicone-Elite mixture provided a representative hyperelastic material to cast the LA chamber.

Three indices, $C.C.$ (Tab. 8.3), E_R (Fig. 8.3) and n_d (Fig. 8.5), were used to investigate which material model represents better the mechanical behavior of the Silicone-Elite mixture. Considering all the calculated indices, the Yeoh model offers higher $C.C.$, and lower E_R and n_d, compared to other fitted material models, which is in well agreement with (Martins, Jorge, and Ferreira 2006). Surprisingly, the Martins model has the highest n_d amongst the models while its $C.C.$ is higher after Yeoh. It is speculated that while an analytical model offers a good fit to experimental data, it may not be a good choice for numerical simulations like FEA. The same was observed when the Mooney-Rivlin model was fitted to the experimental data. Despite of good fitting results, it generated material instability due to the negative σ-λ curve slope. This negative slope on the fitted Mooney-Rivlin curve can be seen in many works (Bahrain and Mahmud 2017; Lagan and LiberKnec 2017; Martins, Jorge, and Ferreira 2006) which causes material instability and generates errors if it is used in numerical simulations. Therefore, it is recommended to interpret the results of curve fitting based on the application of the models in numerical studies.

9.2 Fluid dynamics measurements with normal compliance left atrium chamber

Considering the measured LAP and LVP, both the absolute individual values and the shape of the LAP and the LVP waveforms are in good agreement with the literature (Nagueh 2018, 2020; Zipes et al. 2019). In the LAP, the height of the v-peak is determined by the LA compliance, LA filling, and the descending movement of the MV annulus. Amongst them, the LA compliance plays a key role in the LAP condition (Barbier et al. 1999; Kuecherer et al. 1990). This matter implies the importance of casting a LA chamber

with proper compliance. The LAP decline during the LA conduit phase depends highly on the LV preload (or compliance). However, as the LV chamber of the MCL is rigid, it was tried to mimic the LV compliance by manipulating the amplitude of the early diastolic portion of the pulsatile pump piston waveform (Eq. 7.3). The reason for the high a-wave is because the late diastolic portion of the piston waveform (Eq. 7.4) also contributes to the LA contraction by generating suction and strengthening the effect of the LA chamber pressurization. Apart from the absence of the isovolumic contraction and relaxation because of the rigid LV chamber, all other components of a physiological LVP waveform are visible on the measured one (Fig. 8.10(B)). The synchronization between the LAP and the LVP is shown in Fig. 8.10(C), which confirms the coordination of the LAP and the LVP events.

In this study, one of the important issues under investigation was to find out about the origin of the PVF phases, because it was the key point in deciding how to design and feed the inlets of the LA chamber. There are many debates and disagreements about the determinants of the PVF phases. For the DFF, some researchers ascribed it to the LV relaxation and LAP drop due to the opening of the MV (Chen et al. 1993; Hellevik et al. 1999; Keren et al. 1985; Kuecherer et al. 1990; Nishimura et al. 1990). Other studies, however, showed that the LA recoil due to the stored elastic energy during the LA reservoir filling is the strongest determinants of the DFF (Barbier et al. 2000, 1999). Considering the RF, the LA contraction has been suggested as its main determinant (Appleton 1997; Basnight et al. 1991; Hellevik et al. 1999). Regarding the SFF, it is demonstrated that it is purely driven by the LH systolic events, due to the LA relaxation, the LA compliance and the descending movement of the MV annulus caused by the LV systolic function (Barbier et al. 2000, 1999; Castello et al. 1991; Chen et al. 1993; Klein and Tajik 1991; Nishimura et al. 1990). In other studies, the SFF is attributed to the RV systolic pressure propagation through the pulmonary circulation (Appleton 1997; Rajagopalan et al. 1979; Wiener et al. 1966). However, the SFF has also been ascribed to the LA reservoir, LV and RV systolic functions (Barbier et al. 1999; Smiseth et al. 1999). To conclude, it can be inferred that the PVF phases are predominantly controlled by the LH events and pressure gradient, though the impact of the pressure propagation from the RV cannot be ruled out.

Because the main goal of this study was to build a LH MCL, and because the pulmonary capillary bed can be considered as a reservoir with a large capacity (Rajagopalan et al. 1979), it was assumed that the PVs are completely isolated from the right heart effect, and are only driven by the LH events. Therefore, a rigid reservoir with constant static pressure was designed as the PVs for the LA inlets.

The measured in-vitro PVF, displayed in Fig. 8.11(A), shows a triphasic flow wave pattern. The SFF, DFF and RF are visible, however, the SFF includes only one peak, which is the s_1 peak. Because the LV of the MCL is rigid, and the MCL is an isolated LH with no right heart components, it cannot be confirmed whether the s_2 is generated by the descending movement of the heart base, or by the RV systolic pressure propagation through the pulmonary vasculature. Therefore, the possibility of the RV contribution in the PVs SFF cannot be ruled out. However, the results disclose that the PVF pattern is

predominantly determined by the LH events, i.e. by the LH pressure gradient.

Another observation which proves that the PVF is predominantly controlled by the LH pressure gradient is the mid-diastolic flow pattern of the measured in-vivo PVF profiles of case 2 and case 5, displayed in Fig. 8.6. After the DFF and before the RF, there is a period in which the PV is zero or negative. This mid-diastolic flow pattern shows that as the LV filling pressure increases, the DFF diminishes and reaches a plateau. The plateau before the LA contraction is because the LAP is balancing with the LVP. The negative flowrate before the RF wave in case 2 shows that the LVP exceeds the LAP, and therefore, the flow regurgitates into the PVs. If there were any contribution from the RV pressure propagation, that backward flow before the RF at the end of the diastole would not have happened.

9.3 Effect of compliance on the left atrium fluid dynamics

As it was argued before, the compliance of the LA has a significant impact on the LH hemodynamics. It directly affects the LA and the LV systolic and diastolic functions, the PVF phases, the diastolic MVF pattern and the cardiac output. Therefore, excluding the LA compliance from the cardiovascular evaluations, or considering an inappropriate compliance in designing MCLs results in contentious outcomes. For instance, in Mouret et al. (2004) the measured in-vitro PVF has a weak correspondence with the in-vivo data due to a defect in the LA compliance.

In this work, to show the importance of the LA compliance and to evaluate its effects on the LH hemodynamics, the same in-vivo measurements were conducted on three chambers with various compliance.

Considering the PVF profiles in Fig. 8.14(A) and the reported indices in Tab. 8.7, as the LA compliance declines, it blunts the systolic wave compared to the diastolic wave. Therefore, the VTI SFF, decreases while VTI DFF increases which shifts the systolic predominance to the diastolic predominance. Moreover, it suppresses the S-peak and amplifies the D-peak which reduces the S/D ratio (Kuecherer et al. 1990; Smiseth et al. 1999). The results confirm the in-vivo findings by Kuecherer et al. (1990) that the degree of the SFF is mainly affected by the LA compliance. Furthermore, the RF dramatically diminishes due to the impaired LA contraction as the LA stiffness increases. An interesting observation is, instead of having RF in the LD phase, a negative flowrate appeared in the late systole. It is inferred that because the MV is closed and the mean LAP increases as the result of low LA compliance, the pressure gradient reverses as the LAP exceeds the pressure in the PVs. It can be explained also in this way that the low LA compliance impairs the LA reservoir function by lowering the level of stored strain energy. Hence, it pushes the flow backward because it cannot accommodate the whole SFF.

The effects of the LA compliance deterioration are also reflected in the LAP_{mean} and the absolute values (Tab. 8.6), and the LAP waveform pattern (Fig. 8.13). As the

LA compliance declines, the LAP_{mean}, a-peak and v-peak rise, and the relaxation time shortens. When the LA stiffness increases, it diminishes the LA contraction, and therefore, it lessens the relaxation time. The lower relaxation time causes the LAP to remain elevated. The elevated LAP diminishes the contribution of the LA in the LV filling, impairs the LA phasic functions, and damages the PVF and the MVF patterns. The abnormal negative late systolic PVF can also be explained by the LAP wave pattern. In the chamber with normal compliance, the LAP gradually increases to the v-peak and remains in the same level until the MV opening. However, in the chambers with low compliance, the pressure increases and then drops before the MV opening. As the MV is closed, the LAP drop is because of that negative late systolic PVF which relieves the pressure of the chamber.

The E-peak of the MVF is ascribed to the LV relaxation, the LV filling pressure and the LA compliance (Nishimura et al. 1990). Because the LV chamber in this work is rigid and the same pulsatile pump piston head waveform was prescribed in all the cases, the reduction in the E-peak (Fig. 8.14(B) and Tab. 8.8) can be explained only by the LA compliance. The LA compliance deterioration not only increases the LAP, but also impairs the LA conduit phase function. Moreover, the A-peak (Fig. 8.14(B) and Tab. 8.8) also reduces due to the impaired LA active pump phase function because of the low LA compliance. The DT (Tab. 8.8) is almost the same between all the chambers because it is attributed to the continued relaxation of the LV, and the LV compliance (Nishimura et al. 1990), however, the LV chamber of the MCL is rigid.

Based on the results obtained from the measurements, it can be concluded that the MCL replicated the physiological performance of the LH. The measured pressure and flowrate data showed that the MCL captured the complex interrelated sequences of the LH events and provided a thorough holistic overview of the LH fluid dynamics information. Moreover, conducting the measurements with various LA compliance provided the opportunity to investigate the impacts of the LA compliance on the LH hemodynamics. The obtained results showed a very good concordance with the reported clinical data.

Part IV

Conclusion

CHAPTER 10

Conclusion

In this work, numerical and experimental studies were conducted to investigate the LA and the MV mechanics and hemodynamics. In the numerical study, using the FEA method, a 2D and 3D simplified coupled LA-MV FSI model, and a 3D realistic LA FSI model were designed. In generating the geometries and the BCs for the simplified and the realistic models, different medical imaging modalities, such as MRI and CT imaging, were employed. One of the strengths of the numerical study is to use physiological BCs and material models in developing the FSI models. Using the 2D simplified model, the MVS pathology, which is a prevalent MV complication, was investigated. The results show that the MVS dramatically alters the dynamics and hemodynamics of the LA and the MV. It elevates the LAP_{mean} and disrupts the LA phasic functions, specifically in the conduit and the active pump function. The calculated mechanical and hemodynamic indices from the 3D simplified and the realistic models show that the models are able to mimic the physiological performance of the LA and the MV in a simplified geometry. This implies that the FEA method can be implemented in generating patient specific models to investigate the physiology and pathology of the cardiac structures.

Because of the intricate interplay between the LH events, having a thorough holistic overview of the LH hemodynamics information is crucial. Therefore, in the experimental study, a LH MCL was designed and developed to investigate the hemodynamics of the LA chamber and its impact on the LH function. Because the LA compliance plays a crucial role in the LH function, a hyperelastic LA chamber was molded with a compliance similar to the porcine LA compliance. Pressure and flow data were measured and evaluated, and the results show that the MCL can replicate the physiological performance of the LH. Interestingly, the measured PVF disclosed that it is mainly controlled by the LH pressure gradient, though the impact of the RV on the PVF cannot be ruled out. Moreover, to investigate the impact of the LA compliance on the LH hemodynamics, different LA chambers with various compliance were molded and employed in the MCL measurements. The outcome shows that the LA stiffening impacts drastically the LAP and amplifies the a-peak and v-peak. Moreover, it alters the PVF by diminishing the SFF and the RF, and amplifying the DFF.

Furthermore, a tensile test was conducted on the material, which was used to cast the LA chambers, to extract the mechanical properties of the Silicone-Elite mixture. The tensile test results show that the material has a nonlinear hyperelastic behavior. Amongst the fitted material models, the Yeoh analytical model showed strong performance in representing the mechanical behavior of the material.

CHAPTER 11

Limitations - Future work

Both the numerical and the experimental studies have several limitations. In the numerical study, first the material model for the LA and the MV do not include the tissue fiber directions, which impact the mechanical behavior of the models. Then, the MV geometry is absent in the 3D realistic model which affect the LA hemodynamics. Moreover, the inlet and the outlet BCs are not taken from the same source which causes desynchronization between the BCs. Furthermore, the applied tension force to mimic the depolarization of the LA chamber is not physiological. Hence, in the future studies, the numerical models can be improved by 1) adding fiber directions to the material models, 2) coupling the MV geometry to the 3D realistic model, 3) using BCs which are taken from the same source, and 4) applying a physiological tension force to mimic the LA contraction function.

Because the experimental study is a novel work, it still holds potential for improvements. First, to prepare the final hyperelastic material, the primary materials should be mixed in a vacuum chamber to eliminate all the air bubbles. As there was not a vacuum mixer in the lab, the final material contained a lot of air bubbles. Second, a mechanical valve was used instead of a prosthetic valve. Third, the working fluid was water instead of blood. Fourth, a simplified LA model was molded which also impact the results. For future works, the author suggest to strengthen the weaknesses by 1) improving the purity of the material using a vacuum mixer to eliminate all the air bubbles, 2) utilizing a bioprosthetic MV instead of a mechanical one, 3) using blood mimicking fluid to increase the accuracy of the hemodynamics measurements, and 4) employing biological LA chambers or casting a realistic LA model.

Part V

Bibliography

References from Chapter 1

Doenst, T., K. Spiegel, M. Reik, M. Markl, J. Hennig, S. Nitzsche, F. Beyersdorf, and H. Oertel (2009). "Fluid dynamic modeling of the human left ventricle: methodology and application to surgical ventricular reconstruction". In: *Annals of thoracic surgery* 87.4, pp. 1187–95 (cit. on p. 4).

Domenichini, F. and G. Pedrizzetti (2015). "Asymptotic model of fluid-tissue interaction for mitral valve dynamics". In: *Cardiovascular engineering and technology* 6.2, pp. 95–104 (cit. on p. 4).

Domenichini, F., G. Pedrizzetti, and B. Baccani (2005). "Three-dimensional filling flow into a model left ventricle". In: *Journal of fluid mechanics* 539, pp. 179–198 (cit. on p. 4).

Finegold, J. A., P. Asaria, and D. P. Francis (2013). "Mortality from ischaemic heart disease by country, region, and age: statistics from World Health Organisation and United Nations". In: *International journal of cardiology* 168.2, pp. 934–945 (cit. on p. 3).

Lantz, J., V. Gupta, L. Henriksson, M. Karlsson, A. Persson, C. Carlhall, and T. Ebbers (2019). "Impact of pulmonary venous inflow on cardiac flow simulations: Comparison with in vivo 4D flow MRI". In: *Annals of biomedical engineering* 47.2, pp. 413–424 (cit. on pp. 3, 4).

Long, Q., R. Merrifield, X. Xu, D. Firmin, et al. (2003). "The influence of inflow boundary conditions on intra left ventricle flow predictions". In: *Journal of biomechanical engineering* 125.6, pp. 922–927 (cit. on p. 4).

Mihalef, V., R. Ionasec, P. Sharma, B. Georgescu, I. Voigt, M. Suehling, and D. Comaniciu (2011). "Patient-specific modelling of whole heart anatomy, dynamics and haemodynamics from four-dimensional cardiac CT images". In: *Interface Focus* 1.3, pp. 286–296 (cit. on pp. 3, 4).

Morris, P. D., A. Narracott, H. von Tengg-Kobligk, D. A. S. Soto, S. Hsiao, A. Lungu, P. Evans, N. W. Bressloff, P. V. Lawford, D. R. Hose, et al. (2016). "Computational fluid dynamics modelling in cardiovascular medicine". In: *Heart* 102.1, pp. 18–28 (cit. on p. 3).

Peirlinck, M., K. L. Sack, P. De Backer, P. Morais, P. Segers, T. Franz, and M. De Beule (2019). "Kinematic boundary conditions substantially impact in silico ventricular function". In: *International journal for numerical methods in biomedical engineering* 35.1, e3151 (cit. on p. 4).

Schenkel, T., M. Malve, M. Reik, M. Markl, B. Jung, and H. Oertel (2009). "MRI-based CFD analysis of flow in a human left ventricle: methodology and application to a healthy heart". In: *Annals of biomedical engineering* 37.3, pp. 503–515 (cit. on p. 4).

Taylor, C. A. and C. A. Figueroa (2009). "Patient-specific modeling of cardiovascular mechanics". In: *Annual review of biomedical engineering* 11, pp. 109–134 (cit. on p. 3).

Turi, Z. G. (2004). "Mitral valve disease". In: *Circulation* 109.6, e38–e41 (cit. on p. 3).

Wilkins, E., L. Wilson, K. Wickramasinghe, P. Bhatnagar, J. Leal, R. Luengo-Fernandez, R. Burns, M. Rayner, and N. Townsend (2017). "European cardiovascular disease statistics 2017". In: *European heart network, Brussels* (cit. on p. 3).

Wong, K. K., D. Wang, J. K. Ko, J. Mazumdar, T. Le, and D. Ghista (2017). "Computational medical imaging and hemodynamics framework for functional analysis and assessment of cardiovascular structures". In: *Biomedical engineering online* 16.1, p. 35 (cit. on p. 3).

References from Chapter 2

Dodson, J. A., T. G. Neilan, R. V. Shah, H. Farhad, R. Blankstein, M. Steigner, G. F. Michaud, R. John, S. A. Abbasi, M. Jerosch-Herold, et al. (2014). "Left atrial passive emptying function determined by cardiac magnetic resonance predicts atrial fibrillation recurrence after pulmonary vein isolation". In: *Circulation: Cardiovascular Imaging* 7.4, pp. 586–592 (cit. on p. 9).

Feng, L., H. Gao, B. Griffith, S. Niederer, and X. Luo (2019). "Analysis of a coupled fluid-structure interaction model of the left atrium and mitral valve". In: *International journal for numerical methods in biomedical engineering* 35.11, e3254 (cit. on p. 10).

Gulati, A., T. F. Ismail, A. Jabbour, N. A. Ismail, K. Morarji, A. Ali, S. Raza, J. Khwaja, T. D. Brown, E. Liodakis, et al. (2013). "Clinical utility and prognostic value of left atrial volume assessment by cardiovascular magnetic resonance in non-ischaemic dilated cardiomyopathy". In: *European journal of heart failure* 15.6, pp. 660–670 (cit. on p. 9).

Keren, G., J. Sherez, R. Megidish, B. Levitt, and S. Laniado (1985). "Pulmonary venous flow pattern-its relationship to cardiac dynamics A pulsed Doppler echocardiographic study". In: *Circulation* 71.6, pp. 1105–1112 (cit. on p. 10).

Lamata, P., R. Casero, V. Carapella, S. A. Niederer, M. J. Bishop, and J. Schneider (2014). "Images as drivers of progress in cardiac computational modelling". In: *Progress in biophysics and molecular biology* 115.2-3, pp. 198–212 (cit. on p. 9).

Lemmon, J.D. and A.P. Yoganathan (2000a). "Computational modeling of left heart diastolic function: examination of ventricular dysfunction". In: *Journal of biomechanical engineering* 122.4, pp. 297–303 (cit. on p. 10).

— (2000b). "Three-dimensional computational model of left heart diastolic function with fluid-structure interaction". In: *Journal of biomechanical engineering* 122.2, pp. 109–117 (cit. on p. 10).

Mao, W., A. Caballero, R. McKay, C. Primiano, and W. Sun (2017). "Fully-coupled fluid-structure interaction simulation of the aortic and mitral valves in a realistic 3D left ventricle model". In: *PloS one* 12.9, e0184729 (cit. on p. 9).

Vellguth, K., J. Bruning, L. Goubergrits, L. Tautz, A. Hennemuth, U. Kertzscher, F. Degener, M. Kelm, S. Sundermann, and T. Kuehne (2018). "Development of a modeling pipeline for the prediction of hemodynamic outcome after virtual mitral valve repair

using image-based CFD". In: *International journal of computer assisted radiology and surgery* 13.11, pp. 1795–1805 (cit. on p. 9).
Wong, K. K., D. Wang, J. K. Ko, J. Mazumdar, T. Le, and D. Ghista (2017). "Computational medical imaging and hemodynamics framework for functional analysis and assessment of cardiovascular structures". In: *Biomedical engineering online* 16.1, p. 35 (cit. on p. 9).
Zhang, L. T. and M. Gay (2008). "Characterizing left atrial appendage functions in sinus rhythm and atrial fibrillation using computational models". In: *Journal of biomechanics* 41.11, pp. 2515–2523 (cit. on p. 10).

References from Chapter 3

Arvidsson, P. M., S. J. Kovacs, J. Töger, R. Borgquist, E. Heiberg, M. Carlsson, and H. Arheden (2016). "Vortex ring behavior provides the epigenetic blueprint for the human heart". In: *Scientific reports* 6.22021 (cit. on p. 34).
Barbero, U. and S. Y. Ho (2017). "Anatomy of the atria". In: *German journal of cardiac pacing and electrophysiology* 28.4, pp. 347–354 (cit. on p. 13).
Barbier, P., S. Solomon, N.B. Schiller, and S.A. Glantz (2000). "Determinants of forward pulmonary vein flow: an open pericardium pig model". In: *Journal of the American college of cardiology* 35.7, pp. 1947–1959 (cit. on pp. 21, 22).
Barbier, P., S.B. Solomon, N.B. Schiller, and S.A. Glantz (1999). "Left atrial relaxation and left ventricular systolic function determine left atrial reservoir function". In: *Circulation* 100.4, pp. 427–436 (cit. on pp. 21, 22).
Basnight, M.A, M.S. Gonzalez, S.C. Kershenovich, and C.P. Appleton (1991). "Pulmonary venous flow velocity: relation to hemodynamics, mitral flow velocity and left atrial volume, and ejection fraction". In: *Journal of the American Society of Echocardiography* 4.6, pp. 547–558 (cit. on p. 13).
Blume, G. G., C. J. Mcleod, M. E. Barnes, J. B. Seward, P. A. Pellikka, P. M. Bastiansen, and T. S. Tsang (2011). "Left atrial function: physiology, assessment, and clinical implications". In: *European journal of echocardiography* 12.6, pp. 421–430 (cit. on p. 13).
Chnafa, C., S. Mendez, and F. Nicoud (2014). "Image-based large-eddy simulation in a realistic left heart". In: *Computers and fluids* 94, pp. 173–187 (cit. on p. 15).
Dahl, S. K., E. Thomassen, L. R. Hellevik, and B. Skallerud (2012). "Impact of pulmonary venous locations on the intra-atrial flow and the mitral valve plane velocity profile". In: *Cardiovascular engineering and technology* 3.3, pp. 269–281 (cit. on p. 21).
DalBianco, J. P. and R. A. Levine (2013). "Anatomy of the mitral valve apparatus: role of 2D and 3D echocardiography". In: *Cardiology clinics* 31.2, pp. 151–164 (cit. on pp. 13, 15).

DiMartino, E. S., C. Bellini, and D. S. Schwartzma (2011). “In vivo porcine left atrial wall stress: computational model”. In: *Journal of biomechanics* 44.15, pp. 2589–2594 (cit. on pp. 23, 24).

Feng, L., H. Gao, B. Griffith, S. Niederer, and X. Luo (2019). “Analysis of a coupled fluid-structure interaction model of the left atrium and mitral valve”. In: *International journal for numerical methods in biomedical engineering* 35.11, e3254 (cit. on p. 23).

Fyrenius, A., L. Wigstrom, T. Ebbers, M. Karlsson, J. Engvall, and A.F. Bolger (2001). “Three dimensional flow in the human left atrium”. In: *Heart* 86.4, pp. 448–455 (cit. on p. 34).

Gaeta, S., P. Dyverfeldt, J. Eriksson, and Carlhall (2018). “Fixed volume particle trace emission for the analysis of left atrial blood flow using 4D Flow MRI”. In: *Magnetic resonance imaging* 47, pp. 83–88 (cit. on p. 34).

Gogoladze, G., S.L. Dellis, R. Donnino, G. Ribakove, D.G. Greenhouse, A. Galloway, and E. Grossi (2010). “Analysis of the mitral coaptation zone in normal and functional regurgitant valves”. In: *The Annals of thoracic surgery* 89.4, pp. 1158–1161 (cit. on p. 18).

Hassaballah, A.I., M.A. Hassan, A.N. Mardi, and M. Hamdi (2013). “An inverse finite element method for determining the tissue compressibility of human left ventricular wall during the cardiac cycle”. In: *Plos one* 8.12, e82703 (cit. on p. 19).

Hazan, O., L. Sternik, D. Waiss, M. Eldar, O. Hoffer, O. Goitein, R. Kuperstein, E. Konen, and Z. OvadiaBlechman (2018). “An innovative appendage invagination procedure to reduce thrombus formation-a numerical model”. In: *Computer methods in biomechanics and biomedical engineering* 21.4, pp. 370–378 (cit. on pp. 19, 21).

Hellevik, L. R., P. Segers, N. Stergiopulos, F. Irgens, P. Verdonck, C. R. Thompson, K. Lo, R. T. Miyagishima, and O. A. Smiseth (1999). “Mechanism of pulmonary venous pressure and flow waves”. In: *Heart and vessels* 14.2, pp. 67–71 (cit. on pp. 21, 22).

Henein, M. Y. (2012). *Clinical echocardiography*. Ed. by M. Y. Henein. 2nd ed. Springer, London (cit. on p. 15).

Hoit, B. D. (2017). “Evaluation of left atrial function: current status”. In: *Structural heart* 1.3-4, pp. 109–120 (cit. on p. 34).

Jarvinen, V., M. Kupari, P. Hekali, and V.P. Poutanen (1994). “Assessment of left atrial volumes and phasic function using cine magnetic resonance imaging in normal subjects”. In: *The American journal of cardiology* 73.15, pp. 1135–1138 (cit. on p. 15).

Jensen, J. A. (2013). *Estimation of blood velocities using ultrasound: A signal processing approach*. 3rd ed. Cambridge University Press (cit. on pp. 20, 24).

Kheradvar, A. and G. Pedrizzetti (2012). “Vortex formation in the heart”. In: *Vortex formation in the cardiovascular system*. Springer (cit. on pp. 17, 27, 34).

Kuecherer, H. F., I. A. Muhiudeen, F. M. Kusumoto, E. Lee, L. E. Moulinier, M. K. Cahalan, and N. B. Schiller (1990). “Estimation of mean left atrial pressure from transesophageal pulsed Doppler echocardiography of pulmonary venous flow”. In: *Circulation* 82.4, pp. 1127–1139 (cit. on p. 13).

Lau, K., V. Diaz, P. Scambler, and G. Burriesci (2010). “Mitral valve dynamics in structural and fluid-structure interaction models”. In: *Medical engineering and physics* 32.9, pp. 1057–1064 (cit. on p. 24).

Lemmon, J.D. and A.P. Yoganathan (2000a). “Computational modeling of left heart diastolic function: examination of ventricular dysfunction”. In: *Journal of biomechanical engineering* 122.4, pp. 297–303 (cit. on p. 23).

— (2000b). “Three-dimensional computational model of left heart diastolic function with fluid-structure interaction”. In: *Journal of biomechanical engineering* 122.2, pp. 109–117 (cit. on pp. 19, 23).

Lintermann, A. (2021). “Computational meshing for CFD simulations”. In: *Clinical and biomedical engineering in the human nose: A computational fluid dynamics approach*. Springer Singapore (cit. on pp. 25, 26).

May-Newman, K. and F. Yin (1995). “Biaxial mechanical behavior of excised porcine mitral valve leaflets”. In: *American journal of physiology-heart and circulatory physiology* 269.4, H1319–H1327 (cit. on p. 24).

— (1998). “A constitutive law for mitral valve tissue”. In: *Journal of biomechanical engineering* 120.1, pp. 38–47 (cit. on p. 24).

Nishimura, R. A. and A. J. Tajik (1997). “Evaluation of diastolic filling of left ventricle in health and disease: Doppler echocardiography is the clinician Rosetta Stone”. In: *Journals of the American college of cardiology* 30.1, pp. 8–18 (cit. on p. 21).

Pan, F. Dal, G. Donzella, C. Fucci, and M. Schreiber (2005). “Structural effects of an innovative surgical technique to repair heart valve defects”. In: *Journal of biomechanics* 38.12, pp. 2460–2471 (cit. on p. 18).

Pibarot, P. and J. G. Dumesnil (2000). “Hemodynamic and clinical impact of prosthesis–patient mismatch in the aortic valve position and its prevention”. In: *Journal of the American College of Cardiology* 36.4, pp. 1131–1141 (cit. on p. 24).

Rajagopalan, B., C. D. Bertram, T. Stallard, and G. DE J. Lee (1979). “Blood flow in pulmonary veins: III Simultaneous measurements of their dimensions, intravascular pressure and flow”. In: *Cardiovascular research* 13.12, pp. 684–692 (cit. on pp. 19, 21).

Roudaut, R., K. Serri, and S. Lafitte (2007). “Thrombosis of prosthetic heart valves: diagnosis and therapeutic considerations”. In: *Heart* 93.1, pp. 137–142 (cit. on p. 24).

Sahasakul, Y., W.D. Edwards, J.M. Naessens, and A.J. Tajik (1988). “Age-related changes in aortic and mitral valve thickness: implications for two-dimensional echocardiography based on an autopsy study of 200 normal human hearts”. In: *The American journal of cardiology* 62.7, pp. 424–430 (cit. on p. 18).

Schwartzman, D., J. Lacomis, and W. G. Wigginton (2003). “Characterization of left atrium and distal pulmonary vein morphology using multidimensional computed tomography”. In: *Journal of the American College of Cardiology* 41.8, pp. 1349–1357 (cit. on p. 13).

Truskey, G. A., F. Yuan, and D. F. Katz (2004). *Transport Phenomena in Biological Systems*. Pearson Education, Inc., Pearson Prentice Hall (cit. on pp. 24, 25).

Tu, J., K. Inthavong, and K. K. L. Wong (2015). *Computational hemodynamics - Theory, modelling and applications*. Springer Netherlands (cit. on pp. 25, 26).

Votta, E., F. Maisano, S. F. Bolling, O. Alfieri, F. M. Montevecchi, and A. Redaelli (2007). "The geoform disease-specific annuloplasty system: a finite element study". In: *The annals of thoracic surgery* 84.1, pp. 92–101 (cit. on p. 24).

Whitaker, J., R. Rajani, H. Chubb, M. Gabrawi, M. Varela, M. Wright, S. Niederer, and M. D. ONeill (2016). "The role of myocardial wall thickness in atrial arrhythmogenesis". In: *EP Europace* 18.12, pp. 1758–1772 (cit. on p. 15).

Zhang, L. T. and M. Gay (2008). "Characterizing left atrial appendage functions in sinus rhythm and atrial fibrillation using computational models". In: *Journal of biomechanics* 41.11, pp. 2515–2523 (cit. on pp. 19, 21, 22).

References from Chapter 4

Arvidsson, P. M., J. Toger, E. Heiberg, M. Carlsson, and H. Arheden (2013). "Quantification of left and right atrial kinetic energy using four-dimensional intracardiac magnetic resonance imaging flow measurements". In: *Journal of applied physiology* 114.10, pp. 1472–1481 (cit. on pp. 52–54, 68).

Barbier, P., S.B. Solomon, N.B. Schiller, and S.A. Glantz (1999). "Left atrial relaxation and left ventricular systolic function determine left atrial reservoir function". In: *Circulation* 100.4, pp. 427–436 (cit. on pp. 46, 48, 66).

Blume, G. G., C. J. Mcleod, M. E. Barnes, J. B. Seward, P. A. Pellikka, P. M. Bastiansen, and T. S. Tsang (2011). "Left atrial function: physiology, assessment, and clinical implications". In: *European journal of echocardiography* 12.6, pp. 421–430 (cit. on pp. 43, 46, 48, 66).

Dernellis, J. M., C. I. Stefanadis, A. A. Zacharoulis, and P. K. Toutouzas (1998). "Left atrial mechanical adaptation to long-standing hemodynamic loads based on pressure–volume relations". In: *The American journal of cardiology* 81.9, pp. 1138–1143 (cit. on pp. 46, 48, 66).

Feng, L., H. Gao, B. Griffith, S. Niederer, and X. Luo (2019). "Analysis of a coupled fluid-structure interaction model of the left atrium and mitral valve". In: *International journal for numerical methods in biomedical engineering* 35.11, e3254 (cit. on p. 58).

Grant, C., I. L. Bunnell, and D. G. Greene (1964). "The reservoir function of the left atrium during ventricular systole: an angiocardiographic study of atrial stroke volume and work". In: *The American journal of medicine* 37.1, pp. 36–43 (cit. on pp. 46, 48, 66).

Hoit, B. D. (2017). "Evaluation of left atrial function: current status". In: *Structural heart* 1.3-4, pp. 109–120 (cit. on pp. 46, 48, 66).

Jarvinen, V., M. Kupari, P. Hekali, and V.P. Poutanen (1994). "Assessment of left atrial volumes and phasic function using cine magnetic resonance imaging in normal sub-

jects". In: *The American journal of cardiology* 73.15, pp. 1135–1138 (cit. on pp. 43, 45, 46, 66).
Kebed, K. Y., K. Addetia, and R. M. Lang (2019). "Importance of the left atrium: more than a bystander?" In: *Heart failure clinics* 15.2, pp. 191–204 (cit. on pp. 46, 48, 66).
Keren, G., J.S. Meisner, J. Sherez, E.L. Yellin, and S. Laniado (1986). "Interrelationship of mid-diastolic mitral valve motion, pulmonary venous flow, and transmitral flow". In: *Circulation* 74.1, pp. 36–44 (cit. on pp. 48, 50).
Kerut, E. K. (2008). "The mitral L-wave: a relatively common but ignored useful finding: CME". In: *Echocardiography* 25.5, pp. 548–550 (cit. on pp. 49, 50).
Matsuda, Y., Y. Toma, H. Ogawa, M. Matsuzaki, K. Katayama, T. Fujii, F. Yoshino, K. M., T. Kumada, and R. Kusukawa (1983). "Importance of left atrial function in patients with myocardial infarction." In: *Circulation* 67.3, pp. 566–571 (cit. on pp. 46, 48, 66).
McGann, C., N. Akoum, A. Patel, E. Kholmovski, P. Revelo, K. Damal, B. Wilson, J. Cates, A. Harrison, R. . Ranjan, et al. (2014). "Atrial fibrillation ablation outcome is predicted by left atrial remodeling on MRI". In: *Circulation: Arrhythmia and Electrophysiology* 7.1, pp. 23–30 (cit. on p. 43).
Nagueh, S. F. (2018). "Non-invasive assessment of left ventricular filling pressure". In: *European journal of heart failure* 20.1, pp. 38–48 (cit. on p. 50).
Nishimura, A., M.D. Abel, L.K. Hatle, and A.J. Tajik (1990). "Relation of pulmonary vein to mitral flow velocities by transesophageal Doppler echocardiography - Effect of different loading conditions". In: *Circulation* 81.5, pp. 1488–1497 (cit. on pp. 50, 67).
Patel, D. A., C. J. Lavie, R. V. Milani, S. Shah, and Y. Gilliland (2009). "Clinical implications of left atrial enlargement: a review". In: *Ochsner Journal* 9.4, pp. 191–196 (cit. on p. 43).
Reda, A. A., M. A. Soliman, M. K. Ahmed, R. S. Abd El-Ghani, et al. (2015). "Assessment of left atrial function in patients with systolic heart failure: strain imaging study". In: *Menoufia medical journal* 28.2, p. 532 (cit. on pp. 46, 66).
Stefanadis, C., J. Dernellis, S. Lambrou, and P. Toutouzas (1998). "Left atrial energy in normal subjects, in patients with symptomatic mitral stenosis, and in patients with advanced heart failure". In: *The American journal of cardiology* 82.10, pp. 1220–1223 (cit. on pp. 46, 47, 66).
Zipes, D. P., P. Libby, R. O. Bonow, D. L. Mann, G. F. Tomaselli, and E. Braunwald (2019). *Braunwald's Heart Disease: A Textbook of Cardiovascular Medicine*. 11th ed. Elsevier Inc. (cit. on pp. 43, 44, 50, 64, 65, 67).

References from Chapter 5

Arvidsson, P. M., S. J. Kovacs, J. Töger, R. Borgquist, E. Heiberg, M. Carlsson, and H. Arheden (2016). "Vortex ring behavior provides the epigenetic blueprint for the human heart". In: *Scientific reports* 6.22021 (cit. on p. 77).

Dernellis, J. M., C. I. Stefanadis, A. A. Zacharoulis, and P. K. Toutouzas (1998). “Left atrial mechanical adaptation to long-standing hemodynamic loads based on pressure–volume relations”. In: *The American journal of cardiology* 81.9, pp. 1138–1143 (cit. on p. 76).

Eshoo, S., D. L. Ross, and L. Thomas (2009). “Impact of mild hypertension on left atrial size and function”. In: *Circulation: Cardiovascular Imaging* 2.2, pp. 93–99 (cit. on p. 77).

Feng, L., H. Gao, B. Griffith, S. Niederer, and X. Luo (2019). “Analysis of a coupled fluid-structure interaction model of the left atrium and mitral valve”. In: *International journal for numerical methods in biomedical engineering* 35.11, e3254 (cit. on pp. 77, 78).

Fyrenius, A., L. Wigstrom, T. Ebbers, M. Karlsson, J. Engvall, and A.F. Bolger (2001). “Three dimensional flow in the human left atrium”. In: *Heart* 86.4, pp. 448–455 (cit. on p. 77).

Grant, C., I. L. Bunnell, and D. G. Greene (1964). “The reservoir function of the left atrium during ventricular systole: an angiocardiographic study of atrial stroke volume and work”. In: *The American journal of medicine* 37.1, pp. 36–43 (cit. on p. 76).

Hoit, B. D. (2017). “Evaluation of left atrial function: current status”. In: *Structural heart* 1.3-4, pp. 109–120 (cit. on p. 76).

Keren, G., J.S. Meisner, J. Sherez, E.L. Yellin, and S. Laniado (1986). “Interrelationship of mid-diastolic mitral valve motion, pulmonary venous flow, and transmitral flow”. In: *Circulation* 74.1, pp. 36–44 (cit. on p. 76).

Keren, G., J. Sherez, R. Megidish, B. Levitt, and S. Laniado (1985). “Pulmonary venous flow pattern-its relationship to cardiac dynamics A pulsed Doppler echocardiographic study”. In: *Circulation* 71.6, pp. 1105–1112 (cit. on p. 76).

Li, R., C. Luo, Y. Ho, S. Lee, and Y. Kuan (2019). “Heart valve operations associated with reduced risk of death from mitral valve disease but other operations associated with increased risk of death: a national population-based case–control study”. In: *Journal of Cardiothoracic Surgery* 14.1, pp. 1–8 (cit. on p. 75).

Nagueh, S. F. (2018). “Non-invasive assessment of left ventricular filling pressure”. In: *European journal of heart failure* 20.1, pp. 38–48 (cit. on p. 76).

Papaioannou, T.G. and C. Stefanadis (2005). “Vascular wall shear stress: basic principles and methods”. In: *Hellenic journal of cardiology* 46.1, pp. 9–15 (cit. on p. 76).

Vaziri, S. M., M. G. Larson, M. S. Lauer, E. J. Benjamin, and D. Levy (1995). “Influence of blood pressure on left atrial size: The Framingham heart study”. In: *Hypertension* 25.6, pp. 1155–1160 (cit. on p. 77).

Zipes, D. P., P. Libby, R. O. Bonow, D. L. Mann, G. F. Tomaselli, and E. Braunwald (2019). *Braunwald’s Heart Disease: A Textbook of Cardiovascular Medicine*. 11th ed. Elsevier Inc. (cit. on p. 76).

References from Chapter 6

Akutsu, T. and T. Masuda (2003). "Three-dimensional flow analysis of a mechanical bileaflet mitral prosthesis". In: *Journal of Artificial Organs* 6.2, pp. 112–123 (cit. on p. 82).

Balducci, A., M. Grigioni, G. Querzoli, G.P. Romano, C. Daniele, G. DAvenio, and V. Barbaro (2004). "Investigation of the flow field downstream of an artificial heart valve by means of PIV and PTV". In: *Experiments in fluids* 36.1, pp. 204–213 (cit. on p. 82).

Barbier, P., S. Solomon, N.B. Schiller, and S.A. Glantz (2000). "Determinants of forward pulmonary vein flow: an open pericardium pig model". In: *Journal of the American college of cardiology* 35.7, pp. 1947–1959 (cit. on p. 81).

Barbier, P., S.B. Solomon, N.B. Schiller, and S.A. Glantz (1999). "Left atrial relaxation and left ventricular systolic function determine left atrial reservoir function". In: *Circulation* 100.4, pp. 427–436 (cit. on pp. 81, 82).

Basnight, M.A, M.S. Gonzalez, S.C. Kershenovich, and C.P. Appleton (1991). "Pulmonary venous flow velocity: relation to hemodynamics, mitral flow velocity and left atrial volume, and ejection fraction". In: *Journal of the American Society of Echocardiography* 4.6, pp. 547–558 (cit. on p. 81).

Blume, G. G., C. J. Mcleod, M. E. Barnes, J. B. Seward, P. A. Pellikka, P. M. Bastiansen, and T. S. Tsang (2011). "Left atrial function: physiology, assessment, and clinical implications". In: *European journal of echocardiography* 12.6, pp. 421–430 (cit. on p. 81).

Cenedese, A., Z. Del Prete, M. Miozzi, and G. Querzoli (2005). "A laboratory investigation of the flow in the left ventricle of a human heart with prosthetic, tilting-disk valves". In: *Experiments in Fluids* 39.2, pp. 322–335 (cit. on p. 82).

Chao, T. H., L. M. Tsai, W. C. Tsai, Y. H. Li, L. J. Lin, and J. H. Chen (2000). "Effect of atrial fibrillation on pulmonary venous flow patterns assessed by Doppler transesophageal echocardiography". In: *Chest* 117.6, pp. 1546–1550 (cit. on p. 81).

Dimasi, A., D. Piloni, L. Spreafico, E. Votta, R. Vismara, G.B. Fiore, M. Meskin, L. Fusini, M. Muratori, P. Montorsi, et al. (2019). "Fluid-Structure Interaction and In Vitro Analysis of a Real Bileaflet Mitral Prosthetic Valve to Gain Insight Into Doppler-Silent Thrombosis". In: *Journal of biomechanical engineering* 141.10, BIO-18–1058 (cit. on p. 82).

Dodson, J. A., T. G. Neilan, R. V. Shah, H. Farhad, R. Blankstein, M. Steigner, G. F. Michaud, R. John, S. A. Abbasi, M. Jerosch-Herold, et al. (2014). "Left atrial passive emptying function determined by cardiac magnetic resonance predicts atrial fibrillation recurrence after pulmonary vein isolation". In: *Circulation: Cardiovascular Imaging* 7.4, pp. 586–592 (cit. on p. 81).

Gulan, U., A. Saguner, D. Akdis, A. Gotschy, R. Manka, C. Bruncknorst, M. Holzner, and F. Duru (2017). "Investigation of atrial vortices using a novel right heart model and possible implications for atrial thrombus formation". In: *Scientific reports* 7.1, pp. 1–10 (cit. on p. 82).

Gulati, A., T. F. Ismail, A. Jabbour, N. A. Ismail, K. Morarji, A. Ali, S. Raza, J. Khwaja, T. D. Brown, E. Liodakis, et al. (2013). "Clinical utility and prognostic value of left atrial volume assessment by cardiovascular magnetic resonance in non-ischaemic dilated cardiomyopathy". In: *European journal of heart failure* 15.6, pp. 660–670 (cit. on p. 81).

Hellevik, L. R., P. Segers, N. Stergiopulos, F. Irgens, P. Verdonck, C. R. Thompson, K. Lo, R. T. Miyagishima, and O. A. Smiseth (1999). "Mechanism of pulmonary venous pressure and flow waves". In: *Heart and vessels* 14.2, pp. 67–71 (cit. on pp. 81, 82).

Ho, S. Y., J. A. Cabrera, and D. S. (2012). "Left atrial anatomy revisited". In: *Circulation: Arrhythmia and Electrophysiology* 5.1, pp. 220–228 (cit. on p. 82).

Hollander, E.H., G.M. Dobson, J.J. Wang, K.H. Parker, and J.V. Tyberg (2004). "Direct and series transmission of left atrial pressure perturbations to the pulmonary artery: a study using wave-intensity analysis". In: *American Journal of Physiology-Heart and Circulatory Physiology* 286.1, H267–H275 (cit. on p. 81).

Kadem, L., Y. Knapp, P. Pibarot, E. Bertrand, D. Garcia, L. G. Durand, and R. Rieu (2005). "A new experimental method for the determination of the effective orifice area based on the acoustical source term". In: *Experiments in Fluids* 39.6, pp. 1051–1060 (cit. on p. 82).

Keren, G., J.S. Meisner, J. Sherez, E.L. Yellin, and S. Laniado (1986). "Interrelationship of mid-diastolic mitral valve motion, pulmonary venous flow, and transmitral flow". In: *Circulation* 74.1, pp. 36–44 (cit. on p. 81).

Keren, G., J. Sherez, R. Megidish, B. Levitt, and S. Laniado (1985). "Pulmonary venous flow pattern-its relationship to cardiac dynamics A pulsed Doppler echocardiographic study". In: *Circulation* 71.6, pp. 1105–1112 (cit. on p. 81).

Kini, V., C. Bachmann, A. Fontaine, S. Deutsch, and J.M. Tarbell (2001). "Integrating particle image velocimetry and laser Doppler velocimetry measurements of the regurgitant flow field past mechanical heart valves". In: *Artificial organs* 25.2, pp. 136–145 (cit. on p. 82).

Kuecherer, H. F., I. A. Muhiudeen, F. M. Kusumoto, E. Lee, L. E. Moulinier, M. K. Cahalan, and N. B. Schiller (1990). "Estimation of mean left atrial pressure from transesophageal pulsed Doppler echocardiography of pulmonary venous flow". In: *Circulation* 82.4, pp. 1127–1139 (cit. on pp. 81, 82).

Kuhl, J.T., J. Lonborg, A. Fuchs, M.J. Andersen, N. Vejlstrup, H. Kelbak, T. Engstrom, J.E. Moller, and K.F. Kofoed (2012). "Assessment of left atrial volume and function: a comparative study between echocardiography, magnetic resonance imaging and multi slice computed tomography". In: *The international journal of cardiovascular imaging* 28.5, pp. 1061–1071 (cit. on p. 81).

Leopaldi, A.M., R. Vismara, M. Lemma, L. Valerio, M. Cervo, A. Mangini, M. Contino, A. Redaelli, C. Antona, and G.B. Fiore (2012). "In vitro hemodynamics and valve imaging in passive beating hearts". In: *Journal of biomechanics* 45.7, pp. 1133–1139 (cit. on p. 82).

Leopaldi, A.M., R. Vismara, S. Van Tuijl, A. Redaelli, F.N. van de Vosse, G.B. Fiore, and M.C.M. Rutten (2015). "A novel passive left heart platform for device testing and research". In: *Medical engineering & physics* 37.4, pp. 361–366 (cit. on p. 82).

Marassi, M., P. Castellini, M. Pinotti, and L. Scalise (2004). "Cardiac valve prosthesis flow performances measured by 2D and 3D-stereo particle image velocimetry". In: *Experiments in Fluids* 36.1, pp. 176–186 (cit. on p. 82).

Maron, B. J., T. S. Haas, M. S. Maron, J. R. Lesser, J. A. Browning, R. H. Chan, I. Olivotto, R. F. Garberich, and R. S. Schwartz (2014). "Left atrial remodeling in hypertrophic cardiomyopathy and susceptibility markers for atrial fibrillation identified by cardiovascular magnetic resonance". In: *The American journal of cardiology* 113.8, pp. 1394–1400 (cit. on p. 81).

Matsuda, Y., Y. Toma, H. Ogawa, M. Matsuzaki, K. Katayama, T. Fujii, F. Yoshino, K. M., T. Kumada, and R. Kusukawa (1983). "Importance of left atrial function in patients with myocardial infarction." In: *Circulation* 67.3, pp. 566–571 (cit. on p. 81).

McGann, C., N. Akoum, A. Patel, E. Kholmovski, P. Revelo, K. Damal, B. Wilson, J. Cates, A. Harrison, R. . Ranjan, et al. (2014). "Atrial fibrillation ablation outcome is predicted by left atrial remodeling on MRI". In: *Circulation: Arrhythmia and Electrophysiology* 7.1, pp. 23–30 (cit. on p. 81).

Meskin, M., A. Dimasi, E. V., M. Jaworek, L. Fusini, M. Muratori, P. Montorsi, E. Zappa, I. Epifani, M. Pepi, et al. (2019). "A Novel Multiparametric Score for the Detection and Grading of Prosthetic Mitral Valve Obstruction in Cases With Different Disc Motion Abnormalities". In: *Ultrasound in medicine and biology* 45.7, pp. 1708–1720 (cit. on p. 82).

Morsi, Y.S. and A.A. Sakhaeimanesh (2000). "Flow characteristics past jellyfish and St. Vincent valves in the aortic position under physiological pulsatile flow conditions". In: *Artificial organs* 24.7, pp. 564–574 (cit. on p. 82).

Mouret, F., V. Garitey, E. Bertrand, F. Derivaux, J. Fuseri, and R. Regis (2004). "In vitro atrial flow dynamics: normal conditions versus atrial fibrillation". In: *Journal of biomechanics* 37.11, pp. 1749–1755 (cit. on p. 82).

Nagueh, S. F. (2018). "Non-invasive assessment of left ventricular filling pressure". In: *European journal of heart failure* 20.1, pp. 38–48 (cit. on p. 81).

— (2020). "Left ventricular diastolic function: understanding pathophysiology, diagnosis, and prognosis with echocardiography". In: *JACC: Cardiovascular Imaging* 13.1 Part 2, pp. 228–244 (cit. on p. 81).

Nishimura, A., M.D. Abel, L.K. Hatle, and A.J. Tajik (1990). "Relation of pulmonary vein to mitral flow velocities by transesophageal Doppler echocardiography - Effect of different loading conditions". In: *Circulation* 81.5, pp. 1488–1497 (cit. on p. 81).

Pierrakos, O., P.P. Vlachos, and D.P. Telionis (2004). "Time-resolved DPIV analysis of vortex dynamics in a left ventricular model through bileaflet mechanical and porcine heart valve prostheses". In: *J. Biomech. Eng.* 126.6, pp. 714–726 (cit. on p. 82).

Rasmussen, J., S. N. Skov, D. B. Nielsen, I. L. Jensen, M. J. Tjornild, P. Johansen, and V. E. Hjortdal (2019). "In-vitro and in-vivo evaluation of a novel bioprosthetic pulmonary

valve for use in congenital heart surgery". In: *Journal of cardiothoracic surgery* 14.1, pp. 1–6 (cit. on p. 82).

Reul, H., N. Talukder, E.W. Mu, et al. (1981). "Fluid mechanics of the natural mitral valve". In: *Journal of biomechanics* 14.5, pp. 361–372 (cit. on p. 82).

Rosca, M., P. Lancellotti, B.A. Popescu, and L.A. Pierard (2011). "Left atrial function: pathophysiology, echocardiographic assessment, and clinical applications". In: *Heart* 97.23, pp. 1982–1989 (cit. on p. 81).

Sharghbin, M., L. L. Benhassen, T. Lading, T. Bechsgaard, S. N. Skov, D. M. Ropcke, S. L. Nielsen, J. M. Hasenkam, and P. Johansen (2018). "Comparison of the Dacron ring and suture annuloplasty for aortic root repair: an in vitro evaluation". In: *Interactive cardiovascular and thoracic surgery* 27.6, pp. 819–827 (cit. on p. 82).

Smiseth, O. A., C. R. Thompson, K. L. Lohavanichbutr, H. Ling, J. G. Abel, R. T. Miyagishima, S. V. Lichtenstein, and J. Bowering (1999). "The pulmonary venous systolic flow pulse - its origin and relationship to left atrial pressure". In: *Journal of the American college of Cardiology* 34.3, pp. 802–809 (cit. on p. 81).

Steen, T. and S. Steen (1994). "Filling of a model left ventricle studied by colour M mode Doppler". In: *Cardiovascular research* 28.12, pp. 1821–1827 (cit. on p. 82).

Tanne, D., E. Bertrand, L. Kadem, P. Pibarot, and R. Rieu (May 2009). "Assessment of left heart and pulmonary circulation flow dynamics by a new pulsed mock circulatory system". In: *Experiments in Fluids* 48, pp. 837–850 (cit. on p. 82).

Thomsen, A.F., J.T. Kuhl, K.F. Kofoed, A. Fuchs, P.M. Udholm, et al. (2017). "Left Atrial Wall Thickness and Pulmonary Vein Size are Increased in Patients with Atrial Fibrillation Compared to Healthy Con-trols-A Multidetector Computed Tomography Study". In: *Int J Clin Cardiol* 4, p. 098 (cit. on p. 81).

Vismara, R., G.B. Fiore, A. Mangini, M. Contino, M. Lemma, A. Redaelli, and C. Antona (2010). "A novel approach to the in vitro hydrodynamic study of the aortic valve: mock loop development and test". In: *Asaio Journal* 56.4, pp. 279–284 (cit. on p. 82).

Vismara, R., A. Pavesi, E. Votta, M. Taramasso, F. Maisano, and G.B. Fiore (2011). "A pulsatile simulator for the in vitro analysis of the mitral valve with tri-axial papillary muscle displacement". In: *The International journal of artificial organs* 34.4, pp. 383–391 (cit. on p. 82).

Whitaker, J., R. Rajani, H. Chubb, M. Gabrawi, M. Varela, M. Wright, S. Niederer, and M. D. ONeill (2016). "The role of myocardial wall thickness in atrial arrhythmogenesis". In: *EP Europace* 18.12, pp. 1758–1772 (cit. on p. 82).

References from Chapter 7

Barbier, P., S.B. Solomon, N.B. Schiller, and S.A. Glantz (1999). "Left atrial relaxation and left ventricular systolic function determine left atrial reservoir function". In: *Circulation* 100.4, pp. 427–436 (cit. on p. 91).

Chnafa, C., S. Mendez, and F. Nicoud (2014). “Image-based large-eddy simulation in a realistic left heart”. In: *Computers and fluids* 94, pp. 173–187 (cit. on p. 87).

Erman, B. and J.E. Mark (1997). *Structures and properties of rubberlike networks*. Oxford University Press (cit. on p. 92).

Jarvinen, V., M. Kupari, P. Hekali, and V.P. Poutanen (1994). “Assessment of left atrial volumes and phasic function using cine magnetic resonance imaging in normal subjects”. In: *The American journal of cardiology* 73.15, pp. 1135–1138 (cit. on p. 87).

Jernigan, S.R., G.D. Buckner, J.W. Eischen, and D.R. Cormier (2007). “Finite element modeling of the left atrium to facilitate the design of an endoscopic atrial retractor”. In: *J Biomech Eng.* 129.6, pp. 825–837 (cit. on p. 91).

Keren, G., J. Sherez, R. Megidish, B. Levitt, and S. Laniado (1985). “Pulmonary venous flow pattern-its relationship to cardiac dynamics A pulsed Doppler echocardiographic study”. In: *Circulation* 71.6, pp. 1105–1112 (cit. on p. 95).

Levenberg, K. (1944). “A method for the solution of certain non-linear problems in least squares”. In: *Quarterly of applied mathematics* 2.2, pp. 164–168 (cit. on p. 92).

Marquardt, D. W. (1963). “An algorithm for least-squares estimation of nonlinear parameters”. In: *Journal of the society for Industrial and Applied Mathematics* 11.2, pp. 431–441 (cit. on p. 92).

Martins, P.A.L.S., R.M. Natal Jorge, and A.J.M. Ferreira (2006). “A comparative study of several material models for prediction of hyperelastic properties: Application to silicone-rubber and soft tissues”. In: *Strain* 42.3, pp. 135–147 (cit. on pp. 92, 94).

Rasmussen, J., S. N. Skov, D. B. Nielsen, I. L. Jensen, M. J. Tjornild, P. Johansen, and V. E. Hjortdal (2019). “In-vitro and in-vivo evaluation of a novel bioprosthetic pulmonary valve for use in congenital heart surgery”. In: *Journal of cardiothoracic surgery* 14.1, pp. 1–6 (cit. on p. 94).

Sharghbin, M., L. L. Benhassen, T. Lading, T. Bechsgaard, S. N. Skov, D. M. Ropcke, S. L. Nielsen, J. M. Hasenkam, and P. Johansen (2018). “Comparison of the Dacron ring and suture annuloplasty for aortic root repair: an in vitro evaluation”. In: *Interactive cardiovascular and thoracic surgery* 27.6, pp. 819–827 (cit. on p. 94).

Whitaker, J., R. Rajani, H. Chubb, M. Gabrawi, M. Varela, M. Wright, S. Niederer, and M. D. ONeill (2016). “The role of myocardial wall thickness in atrial arrhythmogenesis”. In: *EP Europace* 18.12, pp. 1758–1772 (cit. on p. 87).

Zhang, L. T. and M. Gay (2008). “Characterizing left atrial appendage functions in sinus rhythm and atrial fibrillation using computational models”. In: *Journal of biomechanics* 41.11, pp. 2515–2523 (cit. on p. 87).

References from Chapter 8

Barbier, P., S. Solomon, N.B. Schiller, and S.A. Glantz (2000). “Determinants of forward pulmonary vein flow: an open pericardium pig model”. In: *Journal of the American college of cardiology* 35.7, pp. 1947–1959 (cit. on pp. 108, 116).

Barbier, P., S.B. Solomon, N.B. Schiller, and S.A. Glantz (1999). “Left atrial relaxation and left ventricular systolic function determine left atrial reservoir function”. In: *Circulation* 100.4, pp. 427–436 (cit. on p. 115).

Bonow, R. O., D. L. Mann, D. P. Zipes, and P. Libby (2011). *Braunwald’s heart disease e-book: A textbook of cardiovascular medicine*. Elsevier Health Sciences (cit. on pp. 115, 116).

Bukachi, F., A. Waldenstrom, S. Morner, P. Lindqvist, M. Y. Henein, and E. Kazzam (2005). “Pulmonary venous flow reversal and its relationship to atrial mechanical function in normal subjects-Umea General Population Heart Study”. In: *European Journal of Echocardiography* 6.2, pp. 107–116 (cit. on p. 108).

Chao, T. H., L. M. Tsai, W. C. Tsai, Y. H. Li, L. J. Lin, and J. H. Chen (2000). “Effect of atrial fibrillation on pulmonary venous flow patterns assessed by Doppler transesophageal echocardiography”. In: *Chest* 117.6, pp. 1546–1550 (cit. on p. 108).

Hellevik, L. R., P. Segers, N. Stergiopulos, F. Irgens, P. Verdonck, C. R. Thompson, K. Lo, R. T. Miyagishima, and O. A. Smiseth (1999). “Mechanism of pulmonary venous pressure and flow waves”. In: *Heart and vessels* 14.2, pp. 67–71 (cit. on p. 108).

Humphrey, J. D. (2013). *Cardiovascular solid mechanics: cells, tissues, and organs*. Springer Science
Business Media (cit. on p. 104).

Keren, G., J.S. Meisner, J. Sherez, E.L. Yellin, and S. Laniado (1986). “Interrelationship of mid-diastolic mitral valve motion, pulmonary venous flow, and transmitral flow”. In: *Circulation* 74.1, pp. 36–44 (cit. on pp. 108, 112, 116).

Keren, G., J. Sherez, R. Megidish, B. Levitt, and S. Laniado (1985). “Pulmonary venous flow pattern-its relationship to cardiac dynamics A pulsed Doppler echocardiographic study”. In: *Circulation* 71.6, pp. 1105–1112 (cit. on pp. 108, 112, 116).

Kheradvar, A. and G. Pedrizzetti (2012). “Vortex formation in the heart”. In: *Vortex formation in the cardiovascular system*. Springer (cit. on p. 111).

Kuecherer, H. F., I. A. Muhiudeen, F. M. Kusumoto, E. Lee, L. E. Moulinier, M. K. Cahalan, and N. B. Schiller (1990). “Estimation of mean left atrial pressure from transesophageal pulsed Doppler echocardiography of pulmonary venous flow”. In: *Circulation* 82.4, pp. 1127–1139 (cit. on pp. 108, 115, 116).

Martins, P.A.L.S., R.M. Natal Jorge, and A.J.M. Ferreira (2006). “A comparative study of several material models for prediction of hyperelastic properties: Application to silicone-rubber and soft tissues”. In: *Strain* 42.3, pp. 135–147 (cit. on pp. 105, 106).

Meaney, D. F. (2003). “Relationship between structural modeling and hyperelastic material behavior: application to CNS white matter”. In: *Biomechanics and modeling in mechanobiology* 1.4, pp. 279–293 (cit. on p. 105).

Nagueh, S. F. (2018). “Non-invasive assessment of left ventricular filling pressure”. In: *European journal of heart failure* 20.1, pp. 38–48 (cit. on pp. 112, 116).

Nishimura, A., M.D. Abel, L.K. Hatle, and A.J. Tajik (1990). “Relation of pulmonary vein to mitral flow velocities by transesophageal Doppler echocardiography - Effect

of different loading conditions". In: *Circulation* 81.5, pp. 1488–1497 (cit. on pp. 108, 112, 116).
Rajagopalan, B., C. D. Bertram, T. Stallard, and G. DE J. Lee (1979). "Blood flow in pulmonary veins: III Simultaneous measurements of their dimensions, intravascular pressure and flow". In: *Cardiovascular research* 13.12, pp. 684–692 (cit. on p. 110).
Smallhorn, J. F., R. M. Freedom, and P. M. Olley (1987). "Pulsed Doppler echocardiography assessment of extraparenchymal pulmonary vein flow". In: *Journal of the American College of Cardiology* 9.3, pp. 573–579 (cit. on p. 116).
Smiseth, O. A., C. R. Thompson, K. L. Lohavanichbutr, H. Ling, J. G. Abel, R. T. Miyagishima, S. V. Lichtenstein, and J. Bowering (1999). "The pulmonary venous systolic flow pulse - its origin and relationship to left atrial pressure". In: *Journal of the American college of Cardiology* 34.3, pp. 802–809 (cit. on pp. 108, 116).
Zipes, D. P., P. Libby, R. O. Bonow, D. L. Mann, G. F. Tomaselli, and E. Braunwald (2019). *Braunwald's Heart Disease: A Textbook of Cardiovascular Medicine*. 11th ed. Elsevier Inc. (cit. on pp. 112, 115, 116).

References from Chapter 9

Appleton, C.P. (1997). "Hemodynamic determinants of Doppler pulmonary venous flow velocity components: new insights from studies in lightly sedated normal dogs". In: *Journal of the American College of Cardiology* 30.6, pp. 1562–1574 (cit. on p. 124).
Bahrain, S.H.K. and J. Mahmud (2017). "Tensile properties of silicone rubber via. experimental and analytical method adapting hyperelastic constitutive models". In: *Journal of Engineering and Applied Sciences* 12.Specia, pp. 7703–7707 (cit. on p. 123).
Barbier, P., S. Solomon, N.B. Schiller, and S.A. Glantz (2000). "Determinants of forward pulmonary vein flow: an open pericardium pig model". In: *Journal of the American college of cardiology* 35.7, pp. 1947–1959 (cit. on p. 124).
Barbier, P., S.B. Solomon, N.B. Schiller, and S.A. Glantz (1999). "Left atrial relaxation and left ventricular systolic function determine left atrial reservoir function". In: *Circulation* 100.4, pp. 427–436 (cit. on pp. 123, 124).
Basnight, M.A, M.S. Gonzalez, S.C. Kershenovich, and C.P. Appleton (1991). "Pulmonary venous flow velocity: relation to hemodynamics, mitral flow velocity and left atrial volume, and ejection fraction". In: *Journal of the American Society of Echocardiography* 4.6, pp. 547–558 (cit. on p. 124).
Castello, R., A. C. Pearson, P. Lenzen, and A. J. Labovitz (1991). "Evaluation of pulmonary venous flow by transesophageal echocardiography in subjects with a normal heart: comparison with transthoracic echocardiography". In: *Journal of the American College of Cardiology* 18.1, pp. 65–71 (cit. on p. 124).
Chen, Y. T., M. N. Kan, A. Y. S. Lee, J. S. Chen, and B. N. Chiang (1993). "Pulmonary venous flow: its relationship to left atrial and mitral valve motion". In: *Journal of the American Society of Echocardiography* 6.4, pp. 387–394 (cit. on p. 124).

Hellevik, L. R., P. Segers, N. Stergiopulos, F. Irgens, P. Verdonck, C. R. Thompson, K. Lo, R. T. Miyagishima, and O. A. Smiseth (1999). "Mechanism of pulmonary venous pressure and flow waves". In: *Heart and vessels* 14.2, pp. 67–71 (cit. on p. 124).

Keren, G., J. Sherez, R. Megidish, B. Levitt, and S. Laniado (1985). "Pulmonary venous flow pattern-its relationship to cardiac dynamics A pulsed Doppler echocardiographic study". In: *Circulation* 71.6, pp. 1105–1112 (cit. on p. 124).

Klein, A.L. and A.J. Tajik (1991). "Doppler assessment of pulmonary venous flow in healthy subjects and in patients with heart disease". In: *Journal of the American Society of Echocardiography* 4.4, pp. 379–392 (cit. on p. 124).

Kuecherer, H. F., I. A. Muhiudeen, F. M. Kusumoto, E. Lee, L. E. Moulinier, M. K. Cahalan, and N. B. Schiller (1990). "Estimation of mean left atrial pressure from transesophageal pulsed Doppler echocardiography of pulmonary venous flow". In: *Circulation* 82.4, pp. 1127–1139 (cit. on pp. 123–125).

Lagan, S. D. and A. LiberKnec (2017). "Experimental testing and constitutive modeling of the mechanical properties of the swine skin tissue". In: *Acta of bioengineering and biomechanics* 19.2, pp. 93–102 (cit. on p. 123).

Martins, P.A.L.S., R.M. Natal Jorge, and A.J.M. Ferreira (2006). "A comparative study of several material models for prediction of hyperelastic properties: Application to silicone-rubber and soft tissues". In: *Strain* 42.3, pp. 135–147 (cit. on p. 123).

Mouret, F., V. Garitey, E. Bertrand, F. Derivaux, J. Fuseri, and R. Regis (2004). "In vitro atrial flow dynamics: normal conditions versus atrial fibrillation". In: *Journal of biomechanics* 37.11, pp. 1749–1755 (cit. on p. 125).

Nagueh, S. F. (2018). "Non-invasive assessment of left ventricular filling pressure". In: *European journal of heart failure* 20.1, pp. 38–48 (cit. on p. 123).

— (2020). "Left ventricular diastolic function: understanding pathophysiology, diagnosis, and prognosis with echocardiography". In: *JACC: Cardiovascular Imaging* 13.1 Part 2, pp. 228–244 (cit. on p. 123).

Nishimura, A., M.D. Abel, L.K. Hatle, and A.J. Tajik (1990). "Relation of pulmonary vein to mitral flow velocities by transesophageal Doppler echocardiography - Effect of different loading conditions". In: *Circulation* 81.5, pp. 1488–1497 (cit. on pp. 124, 126).

Rajagopalan, B., C. D. Bertram, T. Stallard, and G. DE J. Lee (1979). "Blood flow in pulmonary veins: III Simultaneous measurements of their dimensions, intravascular pressure and flow". In: *Cardiovascular research* 13.12, pp. 684–692 (cit. on p. 124).

Smiseth, O. A., C. R. Thompson, K. L. Lohavanichbutr, H. Ling, J. G. Abel, R. T. Miyagishima, S. V. Lichtenstein, and J. Bowering (1999). "The pulmonary venous systolic flow pulse - its origin and relationship to left atrial pressure". In: *Journal of the American college of Cardiology* 34.3, pp. 802–809 (cit. on pp. 124, 125).

Wiener, F., E. Morkin, R. Skalak, and A. P. FISHMAN (1966). "Wave propagation in the pulmonary circulation". In: *Circulation research* 19.4, pp. 834–850 (cit. on p. 124).

Zipes, D. P., P. Libby, R. O. Bonow, D. L. Mann, G. F. Tomaselli, and E. Braunwald (2019). *Braunwald's Heart Disease: A Textbook of Cardiovascular Medicine*. 11th ed. Elsevier Inc. (cit. on p. 123).

Part VI

Appendices

Appendix A

In the following images, the LA position with respect to other structures was assigned in Axial view of the CT images. Five images, showing clearly the LA and surrounding structures, were chosen and landmarked. The images are from superior to inferior in the Right-Anterior-Superio coordinate system. In Fig. 11.1, the LA is not visible yet, because it is inferior with respect to the Aorta, the pulmonary artery, the Trachea and the superior Vena Cava.

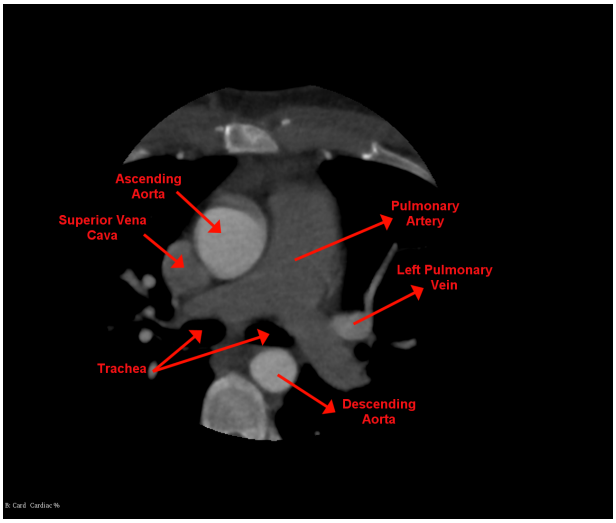

Figure 11.1: Axial view of the structures surrounding the LA. The LA is not visible because it is inferior with respect to the pulmonary artery.

As it goes inferiorly, the LA appears gradually, starting from the LAA. In Fig. 11.2 the LAA, the left coronary artery (which is covered by the LAA), the RA and the LA are visible. In Fig. 11.3, the LA and the RA along with the LV and the RV are completely evident.

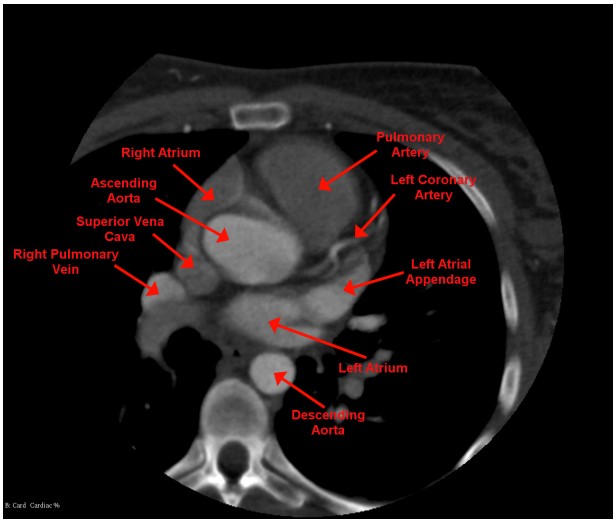

Figure 11.2: Axial view of the cardiac structure. The LA, the LAA and the PVs, are visible in this image.

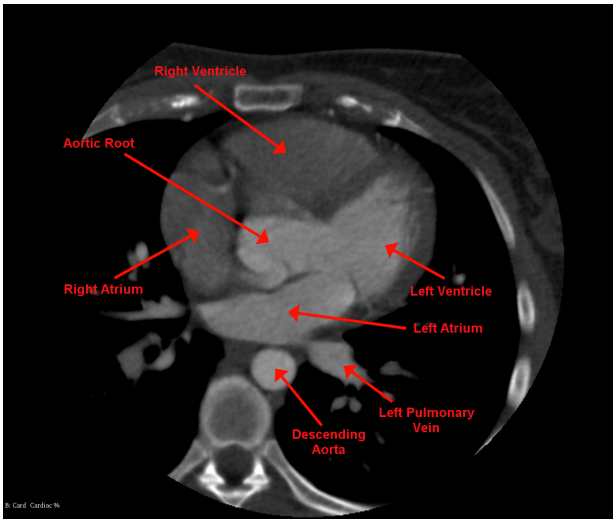

Figure 11.3: Axial 4-chambers view. The LA is completely apparent in this view.

Fig. 11.4 depict a very clear 4-chambers view in which the LV, the RV, the LA and the RA are clearly seen. The final image in Fig. 11.5 shows the view in which the LA and

the RA completely disappeared. Therefore, only the ventricles are visible in the image.

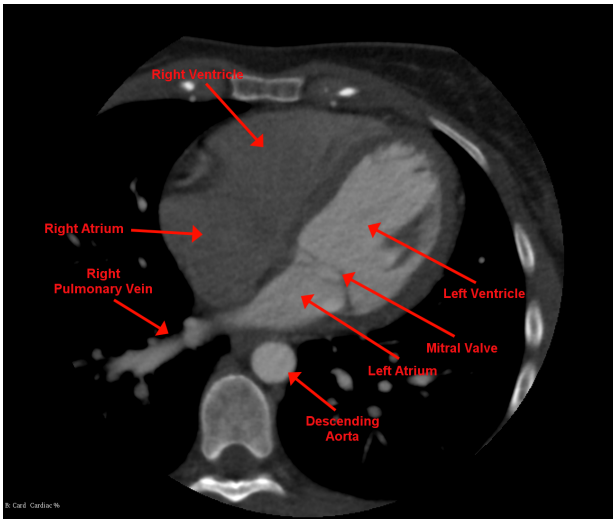

Figure 11.4: Axial 4-chambers view. The LA is completely visible in this view.

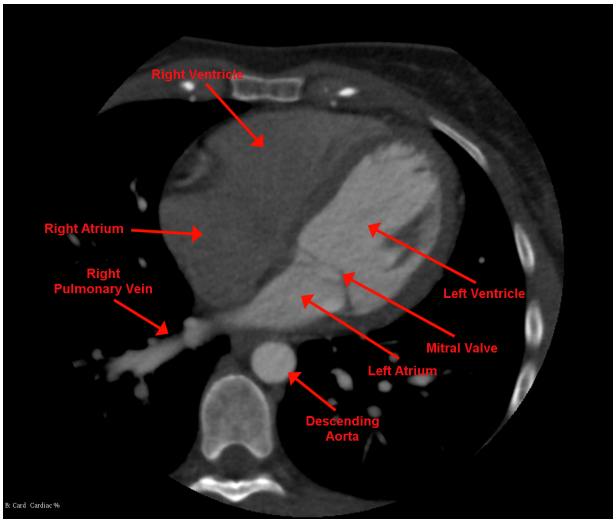

Figure 11.5: Axial view of two ventricles. The LA and the RA completely disappeared as they are inferior with respect to the atrial chambers. Inferior vena cava is also visible.

Appendix B

```
%% PhD student Masoud Meskin 23-01-2020.
% Pulsatile flow - Womersley model
% This script generates pulsatile velocity profile from
% in-vivo measured flowrate profile.
% The code is developed originally in CFU group at DTU but
% modified and changed to be utilized in comsol software.

clc; clear; close all

%% Load flowrate profile
B = readmatrix('Masoud_MRscan5_LIPV_Time.csv'); % total flowrate divided by 4
Q = B(:,2); %[ml/s] flowrate data for one inlet
time_axis = B(:,1); % [ms]
R = 6.62 ; %[mm] cross section radius
A = pi*R^2; % [mm^2] inlet (PV) cross sectional area
v_bar = Q/A; % mean velocitu profile [m/s]

%% Define parameters

opt.radius = R*1e-3;                % Pulmonary Vein radius [m] - it is assumed to be circular
opt.rho = 1060;                     % fluid density [kg/m^3]
opt.mu  = 4e-3;                     % fluid dynamic viscosity [Pa*s]
opt.num_harmonics = 8;              % number of harmonics used
opt.num_r_samples = 25;             % number of radial samples
opt.num_t_samples = 325;            % number of time samples
opt.save = false;                   % save results
opt.dt = mean(diff(time_axis));     % Sampling time [sec]
opt.fs = 1 / opt.dt;                % Sampling frequency [Hz]
opt.T = time_axis(end);             % Length of flow cycle [sec]

%% calculate velocity profiles

[ts, rs, vel_prof] = reconstruct_vel_prof(v_bar, opt); % reconstructing the average velocity profile

%% transalting the velocity profile to Comsol for the 2D model using "s" function

vel_prof1 = vel_prof(:,end:-1:2); % Velocity profile from s=1/2 to s=1. The vel_prof is only for the half of the length becasue it is
```

```
    originally made for the
% circular cross section. But for the 2D model, becasue ofthe "s" ↩
    function in the 2D model, the velocity profile
% should start from s=0 to s=1 and not like the 3D molde which the ↩
    starts from r=0 to r=R.
% end:-1:2 means it reads the table from end to the bginning. but we ↩
    read
% til column 2 becasue the 1st column should not be repeated.
vel_prof_complete = [vel_prof1 , vel_prof]; % Complete velocity profile↩
     from s=0 to s=1.
vel_prof_complete = vel_prof_complete';
t_new = (0:0.001:0.324);
s_new = linspace(0,1,49);
[T,S] = meshgrid(t_new,s_new);
womersley_velocity_profile = [T(:),S(:),vel_prof_complete(:)];
% each line segment of 0 < s < 1.
T1 = array2table(womersley_velocity_profile,'VariableNames',{'Time','↩
    S_function','Velocity'});
writetable(T1,'womersley_velocity_profile.csv')

%% transalting the velocity profile to Comsol for the 3D model using "↩
    sys.r" function

t_new_r = (0:0.001:0.324);
r_new = rs*1e3;
vel_prof_new = vel_prof';
[T2,R2] = meshgrid(t_new_r,r_new);
womersley_velocity_profile_r = [T2(:),R2(:),vel_prof_new(:)];
T3 = array2table(womersley_velocity_profile_r,'VariableNames',{'Time','↩
    sys.r','Velocity'});
writetable(T3,'womersley_velocity_profile_r.csv')

%% plotting the velocity profile in a cylindrical coordinate

[a,b]=size(t_new_r);
M = cell(b , 1);

for i=1:1:b

    v=vel_prof_new(:,i);

    for j=1:1:360
        g(:,j)=v;
    end

    M{i}=g;

end

%% cylindrical plot

phi = linspace(0,2*pi,360);
```

```
[R3,PHI] = meshgrid (r_new,phi);

% make a GIF
filename = 'pulsatile_velocity_profile.gif';
fig = figure();
fig.Position(3) = fig.Position(3)*2;
fig.Position(4) = fig.Position(4)*2;
for i = 1:12:b
    surf(R3.*cos(PHI), R3.*sin(PHI), M{i});
    xlim auto
    ylim auto
    zlim ([-0.05 0.7])
    title(sprintf('t=%.03f (s)', ts(i)))
    set(gca, 'FontSize', 16)
    xlabel('(mm)')
    ylabel('(mm)')
    zlabel('Velocity (m/s)')
    makegif(filename, fig, i, 0.1)
end

%% display results

fig = figure();
fig.Position(3) = fig.Position(3) * 2;
fig.Position(4) = fig.Position(4) * 2;
surf(rs*1e3, ts, vel_prof) % rs in [mm]
set(gca, 'YDir', 'reverse')
xlabel('radius (mm)')
ylabel('time (s)')
zlabel('velocity (m/s)')
set(gca, 'FontSize', 16)

%% subfunction
function [ts, rs, vel_prof] = reconstruct_vel_prof(v_bar, opt)
%% Define axis
ts = (0:opt.num_t_samples - 1) / (opt.num_t_samples - 1) * opt.T;
rs = (0:opt.num_r_samples - 1) / (opt.num_r_samples - 1) * opt.radius;
vel_prof = zeros(opt.num_t_samples, opt.num_r_samples);

%% V_m
num_samples = numel(v_bar);
v_bar_f = fft(v_bar);
v_amp = abs(v_bar_f) / numel(v_bar);
v_amp = v_amp(1:round(num_samples/2)+1);
v_phase = angle(v_bar_f);
v_phase = v_phase(1:round(num_samples/2)+1);

freq_axis = (0:round(num_samples/2)) / num_samples * opt.fs;
% figure()
% plot(freq_axis, v_amp)
% hold on

```

```
harmonic_freqs = freq_axis(1:opt.num_harmonics);
harmonic_angular_freqs = 2 * pi * harmonic_freqs;
w = harmonic_angular_freqs(2);

v_harmonic_amplitudes = interp1(freq_axis, v_amp, harmonic_freqs);
plot(harmonic_freqs, v_harmonic_amplitudes, 'ro')
xlabel('frequency (Hz)')
ylabel('amplitude')
hold off
figure()
plot(freq_axis, v_phase)
hold on
v_harmonic_phases = interp1(freq_axis, v_phase, harmonic_freqs);
plot(harmonic_freqs, v_harmonic_phases, 'ro')
xlabel('frequency (Hz)')
ylabel('phase (rad)')

for i = 1:opt.num_r_samples
    %% Psi_m
    r = rs(i);
    tau = 1i^(3/2) * opt.radius * sqrt(opt.rho / opt.mu * ↩
        harmonic_angular_freqs);
    alpha = tau .* (besselj(0, tau)); % This is not the womersely ↩
        number

    psi_numerator = alpha - tau .* besselj(0, r / opt.radius .* tau);
    psi_denominator = alpha - 2*besselj(1, tau);
    psi = psi_numerator ./ psi_denominator;

    psi_amplitudes = abs(psi);
    psi_amplitudes(1) = 0;
    psi_phase = angle(psi);
    psi_phase(1) = 0;

    %% reconstruct velocity
    dc_comp = 2 * v_harmonic_amplitudes(1) * (1 - (r/opt.radius)^2);
    harmonic_comp = 0;
    amplitude = v_harmonic_amplitudes .* psi_amplitudes;
    phase = v_harmonic_phases - psi_phase;

    for j = 2:opt.num_harmonics
        harmonic_comp = harmonic_comp + amplitude(j) * cos((j-1) * w * ↩
            ts - phase(j));
    end
    vel_prof(:, i) = dc_comp + harmonic_comp;
end
end
```

appendices/Figures/new_womersely.m

Paper 1

A novel left atrial mock circulatory loop - The impact of the left atrial compliance on the left heart hemodynamics

Masoud Meskin, Philip Starkey, Alexander Emil Kaspersen, Steffen Ringgaard, Signe Gram Sand, Jens Vinge Nygaard, Matthias Bo Stuart, Jørgen Arendt Jensen, Marie Sand Traberg, Peter Johansen

Published in:
Aimed to publish in Nature Scientific Reports

Document Version:
in review by the co-authors

DOI:

A Novel Left Atrial Mock Circulatory loop - The impact of the left atrial compliance on the left heart hemodynamics

Masoud Meski[1], Philip Starkey[2], Steffen Ringgaard[4], Alexander Emil Kaspersen[5], Signe Gram Sand[2], Jens Vinge Nygaard[3], Matthias Bo Stuart[6], Jørgen Arendt Jensen[6], Marie Sand Traberg[1], Peter Johansen[2]

1) Cardiovascular Biomechanics group, Department of Health Technology, Technical University of Denmark,
2) Cardiovascular Experimental Laboratory, Aarhus University
3) Department of Biological and Chemical Engineering - Medical Biotechnology, Aarhus University
4) Department of Clinical Medicine - MR research center, Aarhus university hospital
5) Department of Clinical Medicine - Cardiovascular and Vascular Surgery, Aarhus university hospital
6) Center for Fast Ultrasound Imaging, Department of Health Technology, Technical University of Denmark

***Abstract*—The function and hemodynamics indices of the left atrium (LA) are proven as strong markers of cardiovascular outcomes which augments the prognostics and predictability of many cardiac disease. However, evaluating the LA function and hemodynamics are very complicated because there is a complex interplay and interdependence between the LA, the left ventricle (LV), and the pulmonary veins (PVs). These complications plus uncontrolled phenomena during clinical examinations create intricacies for clinicians and researchers to have accurate and thorough assessments. In recent years, the interest in employing in-vitro mock circulatory loops to mimic cardiovascular system has surged because of their potential to recreate realistic, simplified, and controlled functional and hemodynamic conditions. In this work, a novel fully controlled holistic versatile left atrial mock circulatory loop was designed and built enabling research of various LA pathological and physiological scenarios. The main objectives of the study are 1) to validate the hemodynamic performance of the flow loop by physiological conditions and 2) to investigate the impact of the LA compliance on the left heart (LH) hemodynamics. Our results show that LA complaince has a huge impact on the LA and in general on the LH fluid dynamics.**

I. Introduction

The left atrium (LA) has three phasic functions, 1) the reservoir, 2) the conduit (passive emptying), and 3) the booster pump (active emptying) [1]–[3]. All these three phases are in close interplay with the left ventricle (LV) and the pulmonary veins (PVs). In the reservoir phase, the LA volume and pressure are affected by PVs systolic forward flow (SFF) and the mitral valve (MV) annulus downward displacement due to the systolic contraction of the LV. The PVs SFF and the LV systolic function, on the other hand, are influenced by the LA relaxation and compliance [4]–[11]. During the conduit phase, with the contribution of PVs diastolic forward flow (DFF), the LA passively empties the accumulated blood to the LV and increases its pressure and volume. Mutually, the LV preload and filling pressure during early diastole, has high impact on LA emptying and PVs DFF [10]–[13]. In the active emptying phase, the LA contracts to kick the rest of the accumulated blood to the LV chamber. The LA contraction augments the LV end diastolic volume which in turn increases the stroke volume by 15-30% [1], [2] and strengthens the PVs SFF by reducing the LA pressure [5], [10], [11]. Again the LV filling pressure and PVs pressure have reciprocal influence on the LA afterload in this phase [2], [6], [8], [14]–[16]. Therefore, the interdependence of the LA with LV and PVs is crucial for a healthy functioning LA and for a normal cardiac function.

As the LA plays a pivotal role in the LV and PVs function, evaluating the LA size, shape, function and hemodynamics indices has prognostic implications. For instance, LA enlargement is related to several cardiac disease, like MV dysfunction, LV hypertrophy, systemic and pulmonary hypertension or LA fibrillation [1], [2], [11], [17]–[22]. As another example, the left atrial appendage (LAA) shape and function increases the risk of thromboembolism due to the blood stagnation in LA fibrillation or in valvular disease [23]–[25]. However, assessing the LA physiology is very complicated because of its complex shape and function. Moreover, in clinical examinations, assessing LA hemodynamics, like LA pressure, is often invasive and many uncontrolled phenomena affect the outcome of the measurements. These complexities make it difficult for clinicians to have accurate and thorough investigations of the LA hemodynamics.

The potential of in-vitro mock circulatory loops (MCL) in studying physiology and pathology of the cardiovascular system is well recognized [26] and plays an important role in reducing the amount of animal experiments or invasive operations on patients [27], [28]. Moreover, MCLs are widely employed in testing and validating cardiovascular devices like ventricular assist devices, heart valves, balloon catheters and vascular stents [29]–[31]. They also enable the researchers and clinicians to mimic various pathological scenarios which are impossible to be carried out in vivo [32], [33].

The cardiac chambers have an intricate Fluido-Electro-Mechanical function, which in addition to its complex geometry, makes the cardiac in-vitro studies cumbersome for

researchers. Therefore, in many in-vitro studies with MCLs, simplifications are applied, either in geometry or in function of the LA chamber. For instance, in some works, a porous media [29], [30], [32]–[34], a rigid reservoir [27], [28], [35]–[41] or an elastic spherical-like shape with a voluminous inlet as PVs [42], [43] were embedded as the LA chamber. In Leopaldi.et.al.2012 and Leopaldi.et.al.2015 [31], [44], however, they integrated biological native LA chamber into in vivo MCL in order to preserve the geometry, but it only mimics the LA passive phase functions. There are only two works [45], [46] with holistic MCLs with anatomically-shaped LA chamber and proper active-passive phasic functions. Nevertheless, it seems the LA chamber compliance and thickness are not physiologic. The reported chamber thickness is 0.1 mm while the mean LA chamber wall thickness is 1-4 mm (or 0.5-12) [47], [48]. Moreover, information about the compliance is not reported,however, based on the reported PV flowrate profile in Muret.et.al.2004 [45] and the LA pressure profile in Tanne.et.al.2010 [46], the compliance of the LA chamber seems not physiologic. The impact of the LA compliance on the PV flowrate [6], [11] and the LA pressure [add Ref by Yong] are well defined. Therefore, utilizing a material with correct compliance to cast the LA chamber is of high importance in recreating a physiologic condition.

The main objective of this study was to develop a versatile holistic in vitro MCL of the LH with a geometrically simplified hyperelastic LA chamber to replicate a physiologic dynamic and hemodynamic of the LA chamber. The MCL could be a valuable asset in studying LH disease given that it can meet the following criteria:

1) Including a LA geometry with four PVs and a MV outflow to establish a realistic reservoir and conduit phasic functions.

2) A LA chamber mimics a physiological compliance to provide a physiological passive and active LA function.

3) A contraction phase mimicking the LA active pumping phase.

4) A high interplay and coordination between the LA and LV events.

5) Ability to play with LV volumetric profile to replicate various clinical scenarios.

6) A static PV preload.

To validate the functionality of the MCL, the LA and LV pressure and transmitral, Aortic and PV flowrate profiles were measured and the results are verified with physiological indices reported in the literature. Furthermore, to investigate the effect of LA compliance on the LH hemodynamic, the same measurements were carried out with various LA chambers having different compliance.

II. Materials and Methods

To achieve the aims of this study, several sub-studies were performed. First, the compliance of the left atrium should be physiologically matched to achieve the passive function of the LA (reservoir and conduit phase). Therefore, the choice of the LA material with proper mechanical property is imperative. Then, the inlet flow to the atrium from the pulmonary veins must be fully understood to enable replicating the correct LA preload, specifically during the LA reservoir phase. Moreover, the LA must have a physiological pressure signature and range during the reservoir phase. Furthermore, in synchronous with the LA and PVs functions, the action of the LV must carefully be controlled in order to provide proper adjustment of the LV systolic and diastolic function. And finally, the peripheral unit must assure proper mimicking of the systemic vascular resistance and compliance.

A. Left Atrial Compliance

To establish a reference on LA compliance, a substudy was carried out on nine fresh porcine hearts to measure the LA compliance through pressure-volume measurements. Therefore, the LA needed to be isolated and mounted in an experiment set up (Fig. 4). To isolate the LA, first the left side of the heart was separated from the right side. To identify the attachment of the right ventricular wall on the interventricular septum, the apex was removed by a cross-sectional slice through both ventricles approximately 1 cm from the apex. The right ventricle was opened by an incision in the anterior wall from the cross-sectional opening along the anterior interventricular sulcus to the coronary sulcus. The aortic arch was removed from the ascending aorta by a cross-sectional cut approximately 3 cm from the aortic annulus.

The left atrium was separated from the right atrium with 2 incisions, one in the anterior wall of the right atrium from the coronary sulcus through the pulmonary trunk close to the left leaflet, and another in the posterior wall from the transverse pericardial sinus to the coronary sinus. Finally, the right atrium and ventricle was completely separated from the left side by an incision from the coronary sinus, following the posterior interventricular sulcus.

An incision in the interventricular septum was made from the cross-sectional opening in the left ventricle to approximately 1.5 cm above the aortic ostium to get access to the mitral valve. Both papillary muscles were isolated from the myocardium to fixate the anterior leaflet of the MV above the aortic ostium to prevent leakage, while the posterior leaflet was sutured to the wall to keep the MV open. The pulmonary veins were sutured to completely seal the LA inlets. Then, the tube was installed in the left ventricle, ensuring the tip of the tube to be lined up with the edges of the MV annulus, and it was fixated with zip ties. The final result of the LA isolation is displayed in Fig. 1. When no leakage was detected from the LA, the LA and tube was placed in the experiment setup. Hereafter, the actual expansion test for measuring the compliance was conducted.

B. 3D CAD modeling of the simplified LA Chamber

The geometry of the LA was simplified to reduce the complexity and facilitate the casting of the LA chamber. The LA chamber was considered as a smooth symmetrical spherical chamber with four cylindrical inlets as PVs, a circular outlet as MV ostium and without atrial appendage (LAA) and LA trabeculae. It is shown by Zhang and Gay, 2008 [49] that the LAA is not functional in sinus rythm and therefore it

is expected that excluding the LAA from the model doesn't impact the results. To design the spherical LA chamber, the LA volume at the end of the LA systole [50] was used to calculate the radius of the sphere. The PVs radius is 6.6 mm which was calculated from the averaged PVs ostia area reported in Chnafa et.al.2014 [51] and the MV radius is 25mm, equal to the radius of the mechanical heart valve (MHV) used in the mockloop. The LA chamber wall thickness is 2mm [48]. The model was designed in Autodesk inventor (Autodesk® Inventor LT™) and is shown in Fig. 2A.

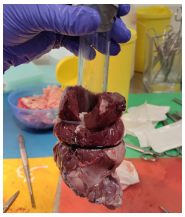

Fig. 1: Isolated porcine LA chamber mounted on the tube of the experiment setup. The tube was placed right on the MV annulus.

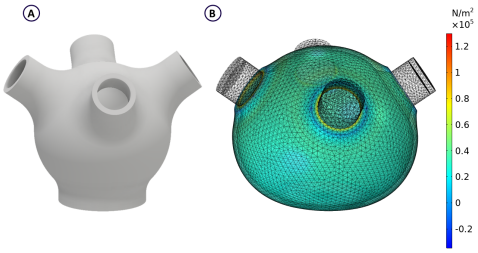

Fig. 2: A) CAD model of the simplified LA chamber. The LA was assumed as a symmetrical spherical chamber with four cylindrical inlets as PVs and a circular outlet as MV ostium. The LAA and LA trabeculae were excluded from the model to reduce the complexity of casting the chamber. B) The first principal stress as the result of the implemented FSI simulation using Yeoh material as the hyperelastic model and LIPV flowrate as the inlet boundary condition.

C. Casting hyperelastic LA chamber

Gravity casting using an elastic mold was employed to cast the LA chamber. Because the LA chamber is a hollow object, casting was done in two steps. In the first step, a water-soluble core was cast with Ferris 2283-A Green soluble wax (Freeman Manufacturing & Supply Company- OH/US) through silicone-mold casting (Appendix IX) and in the second step the hyperelastic chamber was cast with an elastic mold. The elastic mold was designed in Autodesk inventor (Autodesk® Inventor LT™) and 3D printed with Formlabs elastic 50A transparent resin (Formlabs Inc. - MA,USA). To attain a sufficient chamber compliance, two materials, "Elite Double 8" and "Silicon Rubber ZA-SFX-0020 with platinum catalyst" (Zhermack SpA – RO, Italy) were mixed with different proportions together. The portion of mixture was changed in the range of 50%-5% for Elite Double 8 and 50%-95% for Silicon Rubber. 11 chambers (CH1-CH11) were cast in total (Tab. II). The elastic mold and the molded chamber are shown in Fig. 3.

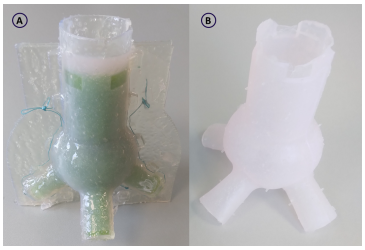

Fig. 3: A) The elastic mold before extracting the chamber is shown. To completely seal the mold, it was sutured. The green water-soluble core can be seen in the mold. B) The molded chamber after dissolving the core in water is shown.

D. Expansion test on porcine and molded LA chambers

After securing the sealing of the porcine and molded LA chambers, their volume prior to pressurization ($V0$) were measured. To measure $V0$, water was poured with syringe into the chambers up to the MV plane and the volume of the water was recorded as $V0$. Then they were installed in the experiment setup (Fig 4). The experiment setup consist of a bucket, a Polica 90 degree elbow joint tube, a transparent straight polycarbonate plastic tube, a transparent container and a measuring cup. The molded and porcine LA chambers were mounted on the transparent straight tube such that the tip of the tube was placed at the MV plane (Fig. 1). Then the chambers were pressurized with water at 2000 Pa ($\approx 15\ mmHg$) and the volume of the accumulated water in the measuring cup was recorded as the volume difference (ΔV). The measurements were repeated three times for each chamber and the averaged volume difference ΔV_{ave} was calculated. The experiment set up mimic the LA reservoir phase function. The reason of choosing 2000 Pa to pressurize the chambers was because it is close to the porcine LA pressure during the reservoir phase [6] and also it facilitates having more tangible expansion. Then the expansion percentage (EP) was simply calculated as:

$$EP = \frac{\Delta V_{ave}}{V0} \times 100 \tag{1}$$

The expansion tests on the porcine LA chambers were done in several days but it was assumed that the aging has minor impact on expansion result as the mechanical properties do not degrade too much [Ref: Jernigan Master dissertation].

E. Tensile test

To obtain the mechanical properties of the Silicone-Elite mixture, destructive uniaxial tensile test were carried out on 13 samples according to ASTM D412 tensile test standard. The Instron low force electromechanical universal testing

Fig. 4: The expansion experiment setup. The experiment setup consists of a bucket, a Polica 90 degree elbow joint tube, a transparent straight polycarbonate plastic tube, a transparent container and a measuring cup. The left panel shows testing the porcine heart and the right panel displays the test on molded LA chambers.

machine (Instron® - MA, US) was employed for conducting the tests. To cast the dumbbell shaped specimens, a mold was designed based on the ASTM D412 Die C, in Autodesk inventor (Autodesk® Inventor LT™) and 3D printed with Formlabs clear V4 resin (Formlabs Inc., MA, USA). The specimens dimensions, the mold for casting the specimens and the specimen installed on the tensile test machine are shown in Fig. 5. The rate of the testing machine was set to 500 mm/min. The thickness of the specimens were measured on three spots based on the ASTM D412 protocols, before installing on the machine. Their thicknesses vary from 2.2-3 mm with the mean value of 2.6 mm.The force-displacement data were recorded with a sampling frequency of 10 Hz.

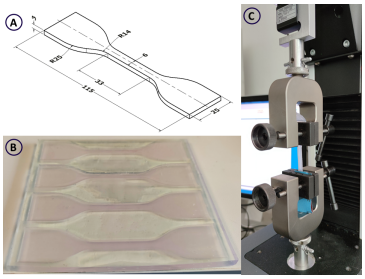

Fig. 5: A) Specimen's dimensions based on the ASTM D412 protocols Die C. B) The mold and the molded specimens with Elite-Silicone mixture material. C) A specimen installed on the Instron low force electromechanical universal testing machine.

F. Numerical Simulation

To analyze the data acquired with tensile test, the data sets were undergone 1) curve fitting procedure and 2) finite element analysis using fluid-structure interaction (FSI) method. For all the numerical simulations, the Silicon-Elite mixture was assumed as an incompressible isotropic material, which is a general assumption for rubber like materials [52], [53]. First, because the Silicon-Elite mixture exhibited large elastic stretch and nonlinear behavior (Fig. 8), hyperelastic material models are ideally suited for characterising its mechanical properties. Therefore, five parametric analytical functions representing five different hyperelastic material models (Tab. III) were chosen to fit to the experimental data. The curve fitting was done by implementing the Levenberg-Marquardt algorithm [54], [55] in MATLAB (The MathWorks Inc., MA, US), using the global optimization toolbox with Multistart option. Second, five FSI simulations were done on the LA CAD model displayed in Fig. 2, using the five fitted hyperelastic models. The model simulates the LA reservoir phase function in which the MV is closed. Therefore, the systolic part of the PVs flowrate profile, case 1 (Fig. 12) was considered as the inlet boundary condition. The fluid domain material is blood which was assumed as a Newtonian incompressible fluid with a density of 1060 kg/m^3 and dynamic viscosity of 4 cP. The FSI simulations (Fig. 2) were performed in COMSOL Multiphysics® v.5.6. (COMSOL AB, Stockholm, Sweden).

G. LH MCL set-up

The mock loop structure, which aims to mimic the LA phasic function, is an upgraded version of the pulsatile left heart in-vitro model used in [27], [28]. For pump control and data acquisition, a software was designed in LabVIEW (National Instruments, Austin, TX) which enables the mock loop operator to generate desirable pulsatile pump piston waveform and collect measured data, simultaneously.

1) Flow loop: The flow loop (Fig. 7) consists of a pulsatile electromechanical pump (SuperPump AR Series, ViVitro Labs, Victoria, Canada) replicating the LV volumetric change in systole and diastole, connected to a rigid LV chamber with an outflow to an aortic valve housing, connecting the LV chamber through a clamped medical silicon tubing to a rigid compliance chamber, simulating arterial compliance. The aortic valve is a mechanical bi-leaflet valve. The outflow from the compliance chamber, which empties into a rigid venous reservoir, was also clamped to control the systemic resistance. The rigid venous reservoir connected to the molded LA chamber (Fig. 3) through four medical silicone tubing serving as PVs. A big rigid reservoir was chosen because the pulmonary capillaries can be considered as a structure with large reservoir capacity which is isolated from the pressure variation in LA chamber [4]. The molded LA chamber is embedded into a container, called LA container, to be pressurized to replicate the LA pulsatility. A MV housing connects the LA container to the LV chamber and it holds a MHV (St. Jude Medical bileaflet 25mm, St. Paul, USA). PV and MV flowrates are measured using tubing flowsensors connected to a Dual-Channel tubing module (PXL11,PXL25, TS410, Transonic Systems Inc., Ithaca, NY, USA). LA and LV pressures are recorded using fluid-filled pressure probes connected to a patient monitoring screen and Micro-tip pressure catheters (SPC-350MR; Millar Inc.,Houston, TX, USA) connected to a two-channel amplifier pressure control unit (PCU-2000, Millar Instruments). The LA contraction phase is replicated by pressurizing and venting the LA container using normally

closed (N.C.) and normally open (N.O.) solenoid valves type EV210A (Danfoss A/S, Denmark), respectively. Therefore, the N.C. valve is connected to a compressor and the N.O. valve opens to the atmospheric pressure. Compressors are utilized for pressurizing the LA container and compliance chamber. The working fluid is distilled water.

2) Software for data generation and acquisition: A harmonious interplay between all the cardiac events is crucial for a well-functioning cardiac system because the cardiac components are all interconnected and have mutual impacts on each other. Hence, the hemodynamic and mechanical functions of PVs, LA, MV and LV should be synchronous for maintaining the normal LH operating condition.

To control and synchronize the LV and LA pulsatile behaviour of the mock loop, a dedicated custom made software was designed. The software specifically generates LV volumetric waveform to control the pulsatile pump piston position, and triggering signal to control the LA pulsatility through controlling the N.C. and N.O. valves. Moreover, while controlling the pump and the valves, the software is also able to calibrate, display and record the flowrate [l/min] and pressure [mmHg] data through a NI USB-6259 module (National Instruments, Austin,TX).

To generate the LV volumetric waveform, the displacement course of the pulsatile pump piston head should be controlled during the three cardiac phases; systole, early diastole and late diastole. Therefore, a waveform, made up of three separated cosine waveforms related to these three cardiac phases, was generated (Eq. 2-5).

$$n : [0 \rightarrow t_1] : f(t) = -a_1 \times cos[n \times \frac{\pi}{t_1}] + 0.5 \quad (2)$$

$$n : [t_1 \rightarrow t_1 + t_2] : f(t) = -a_2 \times cos[(n - t_1) \times \frac{\pi}{t_2}] + 0.6 \quad (3)$$

$$n : [t_1 + t_2 \rightarrow t_1 + t_2 + t_3] : f(t) = -a_3 \times cos[(n - (t_1 + t_2)) \times \frac{\pi}{t_3}] + 0.1 \quad (4)$$

$$-a_1 + a_2 + a_3 = 0 \quad (5)$$

In these equations, n is the length of the cardiac cycle, and t_1, t_2, t_3 and a_1, a_2, a_3 are the systolic, early diastolic and late diastolic time spans and amplitudes, respectively. The Eq. 5 ensures that the waveform starts and stops at the same voltage.

This custom waveform enhanced the versatility of the mock loop because the time span and the amplitude of each cosine waveform can be adjusted for replicating different clinical scenarios. The output rate was set to 1000 Hz and changing the length of the waveform would alternate the heart rate.

The triggering signal for the valves was constructed as a TTL signal. Since the N.O. and N.C. valves are operating in asynchrony, the same control signal was used. To replicate the LA contraction phase, the triggering signal is high, causing opening of the N.C. valve to pressurize the LA container. The low triggering signal, however, causes the N.O. valve to open to the atmospheric pressure to replicate LA relaxation phase. The piston waveform and the triggering signal are shown in Fig. 6 .

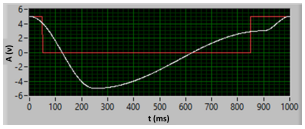

Fig. 6: The white curve shows the pulsatile piston head waveform which is constituted with three cosine waveform (Eq. 2-5). The red curve displays the valves triggering signal, which opens the N.C. valve when it is high and opens the N.O. valve when it is low. The vertical axis is the amplitude in voltage (v) and the horizontal axis is time in millisecond (ms).

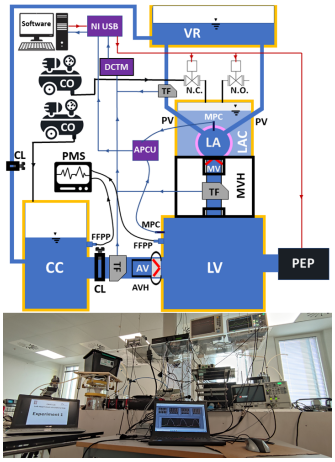

Fig. 7: Top panel shows a schematic representation of the mock loop. VR = Venous reservoir, N.C. = Normally closed valve, N.O. = Normally open valve, TF = Tubing flowsensor, PV = Pulmonary vein, MPC = Micro-tip pressure catheter, LA = Left atrial chamber, LAC = Left atrial container, MV = Mitrl valve, MVH = Mitral valve house, LV = Left ventricular chamber, PEP = Pulsatile electromechanical pump, FFPP = Fluid filled pressure probes, AV = Aortic valve, AVH = Aortic valve house, CL = Clamp, CC = Compliance chamber, PMS = Patient monitoring screen, CO = Compressor, APCU = Amplifier pressure control unit, DCTM = Dual channel tubing module, NI USB = NI USB-6259 module The red arrow lines indicate the generated triggering signal from the software, controlling the PEP piston head, the N.C. and the N.O. valves. The blue arrow lines are the measured pressure and flowrate data which is sent to the designed software. The pressure measured by the FFPP were only visualized on the PMS to watch the mock loop condition. The working fluid inside the LAC is static and only used to pressurize the LA. The clamps are utilized to adjust the systemic and pulmonary vascular resistance. The bottom panel displays the mock loop setup in the laboratory.

3) MCL hemodynamics measurements: Four molded LA chambers, CH1,CH5, CH10 and CH11, with different compliance (Tab. II) were selected for the measurements. The flowsensors, Micro-tip pressure catheters and fluid-filled pressure probes were calibrated and connected to the measurement sites. The duration of the cardiac phases and the cardiac output was adjusted by regulating the time and amplitude of the three cosine waveforms (Eq. 2-5). The systolic time span was set to 350 ms, early diastole to 500 ms and late diastole to 150 ms. The amplitudes were set to obtain cardiac output of 4.5 L/min. The mock loop was run for some time to make sure that 1) there is no air bubble in the system and 2) the cardiac output reaches to 4.5 L/min. The pressure and flowrate data was recorded for 60 cycles. To check the stability and reproducibility of the measurements, the mean standard deviation (S_{mean}) was calculated over 20, randomly selected, cycles:

$$S_j = \sqrt{\frac{1}{N-1}\sum_{i=1}^{N}(x_{ij}-\bar{x})^2} \quad , \quad j = 1:n \tag{6}$$

$$S_{mean} = \sqrt{\frac{\sum_{j=1}^{N} S_j^2}{N}} \tag{7}$$

N is the number of cycles, n is the number of samples in each cycle and $\bar{x}$ is the mean value of a component of a cycle over N cycles. In the conducted measurements, n=1000 as the sampling rate was set to 1000 Hz and the cardiac cycle duration was set to 1s.

H. Magnetic resonance phase contrast flow imaging

In-vivo 2D phase contrast magnetic resonance flow imaging (PC-MRI) was conducted on five healthy young volunteers (four males and one female, ages 23-33) to measure the PVs and transmitral flowrate profiles. The imaging was done with a Philips MR scanner (Achieva dStream 1.5T, Philips Healthcare, The Netherlands). Initially, a multislice, multiphase Balanced-Steady-State-Free-Precession sequence was applied over the whole heart for localizing the position and orientation of the vessels. The flow in each of the four pulmonary veins was measured with a 2D phase contrast sequence. Slice thickness was 8 mm and pixel size was 1.2 mm. 40 cardiac phases were acquired and the Velocity Encoding parameter was 60 cm/s. The flowrate of each PV was measured in a slice orthogonal to and 3 mm proximal to the PV ostium. The images where analyzed with an in-house written software (Siswin).

III. Results

A. Expansion test on porcine and molded LA chambers

The results of the expansion tests on the porcine hearts are reported in Tab. I. The EP% of porcine LA chambers are between 105%-270%. The results of the expansion tests on the molded LA chambers are presented in Tab. II. The molded chambers are divided into three groups, 1) the ones with expansion in the range of porcine LA chambers are considered as normal-compliance chambers, 2) the chambers below the porcine expansion range are tagged as low-compliance chambers and 3) the chambers above the porcine expansion range are categorized as high-compliance chambers.Amongst the 11 chambers, CH1, CH5, CH10 and CH11 were chosen. CH1 and CH5 are the low-compliance, CH10 is the normal-compliance and CH11 is the high-compliance chamber.

Heart #	$V0(ml)$	$\Delta V_{ave}(ml)$	EP%
1	27	29	107
2	32	50	156
3	38	100	263
4	30	40	133
5	45	70	156
6	14	30	214
7	34	48	141
8	37	46	124
9	38	74	195

TABLE I: Porcine LA chamber expansion test results. $V0$ is the primary volume, ΔV_{ave} is the volume difference after pressurization and the EP% is the expansion percentage.

Chamber	$V0(ml)$	$\Delta V_{ave}(ml)$	EP%
CH1	67	19	28.4
CH2	65	22	33.8
CH3	66	21	31.8
CH4	66	24.3	36.9
CH5	70	30	42.9
CH6	65	29	44.6
CH7	68	32.3	47.5
CH8	68	34.7	51
CH9	70	64.7	92.4
CH10	69	76.3	110.6
CH11	69	>500	>300

TABLE II: Molded LA chamber expansion test results. $V0$ is the primary volume, ΔV_{ave} is the volume difference after pressurization and the EP% is the expansion percentage.

B. Hyperelastic curve fitting on the tensile test data

The tensile test was done on the specimens which were cast with the same Silicon-Elite mixture ratio as the normal-compliance chamber CH10 (Tab. II). Having the specimens dimensions, the engineering stress was calculated. Then the true stress components, obtained by multiplying the engineering stress by the stretch values, plotted vs stretch for all the 13 specimens. The stress values were averaged over all the specimens to plot mean stress vs stretch. Moreover, the minimum (Min) and maximum (Max) stress values were selected amongst all the stress components and plotted. The results are displayed in Fig. 8.

The outcome of the fitted five hyperelastic analytical models on the mean stress-stretch curve are displayed in Fig. 9. The Cauchy stress for each hyperelastic model was fitted to the experimental data.

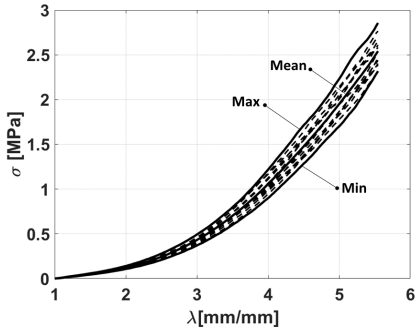

Fig. 8: True stress (σ) vs Stretch (λ) curve of the 13 specimens underwent uniaxial tensile test. The dashed lines ($--$) represent the stress-stretch curves of the 13 specimens. The solid lines (—) display the Min, Mean and Max stress values plotted vs stretch.

To assess whether a good fit to data was obtained, the correlation coefficient (C.C.) (Eq. 8) between experimental data and theoretical predictions was calculated [56].

$$C.C. = \frac{\sum_{i=1}^{m}(y_i-\bar{y})_t(y_i-\bar{y})_e}{\sqrt{\sum_{i=1}^{m}(y_i-\bar{y})_t^2}\quad\sqrt{\sum_{i=1}^{m}(y_i-\bar{y})_e^2}} \tag{8}$$

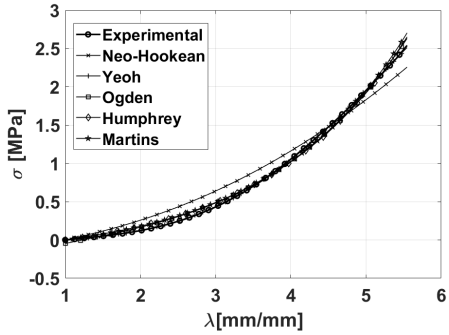

Fig. 9: five fitted hyperelastic models on the mean stress-stretc experimental data

.

The five hyperelastic models strain energy and Cauchy stress expressions, the extracted model parameters and calculated C.C. are summarized in Tab. III . For detailed information on the cauchy stress expressions of the fitted hyperelastic models, refer to [53], [57].

Another index for evaluating the goodness of the fit is the error residual ($ER(\lambda)$) (Eq. 9) which calculates the relative difference between theoretical and experimental data at each stretch level [53], [58]. The calcaulated $ER(\lambda)$ for each fitted hyperelastic model is displayed in Fig. 10 .

$$ER(\lambda) = \frac{|y_e(\lambda)-y_t(\lambda)|}{y_e(\lambda)} \times 100 \tag{9}$$

Material model	Analytical expression	Parameters
Neo-Hookean	$\psi = c_1(I_1-3)$ $\sigma = 2c_1(\lambda^2-\frac{1}{\lambda})$	$c_1 = 3.692e4\,[Pa]$
Yeoh	$\psi = \sum_{i=1}^{3} C_i(I_1-1)^i$ $\sigma = 2(\lambda^2-\frac{1}{\lambda})(c_1+2c_2(\lambda^2+\frac{2}{\lambda}-3)+3c_3(\lambda^2+\frac{2}{\lambda}-3)^2)$	$c_1 = 1.450e4\,[Pa]$ $c_2 = 898.5\,[Pa]$ $c_3 = -10.1\,[Pa]$
Ogden (N=3)	$\psi = \sum_{i=1}^{N} \frac{c_{(2i-1)}}{c_{2i}}[\lambda^{c_{2i}}+2(\frac{1}{\sqrt{\lambda}})^{c_{2i}}-3]$ $\sigma = \sum_{i=1}^{N} c_{2i-1}(\lambda^{c_{2i}}-\lambda^{-c_{2i}/2})$	$c_1 = -5.334e4\,[Pa]$ $c_2 = 1.578$ $c_3 = 2.021e4\,[Pa]$ $c_4 = 3.913$ $c_5 = 1.182e4\,[Pa]$ $c_6 = 1.591$
Humphrey	$\psi = c_1(e^{c_2(I_1-3)}-1)$ $\sigma = 2(\lambda^2-\frac{1}{\lambda})c_1c_2e^{c_2(\lambda^2+\frac{2}{\lambda}-3)}$	$c_1 = 1.239e6\,[Pa]$ $c_2 = 0.02$
Martins	$\psi = c_1(e^{c_2(I_1-3)}-1)+c_3(e^{c_4(\lambda-3)^2}-1)$ $\sigma = 2(\lambda^2-\frac{1}{\lambda})c_1c_2e^{c_2(\lambda^2+\frac{2}{\lambda}-3)}+2\lambda(\lambda-1)c_3c_4e^{c_4(\lambda-1)^2}$	$c_1 = 1.168e6\,[Pa]$ $c_2 = 0.021$ $c_3 = 3.202e4\,[Pa]$ $c_4 = 0.015$

TABLE III: The five hyperelastic models fitted on the mean experimental stress-stretch curve, the model parameters and the calculated C.C. are presented. Because the material was considered as an incompressible isotropic hyperelastic material, there is no dependency on second and third principal stretches (λ_2, λ_3) and on the third invariants of the right Cauchy-Green tensor (I_3). Therefore, the analytical expressions of the hyperelastic models were simplified.

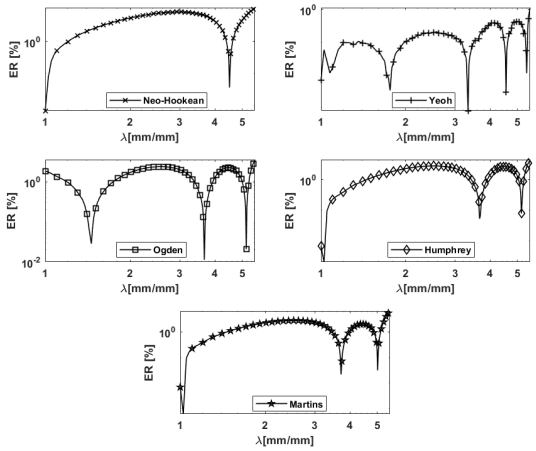

Fig. 10: the calculated ER for each hyperelastic model showing the relative difference between theoretical and experimental data.

Furthermore, to investigate which model represents better the mechanical behavior of the material, finite element analysis (FEA) was implemented on the LA simplified model (Fig. 2). Then the five hyperelastic models were fitted on the Max and Min curves (Fig. 8) and optimal model parameters were calculated. For each set of the model parameters extracted from curve fitting on the Max and Min curves, the maximum first principal stress (FPS) over the whole solid domain was

obtained through the FSI simulation. Then, the normalized difference ($ND(\lambda)$) was calculated at each stretch level between the maximum FPS obtained by model parameters of the curve fitting on the Min curve and the maximum FPS of the model parameters of the curve fitting on the Max curve was calculated (Eq. 10). The results of the $ND(\lambda)$ are shown in Fig. 11. To best of the authors knowledge, this is the first time such an index is employed for evaluating analytical models in curve fitting exercises.

$$nd(\lambda) = \frac{|FPS_{max}(\lambda) - FPS_{min}(\lambda)|}{FPS_{max}(\lambda)} \tag{10}$$

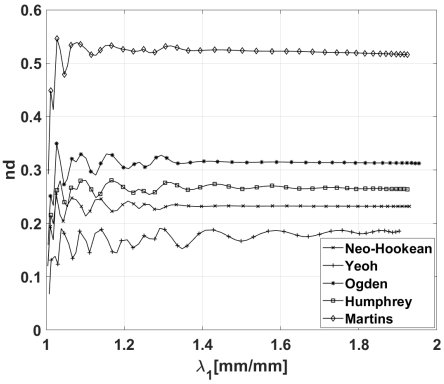

Fig. 11: The graph displays the normalised first principal stress difference (nd) vs first principal stretch. The nd was calculated based on the difference of the maximum FPS between model parameters of the curve fitting on the Max and Min curve.

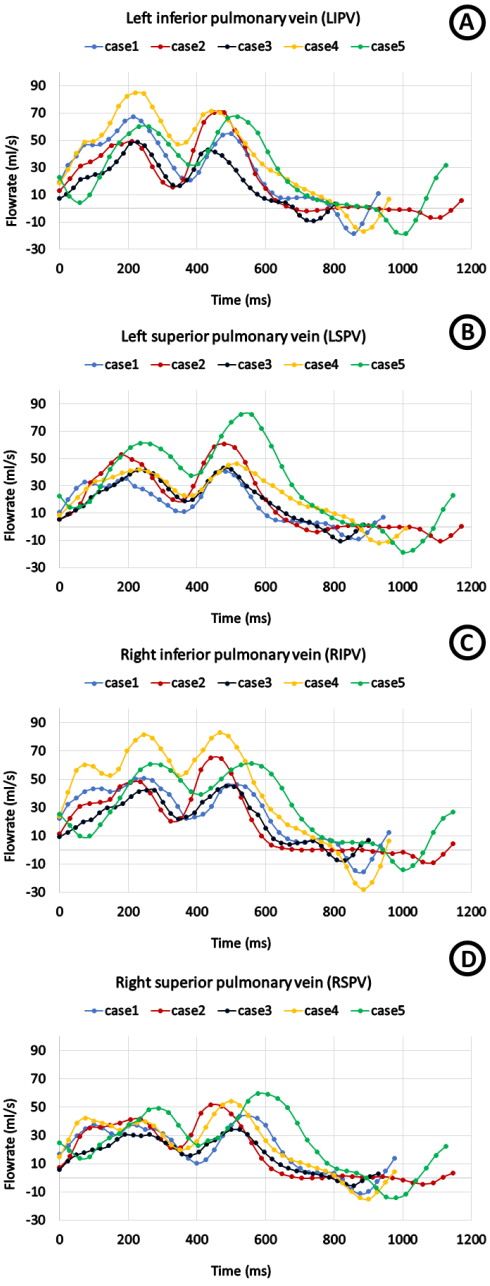

Fig. 12: PV flowrate profiles of five healthy young volunteers. A) Left inferior pulmonary vein (LIPV). B) Left superior pulmonary vein (LSPV). C) Right inferior pulmonary vein (RIPV). D) Right superior pulmonary vein (RSPV). The flowrate was measured 3 mm proximal to the PVs ostium.

C. In-vivo PV flowrate profiles

All volunteers had four PVs, i.e. left inferior pulmonary vein (LIPV), left superior pulmonary vein (LSPV), right inferior pulmonary vein (RIPV) and right superior pulmonary vein (RSPV). For each PV, the flowrate profile was measured proximal to the PV ostium. The measured data points were interpolated with a quadratic polynomial function. The results are shown in Fig. 12. The graphical treatment was done in Microsoft Excell (Microsoft corporation, WA, US).

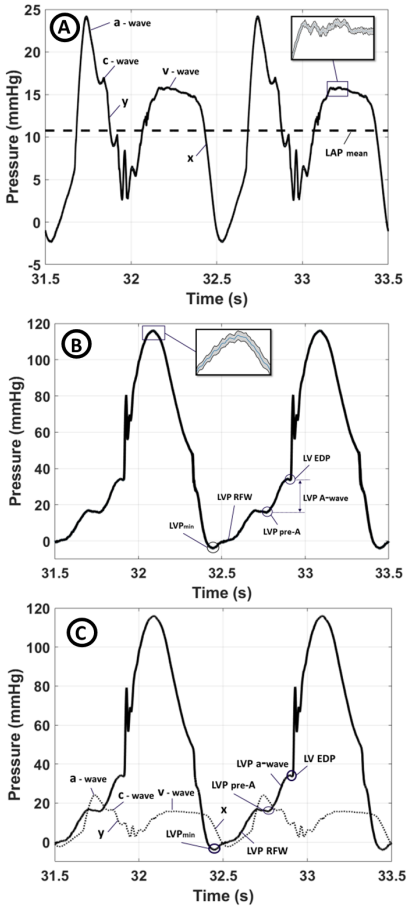

Fig. 13: The MCL fluid dynamics measurements with normal-compliance CH1. A) The measured LAP in two cycles. The a-wave, v-wave, c-wave and x and y troughs are marked on the graph. The mean LAP is shown with dashed line (−−). B) The measured LVP in two cycles. LVP_{min} = minimum LVP, LVP RFW = LVP rapid filling wave, LVP pre-A = LVP prior to the LA contraction, LVP EDP = end diastolic LVP. C) The LAP (dotted line ....) is displayed over LVP (solid line —) to compare the pressure components of the two chambers.In all the graphs, the zoomed area shows the mean and the standard deviation.

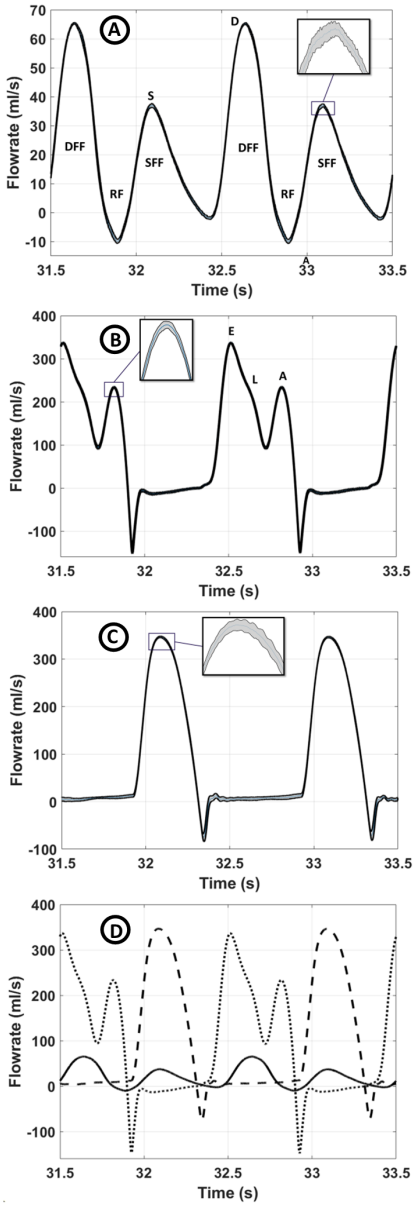

Fig. 14: A) Shows the PV flowrate profile. The diastolic forward flow (DFF), the systolic forward flow (SFF), the retrograde floe (RF), the diastolic peak (D) and systolic peak (S) are marked on the graph. B) Displays the MV flowrate profile. The early diastolic peak (E), the mid-diastolic peak (L) and the atrial kick (A) are specified. C) The AV flowrate profile. D) The MV, PV and AV flowrate profiles are displayed on top of each other for comparison. In all the graphs, the zoomed are shows the mean and the standard deviation.

D. MCL fluid dynamics measurements with normal compliance LA chamber

The results of the in-vitro LH fluid dynamics measurements with the normal-compliance CH10 (Tab. II) are displayed in Fig. 13 and Fig.14. The measured left atrial pressure (LAP), left ventricular pressure (LVP) and MV, PV and AV flowrate profiles with all the components of the pressure and the flowrate structures are displayed on the figures and their values are reported in Tab. V-VII. The zoomed areas represent the mean and the standard deviation of the measured values. The calculated S_{mean} (Eq. 7) of the pressure and flowrate measurements are reported in Tab. IV.

Measurement	S_{mean}
LAP	0.14
LVP	0.61
PV flowrate	0.72
MV flowrate	2.32
AV flowrate	4.13

TABLE IV: Calculated S_{mean} of the MCL measurements with normal-compliance CH10.

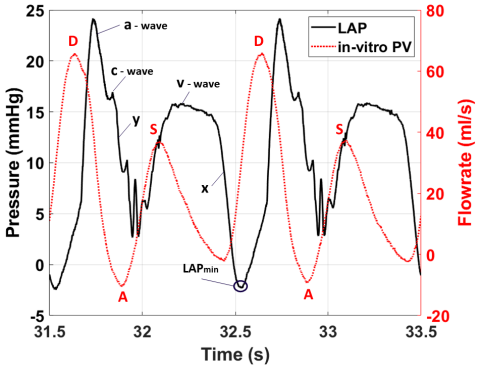

Fig. 15: The measured in-vitro LAP and PV flowrate plotted together to show their reverse relation.

E. MCL fluid dynamics measurements with different LA chamber compliance

The results of the LH in-vitro pressure and flowrate measurements with different LA chambers with various compliance are displayed in Fig. 16 and Fig. 17. The pressure and flowrate values and indices, which are commonly used in clinical diagnosis, are presented in Tab. V-VII.

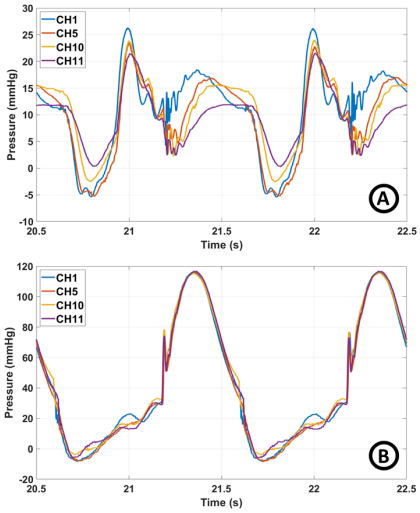

Fig. 16: The measured LAP and LVP with CH1, CH5, CH10 and CH11 to investigate the impact of the LA compliance on the pressure. A) Displays the measured LAP. As the LA compliance decreases, the a-wave and mean LAP increase. B) Shows the measured LVP. The impact of the compliance is not considerable on the LVP as the LV chamber is rigid.

Chamber	v peak (mmHg)	a peak (mmHg)	LAP mean (mmHg)	LAP min (mmHg)
ch11	12	21.7	9.5	0.4
ch10	15.8	24.1	10.8	-2.3
ch5	17.2	23.4	9.5	-5.4
ch1	18.7	26.4	10.6	-5.5

TABLE V: The measured LAP components are reported in the table. All the reported values are marked on Fig. 13.A.

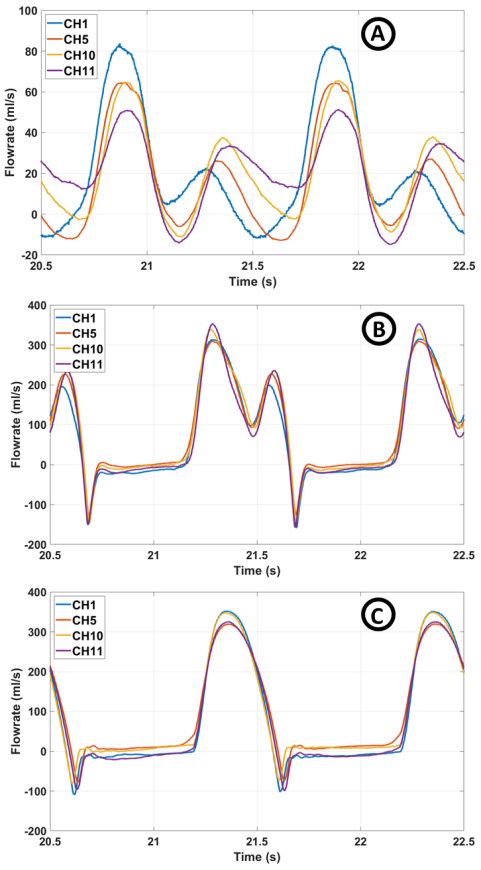

Fig. 17: The measured in-vitro flowrate with with CH1, CH5, CH10 and CH11 to investigate the impact of the LA compliance on the flowrate. A) Shows the PV flowrate profile. As the compliance decreases, the D wave amplifies while the S and A waves diminish. B) displays the MV flowrate profile. The compliance of LA affected the E and A peak. C) Presents The AV flowrate profile. The LA compliance doesn't affect the AV flowrate because the LV chamber is rigid.

Chamber	VTI SFF (ml)	VTI DFF (ml)	VTI RF (ml)	A (ml/s)	S (ml/s)	D (ml/s)	S/D
ch11	10.4?	11.7?	-1.70	-14.9	34.9	51.5	1.48
ch10	8.1	13.5	-0.81	-10.1	37.1	65.3	0.57
ch5	4.9	14.5	-0.54	-6.9	29.2	64.8	0.45
ch1	4.4?	19.8?	-	-	23.9	82.6	0.29

TABLE VI: The measured PV flowrate components are reported in the table. VTI SFF = velocity time integral of systolic forward flow. VTI DFF = velocity time integral of diastolic forward flow. VTI RF = velocity time integral of retrograde flow. A, S and D waves are all marked on the Fig.14.A.

Chamber	E (ml/s)	A (ml/s)	E/A	DT (ms)
ch11	353.1	234.4	1.51	198?
ch10	336.8	233.6	1.44	209?
ch5	308.4	227.1	1.36	192?
ch1	312.8	195.5	1.6	186?

TABLE VII: The measured MV flowrate components are presented in the table. The E and A peaks are displayed in the Fig. 14.B.

IV. Discussion

A. Hyperelastic curve fitting on the tensile test data

Elite Double 8 is used in dentistry for dental impressions, offering a very high elastic recovery (99.99%), high tear strength and laceration resistance and provides high detail reproduction (Courtesy of Zhermack SpA). However, it was unable to provide the expected compliance because of low elasticity (380%). Then, Silicon Rubber ZA-SFX-0020 was added as it offers a very high elasticity (770%). The $\sigma - \lambda$ graph (Fig. 8) shows the large deformation of the specimens, molded with Silicon-Elite mixture, (Tab. II), under uniaxial tensile test indicating clearly the hyperelastic nonlinear behavior of the mixture.

The fitted hyperelastic models on the $\sigma - \lambda$ curves are displayed in Fig. 9. Amongst the analytical models, the Neo-Hookean has the poorest fit and the Yeoh model resulted the best fit. The C.C. index (8) which evaluates the overall quality of the fit is presented in Tab. III. Evidently, the Yeoh has the highest C.C. and the Neo-Hookean has the lowest one. The C.C. of the Ogden model is also higher compare to the Neo-Hookean, Martins and Humphrey. The ER (Eq. 9) showing the relative difference between experimental data and analytical fitted models (Fig. 10) is lower with Yeoh compare to other models. It is observed by Martins et.al. [53] that the lobes of the ER graph of the Neo-Hookean, Ogden and Humphrey models represent the number of model parameters, but it is inconclusive for the Yeoh and Martins models. A similar observation was made here in this work which confirms their findings.

Considering the calculated ND(λ) (Eq. 10) from FSI simulations showed in Fig. 11, the Yeoh model offers lower ND compare to other fitted models. Surprisingly, the Martins model has the highest ND amongst the models while its C.C. is higher after Yeoh C.C. value. It is speculated that while an analytical model results a good fit to experimental data, it may not be a good choice for numerical simulations like finite element models. The same was observed when the Mooney-Rivlin model was fitted to the experimental data. Despite of good fitting results, it generated material instability due to the negative $\sigma - \lambda$ curve slope. This negative slope on fitted Mooney-Rivlin curve can be seen in many works [53], [57], [59] which causes material instability and generates errors if it is used in numerical simulations.Therefore, the authors highly recommend to interpret the results of curve fitting based on the application of the models in numerical studies.

Taking into account all the indices, the Yeoh model offers the best fit with very high C.C. and lower ER and ND which is

in well agreement with Martins et.al. [53]. Moreover, the FSI simulation Yeoh material model parameters was very stable compare to other models.

B. MCL fluid dynamics measurements with normal compliance LA chamber

Because of the complex interrelated sequences of the LH events, having a thorough holistic overview of the LH hemodynamics information is crucial for a well-validated diagnostic. Considering the transmitral indices and flow pattern, they are strong representatives of the heart diastolic function. However, they are not sufficient or in some cases are misleading in assessing the diastolic function if they are considered alone. For instance, in pseudonormal condition the transmitral E/A ratio appears normal, while the LAP is elevated and diastolic function is worsen [60]. Therefore, all the pressure and flow data were evaluated to validate the functionality of the MCL. The calculated S_{mean} (Eq. 7) presented in Tab. IV verifies the stability and reproducibility of the conducted measurements.

1) LAP-LVP: Both the absolute individual values and the shape of the measured LAP and LVP waveforms are in very good agreement with the literature.

Considering the LA pressure waveform (Fig. 13.A), the three positive deflections (a,c,v) and the two negative deflections (x and y troughs) are visible [6], [11], [60]. The v wave reflects the LAP increase during reservoir phase function due to the PV SFF while the MV is closed. The height of the v peak is determined by the LA compliance, LA filling and the descent movement of the MV annulus [6], [11]. The y trough shows an abrupt LAP drop due to the LA passive emptying into the LV following the MV opening when the LV pressure drops below the LA pressure. The LAP decline during LA conduit phase depends highly on the LV preload (or compliance). However, as the LV chamber of the MCL is rigid, it was tried to mimic the LV compliance by the amplitude of the early diastolic portion of the pulsatile pump piston waveform (Eq. 3). The a wave reflects the 3rd phase of the LA phasic function in which LA contracts and as the result, the LAP increases instantly. The x trough shows the LAP decline caused by the LA relaxation following the LA contraction. The c deflection reflects the sudden rise in LAP due to the closure of the MV. The value of the v wave is within the normal range 6-21 mmHg, however, the a wave is a bit higher than the range 4-16 mmHg [60]. The reason for the high a wave is because the late diastolic portion of the piston waveform (Eq. 4) also contributes in LA contraction by generating suction and strengthens the effect of LA chamber pressurization.

Apart from the absence of isovolumic contraction and relaxation because of the rigid LV chamber, the LVP profile pattern (Fig. 13.B) is in very good agreement with reported physiologic LVP profiles [15], [16], [60]. The LVP drops to minimum value, LVmin, right after the MV opening. Then the LVP increases during LVP RFW to the inflection point, LV pre-A, before LA contraction. Due to the LA contraction, the LVP surges upward and generates LV A-wave. The LVP ED trough reflects the LVP decline before the LVP systolic rise. The values of the LVP peak systolic and LVP ED are within the reported range of 90-140 mmHg and 5-12 mmHg, respectively [60]. The oscillations on the LVP profile reflects the AV and MV closures, recorded by the micro-tip catheter. The perfect synchronization between LAP and LVP is shown in Fig. 13.C. All the LAP events are well coordinated with LVP components.

2) PV flowrate: In this study, one of the important issues under investigation was to find out about the origin of the PV flowrate phases, because it was the key point in deciding how to design and feed the inlets of the LA chamber. The in-vivo 4D-MRI measurements of the PV flowrate in Fig. 12 shows a four-wave pattern reported in the literature [4], [5], [7], [8], [10]–[13], [61], including three antegrade flow waves and a retrograde flow wave. The two peaks (s1 and s2) in systole, which builds SFF, and the DFF during early diastole are antegrade waves. After the DFF wave at the end of diastole, the retrograde flow (RF) wave occurs due to the LA contraction. However, there is a new observation that the RF at the end of systole is not a pure backward flow rather a combination of backward and forward flow. It is speculated that the flow reverses quickly due to the sharp LAP drop at the end of LA contraction and that's why there is a very short instance of forward flow following the RF.

There are many debates and disagreements about the determinants of the PV flow phases. For the DFF, some researches ascribed it to the LV relaxation and LA pressure drop due to the opening of the MV [4], [10], [11], [13], [62]. Other studies, however, showed that LA recoil due to the stored elastic energy during LA reservoir filling is the strongest determinants of the DFF [6], [7]. Considering the RF, the LA contraction have been suggested as its main determinant [13], [14], [63] [Ref]. Talking about SFF, it is demonstrated in some works that it is purely driven by the LH systolic events, due to the LA relaxation, LA compliance and the descent movement of the MV annulus caused by LV systolic function [6], [7], [10], [62], [64], [65]. In some other studies, SFF is attributed to the right ventricle (RV) systolic pressure propagation through pulmonary circulation [63], [66], [67]. In some researches, however, the SFF has been ascribed to LA reservoir, LV and RV systolic functions [6], [8].

As the main goal of the study was to build a LA MCL, and because the pulmonary capillary bed can be considered as a reservoir with large capacity [66], a rigid reservoir with constant static pressure was designed as the PVs for the LA inlets. In this way, the PVs are also completely isolated from the RV effects and they are only driven by the LH events.

The measured in-vitro PV flowrate (Fig. 14.A) shows a thriphasic flow wave pattern. The SFF, DFF and RF are visible, however, the SFF includes only one peak, which is the s1 peak. Because the LV of the MCL is rigid and the MCL is an isolated LH with no RH components, we cannot confirm whether the s2 is generated by the descent movement of the heart base or by the RV systolic pressure propagation through pulmonary vasculature. Therefore, the possibility of the RV contribution in PV SFF cannot be ruled out. However, the results disclose that the PV flow pattern is predominantly determined by the LH events, or it would be better to say by

the LH pressure gradient. Fig. 15 shows the reverse relation between PV flowrate and LAP, reported in the literature [7], [8], [68]. While the LAP increases, the PV SFF declines until the MV opens. The DFF starts to rise as the LAP drops because of LA passive emptying into the LV. As the LV filling pressure increases, the DFF diminishes to zero and in continue, due to the LA contraction, the LAP propagates through extra parenchymal PVs and generates RF.

Another observation which proves that the PV flow is predominantly controlled by the LH pressure gradient is the mid-diastolic flow pattern of the measured in-vivo PV flowrate profiles of case 2 and case 5, displayed in Fig. 12. After the DFF and before the RF, there is a period in which the PV is zero or negative. This mid-diastolic flow pattern shows that As the LV filling pressure increases, the DFF diminishes and reaches a plateau. The plateau before LA contraction is because the LAP and LVP are balancing. The negative flowrate before RF wave in case 2 shows that the LVP exceeds the LAP and therefore the flow regurgitates into the PVs. If there were any contribution from the RV pressure propagation, that backward flow before RF at the end of diastole would have not happened.

3) Transmitral flowrate: The measured in-vitro MCL transmitral flowrate is in well agreement with the literature. The E/A ratio and DT are within the physiologic ranges [Ref]. Because the transmitral flow has a very high correlation with the LH pressure gradient, it contains vital prognostic information. When the LVP drops below the LAP, the MV opens. The E peak represents the passive early diastolic LV filling and have been ascribed to many factors, including LV relaxation, LV compliance and LAP [10], [60]. The A wave represents the LA contraction and is attributed to the LA contractility and LA afterload [Ref]. The synchronized interplay between PV, MV and AV are shown in Fig. 14.

C. Effect of LA compliance on the LAP, Transmitral and PV flowrate

As it was argued before, the compliance of the LA has a huge impact on the LH hemodynamics. It directly affects the LA and LV systolic and diastolic functions, the PV flowrate phases, transmitral diastolic flow pattern and cardiac output. Therefore, excluding the LA compliance from the cardiovascular evaluations or considering an inappropriate compliance in designing MCLs results in wrong outcomes. For instance, in Mouret et.al. 2004 [45] the measured in-vitro PV flow has a weak correspondence with in-vivo data due to a defect in LA compliance.

In this work, to show the importance of LA compliance and to evaluate its effects on the LH hemodynamics, the same in-vivo measurements were conducted on three more chambers, CH1, CH5 and CH11 with different compliance (Tab. II). The results obtained from MCL show a very good concordance with reported clinical data.

Considering the PV flowrate profiles in Fig. 17.A and the reported indices in Tab. VI, as the LA compliance declines, it blunts the systolic wave compare to the diastolic wave. Therefore, the SFF VTI decreases while DFF VTI increases which shifts the systolic predominance to the diastolic predominance. Moreover, it suppresses the SFF peak and amplifies the DFF peak which reduces the S/D ratio [8]. The results confirm the in-vivo findings by Kuecherer et.al.,1990 [11] that the degree of the PV SFF is mainly affected by the LA compliance. Furthermore, the RF dramatically diminishes due to the impaired LA contraction as the LA stiffness increases [Ref]. An interesting observation is, instead of having RF in the late diastole, a RF phase appeared in late systole. it is inferred that because the MV is closed and the mean LAP increases as the result of low LA compliance, the pressure gradient reverses as the LAP exceeds the pressure in PVs. It can be explained also in this way that low LA compliance impairs the LA reservoir function by lowering the level of stored strain energy (or lowering the ability of storing elastic energy). Hence, it pushes the flow backward because it cannot accommodate the whole SFF.

The effects of LA compliance deterioration are also reflected in LAP mean and absolute values (Tab. V) and the LAP wave pattern (Fig. 16). As the LA compliance declines, the mean LAP, a and v peaks rise, and the relaxation time shortens. When the LA stiffness increases, it diminishes the LA contraction and therefore, it lessens the relaxation time. The lower relaxation time causes the LAP to remain elevated. The elevated LAP diminishes the contribution of the LA in LV filling, impairs the LA phasic functions, and damages the PV and transmitral flowrate pattern. The abnormal late systolic PV RF can be explained also by the LAP wave pattern. In chamber with normal compliance, the LAP gradually increases to the v peak and remains in the same level until the MV opening. However, in chambers with low compliance, the pressure increases and then drops before the MV opening. As the MV is closed, this pressure drop is because of that late systolic PV RF which relieves the pressure of the chamber.

The transmitral E peak is ascribed to the LV relaxation, the LV filling pressure and LA compliance [10]. Because in this work the LV chamber is rigid and the same pulsatile pump piston head waveform was prescribed in all cases, the reduction in E peak (Fig. 17.B and Tab. VII) can be explained only by the LA compliance. The LA compliance deterioration not only increases the LAP, but also impairs the LA conduit phase function. Moreover, the A peak (Fig. 17.B and Tab. VII) also reduces due to the impaired LA active pump phase function because of low LA compliance. The DT (Tab. VII) is almost the same between all the chambers because DT is attributed to the continued relaxation of the LV and the LV compliance [10], however, the LV chamber is rigid in this work.

V. Conclusion

In spite of its simplicity, the designed MCL works like a fine Swiss watch.

VI. limitations

1) Using more powerful vacuum machine 2) using prosthetic valves instead of mechanical valves. 3) realistic LA geom - Focusing on the LA, it is posteriorly connected to the PVs

and anteriorly connected to the MV and LV [69]. Mention that despite of a difference between realistic and simplified geom, the data recordings are very good. 4) improve the piston waveform 5) the working fluid is water 6) LA volume data to be able to draw the V-P loop.

VII. Acknowledgement

Alberto Redaelli, J. Michael Hasenkam, Hilde Larsen,

VIII. References

[1] G. G. Blume, C. J. Mcleod, M. E. Barnes, J. B. Seward, P. A. Pellikka, P. M. Bastiansen, and T. S. Tsang, "Left atrial function: physiology, assessment, and clinical implications," *European Journal of Echocardiography*, vol. 12, no. 6, pp. 421–430, 05 2011. [Online]. Available: https://doi.org/10.1093/ejechocard/jeq175

[2] M. Rosca, P. Lancellotti, B. Popescu, and L. Pierard, "Left atrial function: pathophysiology, echocardiographic assessment, and clinical applications," *Heart*, vol. 97, no. 23, pp. 1982–1989, 2011.

[3] J. T. Kuhl, J. Lonborg, A. Fuchs, M. J. Andersen, N. Vejlstrup, H. Kelbak, T. Engstrom, J. E. Moller, and K. F. Kofoed, "Assessment of left atrial volume and function: a comparative study between echocardiography, magnetic resonance imaging and multi slice computed tomography," *The international journal of cardiovascular imaging*, vol. 28, no. 5, pp. 1061–1071, 2012.

[4] G. Keren, J. Sherez, R. Megidish, B. Levitt, and S. Laniado, "Pulmonary venous flow pattern-its relationship to cardiac dynamics A pulsed Doppler echocardiographic study," *Circulation*, vol. 71, no. 6, pp. 1105–1112, 1985.

[5] T. H. Chao, L. M. Tsai, W. C. Tsai, Y. H. Li, L. J. Lin, and J. H. Chen, "Effect of atrial fibrillation on pulmonary venous flow patterns assessed by Doppler transesophageal echocardiography," *Chest*, vol. 117, no. 6, pp. 1546–1550, 2000.

[6] P. Barbier, S. B. Solomon, N. B. Schiller, and S. A. Glantz, "Left atrial relaxation and left ventricular systolic function determine left atrial reservoir function," *Circulation*, vol. 100, no. 4, pp. 427–436, 1999.

[7] P. Barbier, S. Solomon, N. Schiller, and S. Glantz, "Determinants of forward pulmonary vein flow: an open pericardium pig model," *Journal of the American College of Cardiology*, vol. 35, no. 7, pp. 1947–1959, 2000.

[8] O. A. Smiseth, C. R. Thompson, K. L. Lohavanichbutr, H. Ling, J. G. Abel, R. T. Miyagishima, S. V. Lichtenstein, and J. Bowering, "The pulmonary venous systolic flow pulse - its origin and relationship to left atrial pressure," *Journal of the American college of Cardiology*, vol. 34, no. 3, pp. 802–809, 1999.

[9] E. Hollander, G. Dobson, J. Wang, K. Parker, and J. Tyberg, "Direct and series transmission of left atrial pressure perturbations to the pulmonary artery: a study using wave-intensity analysis," *American Journal of Physiology-Heart and Circulatory Physiology*, vol. 286, no. 1, pp. H267–H275, 2004.

[10] A. Nishimura, M. Abel, L. Hatle, and A. Tajik, "Relation of pulmonary vein to mitral flow velocities by transesophageal Doppler echocardiography - Effect of different loading conditions," *Circulation*, vol. 81, no. 5, pp. 1488–1497, 1990.

[11] H. F. Kuecherer, I. A. Muhiudeen, F. M. Kusumoto, E. Lee, L. E. Moulinier, M. K. Cahalan, and N. B. Schiller, "Estimation of mean left atrial pressure from transesophageal pulsed Doppler echocardiography of pulmonary venous flow," *Circulation*, vol. 82, no. 4, pp. 1127–1139, 1990.

[12] G. Keren, J. Meisner, J. Sherez, E. Yellin, and S. Laniado, "Interrelationship of mid-diastolic mitral valve motion, pulmonary venous flow, and transmitral flow," *Circulation*, vol. 74, no. 1, pp. 36–44, 1986.

[13] L. R. Hellevik, P. Segers, N. Stergiopulos, F. Irgens, P. Verdonck, C. R. Thompson, K. Lo, R. T. Miyagishima, and O. A. Smiseth, "Mechanism of pulmonary venous pressure and flow waves," *Heart and vessels*, vol. 14, no. 2, pp. 67–71, 1999.

[14] M. Basnight, M. Gonzalez, S. Kershenovich, and C. Appleton, "Pulmonary venous flow velocity: relation to hemodynamics, mitral flow velocity and left atrial volume, and ejection fraction," *Journal of the American Society of Echocardiography*, vol. 4, no. 6, pp. 547–558, 1991.

[15] S. F. Nagueh, "Non-invasive assessment of left ventricular filling pressure," *European journal of heart failure*, vol. 20, no. 1, pp. 38–48, 2018.

[16] ——, "Left ventricular diastolic function: understanding pathophysiology, diagnosis, and prognosis with echocardiography," *JACC: Cardiovascular Imaging*, vol. 13, no. 1 Part 2, pp. 228–244, 2020.

[17] Y. Matsuda, Y. Toma, H. Ogawa, M. Matsuzaki, K. Katayama, T. Fujii, F. Yoshino, K. Moritani, T. Kumada, and R. Kusukawa, "Importance of left atrial function in patients with myocardial infarction." *Circulation*, vol. 67, no. 3, pp. 566–571, 1983.

[18] B. J. Maron, T. S. Haas, M. S. Maron, J. R. Lesser, J. A. Browning, R. H. Chan, I. Olivotto, R. F. Garberich, and R. S. Schwartz, "Left atrial remodeling in hypertrophic cardiomyopathy and susceptibility markers for atrial fibrillation identified by cardiovascular magnetic resonance," *The American journal of cardiology*, vol. 113, no. 8, pp. 1394–1400, 2014.

[19] A. Gulati, T. F. Ismail, A. Jabbour, N. A. Ismail, K. Morarji, A. Ali, S. Raza, J. Khwaja, T. D. Brown, E. Liodakis *et al.*, "Clinical utility and prognostic value of left atrial volume assessment by cardiovascular magnetic resonance in non-ischaemic dilated cardiomyopathy," *European journal of heart failure*, vol. 15, no. 6, pp. 660–670, 2013.

[20] C. McGann, N. Akoum, A. Patel, E. Kholmovski, P. Revelo, K. Damal, B. Wilson, J. Cates, A. Harrison, R. Ranjan *et al.*, "Atrial fibrillation ablation outcome is predicted by left atrial remodeling on mri," *Circulation: Arrhythmia and Electrophysiology*, vol. 7, no. 1, pp. 23–30, 2014.

[21] J. A. Dodson, T. G. Neilan, R. V. Shah, H. Farhad, R. Blankstein, M. Steigner, G. F. Michaud, R. John, S. A. Abbasi, M. Jerosch-Herold *et al.*, "Left atrial passive emptying function determined by cardiac magnetic resonance predicts atrial fibrillation recurrence after pulmonary vein isolation," *Circulation: Cardiovascular Imaging*, vol. 7, no. 4, pp. 586–592, 2014.

[22] A. Thomsen, J. Kuhl, K. Kofoed, A. Fuchs, P. Udholm *et al.*, "Left atrial wall thickness and pulmonary vein size are increased in patients with atrial fibrillation compared to healthy con-trols-a multidetector computed tomography study," *Int J Clin Cardiol*, vol. 4, p. 098, 2017.

[23] N. Al-Saady, O. Obel, and A. Camm, "Left atrial appendage: structure, function, and role in thromboembolism," *Heart*, vol. 82, no. 5, pp. 547–554, 1999.

[24] M. Ozkan, C. Kaymaz, C. Kirma, A. Civelek, A. R. Cenal, C. Yakut, and U. Deligonul, "Predictors of left atrial thrombus and spontaneous echo contrast in rheumatic valve disease before and after mitral valve replacement," *The American journal of cardiology*, vol. 82, no. 9, pp. 1066–1070, 1998.

[25] P. Safavi-Naeini and A. Rasekh, "Thromboembolism in atrial fibrillation: role of the left atrial appendage," *Cardiac electrophysiology clinics*, vol. 12, no. 1, pp. 13–20, 2020.

[26] U. Gulan, A. Saguner, D. Akdis, A. Gotschy, R. Manka, C. Brunckhorst, M. Holzner, and F. Duru, "Investigation of atrial vortices using a novel right heart model and possible implications for atrial thrombus formation," *Scientific reports*, vol. 7, no. 1, pp. 1–10, 2017.

[27] J. Rasmussen, S. N. Skov, D. B. Nielsen, I. L. Jensen, M. J. Tjornild, P. Johansen, and V. E. Hjortdal, "In-vitro and in-vivo evaluation of a novel bioprosthetic pulmonary valve for use in congenital heart surgery," *Journal of cardiothoracic surgery*, vol. 14, no. 1, pp. 1–6, 2019.

[28] M. Sharghbin, L. L. Benhassen, T. Lading, T. Bechsgaard, S. N. Skov, D. M. Ropcke, S. L. Nielsen, J. M. Hasenkam, and P. Johansen, "Comparison of the dacron ring and suture annuloplasty for aortic root repair: an in vitro evaluation," *Interactive cardiovascular and thoracic surgery*, vol. 27, no. 6, pp. 819–827, 2018.

[29] R. Vismara, G. Fiore, A. Mangini, M. Contino, M. Lemma, A. Redaelli, and C. Antona, "A novel approach to the in vitro hydrodynamic study of the aortic valve: mock loop development and test," *Asaio Journal*, vol. 56, no. 4, pp. 279–284, 2010.

[30] R. Vismara, A. Pavesi, E. Votta, M. Taramasso, F. Maisano, and G. B. Fiore, "A pulsatile simulator for the in vitro analysis of the mitral valve with tri-axial papillary muscle displacement," *The International journal of artificial organs*, vol. 34, no. 4, pp. 383–391, 2011.

[31] A. M. Leopaldi, R. Vismara, S. V. Tuijl, A. Redaelli, F. N. van de Vosse, G. B. Fiore, and M. C. M. Rutten, "A novel passive left heart platform for device testing and research," *Medical engineering & physics*, vol. 37, no. 4, pp. 361–366, 2015.

[32] M. Meskin, A. Dimasi, E. Votta, M. Jaworek, L. Fusini, M. Muratori, P. Montorsi, E. Zappa, I. Epifani, M. Pepi *et al.*, "A novel multi-parametric score for the detection and grading of prosthetic mitral valve obstruction in cases with different disc motion abnormalities," *Ultrasound in medicine and biology*, vol. 45, no. 7, pp. 1708–1720, 2019.

[33] A. Dimasi, D. Piloni, L. Spreafico, E. Votta, R. Vismara, G. B. Fiore, M. Meskin, L. Fusini, M. Muratori, P. Montorsi *et al.*, "Fluid–structure

interaction and in vitro analysis of a real bileaflet mitral prosthetic valve to gain insight into doppler-silent thrombosis," *Journal of biomechanical engineering*, vol. 141, no. 10, pp. BIO–18–1058, 2019.

[34] A. Balducci, M. Grigioni, G. Querzoli, G. Romano, C. Daniele, G. DAvenio, and V. Barbaro, "Investigation of the flow field downstream of an artificial heart valve by means of piv and ptv," *Experiments in fluids*, vol. 36, no. 1, pp. 204–213, 2004.

[35] T. Steen and S. Steen, "Filling of a model left ventricle studied by colour m mode doppler," *Cardiovascular research*, vol. 28, no. 12, pp. 1821–1827, 1994.

[36] Y. S. Morsi and A. A. Sakhaeimanesh, "Flow characteristics past jellyfish and st. vincent valves in the aortic position under physiological pulsatile flow conditions," *Artificial organs*, vol. 24, no. 7, pp. 564–574, 2000.

[37] V. Kini, C. Bachmann, A. Fontaine, S. Deutsch, and J. Tarbell, "Integrating particle image velocimetry and laser doppler velocimetry measurements of the regurgitant flow field past mechanical heart valves," *Artificial organs*, vol. 25, no. 2, pp. 136–145, 2001.

[38] T. Akutsu and T. Masuda, "Three-dimensional flow analysis of a mechanical bileaflet mitral prosthesis," *Journal of Artificial Organs*, vol. 6, no. 2, pp. 112–123, 2003.

[39] O. Pierrakos, P. P. Vlachos, and D. P. Telionis, "Time-resolved dpiv analysis of vortex dynamics in a left ventricular model through bileaflet mechanical and porcine heart valve prostheses," *J. Biomech. Eng.*, vol. 126, no. 6, pp. 714–726, 2004.

[40] M. Marassi, P. Castellini, M. Pinotti, and L. Scalise, "Cardiac valve prosthesis flow performances measured by 2d and 3d-stereo particle image velocimetry," *Experiments in Fluids*, vol. 36, no. 1, pp. 176–186, 2004.

[41] A. Cenedese, Z. D. Prete, M. Miozzi, and G. Querzoli, "A laboratory investigation of the flow in the left ventricle of a human heart with prosthetic, tilting-disk valves," *Experiments in Fluids*, vol. 39, no. 2, pp. 322–335, Aug 2005. [Online]. Available: https://doi.org/10.1007/s00348-005-1006-4

[42] H. Reul, N. Talukder, E. W. Mu *et al.*, "Fluid mechanics of the natural mitral valve," *Journal of biomechanics*, vol. 14, no. 5, pp. 361–372, 1981.

[43] L. Kadem, Y. Knapp, P. Pibarot, E. Bertrand, D. Garcia, L. G. Durand, and R. Rieu, "A new experimental method for the determination of the effective orifice area based on the acoustical source term," *Experiments in Fluids*, vol. 39, no. 6, pp. 1051–1060, 2005.

[44] A. Leopaldi, R. Vismara, M. Lemma, L. Valerio, M. Cervo, A. Mangini, M. Contino, A. Redaelli, C. Antona, and G. Fiore, "In vitro hemodynamics and valve imaging in passive beating hearts," *Journal of biomechanics*, vol. 45, no. 7, pp. 1133–1139, 2012.

[45] F. Mouret, V. Garitey, E. Bertrand, F. Derivaux, J. Fuseri, and R. Regis, "In vitro atrial flow dynamics: normal conditions versus atrial fibrillation," *Journal of biomechanics*, vol. 37, no. 11, pp. 1749–1755, 2004.

[46] D. Tanné, E. Bertrand, L. Kadem, P. Pibarot, and R. Rieu, "Assessment of left heart and pulmonary circulation flow dynamics by a new pulsed mock circulatory system," *Experiments in Fluids*, vol. 48, pp. 837–850, 05 2009.

[47] S. Y. Ho, J. A. Cabrera, and D. Sanchez-Quintana, "Left atrial anatomy revisited," *Circulation: Arrhythmia and Electrophysiology*, vol. 5, no. 1, pp. 220–228, 2012.

[48] J. Whitaker, R. Rajani, H. Chubb, M. Gabrawi, M. Varela, M. Wright, S. Niederer, and M. D. ONeill, "The role of myocardial wall thickness in atrial arrhythmogenesis," *Ep Europace*, vol. 18, no. 12, pp. 1758–1772, 2016.

[49] L. T. Zhang and M. Gay, "Characterizing left atrial appendage functions in sinus rhythm and atrial fibrillation using computational models," *Journal of biomechanics*, vol. 41, no. 11, pp. 2515–2523, 2008.

[50] V. Jarvinen, M. Kupari, P. Hekali, and V. Poutanen, "Assessment of left atrial volumes and phasic function using cine magnetic resonance imaging in normal subjects," *The American journal of cardiology*, vol. 73, no. 15, pp. 1135–1138, 1994.

[51] C. Chnafa, S. Mendez, and F. Nicoud, "Image-based large-eddy simulation in a realistic left heart," *Computers and Fluids*, vol. 94, pp. 173–187, 2014, cited By 53. [Online]. Available: https://www.scopus.com/inward/record.uri?eid=2-s2.0-84897730504&doi=10.1016%2fj.compfluid.2014.01.030&partnerID=40&md5=13f20fd1b57871d9afba14a79d9fb3dc

[52] B. Erman and J. Mark, *Structures and properties of rubberlike networks*. Oxford University Press, 1997.

[53] P. Martins, R. N. Jorge, and A. Ferreira, "A comparative study of several material models for prediction of hyperelastic properties: Application to silicone-rubber and soft tissues," *Strain*, vol. 42, no. 3, pp. 135–147, 2006.

[54] K. Levenberg, "A method for the solution of certain non-linear problems in least squares," *Quarterly of applied mathematics*, vol. 2, no. 2, pp. 164–168, 1944.

[55] D. W. Marquardt, "An algorithm for least-squares estimation of nonlinear parameters," *Journal of the society for Industrial and Applied Mathematics*, vol. 11, no. 2, pp. 431–441, 1963.

[56] J. D. Humphrey, *Cardiovascular solid mechanics: cells, tissues, and organs*. Springer Science
Business Media, 2013.

[57] S. D. Lagan and A. LiberKnec, "Experimental testing and constitutive modeling of the mechanical properties of the swine skin tissue," *Acta of bioengineering and biomechanics*, vol. 19, no. 2, pp. 93–102, 2017.

[58] D. F. Meaney, "Relationship between structural modeling and hyperelastic material behavior: application to cns white matter," *Biomechanics and modeling in mechanobiology*, vol. 1, no. 4, pp. 279–293, 2003.

[59] S. Bahrain and J. Mahmud, "Tensile properties of silicone rubber via. experimental and analytical method adapting hyperelastic constitutive models," *Journal of Engineering and Applied Sciences*, vol. 12, no. Specia, pp. 7703–7707, 2017.

[60] R. O. Bonow, D. L. Mann, D. P. Zipes, and P. Libby, *Braunwald's heart disease e-book: A textbook of cardiovascular medicine*. Elsevier Health Sciences, 2011.

[61] F. Bukachi, A. Waldenstrom, S. Morner, P. Lindqvist, M. Y. Henein, and E. Kazzam, "Pulmonary venous flow reversal and its relationship to atrial mechanical function in normal subjects-Umea General Population Heart Study," *European Journal of Echocardiography*, vol. 6, no. 2, pp. 107–116, 2005.

[62] Y. Chen, M. Kan, A. Y. Lee, J. Chen, and B. N. Chiang, "Pulmonary venous flow: its relationship to left atrial and mitral valve motion," *Journal of the American Society of Echocardiography*, vol. 6, no. 4, pp. 387–394, 1993.

[63] C. Appleton, "Hemodynamic determinants of doppler pulmonary venous flow velocity components: new insights from studies in lightly sedated normal dogs," *Journal of the American College of Cardiology*, vol. 30, no. 6, pp. 1562–1574, 1997.

[64] A. Klein and A. Tajik, "Doppler assessment of pulmonary venous flow in healthy subjects and in patients with heart disease," *Journal of the American Society of Echocardiography*, vol. 4, no. 4, pp. 379–392, 1991.

[65] R. Castello, A. C. Pearson, P. Lenzen, and A. J. Labovitz, "Evaluation of pulmonary venous flow by transesophageal echocardiography in subjects with a normal heart: comparison with transthoracic echocardiography," *Journal of the American College of Cardiology*, vol. 18, no. 1, pp. 65–71, 1991.

[66] B. Rajagopalan, C. Bertram, T. Stallard, and G. de. J. Lee, "Blood flow in pulmonary veins: Iii simultaneous measurements of their dimensions, intravascular pressure and flow," *Cardiovascular research*, vol. 13, no. 12, pp. 684–692, 1979.

[67] F. Wiener, E. Morkin, R. Skalak, and A. P. FISHMAN, "Wave propagation in the pulmonary circulation," *Circulation research*, vol. 19, no. 4, pp. 834–850, 1966.

[68] J. F. Smallhorn, R. M. Freedom, and P. M. Olley, "Pulsed doppler echocardiography assessment of extraparenchymal pulmonary vein flow," *Journal of the American College of Cardiology*, vol. 9, no. 3, pp. 573–579, 1987.

[69] D. Schwartzman, J. Lacomis, and W. G. Wigginton, "Characterization of left atrium and distal pulmonary vein morphology using multidimensional computed tomography," *Journal of the American College of Cardiology*, vol. 41, no. 8, pp. 1349–1357, 2003.

IX. Appendix A - casting silicone mold

Before starting the silicone rubber mold casting, the master (male) part was designed and 3D-printed with rigid clear resin. The master part will then be encapsulated with molding material to form the negative (female) part. To start the casting process, a frame made from a cardboard box, with dimensions 3-5cm bigger than the master part in all directions to avoid any contact between the frame and the master, was prepared. The frame is made from cardboard, because 1) it is cheaper, 2)

the dimensions can be modified conveniently and 3) the frame can be separated or be destroyed easily to extract the mold. To prevent the integration of play dough with the cardboard, the inside of the box was covered with transparent tape.

Fig. 18

Half of the box was filled with play dough and the master part was positioned in the box in such a way that half of the master is in the playdough and the other half is out of the playdough. To create a sprue for the mold, more playdough is added to the top of the core to keep this place free from silicone material. To prevent the two halves of the mold from sticking together, conic indentations were created on the surface of the play dough with a conic-tip object. For the same purpose, the surface of the play dough is coated with a thin layer of Vaseline.

Fig. 19

The mixing ration for making the silicone material is 1 kg silicone with 0,8 deciliters of hardener. To have an idea of how much the mixture should be stirred, food coloring is added to the mixture. The stirring should be continued until the mixture is colored homogenously. Then the silicone mixture is poured into the box to 3cm above the level of the master part. The mold was shaken slightly to remove the air bubbles and then it was left for 7 hours to cure. To make the other half, the top of the box was closed off and it was turned upside down. The bottom was opened, the play dough was removed, and again the silicone mixture was poured into the other half of the box. Pay attention to not remove the playdough of the sprue to avoid blocking the inlet of the mold.

Fig. 20

When the silicone mold is completely cured, it is removed from the box and the two halves were separated with a scalpel. Be careful not to damage the cavity of the mold. The master part and the rest of the playdough is removed, and the mold is ready to use. To fasten the two halves of the mold, elastic bands were used.

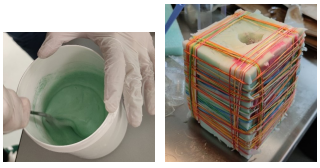

Fig. 21: pics

X. Appendix B - Casting water-soluble wax

The Ferris 2283-A Green soluble wax was chosen for casting the core for casting LA chambers. This kind of wax is suitable for melt and pour and it is great for picking up all the details of the object. The melting temperature should be kept bellow 90c. After liquifying the solid wax, it should be stirred to obtain a homogenize temperature all over the liquid wax. The wax then is poured into the mold and left for 3 hours in the fridge to solidify. After 3 hours, the core was extracted out of the mold and put in the fridge for 2 more hours to solidify completely.

Fig. 22: description of figure

Paper 2

Fluid-Structure Interaction Modeling of A 2D Left Atrium during Reservoir Phase Function

Masoud Meskin, Matthias Bo Stuart, Jørgen Arendt Jensen, Marie Sand Traberg

Name of journal:
Congress of the European Society of Biomechanics

Document Version:
Conference got canceled due to the pandemic

DOI:

FLUID-STRUCTURE INTERACTION MODELING OF A 2D LEFT ATRIUM DURING RESERVOIR PHASE FUNCTION

Masoud Meskin (1), Matthias Bo Stuart (1), Jørgen Arendt Jensen (1), Marie Sand Traberg (1)

1.Department of Health Technology, Technical University of Denmark , 2800 Kgs. Lyngby, Denmark

Introduction

The left atrium (LA) has three phase functions, reservoir, conduit, and a booster pump function. Each of these LA phase functions is assigned with certain physiological vorticity and pressure indices. Any alteration in cardiac tissue behavior, caused by heart disease, may affect these measured indices [1]. There are many fluid dynamics studies about LA, however, there is not any specific fluid-structure interaction (FSI) modeling of the LA because of its intrinsic intricate geometric, functional and material characteristics. In this study, a FSI model has been developed on a simplified 2D geometry representing the LA during the reservoir phase to investigate how different LA wall material influence the hemodynamics.

Methods

To develop the 2D model, it is assumed that the shape of the LA is the midsection slice of a sphere including two inlets, i.e. the pulmonary veins (PVs). The radius of the model is calculated from volume information of the standard LA volume-time curve over the cardiac cycle. The LA diameter is 51.8 mm and the wall thickness is 4 mm. The inlet dimensions were determined by presuming a circular cross section for the PVs, averaging the cross sectional area over four PVs, and calculating the diameter from the area. The PVs diameter is 13.2 mm. Poiseuille flow velocity profile was applied at the inlets. The blood was considered as an incompressible fluid with a density and viscosity of 1060 kg/m^3 and 0.005 Pa s, respectively. Three sets of hyperelastic materials, a nearly incompressible Ogden, an incompressible Neo-Hookean, and a nearly incompressible Neo-Hookean model were prescribed as the wall materials. The material parameters were set to make the nearly incompressible Neo-Hookean more similar and the nearly incompressible Ogden more dissimilar to biological cardiac tissue. A fully coupled FSI simulation was conducted in Comsol Multiphysics.

Results and Discussion

Figure 1 shows some measured indices during LA reservoir phase. Vorticity and pressure, as the important blood flow drivers in the cardiac chambers, can be used as diagnostic parameters and wall shear stress (WSS) has been suggested as a marker of thrombosis formation [2,3]. Our results show that different hyperelastic materials result in different pressure, vorticity and WSS. As the vorticity affect pressure and WSS, higher vorticity generates higher pressure and WSS. High pressure results in greater energy loss and high WSS may cause tissue remodeling or thrombosis formation. The results also show that the closer is the material model to the biological cardiac tissue behavior, the lower is the vorticity, the pressure and the WSS.

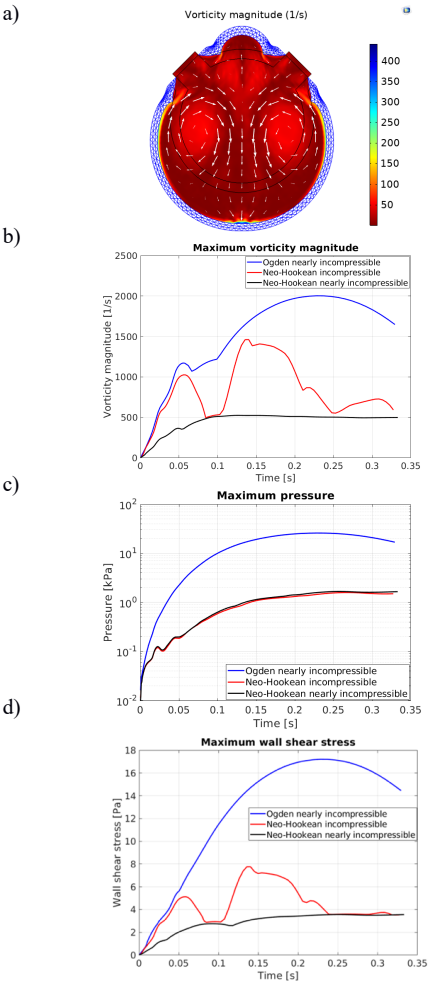

Figure 1: a) Wall deformation and Vortex rings at the end of LA reservoir phase (the color bar represents the vorticity magnitude). b) Max. vorticity magnitude. c) Max. pressure. d) Max. wall shear stress

References

1. Masci et al. J Biomech Eng, 142/011002-1 (2020).
2. Pedrizzetti et al. Nat. Rev. Cardiol, **11**, 545-553 (2014).
3. Güla et al. Sci Rep **7**, 16772 (2017).

Paper 3

A Fully Coupled Fluid-Structure Interaction Simulation of A Simplified Left Atrium

Masoud Meskin, Matthias Bo Stuart, Jørgen Arendt Jensen, Marie Sand Traberg

Name of journal:
Annual meeting of Biomedical engineering society

Document Version:
Published in proceedings of BMES2020

DOI:

A Fully Coupled Fluid-Structure Interaction Simulation Of A Simplified Left Atrium Model

Masoud Meskin , Matthias Bo Stuart , Jørgen Arendt Jensen, Marie Sand Traberg
Department of Health Technology, Technical University of Denmark, 2800 Kgs. Lyngby, Denmark

Introduction: Assessment of the hemodynamics in the left atrium (LA) contains crucial pathophysiological information. The LA has three phase functions, reservoir, conduit, and a booster pump function. Each of these LA phases is assigned with certain physiological indices, providing prognostic information in cardiac disease diagnosis. Many LA fluid dynamics studies exist, however, there are currently no specific fluid-structure interaction (FSI) simulations of the LA. One difficulty in FSI modeling of the LA is its complex material characteristics. In this study, three FSI models with three different hyperelastic materials have been developed based on a simplified 3D geometry representing the LA during the reservoir phase. The aim of the study is to investigate which model represents the LA physiological characteristics and is more accurate for FSI modeling of the LA.

Figure 1. Simplified 3D LA model with four inlets as PVs.

Materials and Methods: To develop the 3D model (Fig. 1), it is assumed that the LA is spherical with four circular pulmonary veins (PVs). The model diameter is 45.7 mm obtained from volume information of a standard LA volume-time curve over one cardiac cycle. The wall thickness is 2 mm, and the PVs diameter is 13.2 mm. The inlet flowrate profile was taken from Chnafa et al. 2015 with the peak flowrate of 33 ml/s. The initial pressure was set to zero. The blood was considered incompressible with a density of 1060 kg/m^3 and a viscosity of 4 mPa.s. Three sets of isotropic hyperelastic materials, presented in Tab.1, were prescribed as the wall material. The Ogden model with N=3 have a rubber behavior and the Neo-Hookean models are closer to biological LA tissue characteristics (Di Martino et al. 2011). A tetrahedral mesh with 92810 elements was applied. The difference between the results was zero after conducting mesh sensitivity analysis. The reservoir time span is 0.325 s. Simulations were conducted in Comsol Multiphysics v5.5.

	μ (kPa)	k (kPa)	ρ (kg/m^3)	G (kPa)	α
Nearly incompressible Neo-Hookean	14.9	450	1055	-	-
Incompressible Neo-Hookean	14.9	-	1055	-	-
Nearly incompressible Ogden	-	4.2x10^7	1055	6.3 1.2 -10	1.3 5 -2

Table1. Material parameters for the hyperelastic materials. μ is the lamé parameter, k is the bulk modulus, ρ is the density, G is the shear modulus and α is the constant parameter.

Results and Discussion: The maximum of Vorticity magnitude, wall shear stress (WSS), pressure, and Von Mises stress, in the fluid domain volume, were calculated (Figs.2). Comparing the trend of the WSS and vorticity, the WSS behaves similarly as the vorticity, which confirms the existence of correlation between them mentioned by Güla et al. 2017. The low mean absolute percentage difference amongst the models, 5% for WSS and 4% for vorticity, suggests that the LA hemodynamics is not affected by the LA wall during the reservoir phase. A considerable difference of 750 Pa exists in the maximum pressure; however, they are all in the v-wave pressure range (800-2800 Pa). But as the higher pressure causes higher energy loses, the Neo-Hookean models better represents the LA v-wave pressure. As a high wall stress causes abnormal stretches and permanent remodeling, the nearly incompressible Neo-Hookean shows lower maximum stress (0.5 MPa) compare to Ogden nearly incompressible (3.3 MPa), represents better a healthy LA wall behavior.

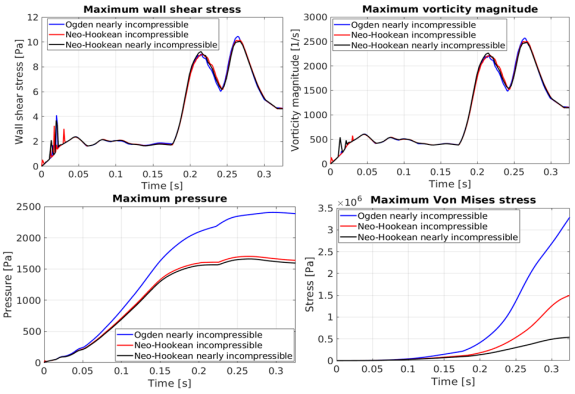

Figure 2. Calculated max wall shear stress, max vorticity magnitude, max pressure, and max von mises stress.

Conclusions: The results show that the LA wall behavior can be represented by a nearly incompressible Neo-Hookean in a FSI model setup because maximum pressure falls within the physiological range and exhibits lower maximum wall stress and lower maximum pressure.

Paper 4

2D Fluid-Structure Interaction Modeling of the Left - Impact of Mitral Valve Stiffening

Masoud Meskin, Jørgen Arendt Jensen, Matthias Bo Stuart, Marie Sand Traberg

Name of journal:
Congress of the European Society of Biomechanics

Document Version:
Accepted for the 27th Congress of the European Society of Biomechanics.

DOI:

2D FLUID-STRUCTURE INTERACTION MODELING OF THE LEFT ATRIUM – IMPACT OF MITRAL VALVE STIFFENING

Masoud Meskin (1), Jørgen Arendt Jensen (2), Matthias Bo Stuart (2), Marie Sand Traberg (1)

1. Cardiovascular biomechanics group, Technical University of Denmark, Denmark; 2. Center for fast ultrasound imaging, Technical University of Denmark, Denmark

Introduction

The mitral valve (MV) plays a crucial role in a healthy cardiac function and is associated more to the heart valve diseases amongst the four heart valves. Some MV diseases cause MV leaflets stiffening, and result in malfunctioning MV and disruption of the physiologic performance of the left heart. The impacts of MV stiffening (MVS) on the left atrium (LA) hemodynamics are not completely known. This study presents a 2D simplified fluid-structure interaction (FSI) model of the LA and the MV over a full cardiac cycle to investigate the impact of MVS on the LA hemodynamics.

Methods

To build the 2D model (Fig.1A), it is assumed that the 3D LA has a symmetric spherical shape with four circular pulmonary veins (PVs), and therefore the 2D model would be a circular plane with rectangular PVs. The LA diameter is 45.7 mm, the LA wall thickness is 2 mm, and the PVs diameter is 13.2 mm. Two sets of nearly incompressible hyperelastic material models were prescribed for the MV [1] and the LA [2]:

$$W_{MV} = \frac{1}{2}\,\mu(I_{1c} - 3) + \frac{1}{2}\,k_{MV}(J-1)^2 \qquad (1)$$

$$W_{LA} = C_{NH}\left[I_{1c}(I_{3c})^{-\frac{1}{3}} - 3\right] + \frac{1}{2}k_{LA}(J-1)^2 \qquad (2)$$

where W_{MV} and W_{LA} are the strain energy density functions, μ and C_{NH} are the stress like material parameters, I_{1c} and I_{3c} are the first and third invariants of the right Cauchy-Green strain tensor, k_{MV} and k_{LA} are the bulk modulus of the MV and the LA, and J is the determinant of the deformation tensor. To mimic the MVS, four different stress like material parameters, μ_1=150, μ_2=450, μ_3=850 and μ_4=1100 [kPa] were assigned to the MV. A realistic PV flowrate profile was applied at the inlets, and a time dependent pressure profile was considered as the outlet boundary condition. A triangular tension force function was applied to the LA wall to mock the LA contraction. Triangle and quad elements were utilized to generate the mesh. The blood was considered incompressible with a density of 1060 kg/m^3 and a viscosity of 4 mPa·s. The FSI simulations were done in Comsol Multiphysics.

Results and Discussion

The LA pressure (LAP), LA volume (LAV), transmitral velocity (TV) and the MV effective orifice length (EOL) were calculated and the hemodynamics indices, a-peak of the LAP, E/A ratio of the TV, late diastolic velocity time integration (VTI_LD) of TV, the maximum early diastolic EOL (EOL_E), and the LA total emptying fraction (TEF) are reported in Tab.1.

Index	a-peak (mmHg)	EOL (mm)	E/A	VTI_LD (cm)	TEF
μ1	11.9	16.1	2.42	1.6	0.47
μ2	16.2	10.6	1.10	3.9	0.43
μ3	20.0	7.9	0.9	4.9	0.3
μ4	21.4	6.4	0.86	4.8	0.22

Table 1: FSI-calculated hemodynamics indices.

The results show that the MVS reduces EOL and increases the TEF, resulting in the LAP enhancement, keeping the LAP elevated and amplifying the a-peak of the LAP (Fig.1B). Considering the TV profile (Fig.1C), the E-peak is suppressed, and the A-peak is amplified which is reflected in the calculated E/A ratio and VTI_LD (Tab.1). In conclusion, the MVS dramatically impairs the LA physiologic performance.

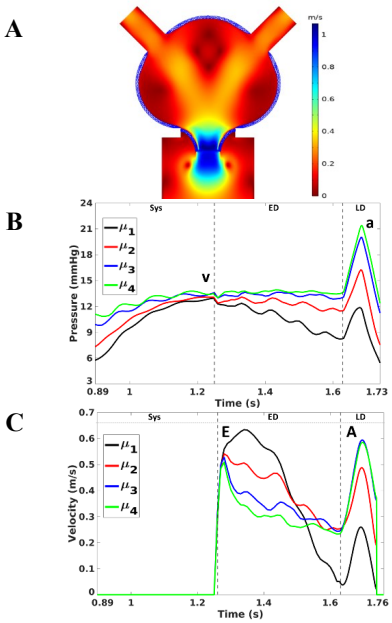

Figure 1: A) Velocity field in ED, B) LAP and C) TV. Sys=systolic ED=early diastolic, LD=late diastolic

References

1. Di Martino et al, J Biomech, 2011,10.1016.
2. Weinberg et al, J Cardiovascular Eng (2005): 37-43.

Paper 5

A New Technique of Reconstructing 3D Geometries From CT Images - A CFD Study

Masoud Meskin, Rasmus Hvid, Marie Sand Traberg

Name of journal:
Congress of the European Society of Biomechanics

Document Version:
Accepted for the 27th Congress of the European Society of Biomechanics.

DOI:

A NEW TECHNIQUE OF RECONSTRUCTING 3D GEOMETRIES FROM CT IMAGES – A CFD STUDY

Masoud Meskin (1), Rasmus Hvid (1), Marie Sand Traberg (1)

1. Cardiovascular Biomechanics Group, Technical University of Denmark, Denmark

Introduction

Numerical models have become a fundamental tool in cardiovascular studies [1]. The first step in numerical modeling is reconstructing a prototypical 3D geometry of the structure of interest from different medical imaging modalities [2]. A way to reconstruct the 3D geometry of the cardiac components is through segmenting computed tomography (CT) images and generating a mesh. However, the generated mesh may be corrupted during segmentation, resulting in a flawed or discontinuous mesh. Moreover, repairing such a corrupted mesh is a tedious task. In this work, the 3D structure of the left atrial (LA) chamber was generated with a new technique by using the "freeform part modeling" feature in the Autodesk Inventor® (Autodesk, Inc., California, USA). The created 3D LA geometry was then used in a computational fluid dynamic (CFD) study of the LA during left ventricular diastolic phase in STAR-CCM+ (Siemens Industries Digital Software).

Methods

To prepare the 3D LA geometry for the CFD study, first the LA structure at the beginning of systole was segmented, using 3DSlicer, from a 4D CT image data set and imported into Autodesk Inventor as a surface mesh (Fig.1a). Then a freeform cylinder with the approximate dimensions of the LA structure was created and divided into a number of rectangular patches (Fig.1b). Next, each rectangular patch was manipulated and formed individually to be shaped like the area of the LA structure it covers. Afterwards, the pulmonary veins (PVs) are added as cylindrical tubes with circular cross-sectional area, and the mitral valve (MV) was embedded as an oval conduit at the outlet of the LA. The LA structure was imported into STAR-CCM+ and polyhedral-shaped cells along with prismatic cells were utilized to generate volume and boundary layer mesh elements (Fig.1c and 1d). The final mesh consists of 215389 elements. The PVs and MV diameters and the inlet flowrate profiles were taken from Dahl et.al [3]. The MV was connected to a long tube and a zero pressure was set as the outlet boundary condition at the end of the tube. Blood is the working fluid and considered incompressible, with density of 1060 kg/m^3 and viscosity of 4 mPa·s.

Results

The results are mesh independent as the relative difference between the results is less than 3% after conducting mesh convergence analysis. The velocity contour on the MV plane and the intra-atrial flow field streamlines during the diastolic phase are displayed in Fig.2. The maximum transmitral velocity is 0.58 m/s and the maximum intra-atrial velocity is 0.47 m/s. The vortex rings formation is also visible in the LA chamber.

Discussion

The topology of the reconstructed LA geometry resembles the one reported by Dahl et al [3]. The values of maximum transmitral velocity and intra-atrial flow reported by Dahl et al [3] are 0.50 m/s and 0.60 m/s respectively, which are close to the findings of this study. In conclusion, the freeform technique could generate a representative model of the LA geometry.

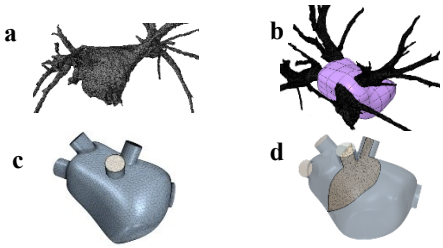

Figure 1: a) 3D surface mesh. b) freeform cylinder. covered the surface mesh. c,d) mesh structure.

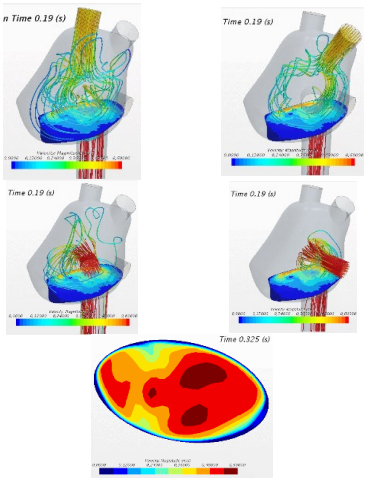

Figure 1: The intra-atrial flow field and transmitral velocity contour.

References

1. Lamata et al, Biophysics and molecular biology,2014
2. Masci et al, J Biomech Eng, 2020.
3. Dahl et al, BMES, 2012.